

# Control Methods for Improving Tracking Accuracy and Disturbance Rejection in Ball Screw Feed Drives

by

Yasin Hosseinkhani

A thesis  
presented to the University of Waterloo  
in fulfillment of the  
thesis requirement for the degree of  
Doctor of Philosophy  
in  
Mechanical Engineering

Waterloo, Ontario, Canada, 2013

©Yasin Hosseinkhani 2013

## **AUTHOR'S DECLARATION**

I hereby declare that I am the sole author of this thesis. This is a true copy of the thesis, including any required final revisions, as accepted by my examiners.

I understand that my thesis may be made electronically available to the public.

Yasin Hosseinkhani

## Abstract

This thesis studies in detail the dynamics of ball screw feed drives and expands understanding of the factors that impose limitations on their performance. This knowledge is then used for developing control strategies that provide adequate command following and disturbance rejection. High performance control strategies proposed in this thesis are designed for, and implemented on, a custom-made ball screw drive.

A hybrid Finite Element (FE) model for the ball screw drive is developed and coded in Matlab programming language. This FE model is employed for prediction of natural frequencies, mode shapes, and Frequency Response Functions (FRFs) of the ball screw setup. The accuracy of FRFs predicted for the ball screw mechanism alone is validated against the experimental measurements obtained through impact hammer testing. Next, the FE model for the entire test setup is validated. The dynamic characteristics of the actuator current controller are also modeled. In addition, the modal parameters of the mechanical structure are extracted from measured FRFs, which include the effects of current loop dynamics.

To ensure adequate command following and disturbance rejection, three motion controllers with active vibration damping capability are developed. The first is based on the sensor averaging concept which facilitates position control of the rigid body dynamics. Active damping is added to suppress vibrations. To achieve satisfactory steady state response, integral action over the tracking error is included. The stability analysis and tuning procedure for this controller is presented together with experimental results that prove the effectiveness of this method in high-speed tracking and cutting applications. The second design uses the pole placement technique to move the real component of two of the oscillatory poles further to the left along the real axis. This yields a faster rigid body response with less vibration. However, the time delay from the current loop dynamics imposes a limitation on how much the poles can be shifted to the left without jeopardizing the system's stability. To overcome this issue, a lead filter is designed to recover the system phase at the crossover frequency. When designing the Pole Placement Controller (PPC) and the lead filter concurrently, the objective is to minimize the load side disturbance response against the disturbances. This controller is also tested in high-speed tracking and cutting experiments. The third control method is developed around the idea of using the pole placement technique for active damping of not only the first mode of vibration, but also the second and third modes as well. A Kalman filter is designed to estimate a

state vector for the system, from the control input and the position measurements obtained from the rotary and linear encoders. The state estimates are then fed back to the PPC controller. Although for this control design, promising results in terms of disturbance rejection are obtained in simulations, the Nyquist stability analysis shows that the closed loop system has poor stability margins. To improve the stability margins, the McFarlane-Glover robustness optimization method is attempted, and as a result, the stability margins are improved, but at the cost of degraded performance. The practical implementation of the third controller, was, unfortunately, not successful.

This thesis concludes by addressing the problem of harmonic disturbance rejection in ball screw drives. It is shown that for cases where a ball screw drive is subject to high-frequency disturbances, the dynamic positioning accuracy of the ball screw drive can be improved significantly by adopting an additional control scheme known as Adaptive Feedforward Cancellation (AFC). Details of parameter tuning and stability analysis for AFC are presented. At the end, successful implementation and effectiveness of AFC is demonstrated in applications involving time periodic or space periodic disturbances. The conclusions drawn about the effectiveness of the AFC are based on results obtained from the high-speed tracking and end-milling experiments.

## **Acknowledgements**

I would like to express my deep gratitude to my supervisor, Professor Kaan Erkorkmaz, whose guidance, support, and patience made this thesis possible. He inspired me throughout my work with his intellect and enthusiasm for teaching and research.

I would also like to thank my thesis committee members: Professor Amir Khajepour, Professor John McPhee, Professor Kaan Inal and Professor Ridha Ben Mrad for their helpful comments and advice.

I gratefully acknowledge the help I received from MME technical staff, in particular, Robert Wagner, Jason Benninger, Andy Barber, James Merli, and Neil Griffett.

Many thanks go to all my colleagues and friends at Precision Controls Laboratory specially Amin Kamalzadeh, Dan Gordon, Amir Rouzrokh, Jeff Gorniak, Wilson Wong, and Dayna Chan from whom I had the privilege of learning something in one way or another.

Finally, I would like to thank my parents for their unconditional love and support throughout my life, and my dearest Faezeh who has always supported me with love and encouragement.

## **Dedication**

To my parents and to my dear wife Faezeh.

## Table of Contents

AUTHOR'S DECLARATION .....	ii
Abstract .....	iii
Acknowledgements .....	v
Dedication .....	vi
List of Figures .....	x
List of Tables.....	xv
Chapter 1 Introduction.....	1
Chapter 2 Literature Review .....	5
2.1 Modeling of Ball Screw Drives.....	5
2.1.1 Rigid Body Modeling.....	6
2.1.2 Lumped Mass-Spring-Damper Modeling.....	7
2.1.3 Continuum Mechanics Based Modeling.....	8
2.1.4 Finite Element Modeling.....	9
2.1.5 Modeling of Friction.....	10
2.1.6 Lead Errors .....	12
2.2 Feed Drive Control Techniques for Wide Bandwidth.....	13
2.2.1 P-PI Position-Velocity Cascade Control (standard industrial solution) .....	14
2.2.2 Plug-in Type Controllers for Vibration Attenuation .....	16
2.2.3 Pole-Placement Based Vibration Damping .....	16
2.2.4 Sliding Mode Control.....	18
2.2.5 Robust Control and Gain Scheduling .....	19
2.3 Compensation of Repetitive Disturbances and Errors.....	19
2.3.1 Internal Model Principle and Repetitive Control.....	20
2.3.2 Adaptive Feedforward Compensation .....	21
2.4 Conclusion.....	22
Chapter 3 Modeling and Identification of Ball Screw Driven Feed Drives .....	24
3.1 Experimental Setup .....	24
3.2 Modeling and Identification of Current Control Loop Dynamics .....	27
3.3 Finite Element Modeling of Ball Screw Mechanism .....	34
3.3.1 Model Updating in Ball Screw-Nut Assembly.....	36
3.3.2 FE Model for the Entire Setup.....	38

3.4 Frequency Domain Model Identification through Modal Analysis .....	50
3.4.1 Lumped Mass Model (Rigid Body Motion + 1st Vibration Mode) .....	50
3.4.2 Multiple-Mode Model (Rigid Body Motion + First Three Modes) .....	51
3.5 Conclusions.....	54
Chapter 4 Wide Bandwidth Controller Design Based on Modal Decomposition.....	55
4.1 Center of Mass Controller (COM).....	56
4.1.1 Experimental Results .....	67
4.2 Pole Placement and Loop Shaping Design for Optimal Disturbance Rejection .....	72
4.2.1 Experimental Results .....	79
4.3 Controller Design for Rigid Body Dynamics and Multiple Vibration Modes .....	83
4.4 Conclusions.....	97
Chapter 5 Rejection of Harmonic Disturbances in Ball Screw Drives .....	99
5.1 Periodic Disturbances in Ball Screw Driven Machines .....	99
5.2 Structure and Frequency Response of AFC Resonators .....	104
5.3 Position Control of Ball screw Drives Using AFC Compensators .....	108
5.3.1 Tuning of Adaptation Gains and Stability Analysis .....	108
5.3.2 Using AFC in Milling Experiments .....	113
5.3.3 Harmonic Disturbance Rejection for Ball Screw Lead, Mechanism, and Encoder Misalignment Errors .....	119
5.3.4 Experimental Results .....	121
5.4 Conclusions.....	125
Chapter 6 Conclusions & Future Work.....	126
6.1 Future Research Directions.....	127
Bibliography .....	128
Appendix A Finite Element Modeling of Ball Screw-Driven Feed Drives .....	137
A.1 Proposed Finite Element Scheme for the Test Setup .....	137
A.2 Finite Element Modeling of the Screw Shaft.....	138
A.2.1 Three-Dimensional Modeling .....	138
A.3 Modeling of the Ball screw-Nut Interface .....	141
A.3.1 Introduction of the Intermediate Coordinate Systems.....	142
A.3.2 Derivation of the Stiffness Matrix for the Ball screw-Nut Interface.....	145
A.3.3 The Mass Matrix for the Ball screw-Nut Interface .....	153

## List of Figures

Figure 2.1: Two-mass model. ....	7
Figure 2.2: Hybrid FE model of a ball screw drive [29]. ....	9
Figure 2.3: N-elementary spring blocks of the GMS frictional model [41]. ....	11
Figure 2.4: Hysteresis phenomena in a ball screw drive (a) Analytical (FE driven) versus experimental friction torque (b) Analytical (FE driven) versus experimental linear displacement [44]. .....	12
Figure 2.5: Simplified ball screw drive model. ....	14
Figure 2.6: (a) Overall scheme of P-PI control (b) $H^\infty$ norm of $G_{12}$ and $G_{22}$ versus normalized crossover frequency of the inner loop [60]. ....	15
Figure 2.7: Active damping of structural vibrations by pole placement. ....	17
Figure 2.8: Disturbance FRF of the PPC controller designed in this thesis versus the one in [3]. ....	18
Figure 2.9: Periodic signal generation in repetitive control [87]. ....	21
Figure 2.10: Different configurations for implementation of AFC [90]. ....	22
Figure 3.1: Ball Screw Test Setup. ....	25
Figure 3.2: Feed drive FRFs from motor torque command to acceleration responses at encoder locations. ....	26
Figure 3.3: Feed drive FRFs from impact force to the table to acceleration responses at encoder locations. ....	27
Figure 3.4: Schematics of a Y-connected stator winding. ....	27
Figure 3.5: Current vector resolved in the d-q frame. ....	28
Figure 3.6: Block diagram of current control loop. ....	30
Figure 3.7: Measured and modeled FRF of the monitored current. ....	32
Figure 3.8: Loop magnitude and phase of current amplifier. ....	33
Figure 3.9: Difference between current FRF at current monitoring measurement point and actual current FRF. ....	33
Figure 3.10: Acceleration FRF measured at encoder #2 before and after correction for current loop dynamics. ....	34
Figure 3.11: Schematic representation of the test setup. ....	35
Figure 3.12: Setup for impact hammer testing on the ball screw with free-free boundary conditions. ....	36
Figure 3.13: Measured and predicted FRFs when nominal nut stiffness is used in the FE model. ....	37
Figure 3.14: Measured and predicted FRFs when updated nut stiffness is used in the FE model. ....	38

Figure 3.15: FRF from motor torque to angular position of the screw shaft at Encoder #2 (nominal value of thrust bearing axial stiffness is used in the FE model). .....	40
Figure 3.16: FRF from motor torque to angular position of the screw shaft at Encoder #2 (updated value of thrust bearing axial stiffness is used in the FE model). .....	40
Figure 3.17: Torsional deformation of screw shaft at mode #1 (141 Hz). .....	41
Figure 3.18: Axial deformation of screw shaft at mode #1 (141 Hz). .....	41
Figure 3.19: Simple model for calculating the natural frequency of the axial mode. ....	42
Figure 3.20: FRF from motor torque excitation to linear displacement of the table. ....	43
Figure 3.21: FRF from impact hammer force applied to the table to linear acceleration of the table when it is located at three different spots within its stroke. ....	44
Figure 3.22: Torsional deformation of screw shaft at mode #2 (459 Hz). .....	45
Figure 3.23: FRF from motor torque to angular position of the screw shaft at Encoder #2. ....	45
Figure 3.24: FRF from motor torque to angular acceleration of the screw shaft at Encoder #2. ....	46
Figure 3.25: Disk-pack versus jaw type coupling [109]. .....	47
Figure 3.26: FRF from motor torque to angular position of the screw shaft at Encoder #2. ....	48
Figure 3.27: Torsional deformation of screw shaft at mode #3 (1020 Hz). .....	48
Figure 3.28: Torsional deformation of screw shaft at mode #4 (1263 Hz). .....	49
Figure 3.29: Torsional deformation of screw shaft at mode #2 (1668 Hz). .....	49
Figure 3.30: Modeled (solid line) and measured (dashed line) open-loop frequency response functions. ....	51
Figure 3.31: Curve fitting to rigid body dynamics and first three resonances. ....	53
Figure 3.32: Modeled and measured open-loop frequency response functions (multiple modes). ....	53
Figure 4.1: Overall control scheme for the COM controller. ....	59
Figure 4.2: Block diagram of the new plant for which COM control law is designed. ....	60
Figure 4.3: Effect of the factor of damping increase on frequency response of the damped plant .....	61
Figure 4.4: Load side disturbance FRF for COM controllers with different values of $\beta$ . ....	62
Figure 4.5: P-PI cascade feedback control plus velocity and acceleration feedforward control. ....	63
Figure 4.6: Loop transfer function magnitude for COM and P-PI schemes. ....	64
Figure 4.7: Nyquist diagrams for COM and P-PI control. ....	65
Figure 4.8: Sensitivity functions for COM and P-PI control. ....	65
Figure 4.9: Load side disturbance response for open- and COM closed-loop cases. ....	66
Figure 4.10: Command following FRF of the designed COM controller. ....	66

Figure 4.11: Simulated stable zones for: (a) COM controller, and (b) P-PI cascade controller. ....	67
Figure 4.12: Experimental setup. ....	67
Figure 4.13: Positioning error in 1 inch slotting at 1475 rpm spindle speed in 6065 aluminum. ....	68
Figure 4.14: Positioning error in 1 inch slotting at 3500 rpm spindle speed in 6065 aluminum. ....	69
Figure 4.15: Spectral content of positioning error in 1 inch slotting at 3500 rpm spindle speed. ....	70
Figure 4.16: High speed tracking (velocity: 1 m/s, acceleration: 10 m/s <sup>2</sup> , jerk: 200 m/s <sup>3</sup> ). ....	71
Figure 4.17: High speed tracking (velocity: 0.5 m/s, acceleration: 8.2 m/s <sup>2</sup> , jerk: 200 m/s <sup>3</sup> ). ....	71
Figure 4.18: Proposed control scheme using pole placement and loop shaping. ....	73
Figure 4.19: Load side disturbance response for open- and closed-loop cases. ....	75
Figure 4.20: Loop transfer function magnitude for PPC+LS and P-PI schemes. ....	76
Figure 4.21: Nyquist diagrams for PPC + loop shaping and P-PI control. ....	77
Figure 4.22: Real and imaginary plots of the load side disturbance response. ....	77
Figure 4.23: Simulated tracking errors for: (a) P-PI cascade controller, and (b) PPC controller. ....	79
Figure 4.24: Table positioning errors during machining. ....	81
Figure 4.25: High speed tracking (velocity: 0.5 m/s, acceleration: 8.2 m/s <sup>2</sup> , jerk: 200 m/s <sup>3</sup> ). ....	82
Figure 4.26: Multi-mode Pole Placement Controller (PPC) with a Kalman filter observer. (Subsystems that are used in derivation of the loop transfer function are indicated by dashed lines.)	87
Figure 4.27: Simulated position response of the load side to a step disturbance on the motor side for $R_w = 1e6$ and different choices of pole shifting factors. ....	88
Figure 4.28: Simulated time response of plant oscillatory states to a step disturbance on the motor side for $R_w = 1e6$ and different choices of pole shifting factors. ....	89
Figure 4.29: Singular values of $K_2(s)$ in Equation (4.40). ....	90
Figure 4.30: Nyquist plot for MMPPC ( $\beta_1=\beta_2=\beta_3=5$ ) with a Kalman filter observer ( $R_w = 1e6$ ). ....	91
Figure 4.31: Nyquist plot for MMPPC ( $\beta_1=\beta_2=\beta_3=5$ ) with a Kalman filter observer ( $R_w = 2e3$ ). ....	91
Figure 4.32: Simulated position response of the load side to a step disturbance on the motor side for $R_w = 2e3$ and different choices of pole shifting factors. ....	92
Figure 4.33: Simulated time response of plant oscillatory states to a step disturbance on the motor side for $R_w = 2e3$ and different choices of pole shifting factors. ....	92
Figure 4.34: Multi-mode Pole Placement Controller (PPC) with Glover–McFarlane robustification. ....	93
Figure 4.35: Nyquist diagrams for MM PPC+Kalman filter ( $R_w = 2e3$ ) with Glover–McFarlane robustification. ....	94

Figure 4.36: Simulated time response of system states to a step disturbance on the motor side for different choices of shifting factors in a robustified MMPPC+Kalman filter ( $R_w = 2e3$ ).....	95
Figure 4.37: Simulated position response of the load side to a step disturbance on the motor side for different choices of shifting factors in a robustified MMPPC+Kalman filter ( $R_w = 2e3$ ).....	95
Figure 4.38: Oscillatory pole map of the plant and the closed loop system. ....	96
Figure 4.39: Load side disturbance response for open- and closed-loop cases. ....	97
Figure 5.1: Simulated forces for machining aluminum 6061 with a 2-flute cutter at 3000 rpm spindle speed and 1524 mm/min feed.....	100
Figure 5.2: Simulated forces for machining aluminum 6061 with a 4-flute cutter at 3000 rpm spindle speed and 1524 mm/min feed.....	101
Figure 5.3: Commanded motion profile in lead error measurement experiment. ....	102
Figure 5.4: Five runs of discrepancy measurement between readings of linear and rotary encoders for feedrate of 10 mm/s. ....	103
Figure 5.5: Periodic profile of lead errors along the screw shaft.....	104
Figure 5.6: Structure of the AFC compensator [93]. ....	104
Figure 5.7: FRF of an AFC resonator with a pair of complex conjugate poles at 100 Hz for different values of the phase advance parameter.....	106
Figure 5.8: Closed control loop including the AFC resonator and a plant. ....	107
Figure 5.9: The effect of the proposed phase advance parameter on the Nyquist plot.....	107
Figure 5.10: AFC for compensation of multiple harmonics.....	108
Figure 5.11: Serial integration of the AFC compensator into the control system. ....	108
Figure 5.12: An alternative perspective on the control loop topology. ....	109
Figure 5.13: Bode plot of the loop transfer function when only one AFC resonator is implemented. ....	111
Figure 5.14: Nyquist plot of the loop transfer function when only one AFC resonator is implemented. ....	111
Figure 5.15: Bode plot of the loop transfer function with two AFC resonators. ....	112
Figure 5.16: Nyquist plot of the loop transfer function with two AFC resonators.....	112
Figure 5.17: Bode plot of the loop transfer function with three AFC resonators.....	113
Figure 5.18: Nyquist plot of the loop transfer function with three AFC resonators.....	113
Figure 5.19: Overall scheme of the AFC integrated control system for machining.....	114

Figure 5.20: Improvement in tracking accuracy when AFC resonators are enabled at target frequencies. ....	115
Figure 5.21: AFC improves table positioning accuracy during machining when the PPC is the main controller. ....	117
Figure 5.22: The effect of AFC on table positioning accuracy during machining when the P-PI is the main controller. ....	118
Figure 5.23: Sensitivity magnitude for P-PI+AFC versus PPC+AFC at target AFC frequencies of 50 Hz and 100 Hz. ....	119
Figure 5.24: Overall scheme of the control system including the AFC and a tracking error predictor for high speed tracking. ....	120
Figure 5.25: Overall scheme of the control system including the AFC and a pre-filter for high speed tracking. ....	121
Figure 5.26: Reference trajectory (displacement: 0.34 m, velocity: 1 m/s, acceleration: 10 m/s <sup>2</sup> , jerk: 200 m/s <sup>3</sup> ). ....	122
Figure 5.27: Tracking errors with PPC+T.E. Predictor before and after enabling the AFC. ....	123
Figure 5.28: Tracking errors with PPC+Pre-filter before and after enabling the AFC. ....	124
Figure 5.29: Change in lead error profile of the ball screw over a two-year period. ....	125
Figure A.1: Proposed FE modeling scheme for ball screw-driven feed drives. ....	137
Figure A.2: Three-dimensional beam element. ....	139
Figure A.3: Linear spring model for an oversized ball (a) and its decomposition into “L” (lower) and “U” (upper) configurations (b and c). ....	141
Figure A.4: CS1 definition shown for L-Configuration in (a) full view and (b) section view. ....	142
Figure A.5: CS1 and CS2 definitions in L and U configurations. ....	143
Figure A.6: The definition of the CS3. ....	143
Figure A.7: Definition of CS5 and CS4. ....	144
Figure A.8: Definition of CS1 <sub>N</sub> and CS1 <sub>BS</sub> with respect to CS1. ....	145
Figure A.9: Definition of CS2 with respect to CS1. ....	147
Figure A.10: Position of CS2 with respect to CS3. ....	148
Figure A.11: Position of CS3 with respect to CS4. ....	149
Figure A.12: Position of CS4 with respect to CS5. ....	150

## List of Tables

Table 3.1: AC motor electrical parameters.....	31
Table 3.2: Identified parameters of the current control loop.....	32
Table 3.3: Inertia of important components of the test setup.....	38
Table 3.4: Important lumped stiffness values.....	39
Table 3.5: Identified modal parameters of the ball screw drive.....	52
Table 4.1: Maximum and RMS values of table positioning errors during machining.....	82
Table 5.1: Tuned AFC resonator gains.....	110
Table 5.2: Maximum and RMS value of the tracking errors for the results presented in Figure 5.20. .....	115
Table 5.3: Cutting and AFC compensator parameters.....	116
Table 5.4: Maximum and RMS value of the tracking errors for the results presented in Figure 5.21. .....	116
Table 5.5: Maximum and RMS value of the tracking errors for the results presented in Figure 5.22. .....	117
Table 5.6: Maximum and RMS value of the tracking errors for the results presented in Figure 5.28. .....	124



# Chapter 1

## Introduction

In recent decades, there has been an ever-increasing demand from machine tool customers for higher productivity and tighter machining tolerances. The continuous progress in developing high performance cutting tools, spindles, feed drives and accurate sensors has enabled machine tool builders to respond to this market demand effectively. Nevertheless, in order to get the best performance out of a machine tool, motions of the feed drives need to be controlled with maximum accuracy. This goal can be achieved through design and implementation of control laws that provide a wide command tracking and disturbance rejection bandwidth, and are robust against variations in the plant model. A wide command tracking bandwidth is especially necessary when the reference trajectory is non-smooth or changes rapidly. In this regard, model-based feedforward inversion techniques are very effective and have been used extensively. Achieving a wide bandwidth for disturbance rejection is even more important. In most practical applications, the positioning errors are predominantly correlated with disturbances. Therefore, the control law should be designed in such a way to attenuate the effect of disturbances as much as possible. Knowing the characteristics of the disturbances involved in a particular application is helpful in this respect. Nevertheless, a controller with a high bandwidth for disturbance rejection can successfully handle a wide range of unknown disturbances. On the other hand, design of such a control law requires thorough understanding and accurate modeling of the dynamics of the controlled plant. Since the feed drives are electromechanical systems, both electrical and mechanical subsystems need to be modeled carefully. In particular, ball screw feed drives have a mechanical structure with multiple resonance modes. These modes impose serious limitations on the achievable control bandwidth.

This thesis studies accurate modeling, and control law design, for ball screw feed drives. Although the machine tools used for metal cutting are the primary focus in this thesis, the proposed control methods are also suitable for use in other industrial applications such as in manufacturing equipment, robots, material inspection equipment and so on. In Chapter 2, different methods for modeling the mechanical structure of a ball screw feed drive are reviewed. These methods vary in complexity from a simple rigid body model, to more complicated continuum mechanics and finite element models that are capable of capturing at least the most critical mode of vibration. Especially, the finite element method provides a powerful framework for not only predicting natural frequencies and mode shapes, but also capturing the effect of moving table on the dynamic response of the feed mechanism. At the

end of this chapter, the literature related to modeling of friction and periodic lead errors, which are important sources of disturbance in ball screw drives, is reviewed.

In Chapter 3, the Finite Element (FE) method is employed to predict the dynamic response of a custom-made ball screw feed drive that is designed and built in the Precision Controls Lab at University of Waterloo. The accuracy of the FE predictions are verified against the Frequency Response Function (FRF) measurements that are taken either through impact hammer testing, or sending stepped-sine excitation signals to the motor, and recording the response from the encoders. In the latter case, the dynamics of the electrical subsystem, which is in charge of regulating the current, also contributes significantly to the measured FRFs. In order to account for that contribution, the proportional and integral gains in the current regulation loop are approximated such that a best fit can be attained between the experimentally measured and modeled FRF of the current regulation loop. The delays due to PWM switching and digital-to-analog conversions are also considered in modeling the current regulation loop.

In the finite element code developed for modal analysis of the ball screw drive, 12 degree-of-freedom Timoshenko beam elements are used for modeling the screw shaft, while the ball screw-nut interface is modeled as a special 12 degree-of-freedom spring. The formulation of this element is derived from Okwudire in [1]. Other parts including the table assembly, the coupling, and the motor shaft are modeled as lumped masses. Stiffness characteristics of the bearings, in the form of lumped springs, are also incorporated in the FE model. Although the developed FE model has not been used directly for controller design in this thesis, it gives a valuable insight into the factors that influence the dynamic behavior of the ball screw drive. This knowledge is useful for optimal design of feed drive components, and also gives a hint about the range of parameter variation in the nominal plant when the table is moving.

In Chapter 3, three different control design ideas are investigated for position control of ball screw drives. Two of these methods were developed based on the assumption of a two-mass model for the plant. This model adequately captures the first mode of vibration which is the most critical in terms of controller design. In the first design, rotary and linear encoder data, representing the location of each mass in the two-mass model, are appropriately weighted and combined to calculate the location of the Center of Mass (COM). Although the possibility of using the COM location feedback in position controllers for ball screw drives is mentioned in [2], the novelty of the present work is the integration of active vibration damping, and load side position control with COM location control. To achieve a

reasonable compromise between the competing effects of each of these controllers, the load side disturbance response of the plant under closed loop control is formulated, and evaluated iteratively. At each iteration, a systematic approach based on loop shaping is used to determine the controller gains. The effectiveness of this method is shown in cutting and high speed tracking tests.

A new contribution of this thesis, implemented in the second design, is the consideration of loop delays and direct optimization of the disturbance response. The phase delay contributed by the power electronics is compensated, by applying loop shaping principles in conjunction with pole placement control. This helps to improve the worst case dynamic stiffness by 33%, over that of an earlier designed controller with active vibration damping [3]. The design also directly targets minimization of the load side disturbance response against cutting forces. This improves the ball screw drive's disturbance rejection across the frequency spectrum, rather than only making a local improvement at the expense of worsening the dynamic stiffness at another frequency.

In the third design, in addition to the first vibration mode, the second and third modes are also targeted for active damping. A Kalman filter is designed to estimate the required states for the feedback control law. The state feedback gain is determined using the pole placement design. Although in simulations, this control law can be tuned to generate promising results, the Nyquist stability analysis indicates that due to plant/model mismatch, the control gains designed for good vibration suppression destabilize the actual plant. To improve stability, a robustifying filter is added to the control loop, following the approach proposed by McFarlane and Glover [4]. Unfortunately, the additional dynamics introduced by this filter impairs the performance of the controller in vibration suppression. Unfortunately, this controller did not yield successful experimental results. Frequency domain disturbance response analyses also predict that this controller would not have performed as favorably as the earlier two methods.

In Chapter 5, a special control technique called Adaptive Feedforward Cancellation (AFC) is employed for rejection of harmonic disturbances. In ball screw feed drives, the harmonic disturbances enter the closed loop system in a number of different ways. Most commonly, they originate from periodic milling forces, but, even in high speed air-cutting movements, they are present due to lead errors and encoder run-out. The AFC compensator is integrated with a main controller to reject harmonic disturbances of known frequency. The frequency of the disturbance is calculated from the commanded spindle speed in milling applications, and from the reference velocity in high-speed tracking applications. The tuning procedure for the control system is explained, and the results of

metal cutting and high speed tracking experiments with AFC are presented, which confirm the effectiveness of the proposed method.

## **Chapter 2**

### **Literature Review**

Since the advent of the first numerically controlled machine tool in 1952, the mathematical development of control theory along with technological advances in constructing higher performance actuators, sensors and motion delivery mechanisms has continually pushed the envelope of achievable positioning accuracy in metal cutting. In the early days of this technology, an analog proportional amplifier used to be implemented as the servo controller while every attempt was made to build the machine tool structure as rigid as possible [5]. It was understood that to obtain a stable control system, the closed loop bandwidth had to be kept well below the natural frequency of the mechanical plant [5]. Although this condition was not deemed to be too constraining at that time, the move toward high speed machining in the following decades changed that mindset drastically. On one hand, the rapid progress in development of powerful actuators led to the realization of high acceleration movements in machines built out of lightweight materials [6]. And on the other hand, the growth of computational power made it possible to run complicated control algorithms in real time with high sampling rates [7]. These advancements have motivated the design of high-bandwidth controllers capable of following rapidly changing commands while attenuating wide spectrum of disturbances. To fulfill this objective, research on detailed and higher-order modeling of the electro-mechanical feed drives has been ongoing for years.

In this chapter, the available techniques for modeling of ball screw feed drives are first reviewed in Section 2.1. Then, some relevant control strategies are discussed in Section 2.2. And finally, a special class of controllers intended for rejecting disturbances of a particular frequency is reviewed in Section 2.3. These controllers are implemented to minimize the detrimental effects of harmonic disturbances on the positioning accuracy of feed drives, especially at frequencies above the closed loop bandwidth.

#### **2.1 Modeling of Ball Screw Drives**

Ball screw mechanisms have been widely used in the machine tool industry for converting rotary motion to linear motion. Compared to linear direct drives, they are less expensive, and, due to their inherent gearing ratio, provide more tolerance against load mass variations [8].

To accurately simulate the dynamic response of a ball screw drive, it is crucial to have reliable mathematical models of electro-mechanical components that constitute the controlled plant. In

addition, incorporating accurate models of disturbances such as cutting forces, friction and lead errors can dramatically improve the simulation results. There is also another aspect of dynamic modeling which relates directly to the controller design. From this aspect, the complexity of the modeled plant depends on the performance requirements of the controller. In some circumstances, a simple rigid body model of a ball screw drive may be sufficient for the purpose of control design, whereas in other situations a detailed higher order model may be necessary.

In the following subsections, first, the literature on different methods of modeling a ball screw mechanism is reviewed. Then, modeling attempts for some important system nonlinearities and disturbances such as friction and lead errors are reviewed.

### 2.1.1 Rigid Body Modeling

When the intended closed-loop bandwidth of a ball-screw driven feed drive is less than fifth of the frequency of the first observable mode of vibration, it is reasonable to use a rigid body model of the ball screw mechanism for the purpose of controller design [9]. In a rigid body dynamic model, the transfer function that relates the velocity response to the input torque is of first order:

$$\omega(s) = \frac{1}{J_s + B}(\tau - T_d) \quad (2.1)$$

Above,  $\omega$  is the output velocity,  $J$  is the reflected inertia on the motor shaft,  $B$  is the lumped viscous friction coefficient,  $\tau$  is the input torque and  $T_d$  is the disturbance torque. The value of  $J$  can be calculated analytically based on the kinetic energy of the entire transmission mechanism [10]:

$$\begin{aligned} J &= J_s + J_L \\ J_s &= M_s \frac{r^2}{2} \\ J_L &= M_L \left( \frac{L}{2\pi} \right)^2 \end{aligned} \quad (2.2)$$

Where  $M_s$  and  $M_L$  are successively the mass of the screw shaft and the mass of the load,  $L$  is the lead, and  $r$  is the equivalent radius of the screw shaft. In contrast, it is very difficult to derive a formula for calculation of the viscous friction coefficient ( $B$ ) based on first physical principles [11]. As such, experimental identification techniques are proposed in the literature for estimating the values of  $J$  and  $B$ . Erkorkmaz and Altintas [12] implemented a time-domain identification algorithm to

estimate the rigid body model parameters using the method of least squares. By refining their formulation, they could also identify the Coulomb friction coefficients simultaneously.

After rigid body model parameters are identified, they can be used in simulations or controller design. However, as mentioned earlier, this approach of modeling is suitable for a certain class of applications in which the frequency content of the control or disturbance signals does not excite the system resonances. If this assumption is not valid, more complicated models that account for structural flexibilities have to be used, as will be discussed in the following sections.

### 2.1.2 Lumped Mass-Spring-Damper Modeling

To account for mechanical flexibilities, lumped mass-spring-damper models have been used frequently in the literature. In particular, the two-mass model (Figure 2.1) has been extensively used to represent the dynamics of ball screw drives [3, 13-17]. This model has physically meaningful parameters which makes it intuitive and easy to understand. In Figure 2.1,  $m_1$  and  $m_2$  represent, in order, the inertia of the rotating and translating components; where  $b_1$  and  $b_2$  are viscous friction coefficients, and  $k$  and  $c$  represent the overall stiffness and damping between the motor shaft and the load. The control force is denoted by  $u$ , and disturbances on the motor and load side are represented by  $d_1$  and  $d_2$ .

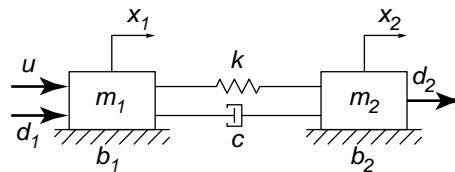


**Figure 2.1: Two-mass model.**

Higher order multi-mass lumped models are proposed by Frey et al. [18] and Holroyd [19]. These multi-mass models are conceptually an extension to the two-mass model, and are capable of capturing more vibration modes. Although lumped-mass models are expedient in terms of simulation and control design, the variation of their parameters with respect to drive position (or machine position) may need to be considered in order to update the model as required. Particularly, in a ball screw mechanism, the relative location of the nut with respect to the screw shaft affects the lumped parameters significantly. Therefore, to have reliable models, experimental identification of the parameters becomes necessary. Okwudire [20] and later Gordon and Erkorkmaz [21] implemented a least squares identification technique to extract the two-mass model parameters from measured FRF

data. This technique is adopted in this thesis for identifying the mechanical parameters of a ball screw setup used in control law design and validation.

Another approach for representing the dynamics of ball screws is to decompose it into dynamics of rigid body, a real pole and multiple second order resonators in the frequency domain:

$$G(s) = \frac{1}{s(Js + B)} + \sum_{n=1}^N \frac{R_n}{s^2 + 2\zeta\omega_n s + \omega_n^2} \quad (2.3)$$

The shortfall of this method is that the identified parameters lack a straight physical interpretation. Ewins [22] presented several Single-Degree-of-Freedom (SDOF) and Multiple-Degree-of-Freedom (MDOF) methods for modal parameter estimation from measured FRF data. These methods are nowadays adopted in commercial software packages for modal analysis. Campomanes [23] used SDOF Rational Fraction Polynomial (RFP) method [24] to identify dynamics of a machine tool structure. A similar approach is followed in this thesis to obtain a high-order model for the ball screw drive in Section 3.4.2.

### 2.1.3 Continuum Mechanics Based Modeling

Dynamic deformations of a ball screw system can be most accurately modeled through equations of wave propagation in an elastic medium (i.e. the screw shaft). This problem was addressed in [25] for a flexible shaft subjected to general linear boundary conditions at both ends. The authors applied the Laplace transform to the partial differential equation of wave propagation, and derived, after imposing the boundary conditions, an infinite dimension transfer function capable of capturing all torsional modes of vibration. However, they did not consider the axial deformations of the shaft which is particularly important in ball screw drives.

In contrast, Varanasi and Nayfeh [11] included the longitudinal wave propagation and the corresponding boundary conditions in their formulation. They also formulated the boundary condition imposed by the screw-nut interface. To obtain a reduced order model, they implemented the Galerkin method [26] using the semi-static deformation as the assumed mode shape. Following this approach, they derived a 2-DOF reduced order model and showed that in addition to a pair of complex conjugate poles that characterize the first dominant mode of vibration, the resulting model also has a non-minimum phase zero. Their method was shown to result in reasonable estimates of the first natural frequency; however, the mathematical derivation of it was complicated and tedious.

Moreover, it only captured one mode of vibration, which may be insufficient when a more thorough model, able to capture higher frequency dynamics, is required.

To overcome the difficulties mentioned above, more sophisticated discretization methods have been proposed in the literature, which are capable of capturing several relevant vibration modes. The most widely used method in this category is the Finite Element (FE) method which is the subject of discussion in the following section.

#### 2.1.4 Finite Element Modeling

The finite element method has proven to be one of the most powerful methods in predicting elastic, thermal and modal behavior of mechanical structures [27]. Van Brussel et al. [28] used this method to derive modal mass and stiffness matrices for building blocks of a three-axis milling machine. They next combined the reduced order models of these components to obtain a single model for the whole machine tool. Although they could successfully implement the reduced order model in simulations and control design, the initial FE model that they ended up creating had thousands of degrees of freedom, which made it computationally very expensive.

To avoid large scale finite element matrix problems, some researchers adopted a hybrid FE approach. In this approach, observing that the screw shaft has a dominant influence over the modal behavior of the feed drive, it is modeled as a flexible distributed-mass component and discretized by FEM, whereas other components are modeled as lumped mass or stiffness elements (Figure 2.2).

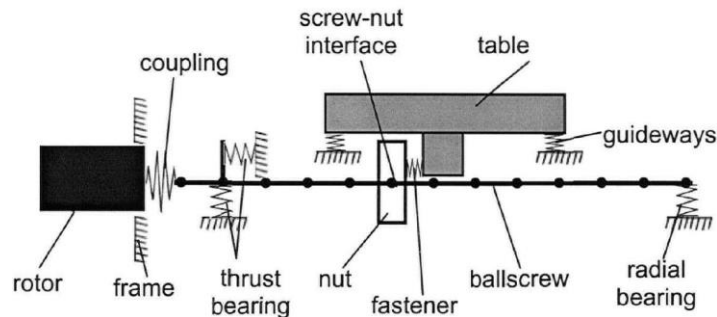


**Figure 2.2: Hybrid FE model of a ball screw drive [29].**

Smith [30] followed this approach to calculate the eigen-frequencies of a feed drive. He used Euler-Bernoulli beam elements, but allowed only axial and torsional deformations by removing degrees of freedom corresponding to lateral displacements. He also used a lumped stiffness element with 3 degrees of freedom for connecting the nut to the screw shaft. Kamalzadeh [31] took a similar

approach, but modeled the nut and table as an equivalent rotational mass which was connected to the screw shaft by a torsional spring. Zaeh et al. [32] expanded the FE analysis to include the bending modes of motion and argued that a 2-DOF spring element cannot sufficiently capture the dynamics of the screw-nut interface. Instead, they showed that a general three dimensional 12 DOF stiffness element would provide a more realistic model of the forces and torques transmitted through the screw-nut interface. In formulating the stiffness matrix, they considered direct stiffness terms as well as cross terms coupling the axial and torsional movements, and neglected all other cross-coupling effects. Later, Okwudire [1] revised Zaeh's formulation and showed that not only axial and torsional movements are coupled together, but they are also coupled to bending deformations as well. He experimentally measured the mode shapes and eigen-frequencies of axial, torsional and bending modes and showed that the predictions from his FE model are reasonably close to the measured values. Dadalau et al. [33] investigated the contribution of the helical groove on the surface of the screw shaft to the mass and stiffness properties of the beam elements used for FE modeling. He analytically derived the area and polar second moment of area of the screw shaft cross section, and proposed an experimental formula for manipulating these parameters based on the pitch of the screw shaft to get more accurate FE predictions.

In Section 3.3 of this thesis, a detailed finite element model of the ball screw setup used in our experiments is developed by adopting the most recent and advanced modeling techniques laid out in the literature [1, 33]. While the FE model is too complicated for control law design, it provides valuable insight into the dynamic response of the feed drive.

### **2.1.5 Modeling of Friction**

In machine tools, friction deteriorates the positioning accuracy by acting as a disturbance force opposing the motion. The steady-state error caused by constant disturbances can be effectively eliminated by using integral action in the controller. However, the output of the integral action cannot instantly change sign when the direction of frictional force is reversed, and hence during motion reversals, the integral action makes the detrimental effect of friction even worse due to incorrect compensation [34].

For lubricated metal-to-metal contacts, the transition between pre-sliding to gross sliding regime occurs at two intermediate phases: boundary lubrication and partial fluid lubrication [35]. In the boundary lubrication phase, the relative velocity of surfaces is low and a consistent film of lubricant cannot be created between the moving surfaces. As relative velocity increases, formation and

expansion of the lubrication film happens gradually. In the partial fluid phase, the lubrication film is still not thick enough to completely separate the sliding surfaces. Eventually, in the full lubrication phase (i.e. gross sliding) the two sliding surfaces become completely separated.

During the past decades, a variety of models for friction in lubricated contact have been proposed by researchers. These methods range from simple static formulations (like Coulomb + viscous friction model) to more sophisticated dynamic models. Armstrong [35] proposed a seven-parameter friction model which is capable of capturing many observed frictional behaviors such as the Stribeck effect, frictional lag, time dependence of Stribeck friction, and spring-like behaviour of friction in pre-sliding. However, it cannot capture hysteresis in the pre-sliding, and stick-slip behaviour in the sliding regime. To overcome the mentioned drawbacks and develop a comprehensive formulation capable of capturing as much of the frictional behaviour as possible, dynamic friction models have been proposed in recent decades [36-39]. In dynamic models, friction is formulated as a function of an internal state vector  $\mathbf{z}$ , the relative velocity  $\dot{x}$  and the relative displacement  $x$ :

$$F_f = F(\mathbf{z}, \dot{x}, x) \quad (2.4)$$

Generalized Maxwell-Slip (GMS) model is one of the most recent dynamic models proposed in the literature [40]. In the GMS, it is assumed that the friction force is a summation of the individual force contributions of N-elementary spring blocks, which are connected in a parallel manner, as shown in Figure 2.3. This model has been shown to be capable of replicating a wide range of observed frictional behaviors. Jamaludin [41] experimentally identified the parameters of the GMS model and used this data to design and implement a feed-forward friction compensator.

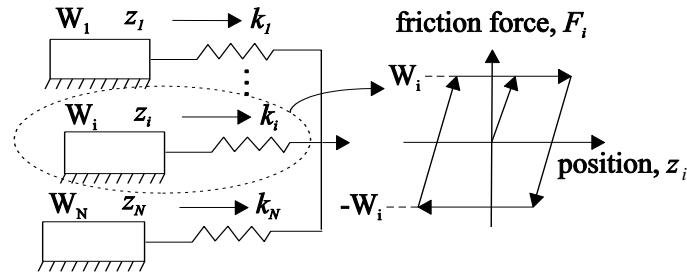


**Figure 2.3: N-elementary spring blocks of the GMS frictional model [41].**

Similar to sliding friction, the evolution of rolling friction is also a two-step process involving pre-rolling followed by gross rolling. Many researchers have attributed the motion loss at velocity reversals in mechanical systems with rolling elements to the transition between the above mentioned

rolling friction regimes [42]. Ro and Hubble [43] addressed this problem when developing a controller for sub-micron positioning of a precision slide system. Cuttino et al. [44] performed three dimensional finite element contact analysis to calculate the friction torque required for realizing the relative motion of the balls in the pre-rolling regime. Based on these results, they could predict the torque and positioning hysteresis curves, which are commonly observed in preloaded ball screw drives (Figure 2.4).

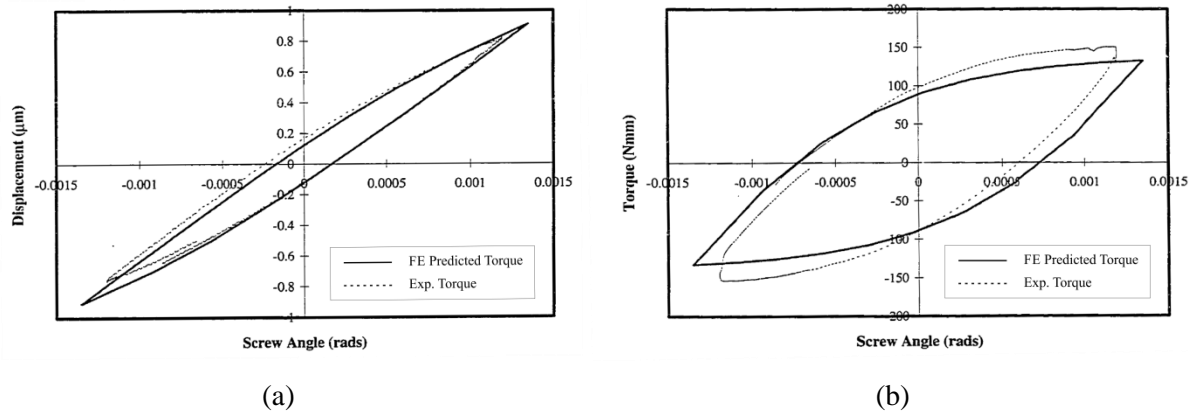


**Figure 2.4: Hysteresis phenomena in a ball screw drive (a) Analytical (FE driven) versus experimental friction torque (b) Analytical (FE driven) versus experimental linear displacement [44].**

Otsuka and Masuda [45] elaborated on the effect of pre-rolling behavior (or nonlinear spring-like behavior ‘NSB’ as they termed it) on the frequency response of mechanical systems with rolling elements. They showed that low-amplitude long-lasting free vibrations in devices with rolling elements are due to NSB.

### 2.1.6 Lead Errors

If the lead parameter of a ball screw is assumed constant over its grooved length, the nominal displacement of the ball-nut will be proportional to the rotation of the screw shaft. However, during the manufacturing of a ball screw, when finish grinding is applied to bring the groove to its final dimensions, the shaft unwinds, and as a result, the lead of the spiral groove varies slightly over the length of the shaft [46]. Consequently, there will be a difference between the nominal and actual displacement when the ball-nut travels along the screw shaft. This difference is referred to as the lead error. Lead errors in general are comprised of cumulative and periodic components [47]. Cumulative

errors for each revolution of the shaft can be sufficiently represented by a quadratic function [48, 49], and then programmed into a CNC control unit in the form of a lookup table for compensation [46, 48]. The effects of the periodic components of the lead errors and the methods for compensating those effects are more complicated and challenging. During high speed movements of the feed axes, periodic lead errors manifest themselves as high frequency disturbances which may become amplified inside the control loop, and further deteriorate the tracking accuracy. Kamalzadeh and Erkorkmaz [13] modeled the periodic lead errors as an output type sinusoidal disturbance and proposed a feedforward compensation scheme. Their method assumes near perfect capability of the controller in tracking harmonic reference commands of desired frequency, and may fall short if the sinusoidal pattern of the errors changes over time. Such changes can happen due to thermal deformation of the ball screw shaft or local wear and corrosion of the ball groove surface.

One important contribution of this thesis, as detailed in Chapter 5, is developing adaptive compensation schemes for minimizing detrimental effects of lead errors on the tracking accuracy of ball screw drives. Specifically, Adaptive Feedforward Cancellation (AFC) method is applied in order to reject harmonic disturbances due to lead errors without a prior knowledge of the error amplitude or phase.

## **2.2 Feed Drive Control Techniques for Wide Bandwidth**

As mentioned earlier in this chapter, the assumption of a rigid body plant sets an upper limit for the achievable control bandwidth. That limit should be respected during controller design to obtain a stable system. However, in many modern applications, complying with that restriction does not lead to the desired performance. Therefore, developing control laws that can interact with the flexible dynamics in a stable manner becomes inevitable. These type of controllers turn out to have a high bandwidth, which results in good tracking performance [50].

In order to widen the command following bandwidth, plant inversion can be used in feedforward control. Here, attention must be paid to obtaining a stable inversion particularly because Zero-Order Hold (ZOH) discretization of a continuous plant with a relative degree of greater than two leads to a non-minimum phase discrete plant [51]. Tomizuka [52] addressed this problem by proposing a Zero-Phase Tracking Error Controller (ZPETC). Another approach proposed by Fujimoto [53] is Multi-rate Perfect Tracking Control (PTC), which is a state-space approach guaranteeing perfect inversion of a controllable plant at every input/output sample.

Although, implementing feedforward control can make a significant improvement in tracking accuracy, it does not provide robustness against unknown disturbances or model uncertainties [54]. Therefore, the importance of feedback control in ensuring good disturbance rejection and performance remains undisputed. Chan [55] used loop shaping technique [56] to design a reference following non-collocated feedback controller for directly controlling the position of the table in a ball screw drive ( $x_2$  in Figure 2.5). Her design was based on notching out the control signal at the frequency of resonance. She also used double lead filters to provide adequate phase margin ( $PM=30^\circ$ ) at the cross over frequency. Although using notch filters is effective in avoiding the control signal from exciting the vibration modes, it may deteriorate the disturbance response ( $G_{\text{dist}}=x_2/d$ ) of the control system at around the resonance frequency. To overcome this shortcoming, the control law should be able to actively damp out the vibrations.

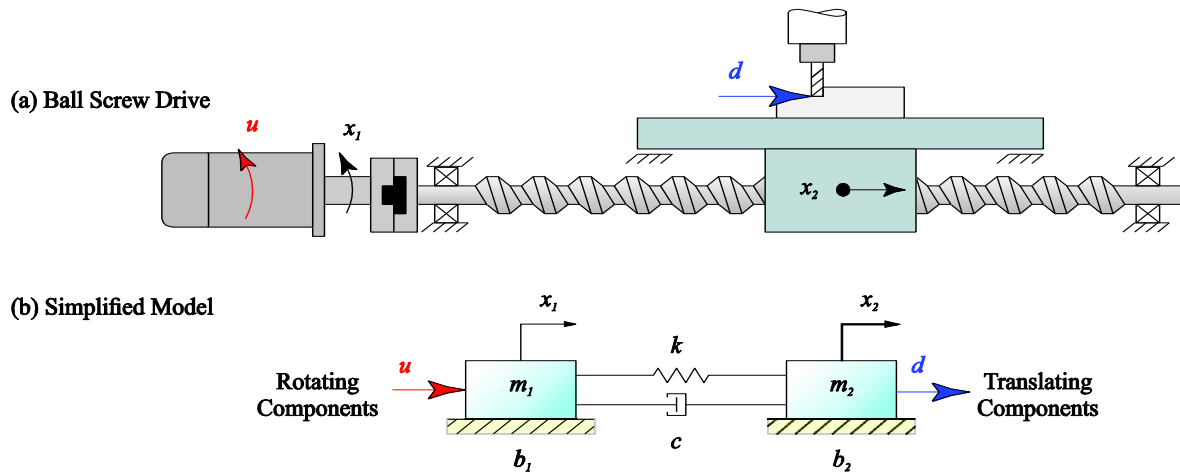


**Figure 2.5: Simplified ball screw drive model.**

In Section 2.2.1, the P-PI cascade controller, which is the standard industrial solution for control of CNC machine tools [57], is introduced. In Section 2.2.2, some extensions that can be added to the main controller to further attenuate the vibrations are discussed. Sections 2.2.3 and 2.2.4 review two methods of designing mode compensating controllers: pole-placement and sliding mode control. Finally, in Section 2.2.5 previous literature on robust control of ball screws using  $H_\infty$  optimization is reviewed.

### 2.2.1 P-PI Position-Velocity Cascade Control (standard industrial solution)

The difficulty in designing robust high-performance controllers for ball screws stems from the fact that the control input (motor torque) and performance output (table position) are non-collocated. In

such systems, the tradeoff between disturbance attenuation and robust stability can be mitigated by adopting additional collocated feedback [58]. The utilization of motor rotational velocity in closing the inner loop of P-PI position-velocity cascade controllers has been a successful solution in this regard.

According to Ellis [59], P-PI controllers are tuned as follows: beginning from the inner PI velocity loop, first the integrator gain ( $k_{iv}$ ) is kept at zero and the proportional gain ( $k_{pv}$ ) is increased until overshoot starts to appear in the step response. Then, the integrator gain ( $k_{iv}$ ) is increased until 5% overshoot is observed in the response. After the inner velocity loop, the outer position loop is tuned by simulating the response to a trapezoidal velocity reference trajectory. In this step, the proportional gain ( $k_{pp}$ ) is increased until overshoot is observed in the response. Finally, velocity and acceleration feedforward terms are added to the controller to improve its tracking accuracy.

Ferretti et al. [60] considered both command following and disturbance rejection performance in tuning P-PI gains for a flexible two-mass plant (Figure 2.6a).

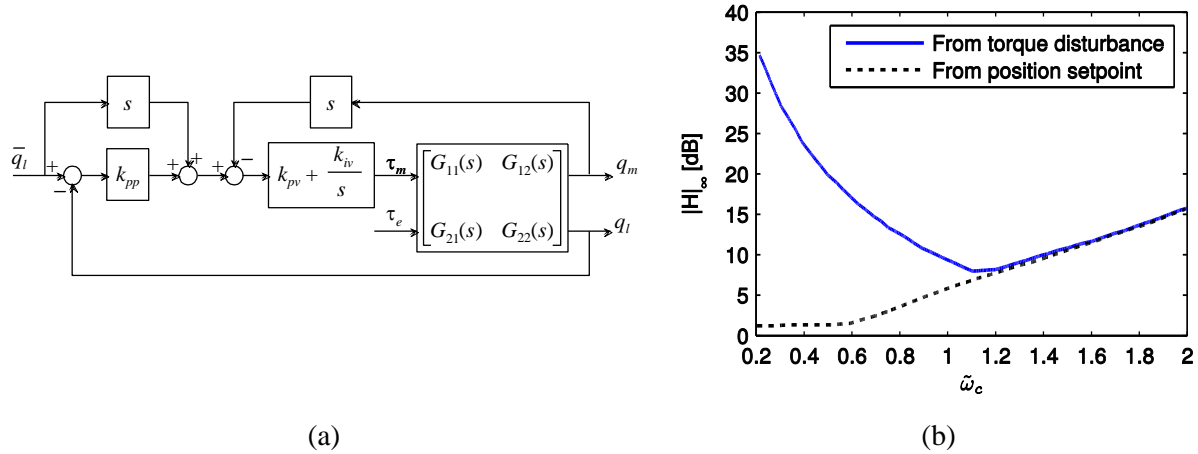


**Figure 2.6: (a) Overall scheme of P-PI control (b)  $H_\infty$  norm of  $G_{12}$  and  $G_{22}$  versus normalized crossover frequency of the inner loop [60].**

To reduce the number of free parameters from three ( $k_{pp}$ ,  $k_{pv}$ ,  $k_{iv}$ ) to one ( $\tilde{\omega}_c$ ), they placed zeros of the closed loop transfer function one decade below the crossover frequency of the inner velocity loop ( $\omega_c$ ). They then tried to establish a trade-off between the infinity norm of  $G_{12}$  (from reference command to load side position) and  $G_{22}$  (from load side disturbance to load side position) by

selecting an appropriate normalized inner loop bandwidth (Figure 2.6b). This method ignores the fact that minimizing the peak magnitude of a transfer function (i.e. the  $H_\infty$  norm), does not necessarily signify a reduction in the magnitude of the frequency response across all frequencies of interest. Unfortunately, the design methodology laid out in [60] was not verified experimentally, and the simulation results presented show that optimal selection of  $\tilde{\omega}_c$  improves mainly the transient response of the load side to a cutting milling force, whereas the steady state response remains less affected.

In this thesis, in Chapter 4, a new control design methodology is proposed that directly targets minimization of the load side disturbance response against cutting forces. In contrary to [60], our method improves the ball screw drive's disturbance rejection across the frequency spectrum, rather than only making a local improvement at the expense of worsening the dynamic stiffness at another frequency. The P-PI control technique is also used in Chapter 4 as a benchmark, against which, new feedback control ideas developed in this thesis are evaluated.

### **2.2.2 Plug-in Type Controllers for Vibration Attenuation**

Since mechanical modification of plant parameters for the purpose of vibration reduction is often impractical or too expensive, active methods of manipulating physical behavior have been researched in the machine tool community as a cost-effective alternative. Some of these methods simply add an extra loop to the main controller, and therefore are referred to as *plug-in type controllers* in this section. Ellis [59] showed that adding an acceleration feedback as proposed in [61, 62] has an equivalent effect of increasing the motor shaft inertia. Similarly, feeding back the difference of motor and load speeds increases the effective damping [2]. The latter method was used by Hosseinkhani and Erkorkmaz [17] to improve the damping properties of a Center of Mass (COM) controlled ball screw system. Kamalzadeh and Erkorkmaz [63] used the difference of rotational positions at two ends of the screw shaft as the feedback signal to damp out torsional vibrations. The downsides of using plug-in type controllers are the additional cost that may incur due to adopting extra hardware such as an accelerometer, and also the prospect of worsening the stability margins or loop gain at other frequencies in situations where the main controller and the add-on damping may end up battling each other.

### **2.2.3 Pole-Placement Based Vibration Damping**

Pole-placement is a well-known technique for placing closed loop system poles (eigenvalues) at desired locations in the s-plane through using appropriate state feedback gains [64]. The state

feedback gains can be calculated using Ackermans’s formula [65] or a more robust method documented in [66], which is also available in off-the-shelf software, such as Matlab. Gordon and Erkorkmaz [3] designed a mode compensating pole-placement controller for a two-mass model plant, representing the dynamics of a ball screw drive up to roughly twice the frequency of the first resonance. They augmented the 4th order state-space plant model with an additional state representing the integral of the load-side position, to enforce integral action in the control law. The idea they took from low authority LQG vibration control [67] for assigning the pole locations was increasing the *amplitude decay ratio* without changing the damped natural frequency (Figure 2.7).

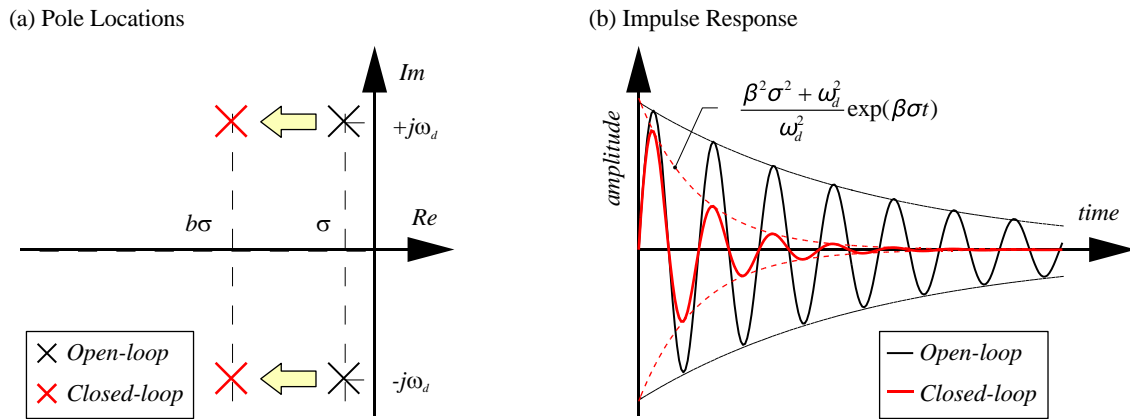


**Figure 2.7: Active damping of structural vibrations by pole placement.**

In Chapter 4 of this thesis, a simple and intuitive design strategy is presented, which builds upon the pole-placement structure proposed in [3]. In the new design, special attention has been paid to direct optimization of the load side disturbance response against cutting forces. Also loop shaping principles are applied to handle system delays due to power electronics and the control computer. As a result, the PPC controller designed in this thesis has a crossover frequency roughly two times higher than that of the one in [3]. It also provides superior performance in term of disturbance rejection in a wide frequency range as can be concluded from Figure 2.8 which compares the disturbance FRF of the two controllers.

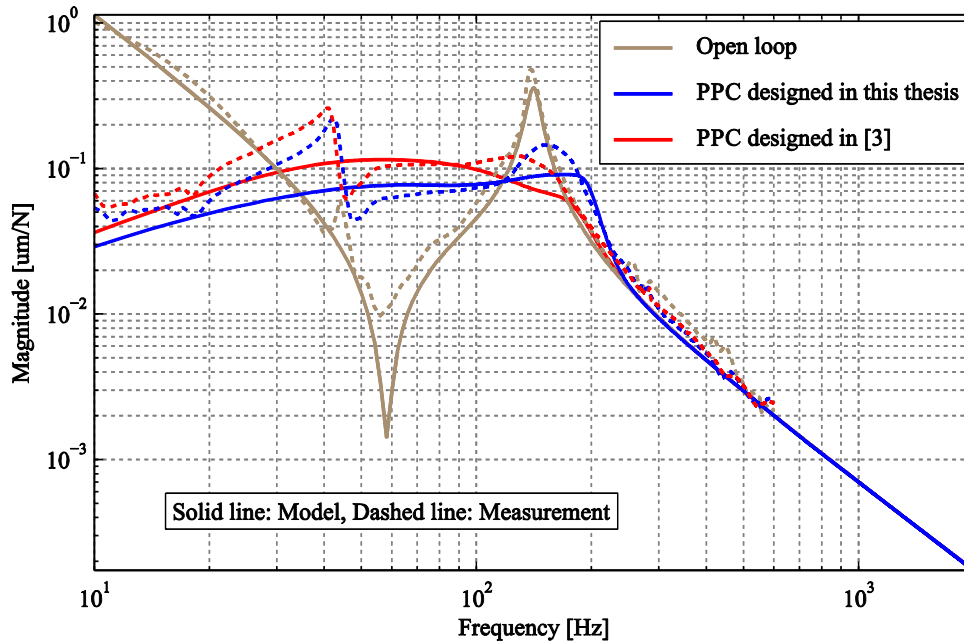


**Figure 2.8: Disturbance FRF of the PPC controller designed in this thesis versus the one in [3].**

#### 2.2.4 Sliding Mode Control

Sliding Mode Control (SMC) is a variable structure control technique first proposed by Utkin [68]. In this method, the trajectory of state errors is driven onto a designed sliding surface. However, the initial version of SMC suffered from discontinuous switching around the sliding surface. Slotine and Li [69] addressed this problem and proposed Adaptive Sliding Mode Control (ASMC) as a remedy. In ASMC, uncertain parameters with known bounds are estimated adaptively in an effort to minimize the effect of model and disturbance variations on the tracking accuracy. Altintas et al. [70] designed an ASMC controller for a ball screw drive considering only the rigid body dynamics and disturbance force variations. Kamalzadeh and Erkokrmaz [13] followed the same concept to design a mode compensating controller for a two-mass plant model. To improve disturbance adaptation, Won and Hedrick [71] proposed a specific selection of adaptation gains that resulted in the decoupling of the disturbance estimation error from the sliding surface dynamics. Okwudire and Altintas [72] adopted that idea and designed a mode compensating disturbance adaptive sliding mode controller for a ball screw drive. They also designed a Robust Minimum Tracking Error Filter (MTEF) that generates appropriate state reference trajectories to enforce the minimization of tracking errors.

### **2.2.5 Robust Control and Gain Scheduling**

When the table carrying the workpiece travels along the screw shaft, or material is cut away from the workpiece, the dynamics of the feed drive changes accordingly. Therefore, it is vital to ensure that the control system can cope with those changes in the plant dynamics. Robust control techniques are well suited in this regard. Itoh et al. [73] synthesized a feedback controller using the  $H_\infty$  framework to achieve robustness against variation in the resonance frequency in a ball screw feed drive. Van Brussel et al. [28] considered variations in the ball screw plant configuration as multiplicative unstructured model uncertainties and performed minimization on the norm of a set of appropriately weighted transfer functions to obtain a robust controller.

Another approach to handle varying dynamics in long-stroke ball screw drives is gain scheduling. Symens et al. [74] designed multiple  $H_\infty$  controllers, each for a different nominal position of a flexible Cartesian robot, and then, used linear interpolation for combining the controllers based on the current table position. As an alternative method of modeling, Sepasi et al. [75] developed a Linear Varying Parameter (LVP) model that took into account both varying position of the table as well as the uncertain load mass. Their controllers were scheduled over measured position and the resulting closed loop system maintained robustness against load mass variations.

### **2.3 Compensation of Repetitive Disturbances and Errors**

Since motion delivery in ball screw drives is based on mechanical contact, imperfections in the mating components result in the deterioration of achievable dynamic accuracy. For example, errors in the pitch angle, as mentioned in Section 2.1.6, cause harmonic positioning errors which can occur at high frequencies when the drive is in high speed motion. Misalignments and grating errors in the encoders may also have a similar effect. These errors are difficult to correct using classical feedback techniques, especially when the frequency of the error harmonics is beyond that of the closed-loop bandwidth. Although model-based feedforward approaches are available for correction purposes [13], such compensation techniques may become ineffective when there are variations in the error characteristics, e.g. a change in the lead error profile due to thermal deformations or wear on the ball screw.

On the other hand, cutting forces in operations such as milling have a periodic nature, where the first few harmonics may typically be beyond the closed-loop bandwidth. In this case, the best that a standard servo controller can do is to counteract the average (d.c.) value of the cutting force, while

leaving the high frequency components unsuppressed, free to cause vibrations and positioning errors. The ability to counteract these harmonics would undoubtedly improve the dynamic positioning accuracy of the drive system, and consequently the quality of parts produced on machine tools.

Moreover, attenuation of periodic disturbances is a recurrent issue in control of industrial devices such as fast tool servos [76, 77], hard disk drives [78, 79], and robotic manipulators [80]. Therefore, the following sections are dedicated to reviewing some well-known closed loop methods for cancellation of harmonic disturbances.

### 2.3.1 Internal Model Principle and Repetitive Control

The Internal Model Principle (IMP) states that in order to asymptotically reject an external disturbance, the controller must include a model of the disturbance [81]. IMP is the core idea behind the design of Repetitive Controllers (RC) [82, 83]. In internal model control and repetitive control, the controller gain is infinite at the frequency of the disturbance, because the controller transfer function has a pair of poles on the imaginary axis corresponding to that frequency. Therefore, in these methods, it is assumed that the fundamental disturbance frequency is well-known and not varying. Then, the sampling frequency needs to be adjusted so that it is an integer multiple of the disturbance frequency [84]. The signal flow of a repetitive controller is illustrated in Figure 2.9. Since the transfer function of an RC (Equation (2.5)) has an infinite number of poles on the imaginary axis, and thus very high gains at target frequencies, low pass filters are used to stabilize the control system.

$$G(s) = \frac{1}{1 - e^{-Ls}} \quad (2.5)$$

Unfortunately, low-pass filtering the RC generated signals also lowers the ability of the controller in tracking or rejecting the intended harmonics [85]. Nevertheless, the successful application of RC in mitigating the detrimental effects of harmonic cutting forces is reported in [41, 86]. In [86], a vertical CNC machine is retrofitted with a dynamometer and a piezoelectric actuator. In their work, the dynamometer measures the component of the cutting force in the direction normal to the feed direction, while an RC controller regulates the amount of this force by manipulating the radial depth of cut through the piezoelectric actuator. It is shown that this strategy is effective in improving the surface finish of the machined part by reducing the amount of fluctuations in cutting forces. In contrary to the method presented in [86], the repetitive control strategy proposed in [41] does not require additional hardware such as dynamometers or piezoelectric actuators, and acts directly upon

position error of the feed drive system. In this respect, it is similar to the approach taken in this thesis in Chapter 5. However, in our approach, the Adaptive Feedforward Cancellation (AFC) technique has been used for harmonic rejection. This allows for more flexibility in targeting specific harmonics without having to deal with all the complexity and difficulty of designing a stable repetitive controller.

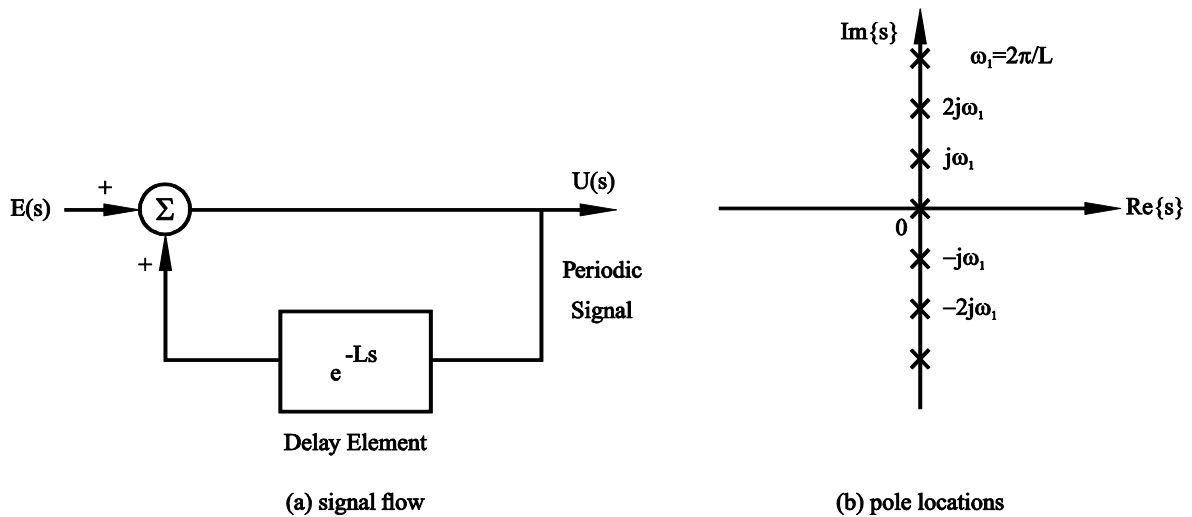
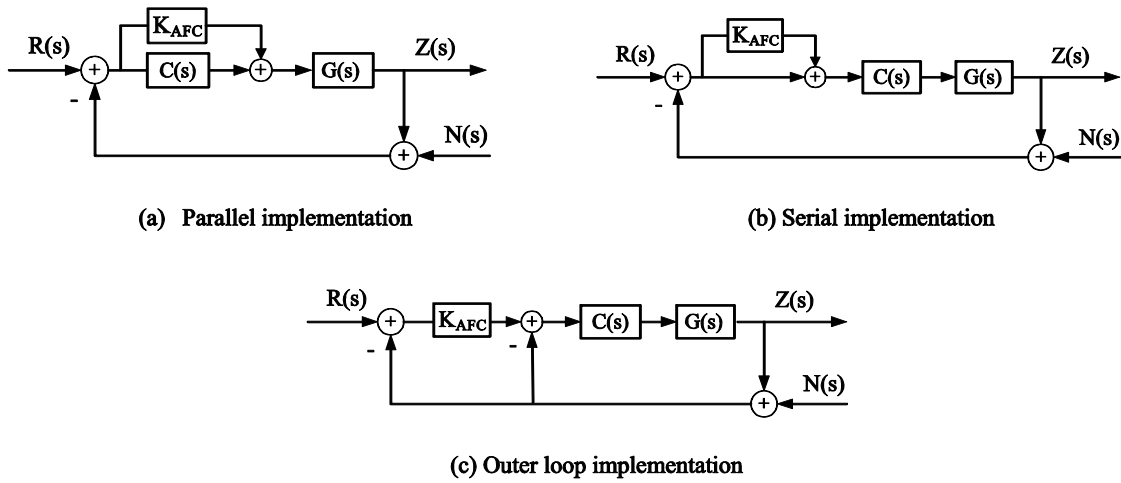


Figure 2.9: Periodic signal generation in repetitive control [87].

### 2.3.2 Adaptive Feedforward Compensation

Adaptive Feedforward Cancellation (AFC) [88, 89] is another harmonic cancellation approach in which the correction signal is not directly generated by the feedback controller. Instead, an external block is used to adaptively estimate the magnitude and phase of the “equivalent” disturbance, causing the harmonic error, and inject an appropriate cancellation signal into the control loop to cancel its effect out. There are different configurations for integrating AFC into the main control system as shown in Figure 2.10. In this thesis, parallel and serial configurations are implemented and tested for harmonic rejection as detailed in Chapter 5.



**Figure 2.10: Different configurations for implementation of AFC [90].**

Although, in general, the AFC is a nonlinear scheme, it becomes equivalent to a Linear Time Invariant (LTI) filter when the disturbance frequency is constant [91-93]. This makes it possible to use the Nyquist criterion for stability analysis of the closed loop system. Recently [94], it has been shown that for certain AFC updating laws, even if the disturbance frequency is time-varying, the AFC scheme is still equivalent to a linear time-varying filter. Based on this principle, a design technique similar to the one in [93] has been extended by Hosseinkhani and Erkorkmaz [95] for improving the dynamic accuracy of ball screw drives. The details of this design are presented in Chapter 5. It is also demonstrated that the proposed controller successfully mitigates the effects of lead and encoder errors, and also high frequency cutting forces, thereby resulting in more accurate motion during high travel speeds and machining.

## 2.4 Conclusion

This chapter has summarized some of the key issues related to modeling and control of ball screw drives. Special attention was paid to the state of the art in finite element modeling of ball screw feed drive systems. This knowledge is used in Chapter 3 of this thesis to develop a finite element model for a ball screw drive setup. Also, the challenging consequences of structural flexibilities on control of ball screw drives were addressed, and some of the practical solutions for enhancing the bandwidth of the controller in this situation were reviewed. In Chapter 4 of this thesis, three novel control strategies are proposed that achieve wide-bandwidth through active damping of vibrations in a ball screw setup. Another important topic discussed in this chapter was harmonic disturbance rejection. Internal model principle, repetitive control, and adaptive feedforward cancellation (AFC) techniques

were cited as well-known methods of dealing with harmonic disturbances. In Chapter 5, an AFC compensator is designed and integrated into a main position controller to enhance the performance of the ball screw drive against harmonic disturbances of known frequency that originate from cutting forces or lead errors.

## Chapter 3

### Modeling and Identification of Ball Screw Driven Feed Drives

Optimal design of the structure and control system of a machine tool demands a thorough understanding of the dynamics from power input(s) to performance output(s) of the machine. This understanding is built up in part through accurate modeling of critical machine components such as the frame, spindles and feed drives. Drawing on a wide range of disciplines, from power-electronics to Finite Element (FE) analysis to tribology and experimental modal testing, the goal of this chapter is to establish mathematical models for important sub-components of a feed drive. The models presented in this chapter are developed for, and verified on, a lab-made single-axis ball screw drive introduced in Section 3.1. In Section 3.2, a dynamic model is developed for the current amplifier and its parameters are determined to best replicate the measured current FRF of the motor. The resulting model is then used for removing the current loop dynamics from measured acceleration Frequency Response Functions (FRFs), when the excitation signal is generated by the motor. In Section 3.3, a finite element model for the mechanical structure of the feed drive is created and utilized for FRF predictions. Simple ball screw models suitable for control design are introduced in Section 3.4. Finally, some concluding remarks are presented in Section 3.5.

#### 3.1 Experimental Setup

The moving table of the test setup, used throughout this thesis (Figure 3.1), is sliding over two cylindrical guideways on 4 air bushings. It is actuated by a 3 kW servo motor through a precision ball screw with both lead and diameter of 20 mm (Figure 3.1). A backlash-free double-flex close-coupled disk-pack style coupling is used for transmitting the torque from the motor to the screw shaft. This coupling has a high torsional stiffness, and accommodates the small amounts of misalignment. Two optical incremental rotary encoders with sinusoidal output (Heidenhain ERN 180) measure the rotation of the screw shaft at different locations along the screw axis: Encoder 2 is mounted in the proximity of the coupling, whereas Encoder 1 is mounted close to the free end of the screw shaft. These encoders generate 5000 cycles per shaft revolution. However, considering the 400 times interpolation of the sinusoidal encoder signals in the data acquisition board, the actual resolution turns out to be equivalent to 10 nm of table motion. In addition, the angular position of the motor is measured by Encoder 3 which has a table motion equivalent resolution of 0.625  $\mu\text{m}$ . A linear encoder

(Heidenhain LIF 101R) with 20 nm resolution measures the axial position of the table. In this setup, limit switches are placed in such a way that allow axis stroke of 350 mm.

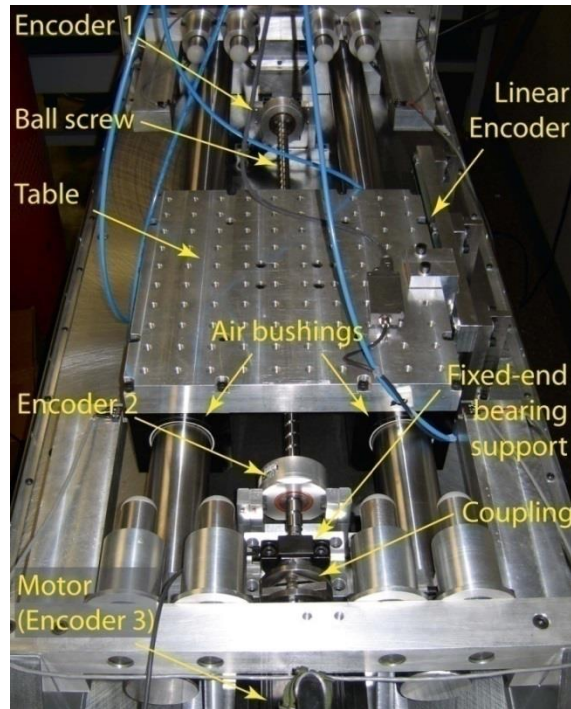


**Figure 3.1: Ball Screw Test Setup.**

To investigate modal characteristics of the setup, stepped sine excitation technique was used to obtain frequency response of the machine at encoder locations to the reference torque signals sent to the motor through an analog input. Since the amplitude of the sinusoidal input commands was kept within the saturation limits of the motor, the current saturation was not a concern in these measurements. However, due to frequency response roll-off effect in the current control loop, the torque excitation above 400 Hz is very little. This inevitably reduces the accuracy of the measured FRFs at high frequency range (400 to 2000 Hz) due to eventual dominance of nonlinear effects such as friction. The results of these measurements are shown in Figure 3.2. From these data, the observable natural frequencies of the setup were identified to be at 141 Hz, 450 Hz, 1080 Hz and 1680 Hz. In order to get more insight into the dynamics of the mechanical structure, impact hammer testing was also carried out by measuring impact force and acceleration response signals to and from the table. As can be seen in Figure 3.3, the first mode (at 141 Hz) shows up strongly in the measured FRF. This indicates that axial deformations are significant in this mode. In contrast, the other modes appear to be dominantly torsional. Since in the stepped sine test, the motor was used as the excitation

device, the obtained FRFs also contain the dynamics of the current amplifier. To obtain the frequency responses to the torque applied by the motor, knowledge of current loop dynamics is necessary. If this knowledge is available, one can simply divide the measured FRFs by the FRF of the current loop, to obtain mechanical FRFs, as done in the proceeding sections.

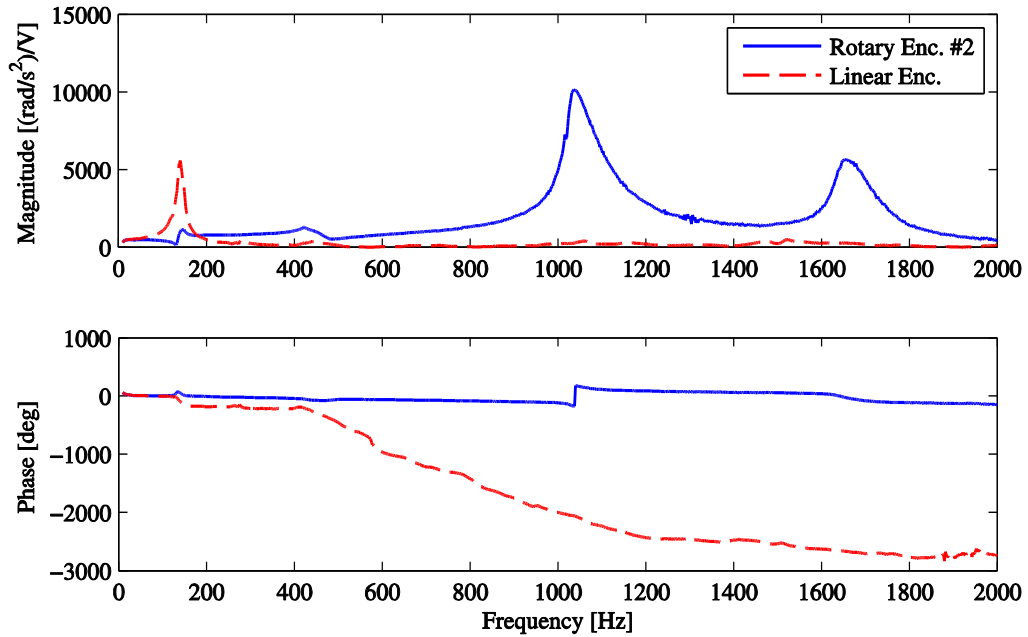


**Figure 3.2: Feed drive FRFs from motor torque command to acceleration responses at encoder locations.**

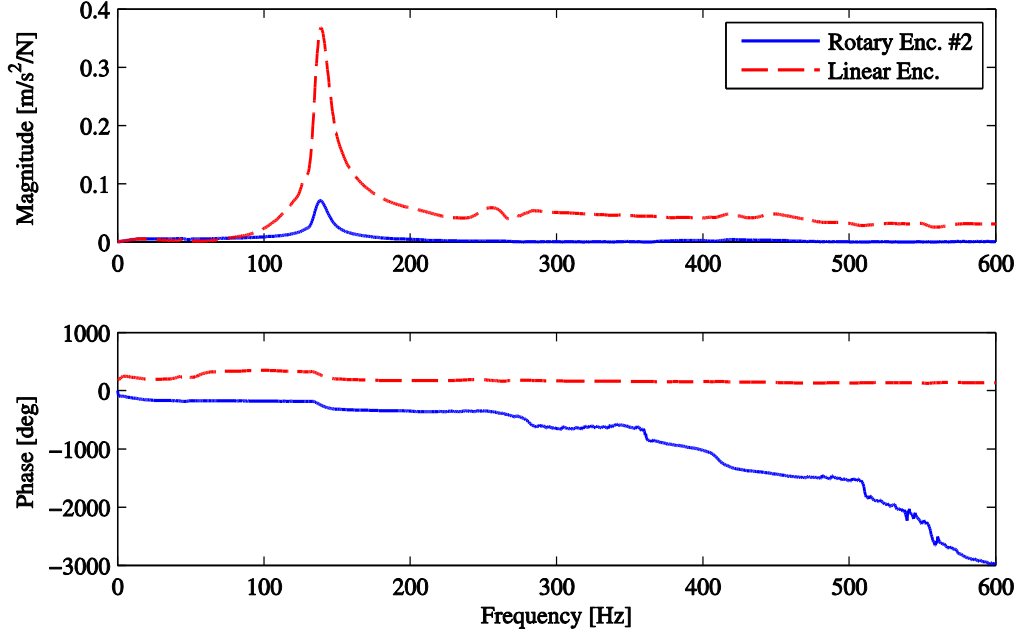


**Figure 3.3: Feed drive FRFs from impact force to the table to acceleration responses at encoder locations.**

### 3.2 Modeling and Identification of Current Control Loop Dynamics

The actuator used in the test setup is a 3-phase surface mounted Permanent Magnet Synchronous Motor (PMSM) manufactured by Omron Corporation. The stator winding of this motor is Y-connected as schematically shown in Figure 3.4.

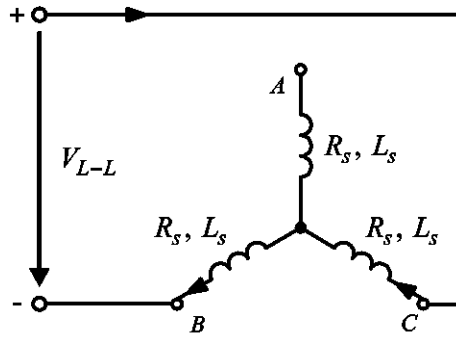


**Figure 3.4: Schematics of a Y-connected stator winding.**

Torque control of a PMSM is commonly carried out by vector control methods such as Field Oriented Control (FOC) [96] and Direct Torque Control (DTC) [97]. Among these methods, FOC is widely

adopted in industrial applications due to its well-developed theory. In FOC, the three phase AC currents are equivalently represented by two current components in a rotating frame synchronous to the rotor (d-q frame) as shown in Figure 3.5.

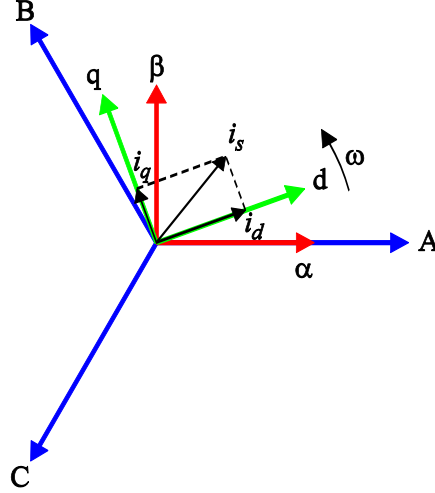


**Figure 3.5: Current vector resolved in the d-q frame.**

The advantage of this transformation is that the d-q current components ( $i_d, i_q$ ) behave similar to DC signals:

$$\begin{aligned} \frac{di_d}{dt} &= -\frac{R_s}{L_d} i_d + \frac{L_q}{L_d} \omega i_q + \frac{u_d}{L_d} \\ \frac{di_q}{dt} &= -\frac{R_s}{L_q} i_q - \frac{L_d}{L_q} \omega i_d + \frac{u_q}{L_q} - \frac{\psi_m}{L_q} \omega \end{aligned} \quad (3.1)$$

Above,  $i_d$  and  $i_q$  are direct and quadrature current components.  $u_d, u_q$  are dq-axis voltages.  $R_s$  is the stator winding resistance which is half of the line-to-line resistance.  $L_d, L_q$  are dq-axis inductances.  $\omega$  is the angular speed of the motor shaft and  $\psi_m$  is the rotor flux linkage. Defining  $P$  as the number of armature pole pairs, the motor torque can be calculated as follows [98]:

$$T = \frac{3}{2} P \left[ \psi_m i_q + (L_d - L_q) i_d i_q \right] \quad (3.2)$$

In the simplest form of FOC, the d-axis current ( $i_d$ ) is held to zero by a Proportional-Integral (PI) controller. This current control strategy is the most commonly used in industrial applications [99]. Therefore, it is assumed here that this control method is implemented in the motor driver of our test

setup. Furthermore, we know that in a surface-mounted PMSM due to symmetry  $L_d$  and  $L_q$  are both equal to  $L_s$  which is half of the line-to-line inductance [100]:

$$L_d = L_q = L_s \quad (3.3)$$

Consequently, Equation (3.2) can be simplified as follows:

$$T = \frac{3}{2} P \Psi_m i_q \quad (3.4)$$

Moreover, a feedforward compensator is usually used to cancel out the effect of back-emf as appeared in Equation (3.1). Therefore, to control motor torque, it is sufficient to control  $i_q$  by manipulating  $u_q$  through a controller. The plant transfer function from  $u_q$  to  $i_q$  is successfully approximated from Equation (3.1) after applying the simplifications mentioned above:

$$G(s) = \frac{i_q(s)}{u_q(s)} = \frac{1}{L_s s + R_s} \quad (3.5)$$

The control of  $i_q$  is easily accomplished by a PI controller:

$$C(s) = K_p + \frac{K_i}{s} = \frac{K_p s + K_i}{s} \quad (3.6)$$

In order to ensure enough phase margin, it is a common practice to select the controller zero in such a way that it cancels the plant pole [101, 102]:

$$\frac{K_i}{K_p} = \frac{R_s}{L_s} \quad (3.7)$$

In an ideal situation, this makes the loop transfer function a pure integrator with constant phase margin of 90 degrees, regardless of the chosen bandwidth. However, in reality, current measurement filters and delays due to Pulse Width Modulation (PWM) inside the current amplifier induce phase lag, and their effect must be also considered when tuning the parameters of the current control loop. The PWM transfer function can be approximated using small signal analysis [103]:

$$G_{PWM}(s) \cong e^{-\frac{T_s s}{2}} \quad (3.8)$$

Above,  $T_s$  is the PWM switching frequency. Since PWM signals are contaminated by harmonic components at the switching frequency and its multiples, measured currents are passed through a low pass filter to remove these harmonics. A first order filter with a corner frequency around half of the switching frequency is typically used for this purpose [104]:

$$H = \frac{1}{s + \omega_f}, \quad \omega_f = \frac{\pi}{T_s} \quad (3.9)$$

The motor driver used in our setup provides an analog output for monitoring motor current. Since current control is performed digitally, the effects of digital to analog (DAC) converter have to be considered when analyzing the measured current data. The DAC effect can be represented by the following transfer function [105]:

$$G_{ZOH} = \frac{1}{T_{sample}} \frac{1 - e^{-sT_{sample}}}{s} \quad (3.10)$$

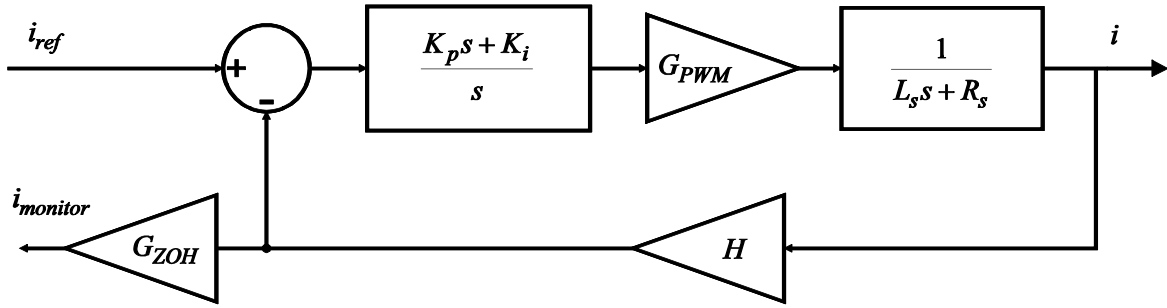


**Figure 3.6: Block diagram of current control loop.**

Considering the above mentioned elements, a block diagram of the current control loop is demonstrated in Figure 3.6. Simplifying this block diagram leads to the following transfer functions for the current loop:

$$\frac{i}{i_{ref}} = \frac{CG_{PWM}G}{1 + CG_{PWM}GH} \quad (3.11)$$

$$\frac{i_{monitor}}{i_{ref}} = G_{ZOH} \frac{CG_{PWM}GH}{1 + CG_{PWM}GH} \quad (3.12)$$

Motor and amplifier parameters related to current controller design along with their values are listed in Table 3.1. Missing in this list is the value of current monitoring signal sampling frequency ( $T_{sample}$ ), which was not specified in motor data sheets.

**Table 3.1: AC motor electrical parameters**

Winding resistance ( $R_s$ )	0.0575 $\Omega$
Winding inductance ( $L_s$ )	0.75 mH
PWM switching frequency	3.9 kHz

In order to estimate controller gains, first the FRF of the generated current to reference current was measured using stepped sine excitation technique ( $i_{monitor} / i_{ref}$  in Figure 3.6). Then, the assumed I-gain ( $K_i$ ) and the sampling frequency ( $T_{sample}$ ) were manually adjusted through trial and error to produce a good match between the predicted FRF from Equation (3.12) and the measured FRF. In each trial, the P-gain ( $K_p$ ) was calculated according to Equation (3.7). When measuring the current FRF, the rotor was locked in place with a brake, to eliminate the effect of back-emf. Measured and modeled current loop FRFs are shown in Figure 3.7. The identified current loop parameters are summarized in Table 3.2.

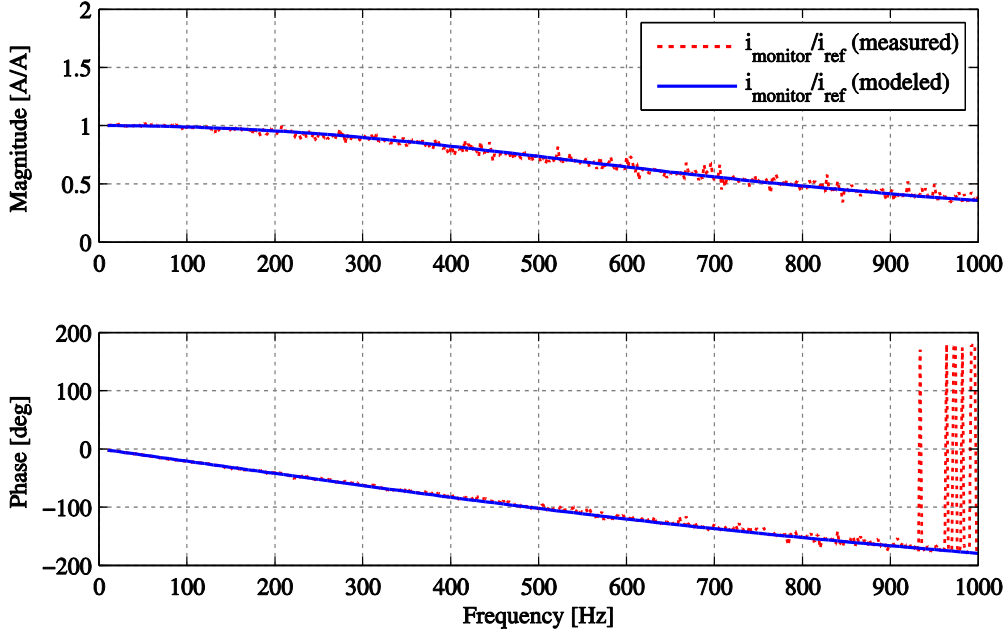


Figure 3.7: Measured and modeled FRF of the monitored current.

Table 3.2: Identified parameters of the current control loop.

$K_i$	110 V/(A.s)
$K_p$	1.435 V/A
$T_s$	0.2564 ms
$T_{sample}$	0.1282 ms
$\omega_f$	12566 rad/s (2000 Hz)

These parameters result in a current loop with 300 Hz crossover frequency and phase margin of 68 degrees as depicted in Figure 3.8. After loop parameters are identified, it becomes possible to construct the actual current response based on Equation (3.11). Figure 3.9 shows the difference between current FRF at measurement point (from Equation (3.12)) and actual current FRF (from Equation (3.11)). To remove the contribution of current loop dynamics from measured FRFs shown in Figure 3.2, the acceleration FRF should be divided by the actual current FRF ( $i/i_{ref}$ ). This results in mechanical FRFs from motor torque to acceleration at encoder locations. This correction is demonstrated in Figure 3.10 for the acceleration FRF measured at encoder #2 location.

The mechanical FRFs will be used in the next section to validate the finite element predictions.

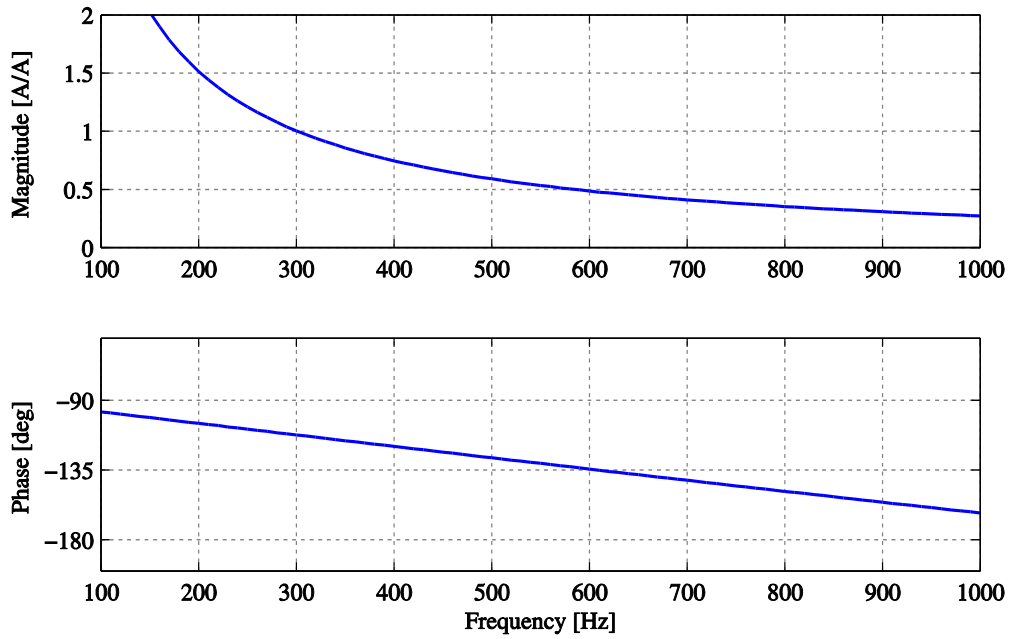


Figure 3.8: Loop magnitude and phase of current amplifier.

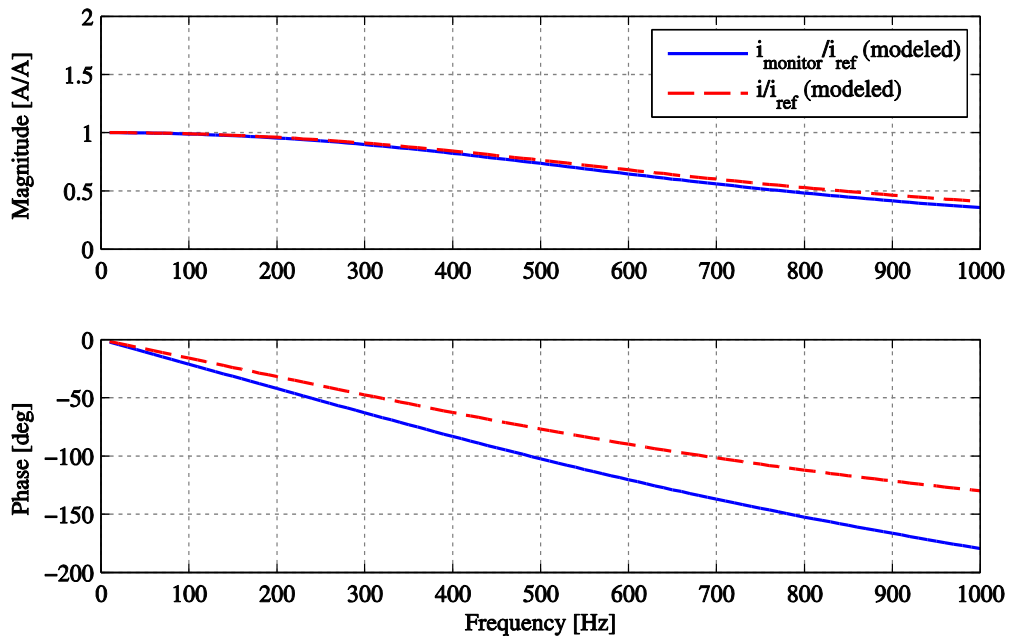
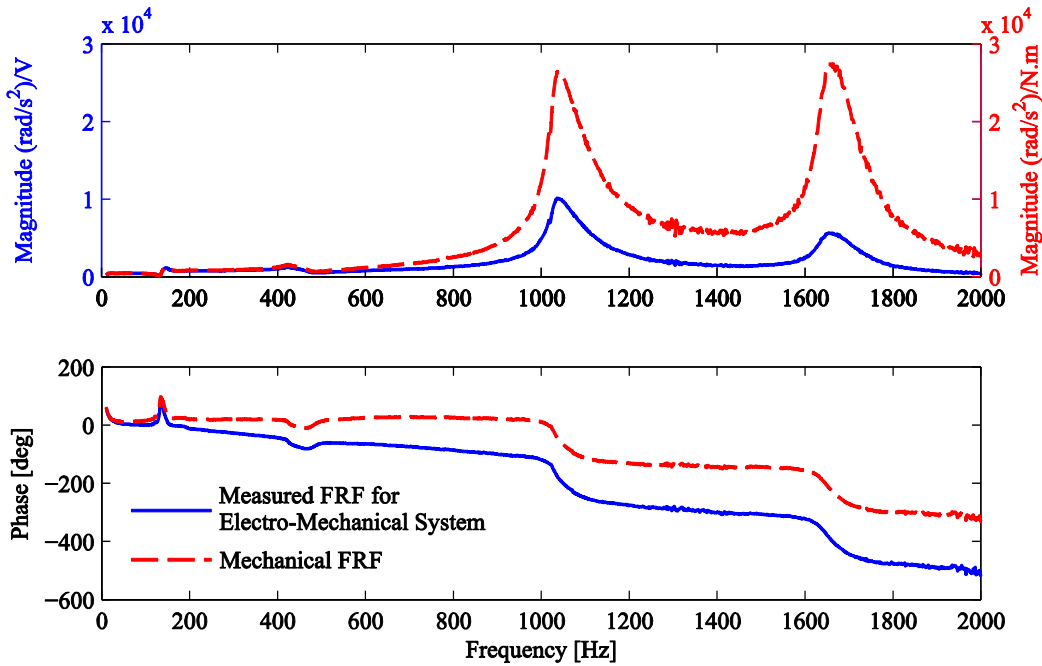


Figure 3.9: Difference between current FRF at current monitoring measurement point and actual current FRF.



**Figure 3.10: Acceleration FRF measured at encoder #2 before and after correction for current loop dynamics.**

### 3.3 Finite Element Modeling of Ball Screw Mechanism

In order to get deeper insight into the dynamics of feed drives, it is necessary to study the contribution of stiffness and mass properties of individual components to the overall modal characteristics of the system. Achieving this goal for a ball screw drive is challenging, particularly due to the distributed nature of inertia and stiffness in the screw shaft. This implies that the modal contribution of the screw shaft depends in general on the relative position of the table. Finite Element Modeling (FEM) approach provides a powerful means for dealing with this situation, and therefore is followed in this section to study the modal characteristics of the test setup.

In this approach, the screw shaft is modeled as a 3D Timoshenko beam [106], while all other sources of inertia, such as the rotors of the motor and encoders, coupling hubs, and the nut-table assembly, are modeled as rigid bodies. On the other hand, linear and torsional spring formulations are used to represent stiffness properties of kinematic joints, such as the ball screw-nut interface, shaft-hub connections, air bearings supporting the table, and the thrust and radial bearings (Figure 3.11). The stiffness value for each of these joints is initially taken from catalog data. However, since there are significant uncertainties associated with the stiffness of the joints, FE model updating [107]

becomes necessary to remove the discrepancies between measured FRFs and FE predictions. Details of finite element equations used in this thesis are presented in Appendix A.

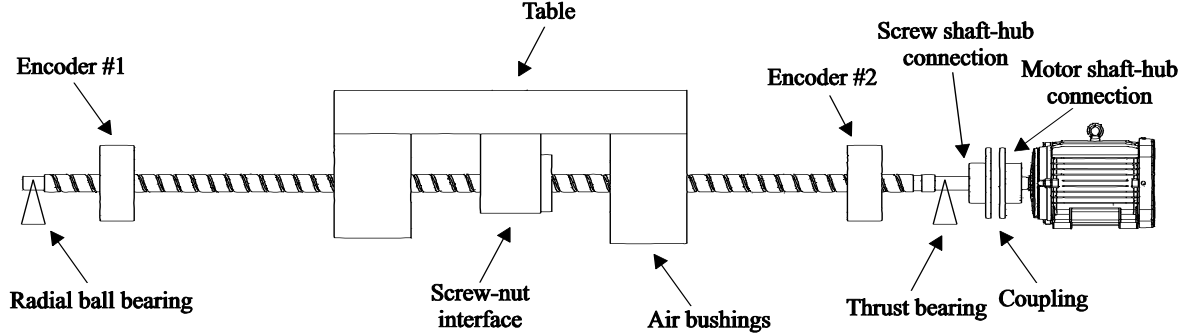


**Figure 3.11: Schematic representation of the test setup.**

In a nutshell, finite element modeling of the setup shown in Figure 3.11 begins with generating a system of equations for the screw shaft by assembling Timoshenko beam elements to construct a global stiffness matrix, and a global mass matrix. Two extra nodes representing respectively the nut-table assembly and the motor shaft are then considered, and the global mass and stiffness matrices are augmented with the degrees of freedom associated with these nodes. In the next step, the global mass matrix is updated to include the rigid body mass properties of these nodes. Also the specific element stiffness matrices developed for flexible joints including the ball screw-nut interface, the coupling, and the bearings are incorporated into the global stiffness matrix. After the final form of these matrices is reached, the associated eigenvalue problem is solved in Matlab for natural frequencies and mode shapes. This information is used in predicting various FRFs of the setup. The position response at nodal DOF  $e$  due to excitation at nodal DOF  $f$  can be obtained in the following form:

$$[H(\omega)]_{ef} = \sum_{k=1}^m \frac{[\phi_e^R(k)][\phi_f^L(k)]}{(\omega_n^2)_k + 2j(\zeta)_k(\omega_n)_k \omega - \omega^2} \quad (3.13)$$

Above,  $(\omega_n)_k$  is the natural frequency,  $\zeta_k$  is the modal damping ratio, and  $[\phi^L]_k, [\phi^R]_k$  are left and right mass normalized mode shapes for the  $k^{th}$  mode ( $k=1,2,\dots,m$ ) [107]. The modal damping values in the following sections are tuned by trial and error to obtain a best fit between the FE-predicted and measured FRFs. It is worth noting that the width and height of resonance peaks in the measured FRF curves depend heavily on the existing damping regime. Accurate modeling of damping in mechanical structures is not a trivial task. As a result, the assumption of modal damping is

usually made in order to approximately take into account the effect of damping. Once the accurate damping coefficients are identified, it is reasonable to assume that this information provide reliable estimates for damping in machines with different configurations but with the similar sources of damping. Therefore, the knowledge obtained from FE model updating for a particular machine tool will have broader applications in design and analysis of a group of somewhat similar machine tools. The reason that Matlab is used in this thesis for finite element modeling and solution is that it provides extended simulation capabilities that can be further used to simulate the dynamic response of the reduced order FE model in the presence of nonlinear effects such as friction and lead error disturbances.

### 3.3.1 Model Updating in Ball Screw-Nut Assembly

To illustrate the necessity for model updating, let us consider first the FE model of the ball screw-nut assembly alone. In that case, the only joint that has to be modeled is the screw joint between the ball screw and the nut. Throughout this thesis, the stiffness matrix for that joint is calculated following the method proposed by Okwudire [1]. In this method, the stiffness matrix is formulated as a function of the nut's axial stiffness. The nominal value of this parameter for the maximum permissible preload is specified in the manufacturer's catalog [108]. However, since the actual preload may be less than the maximum permissible, an updated value for the nut's stiffness must be used in FE simulations to get accurate predictions. In order to find the correct value, experimental data needs to be collected by conducting a frequency response measurement. For that purpose, a ball screw identical to the one used in the test setup was suspended from two bungee cords to emulate the free-free boundary conditions (Figure 3.12). Then, an impact test was carried out by hitting the screw shaft with a hammer at one end, while recording the nut response with an accelerometer.



**Figure 3.12: Setup for impact hammer testing on the ball screw with free-free boundary conditions.**

The resulting FRF is presented in Figure 3.13. This figure also shows the FRF obtained from FE simulation, when the nominal catalog value of the nut's stiffness is used. As can be seen, in this case, the natural frequencies of two modes (at 1862 Hz and 4812 Hz) are overestimated. This indicates that the assumed stiffness of the nut needs to be updated.

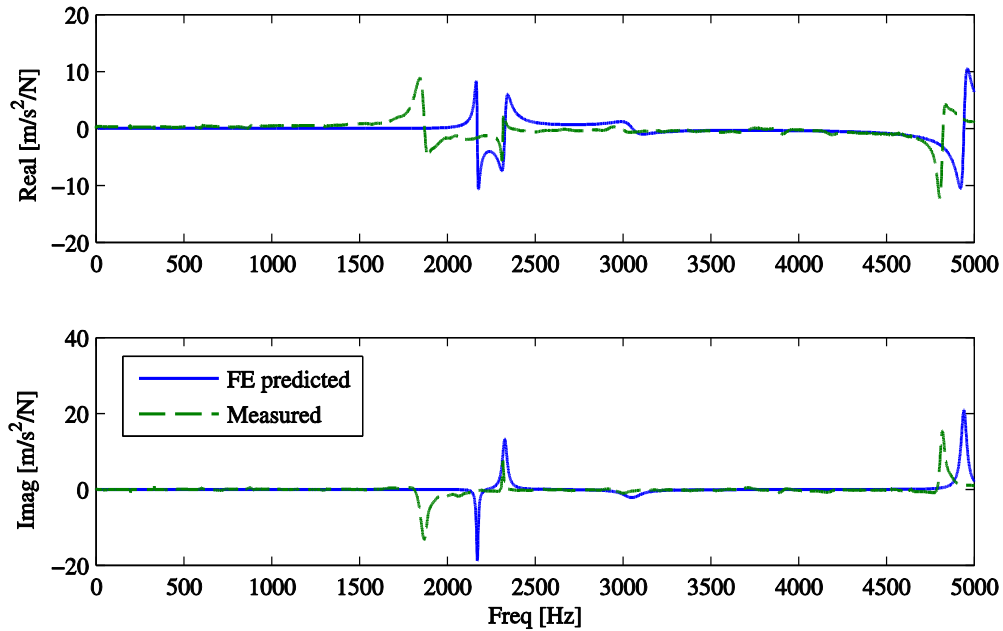


**Figure 3.13: Measured and predicted FRFs when nominal nut stiffness is used in the FE model.**

After a few trials, the correct value of nut's stiffness was deemed to be about 78% of the nominal value. As shown in Figure 3.14, adopting this updated stiffness in the FE model leads to a close match between simulated and measured FRFs.

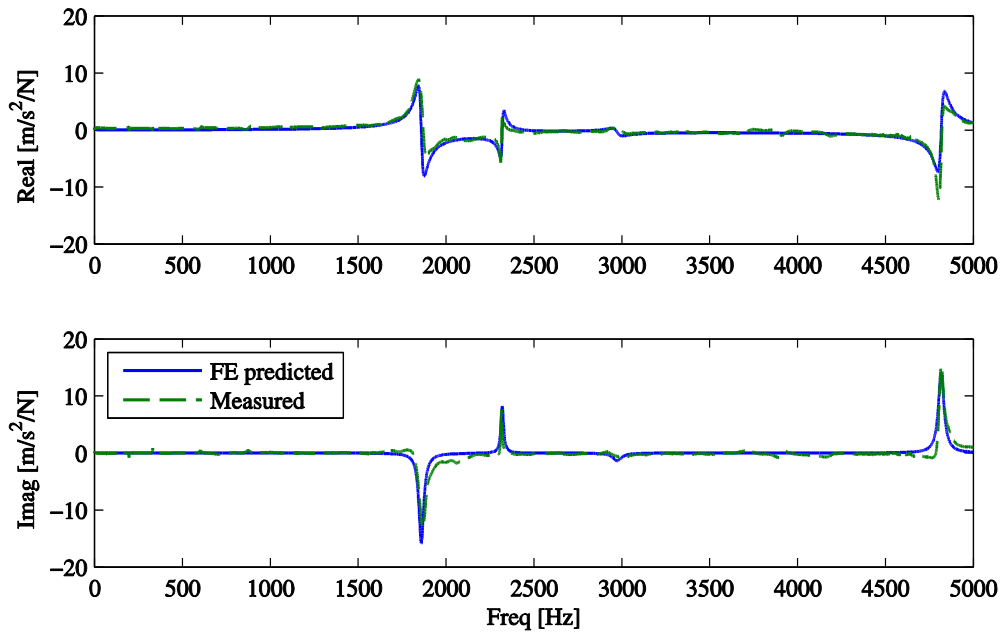


**Figure 3.14: Measured and predicted FRFs when updated nut stiffness is used in the FE model.**

### 3.3.2 FE Model for the Entire Setup

To create an FE model for the entire setup, inertial properties of different parts have to be taken from catalog data, or calculated based on CAD models and weighing. The inertia and stiffness values of components in the setup are listed respectively in Table 3.3 and

Table 3.4.

**Table 3.3: Inertia of important components of the test setup.**

Inertia source	Value
Nut and table assembly mass [kg]	33.474
Inertia of motor's rotor [kg m <sup>2</sup> ]	$7.0 \times 10^{-4}$
Inertia of encoder's rotor [kg m <sup>2</sup> ]	$8.5 \times 10^{-5}$
Inertia of coupling [kg m <sup>2</sup> ]	$9.0 \times 10^{-4}$

**Table 3.4: Important lumped stiffness values.**

Stiffness parameter	Nominal value	FE updated value
Axial stiffness of the nut [N/m]	$109.6 \times 10^6$	$84.94 \times 10^6$
Torsional stiffness of the coupling	39545	39545
Vertical stiffness of each air bearing [N/m]	$159 \times 10^6$	$159 \times 10^6$
Lateral stiffness of each air bearing [N/m]	$159 \times 10^6$	$159 \times 10^6$
Axial stiffness of the thrust bearing [N/m]	$1.13 \times 10^8$	$0.54 \times 10^8$
Radial stiffness of the thrust bearing [N/m]	$1.0 \times 10^8$	$1.0 \times 10^8$
Radial stiffness of the radial bearing [N/m]	$5.0 \times 10^7$	$5.0 \times 10^7$

The necessity for model updating arises again when taking a step forward to model the entire setup. This time, if the nominal value for axial stiffness of the thrust bearing is adopted in FE simulations, the predicted natural frequency for the first observable mode will be an overestimation of the measured value (Figure 3.15). This result is not unexpected, since in reality, the thrust bearing is bolted down to the machine's frame and the bolted joint has certain stiffness which acts in series with the axial stiffness of the bearing. To accommodate this fact, the value of the thrust bearing axial stiffness in the FE model was updated to 48% of its nominal value to reflect the combined stiffness of the bolted joint and the thrust bearing. Figure 3.16 demonstrates that adopting this updated value in the FE model makes the FE prediction of 1st mode's natural frequency far more accurate. This mode imposes a severe limitation on the achievable control bandwidth, as will be discussed later in Chapter 4. The mode shapes associated with this mode are depicted in Figure 3.17 and Figure 3.18 for torsional and axial deformations, respectively. As can be seen in Figure 3.17, in this mode, the coupling does not go through significant torsion. However, part of the screw shaft between the shaft-hub interface up to the screw-nut interface is twisted linearly. The rest of the screw shaft experiences a uniform rotation.

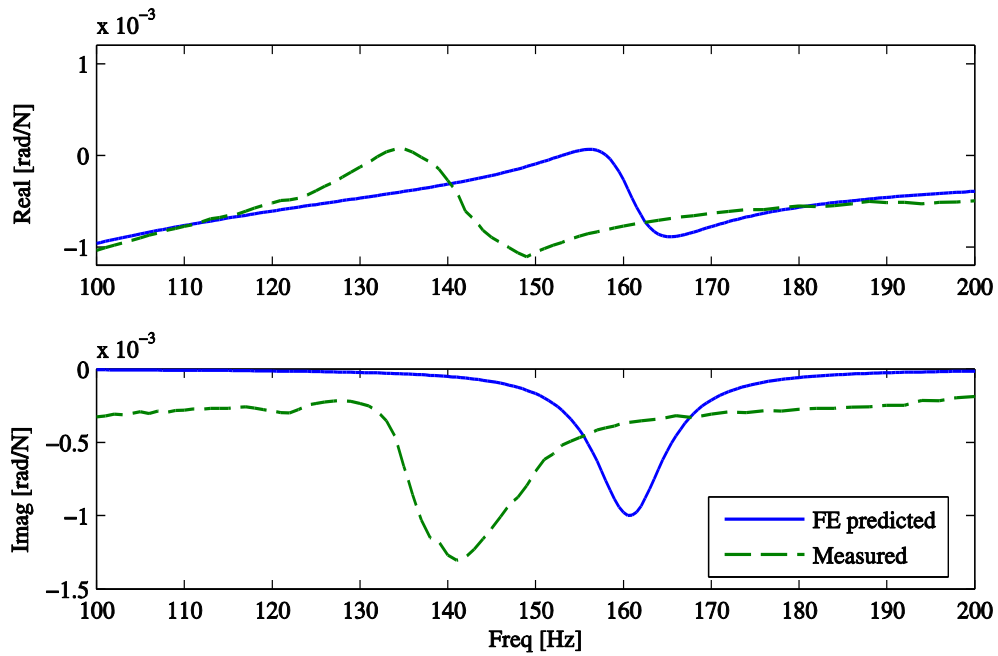


**Figure 3.15: FRF from motor torque to angular position of the screw shaft at Encoder #2 (nominal value of thrust bearing axial stiffness is used in the FE model).**

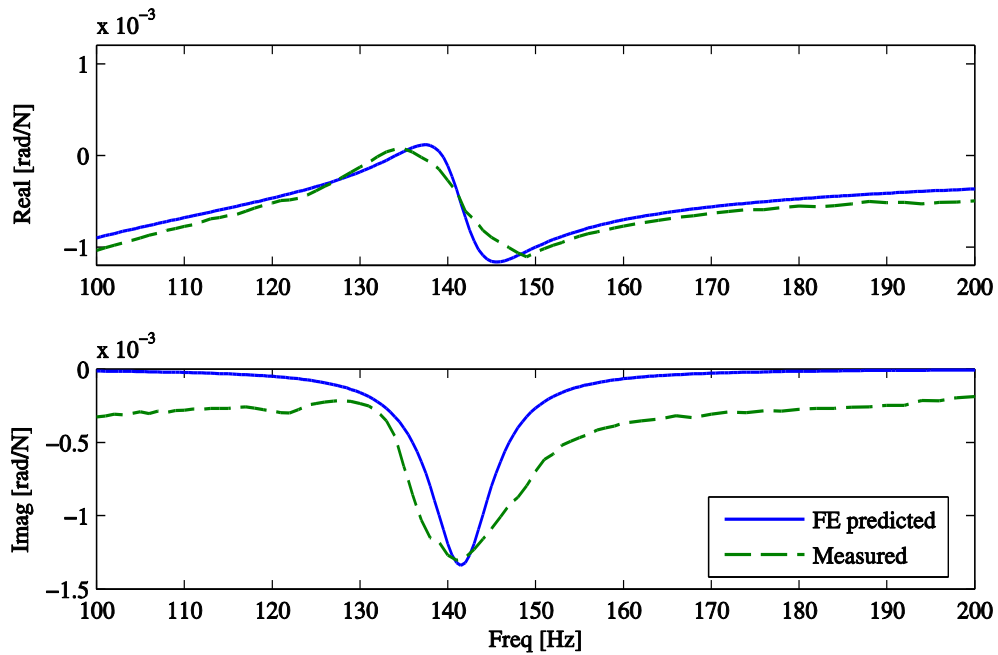


**Figure 3.16: FRF from motor torque to angular position of the screw shaft at Encoder #2 (updated value of thrust bearing axial stiffness is used in the FE model).**

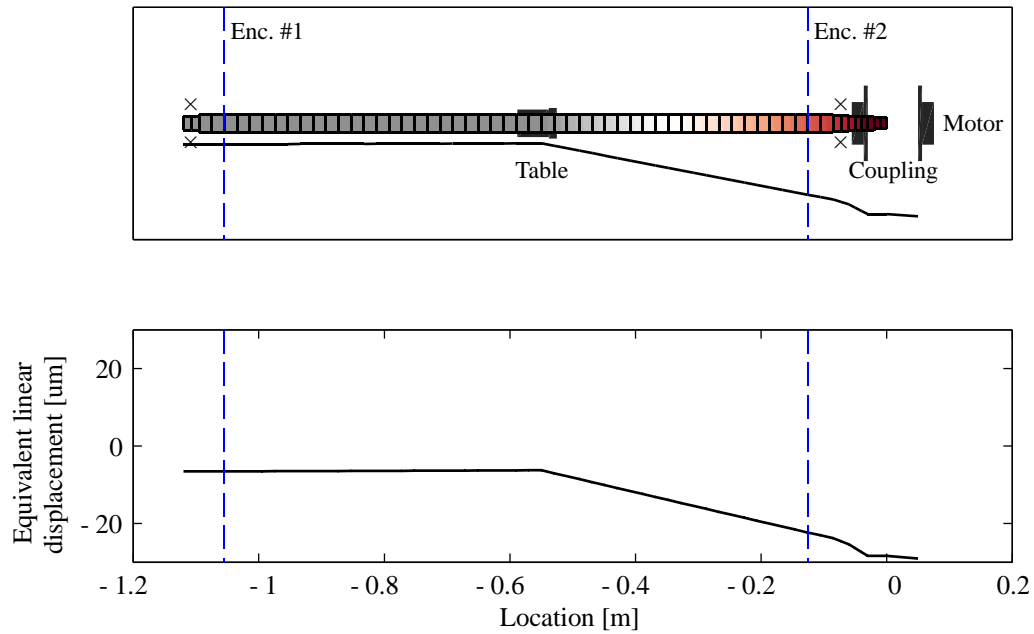


**Figure 3.17: Torsional deformation of screw shaft at mode #1 (141 Hz).**

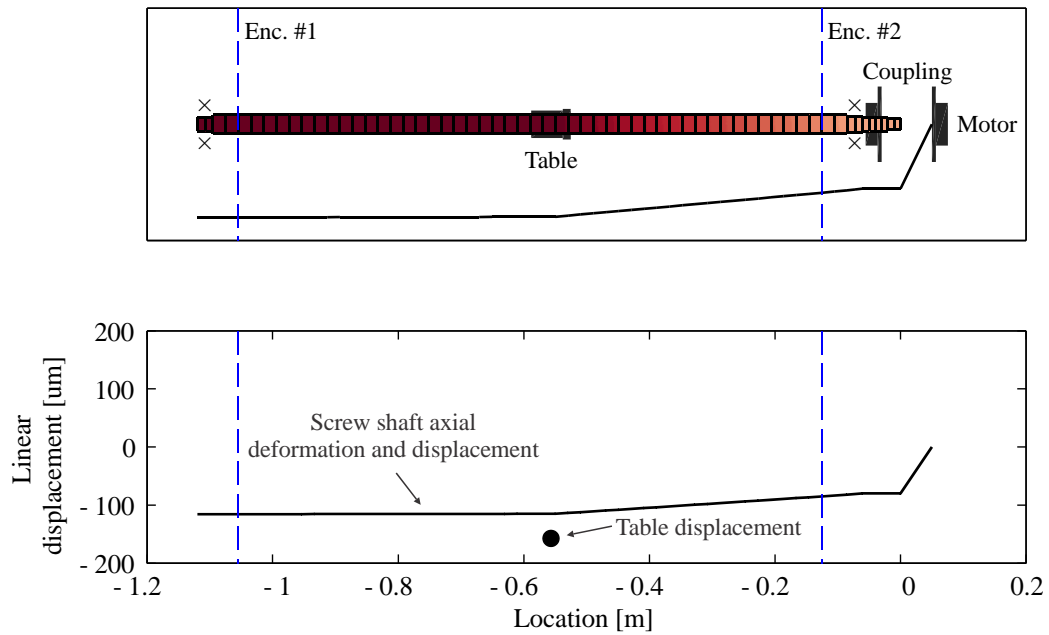


**Figure 3.18: Axial deformation of screw shaft at mode #1 (141 Hz).**

Although torsional deformation of the screw shaft in mode #1 is considerable, it is the intensity of axial deformations that makes this mode characteristically distinct from the other modes. This fact is corroborated by the observation of a strong resonance peak in the FRFs for which the table position is

taken as the output. For example, Figure 3.20 shows the FRF from motor torque excitation to table position. In this FRF, the appearance of a resonance peak at 141 Hz indicates strong linear motion of the table at that frequency. The dominance of longitudinal deformation over torsional deformation in this mode is also evident from Figure 3.2 and Figure 3.3, as the resonance peak recorded by the linear encoder is roughly 5 times larger than the resonance peak recorded by the rotary encoder #2. Another observation in Figure 3.18 is that the main contributor to the axial mode is the combined stiffness of the thrust bearing and the bolts that mount down the supporting bracket of the thrust bearing to the underlying frame. The natural frequency of this mode can be approximated from a simple model including three springs in series as shown in Figure 3.19.

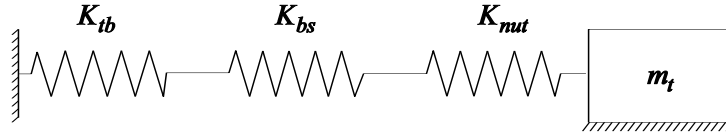


**Figure 3.19: Simple model for calculating the natural frequency of the axial mode.**

The first spring with stiffness  $K_{tb}$  (from Table 3.4) represents the combined effect of the thrust bearing and its mounting support.  $K_{bs}$  is the stiffness value associated with the portion of the screw shaft involved in torque transmission, and  $K_{nut}$  (from Table 3.4) is the stiffness of the ball nut.

For example, when the table is at middle position, the nut is 0.55 m away from the location of the thrust bearing. This distance is considered to be equal to the active length of the screw shaft ( $l_a = 0.55$  m). In this situation,  $K_{bs}$  can be calculated as follows:

$$K_{bs} = \frac{EA}{l_a} = \frac{(210 \times 10^9 \text{ N/m}^2) \times (2.545 \times 10^{-4} \text{ m}^2)}{0.55 \text{ m}} = 97.2 \text{ } \mu\text{m/N} \quad (3.14)$$

Above,  $E$  is the Young's module of elasticity for steel, and  $A$  is the equivalent cross section of the screw shaft.

Therefore, the equivalent axial stiffness is calculated as follows:

$$\frac{1}{K_{eq}} = \frac{1}{K_{tb}} + \frac{1}{K_{bs}} + \frac{1}{K_{nut}} = \frac{1}{54} + \frac{1}{97.2} + \frac{1}{84.94} \frac{\mu\text{m}}{\text{N}} \quad (3.15)$$

$$\therefore K_{eq} = 24.64 \text{ N}/\mu\text{m}$$

The natural frequency is calculated accordingly:

$$\omega_{\text{axial}} = \sqrt{\frac{K_{eq}}{m_t}} = \sqrt{\frac{24.64 \times 10^6}{33.474}} = 858 \text{ rad/s (or 137 Hz)} \quad (3.16)$$

To verify that the developed FE code is capable of capturing the varying dynamics, when the table moves along the screw axis, a set of impact hammer tests were conducted at three different locations of the table within its stroke. The distance between consecutive locations was chosen to be equal to half of the stroke (170 mm). As can be seen in Figure 3.21, the developed FE code can predict with reasonable accuracy the change in the FRF due to movement of the table along its stroke.

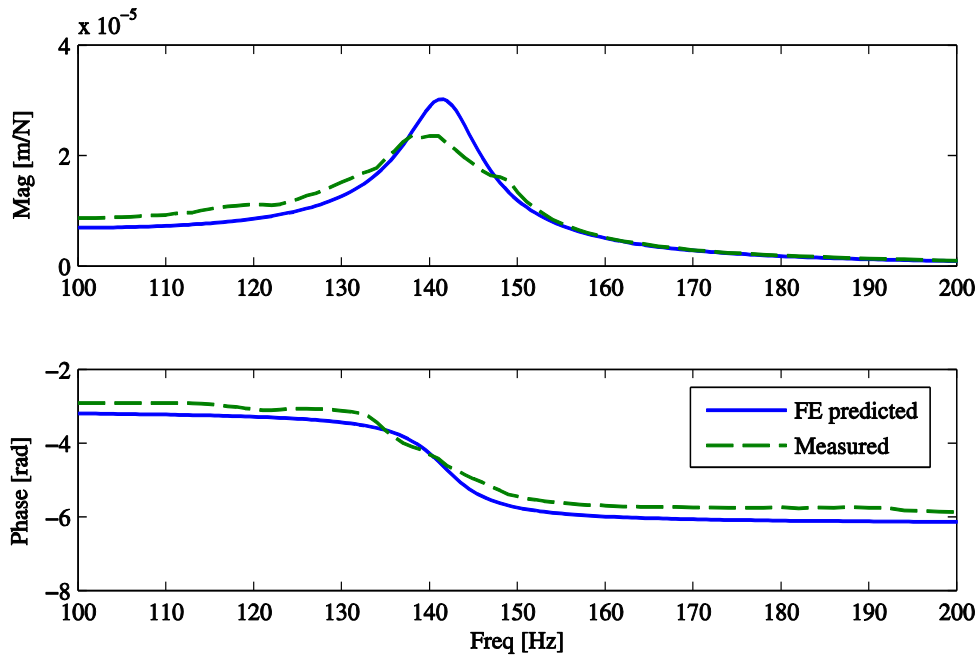


**Figure 3.20: FRF from motor torque excitation to linear displacement of the table.**

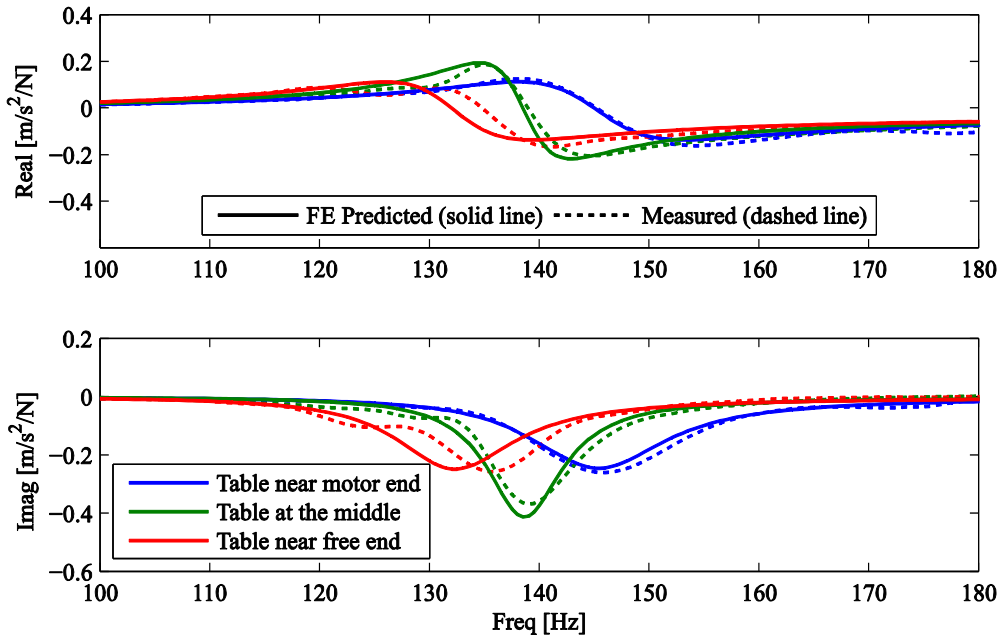


**Figure 3.21: FRF from impact hammer force applied to the table to linear acceleration of the table when it is located at three different spots within its stroke.**

As mentioned earlier, the second observable mode of vibration occurs around 450 Hz. The FE analysis was once again employed to predict this natural frequency, and study the mode shape associated with this vibration mode. Figure 3.22 shows that in this mode, the shaft undergoes a linear twist between the locations of Encoder #2 and Encoder #1. Because the screw shaft undergoes large rotations at the location of Encoder #1, the inertia of that encoder's rotor has a significant influence on the natural frequency of this mode. For example, FE analysis shows that if that encoder is dismounted from the screw shaft, the natural frequency of mode #2 would increase to 650 Hz.

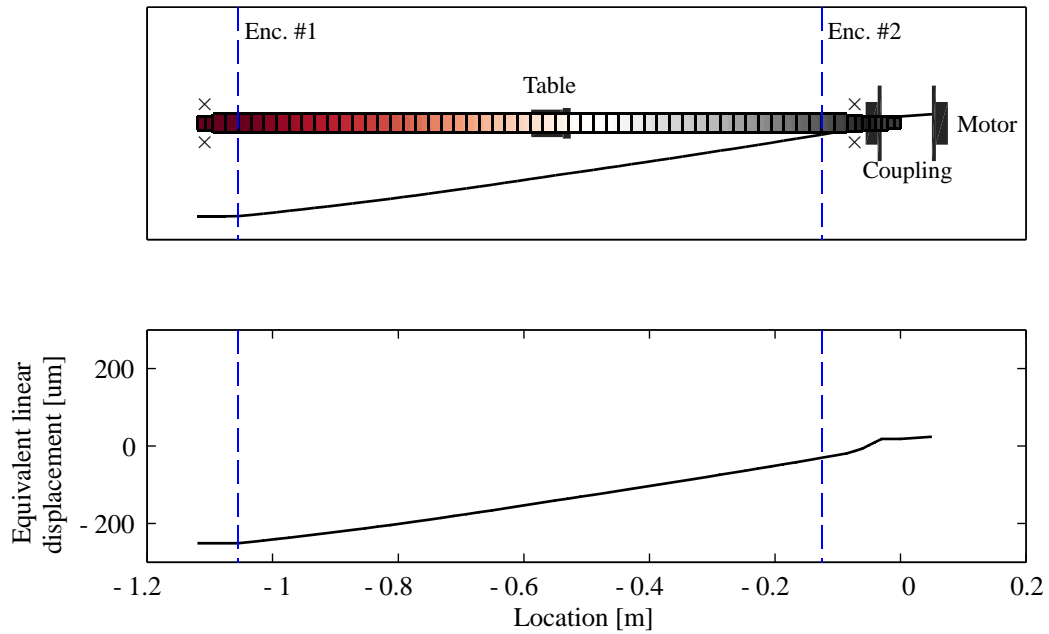


**Figure 3.22: Torsional deformation of screw shaft at mode #2 (459 Hz).**

Position FRF curves involving the second resonance peak related to mode #2 are shown in Figure 3.23. To have a better view of this mode, acceleration FRFs are also shown in Figure 3.24. The drift in the measured FRF is likely due to the over-correction of the current loop dynamics effect.

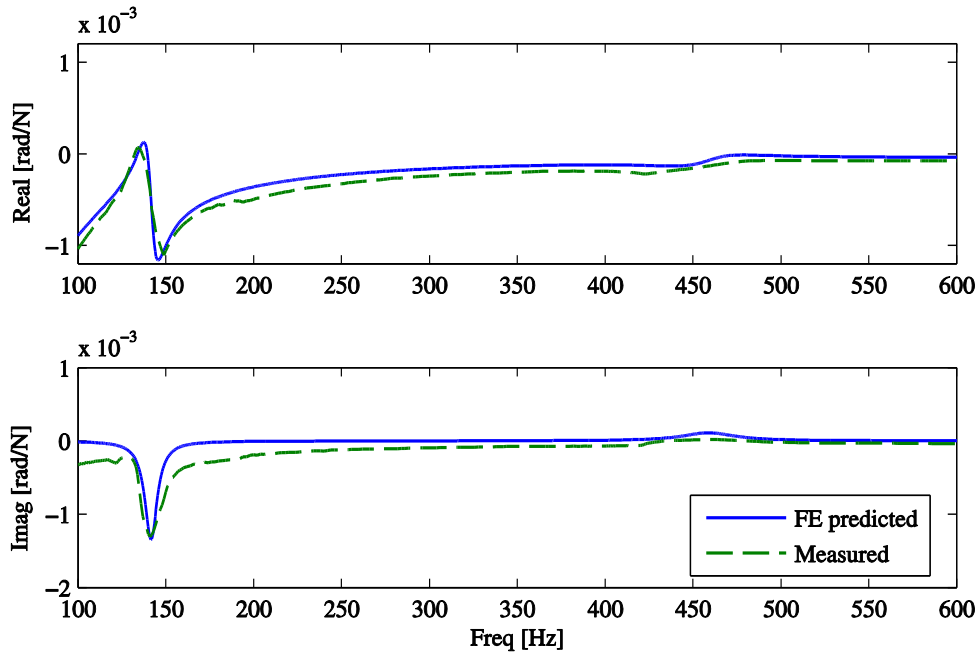


**Figure 3.23: FRF from motor torque to angular position of the screw shaft at Encoder #2.**

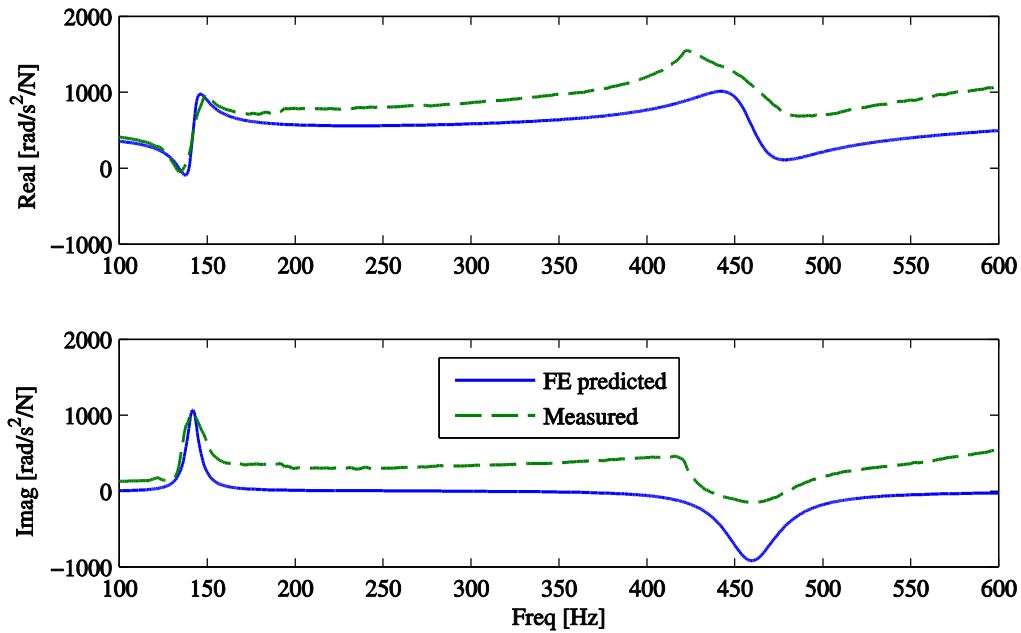
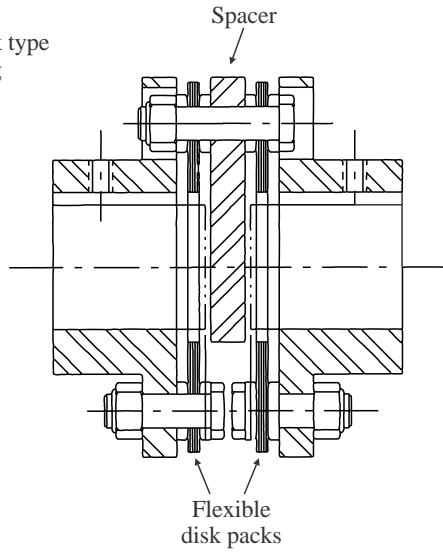


**Figure 3.24: FRF from motor torque to angular acceleration of the screw shaft at Encoder #2.**

A similar approach was followed for the analysis of mode #3 (~1080 Hz) and mode #4 (~1680 Hz). However, this time, the FE analysis indicated the existence of three torsional modes at 1020 Hz, 1263 Hz and 1668 Hz in the frequency range of 1000-2000 Hz, instead of the just two showing up in the measurements (Figure 3.26). Since the shape of the resonance peak for the mode at 1263 Hz is very similar to the measured mode at 1080 Hz, it is believed that the FE-code overestimates the frequency of that mode, and in reality, the first and second modes predicted by FE in that frequency range should be closely spaced so their combined effect is seen in the measured FRF as a single peak. Studying the rotational response mode shapes associated with these modes (Figure 3.27 to Figure 3.29) shows that in contrast to mode #1 and mode #2, these higher modes are significantly influenced by the dynamics of the coupling. Here in this thesis, a two-mass-spring model was used in the FE code to represent the dynamics of the coupling. Although this model is adequate for representing the dynamics of jaw-type couplings (Figure 3.25b), as reported by Okwudire [29], a more complicated model may be required for accurately representing the contribution of a disk-type coupling with a spacer similar to the one used in our setup (Figure 3.25a).



(a) Disk-pack type coupling



(b) Jaw-type coupling

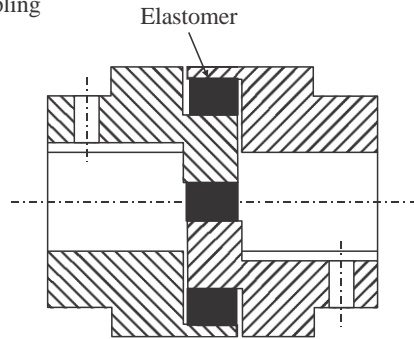


**Figure 3.25: Disk-pack versus jaw type coupling [109].**

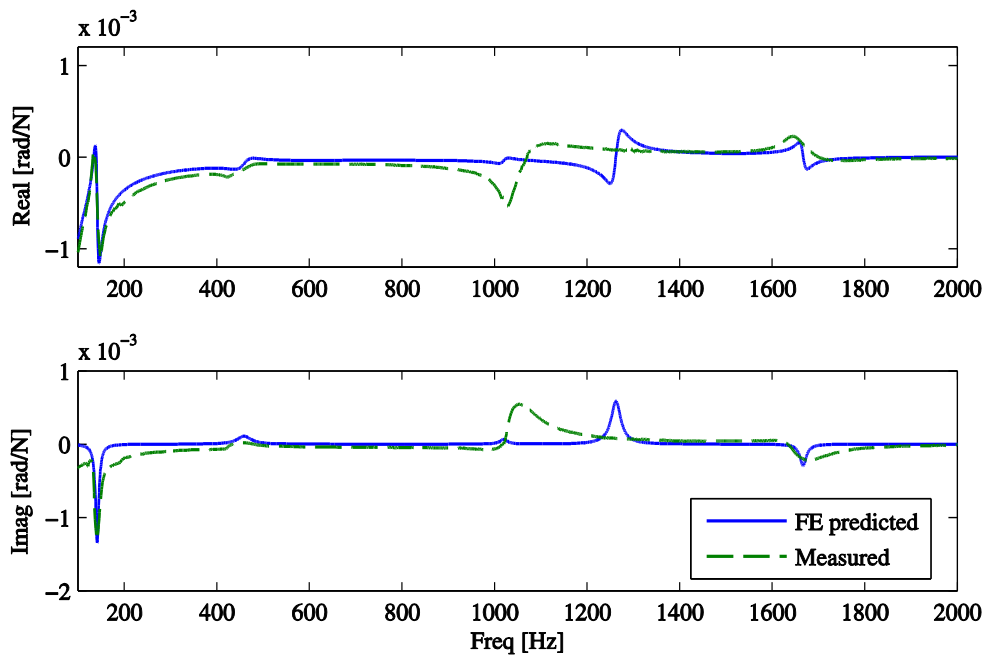


Figure 3.26: FRF from motor torque to angular position of the screw shaft at Encoder #2.

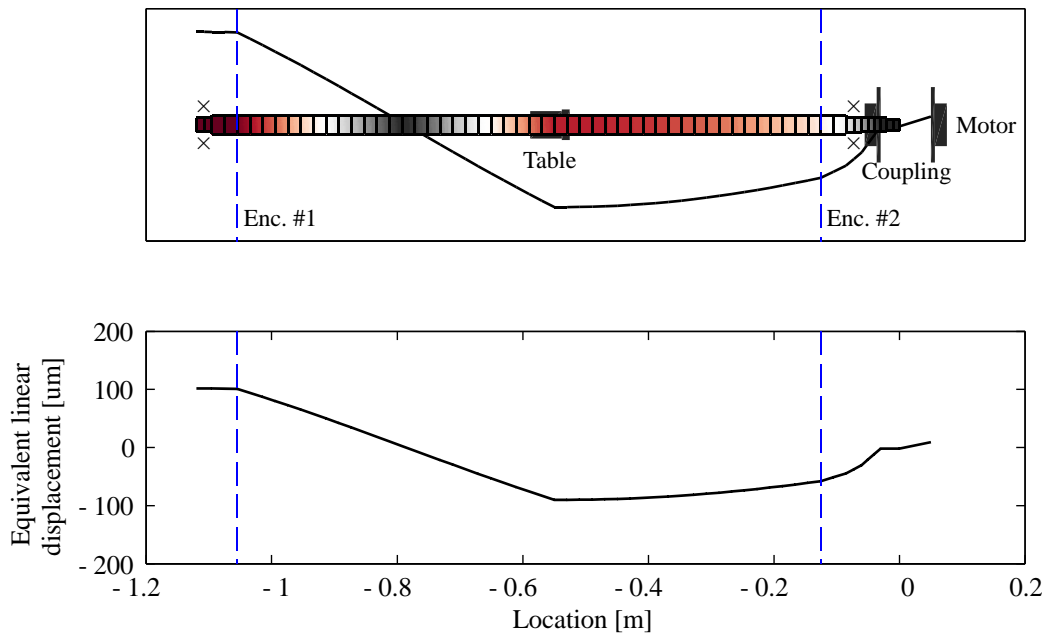
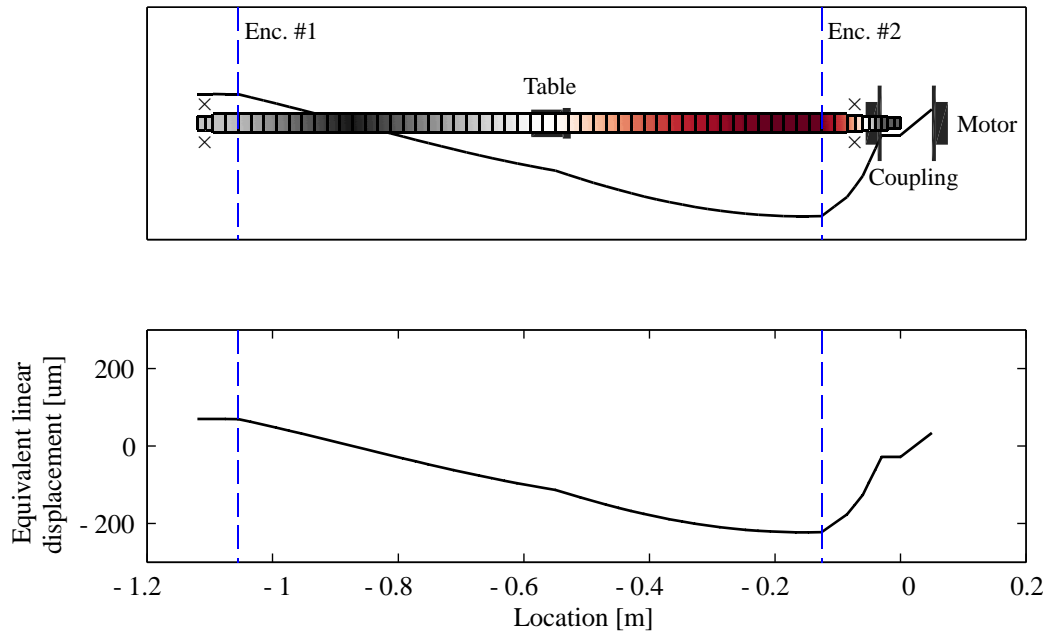
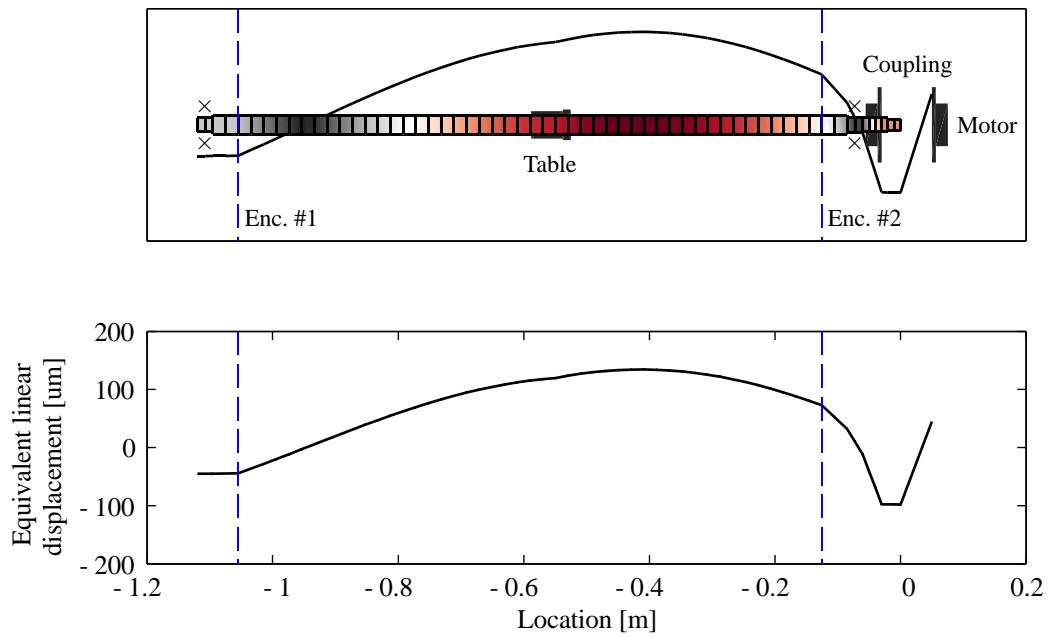


Figure 3.27: Torsional deformation of screw shaft at mode #3 (1020 Hz).



**Figure 3.28: Torsional deformation of screw shaft at mode #4 (1263 Hz).**



**Figure 3.29: Torsional deformation of screw shaft at mode #2 (1668 Hz).**

### 3.4 Frequency Domain Model Identification through Modal Analysis

Although the FE analysis presented in the previous section provides a valuable insight into the dynamics of a feed drive system, the model resulting from this approach is, most often, not suitable for control design purposes. This stems from the fact that often simple sub-models with nominal parameter values are used as building blocks of a FE model. These sub-models do not necessarily represent the involved dynamics with enough accuracy. For example, there is a significant uncertainty associated with the available models for capturing the stiffness of bolted joints. To get around this issue, the plant models used for controller design are usually identified experimentally through modal analysis. In Section 3.4.1, modal data are used to fit parameters of a lumped two-mass model. This model is intuitive, and the calculated parameters have a clear physical interpretation. However, it is only capable of capturing one mode of vibration. Therefore, to obtain higher order models, a more generalized approach must be taken, in which other vibration modes are also modeled. In Section 3.4.2, such an approach is adopted to optimize modal parameters in such a way that the FRF of the assumed model (a rigid body superimposed by a series of second order oscillators) best fits the measured FRF.

#### 3.4.1 Lumped Mass Model (Rigid Body Motion + 1st Vibration Mode)

In order to develop a two mass model, the response of the ball screw drive to control ( $u$ ) and disturbance ( $d$ ) inputs was measured by applying sinusoidal motor current commands and impact hammer testing. The measurements are shown in Figure 3.30. Using the model in Figure 2.5b, the control signal equivalent drive parameters were identified as  $m_1=1.858\times 10^{-3}$  V/(rad/s<sup>2</sup>),  $m_2=0.379\times 10^{-3}$  V/(rad/s<sup>2</sup>),  $b_1=1.020\times 10^{-3}$  V/(rad/s),  $b_2=0$  V/(rad/s) (due to aerostatic guideways),  $k=247.1$  V/rad, and  $c=0.0222$  V/(rad/s). Conversion of these parameters to SI units can be realized by considering the current amplifier gain (1.7193 A/V), motor torque constant (0.57 Nm/A), and lead screw pitch (20 mm). Another important parameter is the loop delay  $T_{delay}=0.333$  ms, which is mainly caused by the 3.9 kHz pulse-width modulation (PWM) in the current amplifier. Frequency response functions (FRF's) predicted by the model have been overlaid on top of the measurements in Figure 3.30.

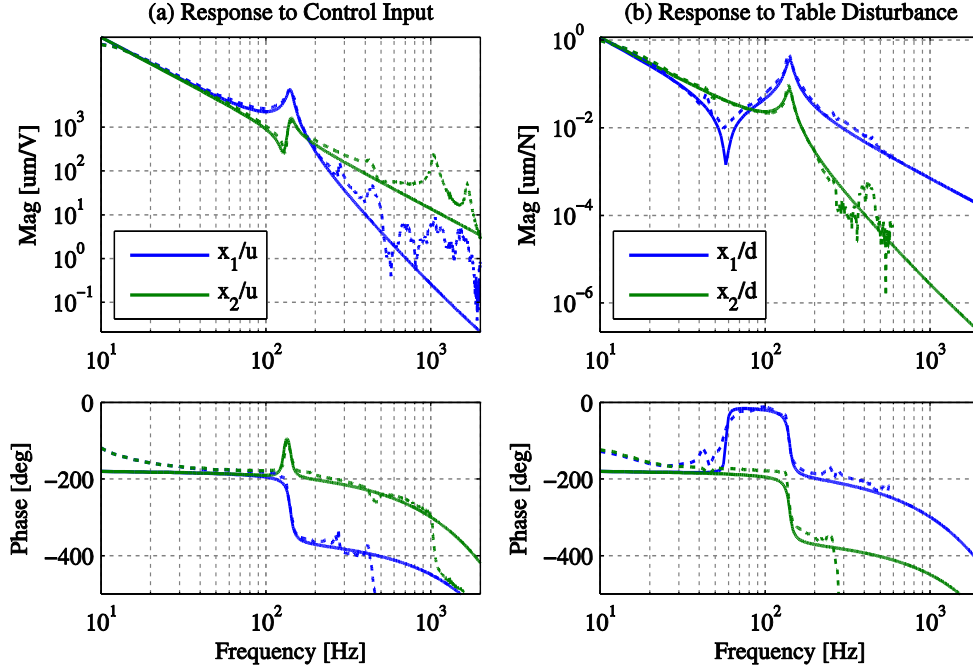


**Figure 3.30: Modeled (solid line) and measured (dashed line) open-loop frequency response functions.**

The state space representation for the two-mass model can be written as follows:

$$\begin{bmatrix} \dot{x}_2 \\ \ddot{x}_2 \\ \dot{x}_1 \\ \ddot{x}_1 \end{bmatrix} = \begin{bmatrix} 0 & 1 & 0 & 0 \\ \frac{k}{m_2} & \frac{c+b_2}{m_2} & \frac{k}{m_2} & \frac{c}{m_2} \\ 0 & 0 & 0 & 1 \\ \frac{k}{m_1} & \frac{c}{m_1} & \frac{k}{m_1} & \frac{c+b_1}{m_1} \end{bmatrix} \begin{bmatrix} x_2 \\ \dot{x}_2 \\ x_1 \\ \dot{x}_1 \end{bmatrix} + \begin{bmatrix} 0 \\ 0 \\ 0 \\ \frac{1}{m_1} \end{bmatrix} [u] \quad (3.17)$$

### 3.4.2 Multiple-Mode Model (Rigid Body Motion + First Three Modes)

Based on the FRFs measured, it was deemed that the modes at 141 Hz, 450 Hz and 1080 Hz dominate the vibratory response. Therefore, in addition to the rigid body mode, the SDOF Rational Fraction Polynomial (RFP) [24] method was used to identify the modal parameters of the vibration modes mentioned above. Equations (3.18) and (3.19) respectively show the assumed form of position response for the motor side, and the load side. The modal parameters identified accordingly are also listed in Table 3.5.

$$\frac{x_1(s)}{u(s)} = \frac{1}{(J_{est}s + B_{est})s} + \sum_{i=1}^3 \frac{\alpha_{1i}s + \beta_{1i}}{s^2 + 2\zeta\omega_{ni}s + \omega_{ni}^2} \quad (3.18)$$

$$\frac{x_2(s)}{u(s)} = \frac{1}{(J_{est}s + B_{est})s} + \sum_{i=1}^3 \frac{\alpha_{2i}s + \beta_{2i}}{s^2 + 2\zeta\omega_{ni}s + \omega_{ni}^2} \quad (3.19)$$

**Table 3.5: Identified modal parameters of the ball screw drive.**

Rigid body mode:		
Vibratory modes:	Natural frequency and damping ratio:	Residuals:
1st mode	$\omega_{n1} = 865 \text{ rad/s}$ $\zeta_{n1} = 0.04$	$\alpha_{11} = 0.02155, \beta_{11} = 67.645$ $\alpha_{21} = -0.12814, \beta_{21} = -479.59$
2nd mode	$\omega_{n2} = 2827 \text{ rad/s}$ $\zeta_{n2} = 0.03$	$\alpha_{12} = 0.0023, \beta_{12} = -49.749$ $\alpha_{22} = 0, \beta_{22} = 0$
3rd mode	$\omega_{n3} = 6722 \text{ rad/s}$ $\zeta_{n3} = 0.03$	$\alpha_{13} = -0.063176, \beta_{13} = -387.46$ $\alpha_{23} = 0, \beta_{23} = 0$

It is noteworthy that the *mechanical* FRF of the system was used in parameter identification procedure. In other words, the effect of loop delay, due to current loop dynamics, was first removed from the measured FRFs, and then the modal parameters were identified (Figure 3.31). Once the modal parameters are known, it is possible to construct the modeled FRF, with effect of the loop delay incorporated (Figure 3.32).

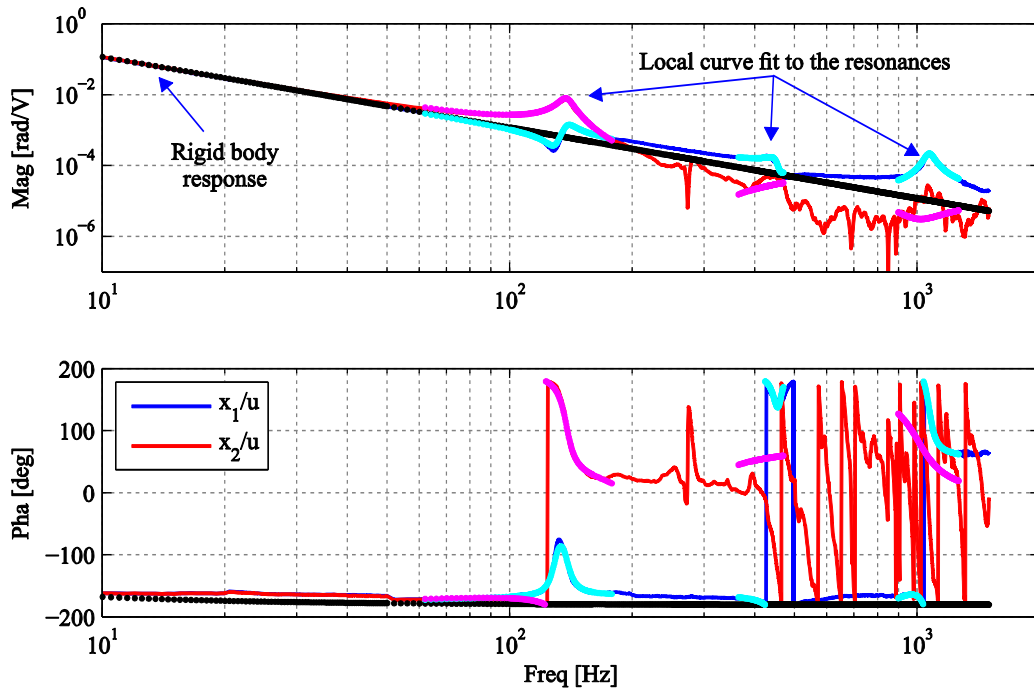


Figure 3.31: Curve fitting to rigid body dynamics and first three resonances.

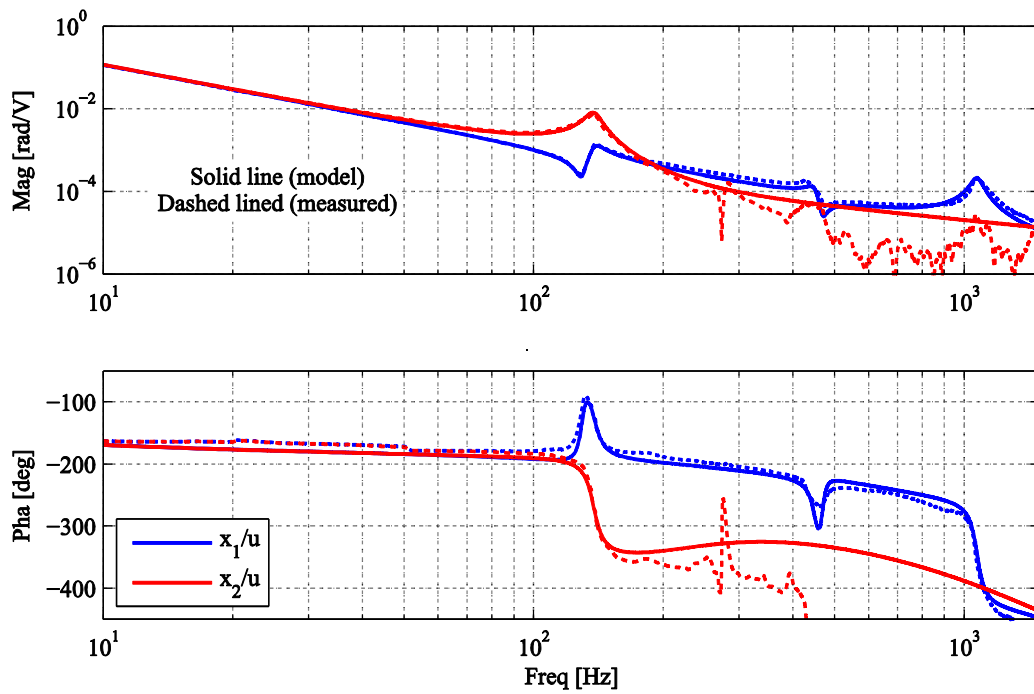


Figure 3.32: Modeled and measured open-loop frequency response functions (multiple modes).

### **3.5 Conclusions**

In this chapter, first a dynamic model for the current controller loop was developed based on matching the frequency response of an assumed PI- controlled first order plant with PWM delays to measured current FRF data. This model was then used to modify the measured FRFs when motor was used as the excitation source, by adjusting the gain and removing extra phase lag. Then, this modified FRF was used for validating a hybrid FE model developed for the ball screw test setup. The results of FE analysis were showed to be in good agreement with the measured data after some parameter updating. Therefore it is safe to say that the insight obtained from the FE model can be reliably used for controller design or structural modifications of the test setup in future work. Finally, a simplified lumped model, as well as, a multi-mode transfer function model was also identified for active vibration damping controller design in Chapter 4.

## Chapter 4

### Wide Bandwidth Controller Design Based on Modal Decomposition

The principal function of machine tool drives is to realize the desired feed motion between the tool and workpiece as accurately as possible, while ensuring that disturbances, such as process forces and nonlinear friction, have the least detrimental impact on the dynamic positioning accuracy. As the general trend in feed drive design continues towards increasing the velocity and acceleration capabilities, and the closed-loop bandwidth, it is inevitable that the control law has to deal with mechanical resonance(s) which may lie within, or very close to, its responsive frequency range [110]. This has motivated research in developing feedforward type command shaping techniques, to avoid exciting the drive's structure by reference inputs [110, 111]; and feedback based vibration damping methods, which conquer the oscillatory response of the mechanical structure and are key to improving the disturbance rejection of the drive around resonances. Feedforward control has also been applied successfully for friction compensation [12]. However, in this thesis, the feedforward friction compensation technique has not been used. Instead, the friction is treated as a disturbance that has to be rejected by the feedback controllers that are designed for this purpose.

In this Chapter, three approaches are proposed for minimizing the detrimental effects of resonance(s) on positioning accuracy and dynamic stiffness of ball screw drives. The first approach, discussed in Section 4.1, is based on the concept of sensor averaging presented in [112]. The idea behind this approach is to make certain vibration modes unobservable to the control loop, and thereby extend the loop bandwidth beyond the frequency of those modes, without jeopardizing the system's stability. This can be done by treating a multi-output control system as a single-output system through appropriate fusion of sensor data. Such a technique was used by Gordon and Erkorkmaz [21] to develop a controller for a dual linear motor driven T-type gantry. The applicability of this concept to control of ball screw drives was initially hinted at by Ellis and Lorenz [2]. However, in their work, analysis of stability and performance, either through simulations or experiments, was not carried out. In Section 4.1 of this thesis, design, tuning, and stability analysis of a proposed Center of Mass (COM) controller is laid out in detail. The performance of the COM controller is then evaluated in simulations as well as in tracking and cutting experiments. Although the COM design concept appears promising for application to an ideal two mass model, in reality, the phase delay from the current loop dynamics poses a serious limitation on the achievable closed loop bandwidth.

Furthermore, there is a loss of degree of freedom in feedback design, compared to the more general pole placement framework.

Consequently, in a second approach presented in Section 4.2, not only the first resonance, but also time delay of the plant is taken into account when designing the control law. This approach applies the principles of pole placement and loop-shaping, and is easy to implement in practice. In addition to good low frequency disturbance rejection, the control law provides active vibration damping, which reduces the magnification of tracking errors near the drive's mechanical resonance. Effectiveness of the proposed strategy is demonstrated in machining and high speed tracking experiments, where its performance is compared to the industry standard P-PI cascade control law. The procedure explained in Section 2.2.1 is used in tuning the gains of the P-PI controller.

Finally, in an attempt to extend the controller bandwidth even further, higher frequency modes of vibration are considered in control law design in Section 4.3. In this approach, a Kalman filter is designed based on a high order identified model of the system (presented in Section 3.4.2). This filter is employed to estimate the state vector. The closed loop poles are then placed such that, without altering the damped natural frequencies, the exponential decay rates of the vibration modes are increased. To improve the stability margin, a loop shaping filter is also added to the control loop at the plant input. This filter is designed following the McFarlane-Glover loop shaping method [4]. This approach is promising in theory, as it leads to a very high closed loop bandwidth. However, it was observed that using the robustifying filter impairs the damping ratios set during the pole placement step. In addition, due to sensitivity of the Kalman filter to plant modeling errors, the controller parameters have to be detuned to ensure stability, and as a result, the disturbance rejection performance predicted in frequency response analyses turned out to be unsatisfactory.

#### 4.1 Center of Mass Controller (COM)

The COM controller is designed assuming a two mass model for the ball screw drive (Figure 2.5). In transfer matrix form, the drive model can be written as:

$$\begin{bmatrix} x_1(s) \\ x_2(s) \end{bmatrix} = \begin{bmatrix} G_1(s) & G_{d1}(s) \\ G_2(s) & G_{d2}(s) \end{bmatrix} \begin{bmatrix} u(s) \\ d(s) \end{bmatrix} = [\mathbf{G}(s) \quad \mathbf{G}_d(s)] \begin{bmatrix} u(s) \\ d(s) \end{bmatrix} \quad (4.1)$$

The location of the center of mass is determined as follows:

$$\bar{x} = \frac{m_1 x_1 + m_2 x_2}{m_1 + m_2} \quad (4.2)$$

If the disturbance and viscous friction forces external to the system are neglected (i.e. assuming  $d = b_1 = b_2 = 0$ ), the acceleration of the center of mass turns out to be proportional to the input force ( $u$ ):

$$u = (m_1 + m_2) \ddot{\bar{x}} \rightarrow G_{\bar{x}u} = \frac{1}{(m_1 + m_2)s^2} \quad (4.3)$$

This is due to the fact that the spring and damper forces are internal to the system, and have no influence on the location of the COM [113]. Later on, external damping and friction forces will be treated as external disturbances and will be handled by the integral action. Equation (4.3) describes the dynamics of a double integrator. The idea here is to use a control law such as a simple PD to enforce the COM to follow a trajectory ( $\bar{x}_r$ ) consistent with the second mass following the reference trajectory ( $x_{2r}$ ):

$$\bar{x}_r(s) = \frac{m_2}{m_1 + m_2} x_{2r} + \frac{m_1}{m_1 + m_2} x_{1r} \quad (4.4)$$

To accomplish this, the rotational position command has to be adjusted to account for the anticipated elastic deformation of the drive. Hence, a command generator is used in the form:

$$\bar{x}_r(s) = \left[ \frac{m_2}{m_1 + m_2} + \frac{m_1}{m_1 + m_2} \frac{m_2 s^2 + (b_2 + c)s + k}{cs + k} \right] x_r \quad (4.5)$$

In order to minimize the internal vibrations of the two-mass system, a control force proportional to the velocity difference between the two masses is applied to the system:

$$u = K_{v12} \frac{d(x_2 - x_1)}{dt} = K_{v12} \frac{d(\Delta x)}{dt} \quad (4.6)$$

To show how this force dampens out the elastic mode of motion, we derive the transfer function from the input force ( $u$ ) to the displacement difference between the two masses ( $\Delta x$ ). The equations of motion for this two-mass system can be written as:

$$\begin{aligned} m_1 \ddot{x}_1 &= u - c(\dot{x}_1 - \dot{x}_2) - k(x_1 - x_2) \\ m_2 \ddot{x}_2 &= c(\dot{x}_1 - \dot{x}_2) + k(x_1 - x_2) \end{aligned} \quad (4.7)$$

Multiplying the first equation by  $-m_2$  and the second one by  $m_1$  and adding them together gives:

$$m_1 m_2 (\ddot{x}_2 - \ddot{x}_1) = (m_1 + m_2) c (\dot{x}_1 - \dot{x}_2) + (m_1 + m_2) k (x_1 - x_2) - m_2 u \quad (4.8)$$

Taking the Laplace transform of Equation (4.8) yields:

$$\left( s^2 + \frac{(m_1 + m_2)c}{m_1 m_2} s + \frac{(m_1 + m_2)k}{m_1 m_2} \right) (x_2(s) - x_1(s)) = -\frac{m_2}{m_1 m_2} u(s) = -\frac{1}{m_1} u(s) \quad (4.9)$$

Or:

$$x_2(s) - x_1(s) = \Delta x(s) = \frac{-\frac{1}{m_1}}{s^2 + 2\zeta\omega_n s + \omega_n^2} u(s) \quad (4.10)$$

Above,

$$\omega_n^2 = \frac{(m_1 + m_2)k}{m_1 m_2}, 2\zeta\omega_n = \frac{(m_1 + m_2)c}{m_1 m_2} \quad (4.11)$$

After substituting the active damping term described by Equation (4.6) into Equation (4.10), we obtain:

$$\begin{aligned} \Delta x(s) &= \frac{-\frac{1}{m_1}}{s^2 + 2\zeta\omega_n s + \omega_n^2} K_{v12} s \Delta x(s) \\ \therefore [s^2 + (2\zeta\omega_n + \frac{K_{v12}}{m_1})s + \omega_n^2] \Delta x(s) &= 0 \rightarrow [s^2 + (2\beta\zeta\omega_n)s + \omega_n^2] \Delta x(s) = 0 \end{aligned} \quad (4.12)$$

Equation (4.12) indicates that applying the proposed active damping increases the damping ratio with a factor of  $\beta$  without altering the natural frequency of the oscillations. To better control the load side of the two-mass system, and push the steady-state tracking error to zero, an integral controller, acting on the load side, was implemented in parallel with the main COM controller. Figure 4.1 shows the overall control scheme that has been implemented in this section.

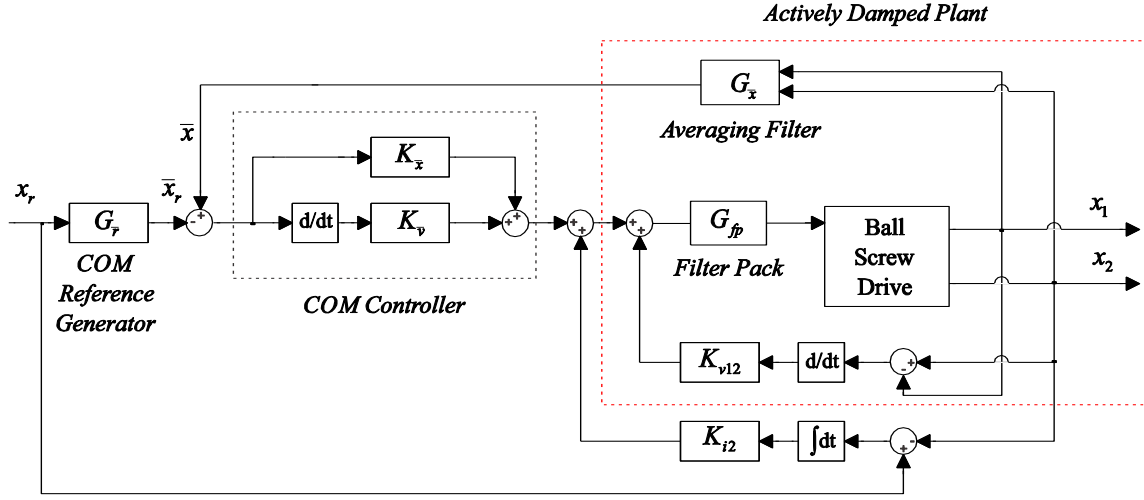


**Figure 4.1: Overall control scheme for the COM controller.**

The averaging filter in Figure 4.1 is used to calculate the COM feedback signal according to Equation (4.2). To mitigate the effect of higher-frequency resonances on the stability of the designed controller, a filter pack comprising of a low pass filter and two notch filters was added to the feedback loop:

$$G_{fp} = \frac{s^2 + 2\zeta_{n1}\omega_{n1}s + \omega_{n1}^2}{s^2 + 2\zeta_{d1}\omega_{n1}s + \omega_{n1}^2} \cdot \frac{s^2 + 2\zeta_{n2}\omega_{n2}s + \omega_{n2}^2}{s^2 + 2\zeta_{d2}\omega_{n2}s + \omega_{n2}^2} \cdot \frac{\omega_{lpf}}{s + \omega_{lpf}} \quad (4.13)$$

Above,  $\omega_{n1} = 2639$  rad/s (420 Hz),  $\zeta_{n1} = 0.2$ ,  $\zeta_{d1} = 0.7$ ,  $\omega_{n2} = 10995$  rad/s (1750 Hz),  $\zeta_{n2} = 0.15$ ,  $\zeta_{d2} = 0.7$ ,  $\omega_{lpf} = 6283$  rad/s (1000 Hz). Designing the controller begins by selecting a value for the active damping gain ( $K_{v12}$  in Figure 4.1). As shown, the feedback loop containing  $K_{v12}$  together with the original plant forms a new plant, for which, other controller gains are selected. This new plant denoted by  $G'_{xu}$  is presented in Figure 4.2. A loop shaping procedure is then employed to design a PID controller for the actively damped plant, such that the resulting control loop has a high crossover frequency with at least 35 degrees of phase margin:

$$C = K_p + \frac{K_i}{s} + K_d s = K_i \frac{(T_d s + 1)(T_i s + 1)}{s} \quad (4.14)$$

$$\begin{aligned} K_d &= K_i (T_i T_d) \\ \therefore K_p &= (T_i + T_d) \end{aligned}$$

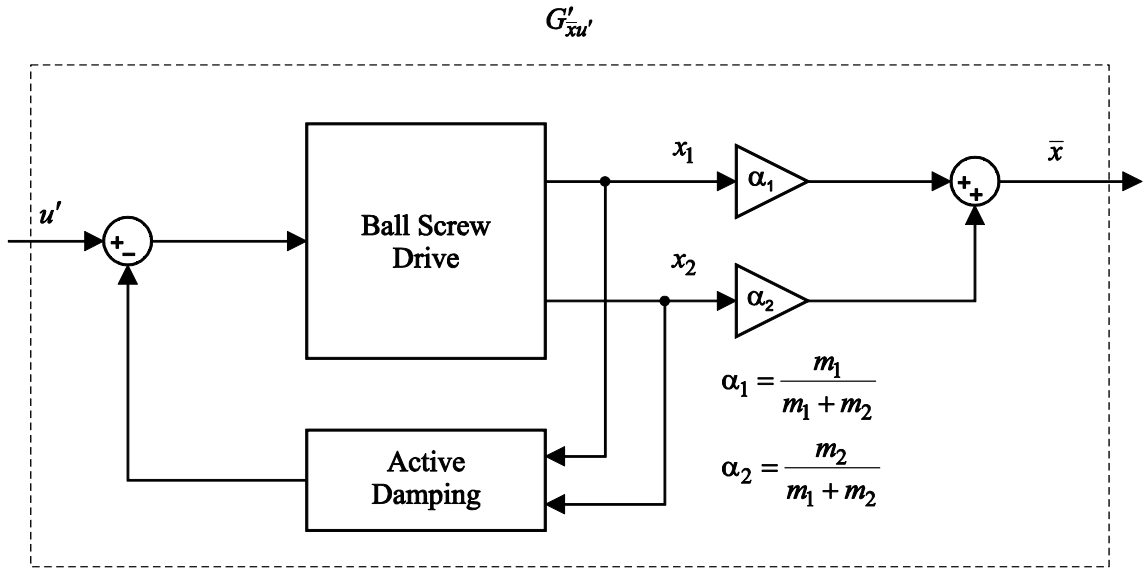


**Figure 4.2: Block diagram of the new plant for which COM control law is designed.**

To achieve the desired phase margin, first, the  $T_i$  is selected in such a way that the phase lag due to the integral action at the target crossover frequency equals a pre-selected value of  $\phi_p$  :

$$\phi_p = \angle \frac{T_i s + 1}{s} \Big|_{s = j\omega_c} = \tan^{-1}(\omega_c T_i) - 90^\circ \rightarrow T_i = \frac{1}{\omega_c} \tan(\phi_p + 90^\circ) \quad (4.15)$$

Then,  $T_d$  is chosen to recover the loop phase and achieve the desired phase margin:

$$\begin{aligned} \phi_d &= -180 + PM - \phi_p - \angle G_{\bar{x}u}(j\omega_c) - \angle G_{fp}(j\omega_c) - \angle G_d(j\omega_c) \\ \phi_d &= \tan^{-1}(\omega_c T_d) \\ \therefore T_d &= \frac{1}{\omega_c} \tan(\phi_d) \end{aligned} \quad (4.16)$$

Above,  $\phi_d$  is the required phase recovery,  $PM$  is the desired phase margin, and  $\angle G_d(j\omega_c)$  is the phase lag due to loop delays at the target crossover frequency. Finally,  $K_i$  is calculated to bring the loop magnitude to unity at the target crossover frequency:

$$K_i = \frac{|j\omega_c|}{|j\omega_c T_i + 1|} \cdot \frac{|G_{\bar{x}u}(j\omega_c)|}{|j\omega_c T_d + 1|} \quad (4.17)$$

For this controller, the target crossover frequency is chosen as 90 Hz ( $\omega_c = 565.47$  rad/s), and 15 degrees of phase lag is pre-budgeted for the integral action ( $\phi_p = 15^\circ$ ). After  $T_i$ ,  $T_d$  and  $K_i$  are determined, the obtained P and D gains are used in the main COM controller, whereas the I-gain is shifted to the load side integrator. It is necessary to mention that designing the controller gains, as explained above, is an iterative procedure which is terminated when the desired stability margins are met, and the disturbance FRF ( $G_{22}$ ) takes a satisfactory shape:

$$G_{22} = S_{21}G_{d1} + S_{22}G_{d2}, \mathbf{S} = \begin{bmatrix} S_{11} & S_{12} \\ S_{21} & S_{22} \end{bmatrix} = (\mathbf{I} + \mathbf{GK})^{-1} \quad (4.18)$$

For example, different choices can be made for the factor of damping increase ( $\beta$ ) that dictates the value of  $K_{v12}$ . Figure 4.3 shows how the value of  $\beta$  affects the shape of the frequency response of the actively damped plant. As can be seen, without active damping ( $\beta=1$ ),  $G_{\bar{x}u}$  behaves like a double integrator. Adding active damping roughly has the same effect on the FRF as adding a notch filter at the frequency of resonance, which brings about unwanted phase lag before the resonance frequency.

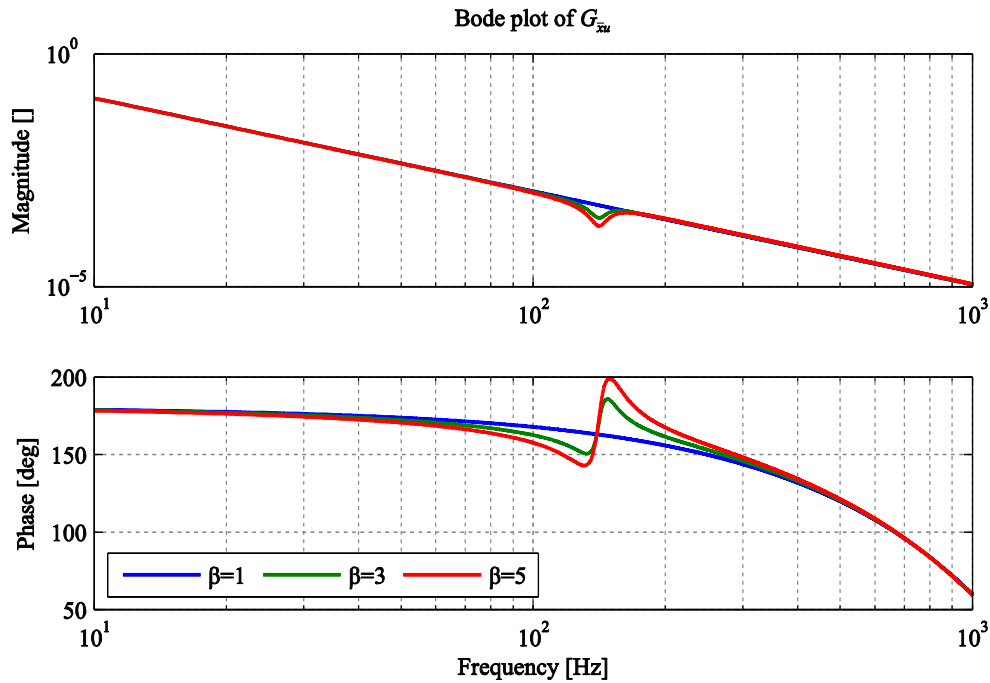


**Figure 4.3: Effect of the factor of damping increase on frequency response of the damped plant**

Although Figure 4.3 indicates that selection of higher values of  $\beta$  leads to better damping of the vibration mode, it should be noted that  $|G_{22}(s)|$  also needs to be minimized as much as possible to reduce the worst case dynamic stiffness. To investigate the effect of  $\beta$  on disturbance rejection,  $|G_{22}(s)|$  was calculated according to Equation (4.15) for different values of  $\beta$ . The target crossover frequency and the desired phase margin were kept the same in all cases. The results are shown in Figure 4.4. As expected, the best resonance damping is realized when the highest value of  $\beta$  is used in the control design. However, as far as the low frequency disturbance rejection is concerned, the correlation is reversed, and the best low frequency disturbance rejection is achieved with lowest value of  $\beta$ . This presents a tradeoff between active vibration damping and low frequency disturbance rejection.

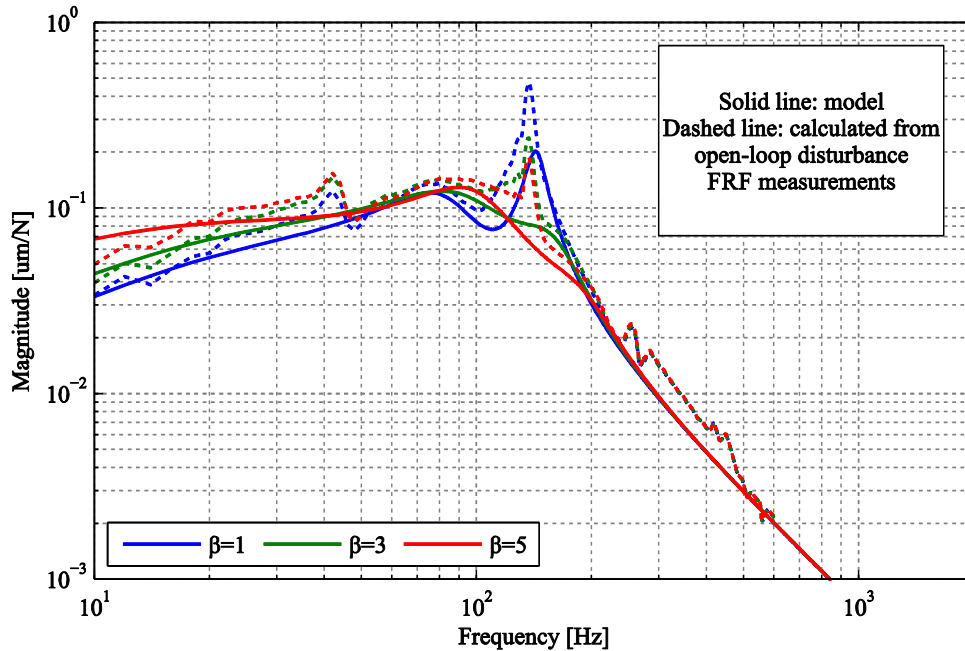


**Figure 4.4: Load side disturbance FRF for COM controllers with different values of  $\beta$ .**

Considering the existing tradeoffs and based on the design procedure explained above, the value of  $\beta = 4$  was eventually selected for the COM control design, along with a target cross frequency of 90 Hz. The controller gains were calculated according to Equations (4.14) to (4.17). The control law was initially designed in the continuous domain, and then discretized using Euler approximation for the derivatives and Tustin transformation for the filters, at a sampling rate of 20 kHz, and implemented on a dSPACE DS1005 platform. From the loop transfer function magnitude plot shown in Figure 4.6,

the crossover frequency of the COM control loop was verified to be 86 Hz. For comparison, a P-PI cascade controller was also designed, where the velocity loop is closed with rotational feedback and the position loop with translational feedback. P-PI cascade represents the industry mainstream. This controller was designed according to the guidelines in [59], and also possesses velocity and acceleration feedforward terms as shown in Figure 4.5.

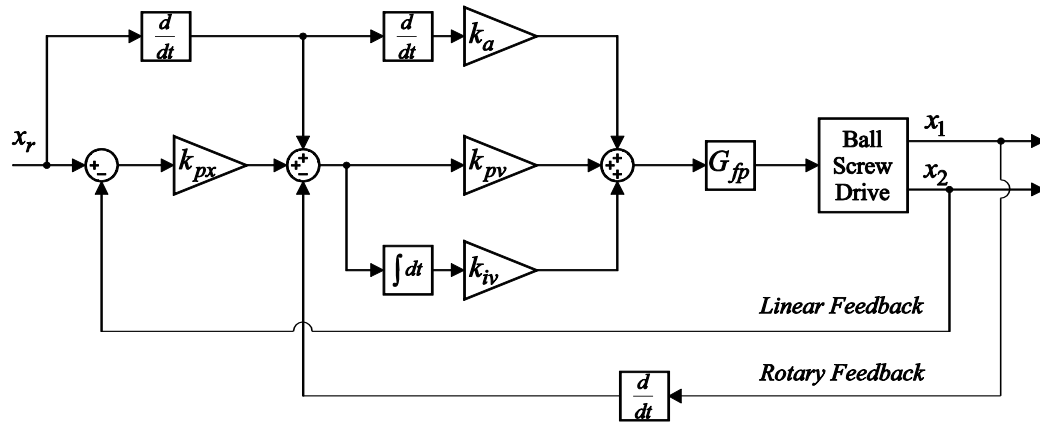


**Figure 4.5: P-PI cascade feedback control plus velocity and acceleration feedforward control.**

It is apparent from Figure 4.6 that the crossover of the P-PI control loop occurs at 74 Hz, which is below the crossover of the COM controller. The Nyquist plots for the COM and P-PI controllers are compared in Figure 4.7. As can be seen, while the phase margin is around 45 degrees for the COM, it is around 40 degrees for the P-PI. The sensitivity plot is shown in Figure 4.8. Here, COM control again shows an advantage over P-PI in terms of peak sensitivity which is another indicator of stability margin.

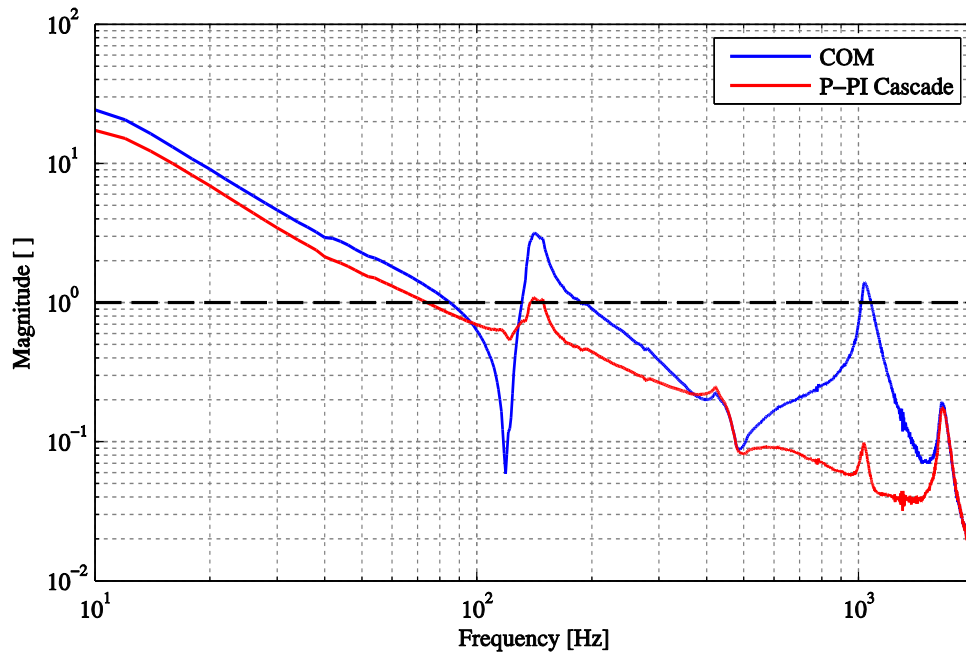


**Figure 4.6: Loop transfer function magnitude for COM and P-PI schemes.**

As mentioned earlier, one of the most important requirements for control system of a feed drive is the ability to provide good disturbance attenuation against cutting forces acting on the load side. As can be seen in Figure 4.9, the designed COM controller improves the dynamic stiffness at low frequencies, as well as in the vicinity of the resonance. However, compared to the main-stream industrial P-PI cascade controller, it provides less disturbance attenuation at low frequencies.

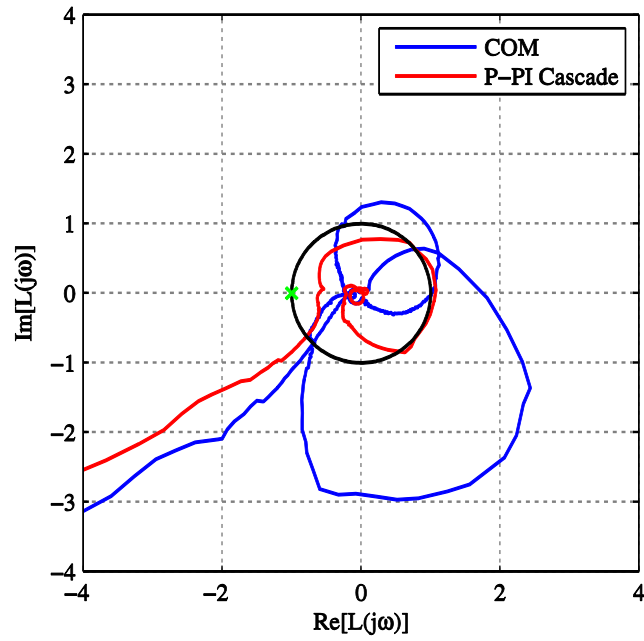


Figure 4.7: Nyquist diagrams for COM and P-PI control.

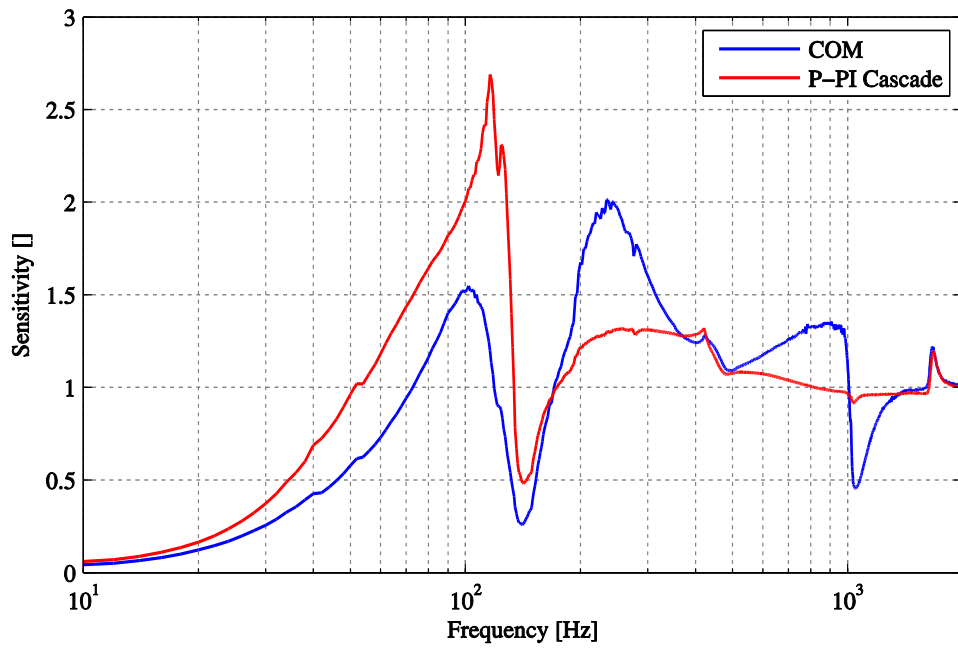
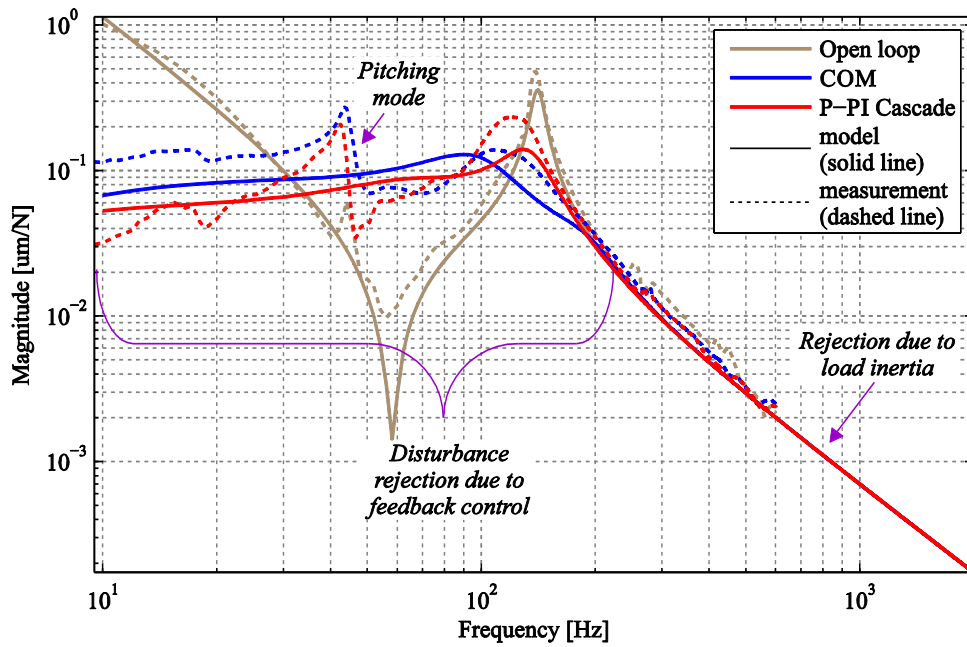
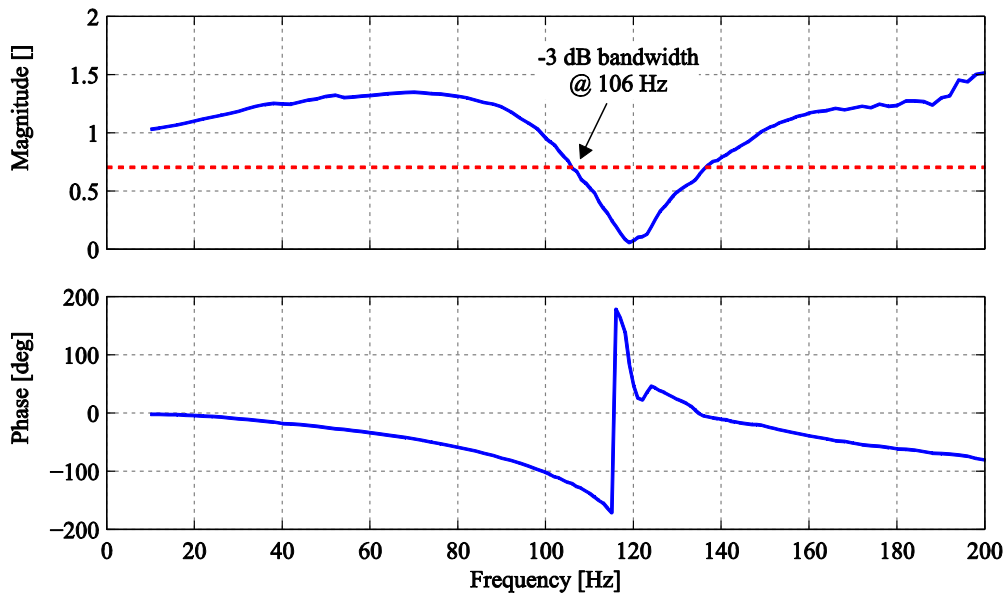


Figure 4.8: Sensitivity functions for COM and P-PI control.



**Figure 4.9: Load side disturbance response for open- and COM closed-loop cases.**

The closed-loop command following FRF of the COM is also shown in Figure 4.10. The designed COM controller achieves a command following bandwidth of 106 Hz.



**Figure 4.10: Command following FRF of the designed COM controller.**

To investigate the range of model parameter variations that the COM controller can tolerate and remain stable, a series of time-domain simulations were conducted in which the load side inertia ( $m_2$ ) and the stiffness coefficient ( $k$ ) were altered by a percentage of their nominal values. The results for this analysis are shown in Figure 4.11. The COM controller is capable of tolerating a slightly wider range of parameter variation in the feed drive. For example, if the load side inertia increases to 13 times of its nominal value (assuming the drive stiffness is at 80% of its nominal value), the COM controller remains stable. However, for the same scenario, using the P-PI controller will result in an unstable system.

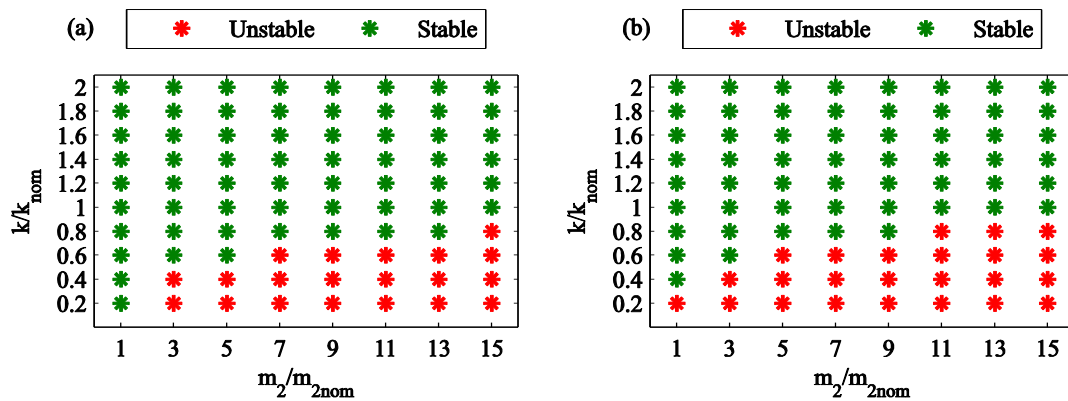


Figure 4.11: Simulated stable zones for: (a) COM controller, and (b) P-PI cascade controller.

#### 4.1.1 Experimental Results

The COM controller was validated in machining and high speed tracking experiments. The ball screw drive was mounted on the x-axis of an OKK Vertical Machining Center 410, equipped with a 3500 rpm spindle (Figure 4.12).



Figure 4.12: Experimental setup.

In the first metal cutting experiment, a 1 inch diameter 2-flute helical end-mill was used to perform slot-cutting on Aluminum 6065 at 6 mm depth of cut, with feedrate of 360 mm/min, and spindle speed of 1475 rpm (24.58 Hz). Measured positioning errors from the linear encoder, due to cutting forces, are shown in Figure 4.13. As anticipated from the disturbance FRF (Figure 4.9), the P-PI controller exhibits superior disturbance rejection at the spindle frequency (24.58 Hz) compared to the COM controller, and as a result, the positioning errors associated with the COM controller in this case are higher compared to those associated with the P-PI controller. The maximum error for the COM controller is 66  $\mu\text{m}$  whereas the maximum error for the P-PI controller is 57  $\mu\text{m}$ . The RMS error values for the COM and P-PI control cases were found to be 19  $\mu\text{m}$  and 13  $\mu\text{m}$  respectively.

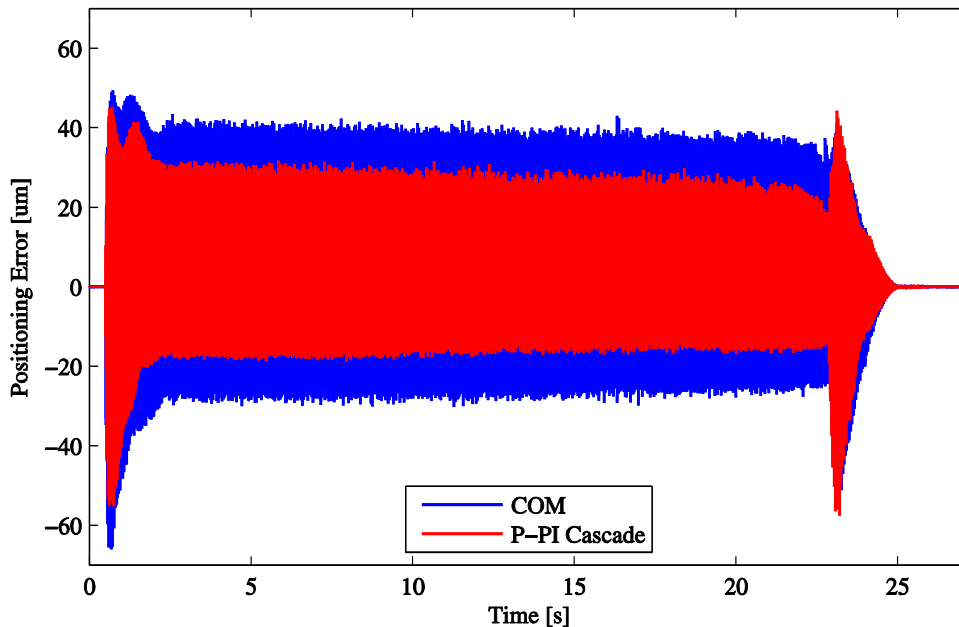


**Figure 4.13: Positioning error in 1 inch slotting at 1475 rpm spindle speed in 6065 aluminum.**

To investigate the controller performance at higher frequency, a second experiment was designed and conducted using the following cutting parameters: 3500 rpm spindle speed (58.33 Hz), 0.2 mm depth of cut, 12000 mm/min feedrate. The positioning errors observed in this experiment are presented in Figure 4.14 for both COM and P-PI cascade controllers. In this case, the difference in performance is less clear-cut. The maximum error for the COM controller is 4.89  $\mu\text{m}$  whereas the maximum error for the P-PI controller is 3.75  $\mu\text{m}$ . The RMS error values for the COM and P-PI control cases, however, were found to be 0.64  $\mu\text{m}$  and 0.69  $\mu\text{m}$  respectively. Therefore, to make a

correct judgement, spectral content of the error signals obtained from Fast Fourier Transform (FFT) was inspected. From Figure 4.15, it is clear that the spectrum of the error signal is concentrated around the run-out frequency (58.33 Hz) and the tooth-passing frequency (116.66 Hz). It is also evident that at these frequencies, the COM outperforms the P-PI in terms of disturbance rejection. These results are consistent with the disturbance rejection FRFs presented in Figure 4.9.

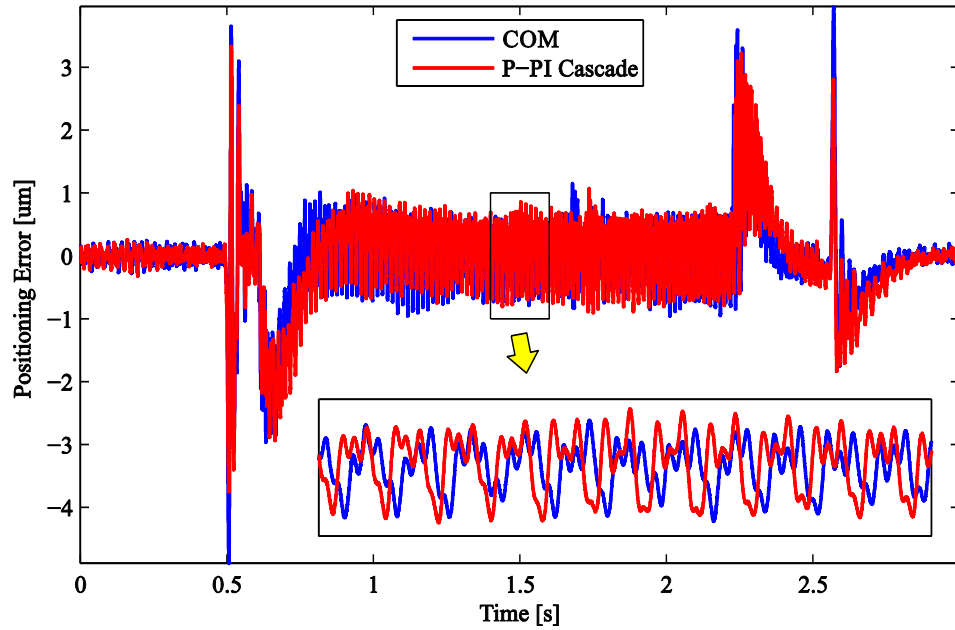


**Figure 4.14: Positioning error in 1 inch slotting at 3500 rpm spindle speed in 6065 aluminum.**

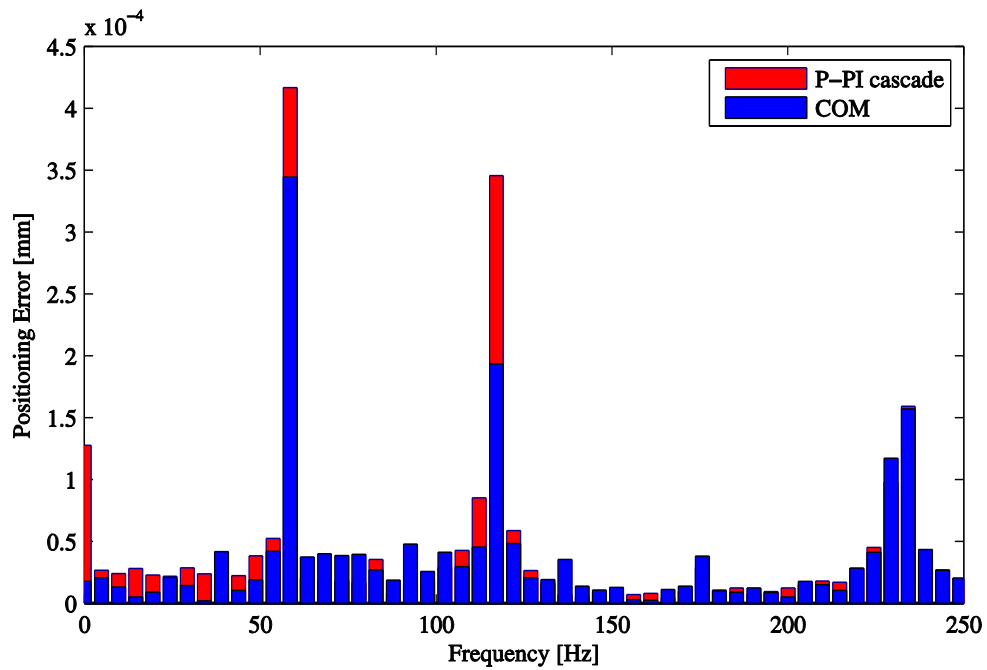


**Figure 4.15: Spectral content of positioning error in 1 inch slotting at 3500 rpm spindle speed.**

Figure 4.16 and Figure 4.17 show that the proposed COM controller outperforms the P-PI cascade controller in high speed tracking experiments. In this experiment, neither friction nor lead error compensation was used when the controllers were implemented.

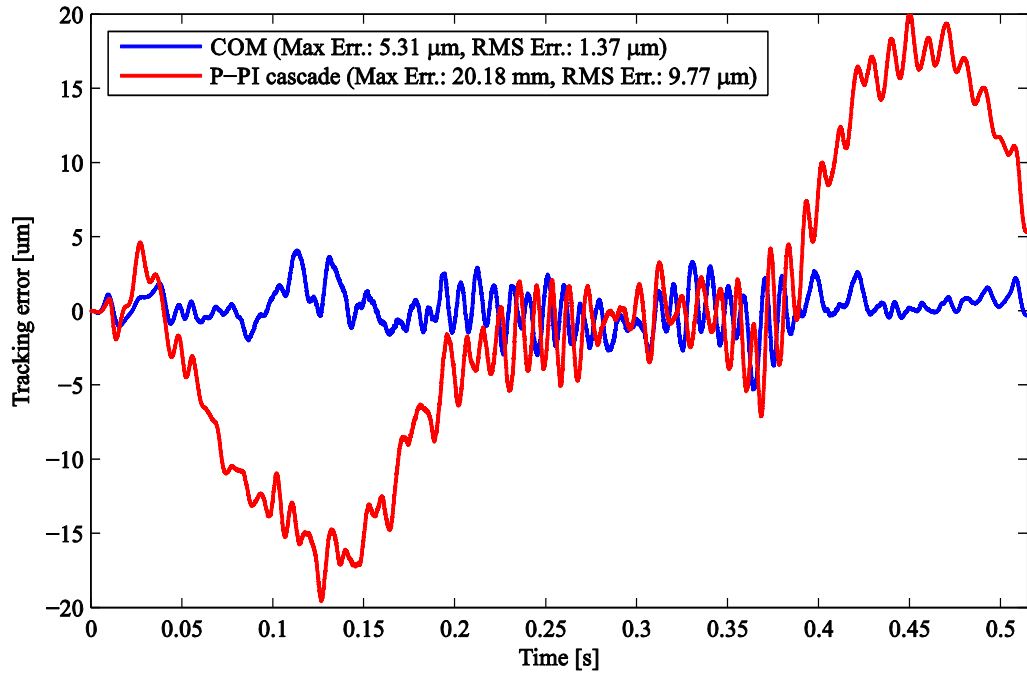


Figure 4.16: High speed tracking (velocity: 1 m/s, acceleration: 10 m/s<sup>2</sup>, jerk: 200 m/s<sup>3</sup>).

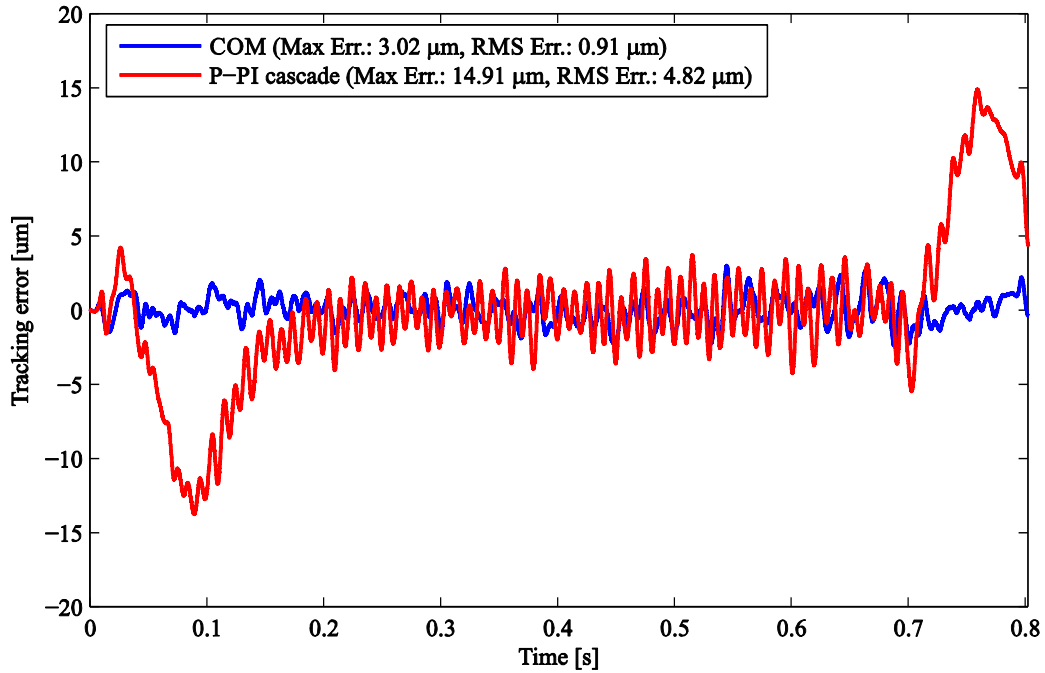


Figure 4.17: High speed tracking (velocity: 0.5 m/s, acceleration: 8.2 m/s<sup>2</sup>, jerk: 200 m/s<sup>3</sup>).

## 4.2 Pole Placement and Loop Shaping Design for Optimal Disturbance Rejection

The objective in this section is to find a feedback controller  $\mathbf{K}(s)=[K_1(s) \ K_2(s)]$  which optimizes the load side closed loop disturbance response against cutting forces for a wide frequency range. Merely boosting loop crossover frequency can sometimes deteriorate the disturbance response near the vibration mode. On the other hand, two controllers designed for different frequency ranges, one for vibration damping and the other for rigid body motion, may interfere with each other when the desired closed loop bandwidth is near the vibration mode. These effects were observed during the tuning of the COM controller in the previous section. Hence, in this section direct minimization of the closed loop disturbance response is targeted, with full attention to all terms in the feedback control law. The design and tuning steps are carried out while inspecting the following two transfer functions:

1. Closed-loop disturbance response:

$$G_{22} = S_{21}G_{d1} + S_{22}G_{d2}, \mathbf{S} = \begin{bmatrix} S_{11} & S_{12} \\ S_{21} & S_{22} \end{bmatrix} = (\mathbf{I} + \mathbf{GK})^{-1} \quad (4.19)$$

Similar to Section 4.1, the objective here is to minimize  $G_{22}(s)$  as much as possible, which helps reduce the worst-case dynamic compliance.

2. The loop transfer function: Although the drive has two outputs, by applying block manipulation the analysis can be transformed into SISO form [3], allowing  $L(s)$  to be found as:

$$L(s) = K_1G_1 + K_2G_2 \quad (4.20)$$

The stability margins, crossover frequency, and minimum distance to ‘-1’ are inspected from Bode and Nyquist plots of  $L(s)$ . Minimum margins of  $GM \geq 1.5$  and  $PM \geq 25^\circ$  are targeted.

The proposed control scheme is shown in Figure 4.18. It consists of jointly applying pole placement and loop shaping principles. The function and design of each component is explained in the following.

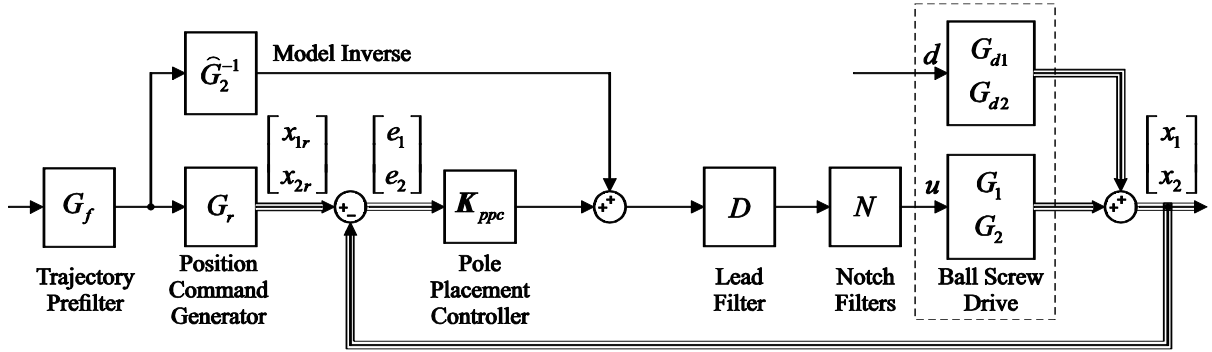


**Figure 4.18: Proposed control scheme using pole placement and loop shaping.**

Pole placement controller (PPC): The position and velocity states  $\mathbf{z} = [x_1 \ x_2 \ \dot{x}_1 \ \dot{x}_2]^T$  of the dynamic model in Figure 2.5b are either measurable or can be estimated by numerical differentiation (due to high encoder resolution). This eliminates the need to use an observer, which can be problematic in terms of modeling errors and estimation delays. The integrated table position is introduced as a fifth state ( $x_{2i}(t) = \int_0^t x_2(\tau) d\tau$ ), to boost low frequency disturbance rejection on the load side by enforcing integral action. This also helps compensate for the motion loss in the preloaded nut [44]. The PPC assumes a simple PD-PID form:

$$u_{ppc} = \underbrace{\begin{bmatrix} K_{x1} + K_{v1}s & , & K_{x2} + \frac{K_{i2}}{s} + K_{v2}s \end{bmatrix}}_{\mathbf{K}_{ppc}(s)} \begin{bmatrix} x_{1r} - x_1 \\ x_{2r} - x_2 \end{bmatrix} \quad (4.21)$$

The feedback gains  $K_{x1}$ ,  $K_{v1}$ ,  $K_{x2}$ ,  $K_{i2}$ ,  $K_{v2}$  are computed to achieve the desired closed loop poles [3]. The oscillatory pole pair at 141 Hz is re-assigned by shifting their real component further to the left in the  $s$ -plane (Figure 2.7), following the concept of low authority LQG vibration control [114]. This accelerates the exponential decay without altering the mechanical structure's damped frequency, which would be costly in terms of control effort. With help of the lead filter (explained next),  $\beta$  could be increased up to 5.5, targeting nearly  $5\times$  improvement in the damping. This dramatically reduces the resonance at 141 Hz in the load disturbance response, as seen in Figure 4.19 for 'PPC + LS'. The remaining poles were tuned, while inspecting  $G_{22}$  and  $L$ , to be:

$$\left. \begin{array}{l} p_3 = -\lambda \\ p_{4,5} = -\zeta\omega \pm \omega\sqrt{\zeta^2 - 1} \end{array} \right\} \text{where: } \begin{array}{l} \lambda = 100 \text{ Hz} \\ \omega = 100 \text{ Hz}, \zeta = 2.0 \end{array} \quad (4.22)$$

Figure 4.19 shows that the disturbance rejection of the PPC+LS controller is in general better than the P-PI cascade controller. This is evident especially around the resonance frequency. Since the resonance is not directly accounted for in the design of the P-PI controller, the deterioration in disturbance response around frequency of resonance is expected and observed, whereas, the PPC+LS controller is maintaining a uniform disturbance response, even in the vicinity of the resonance frequency. Nevertheless, there is a certain frequency range after the resonance for which the P-PI controller outperforms the PPC+LS controller in terms of the disturbance rejection.

It should be noted that while the disturbance response was optimized considering the model transfer function, the actual disturbance responses in Figure 4.19, measured through impact hammer testing, with the feedback controller switched on, displayed two inconsistencies with their model based predictions:

The first one is the mode at 43 Hz, which is due to pitching motion of the table pivoted around the guideway blocks. On the setup, the ball screw and guideways are mounted at the same level. Hence, it is very difficult to excite or control this mode from the motor, unless a mechanical design change is made. However, when an impact is delivered to the top of the table and acceleration is measured at the same level, (which is how the measurements were taken), this mode shows up nearly unaltered regardless of the control law used.

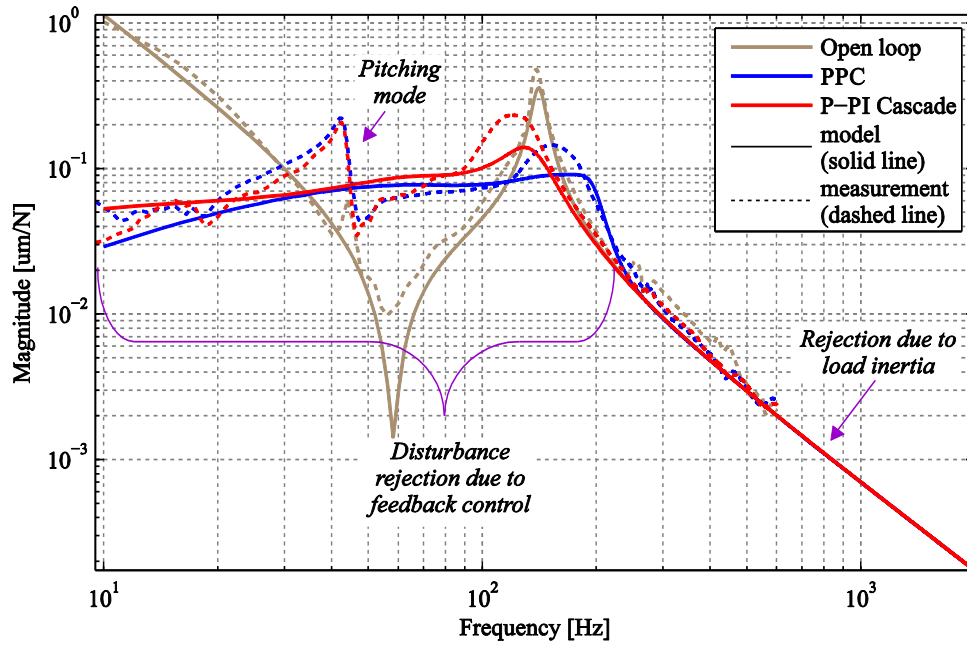


**Figure 4.19: Load side disturbance response for open- and closed-loop cases.**

The second inconsistency is in the actual resonance magnitudes. It is believed that due to motion loss in the nut (in the order of 2-3  $\mu\text{m}$ ), the nut interface does not function like an ideal spring, hence the damping action generated by the motor cannot be fully transferred to the table. This leaves a portion of the vibration unquenched. Nevertheless, the model and experimental results in Figure 4.19 show that improving the theoretical response also improves the actual disturbance rejection. This is further validated in the machining results presented in Section 4.2.1.

Lead filter: The 0.333 ms phase delay contributed by the current control PWM and other loop delays poses a serious limitation on the achievable closed loop bandwidth. This is overcome by careful design of a lead filter  $D(s)$ , which lifts up the loop phase around the cross over frequency  $\omega_c$  (determined to be 230 Hz, as seen in Figure 4.20):

$$D(s) = \frac{K(T_d s + 1)}{T_a s + 1} \quad \text{where:} \quad \begin{array}{l} 1/T_d = 55 \text{ Hz}, 1/T_a = 880 \text{ Hz} \\ K = 0.1667 \end{array} \quad (4.23)$$

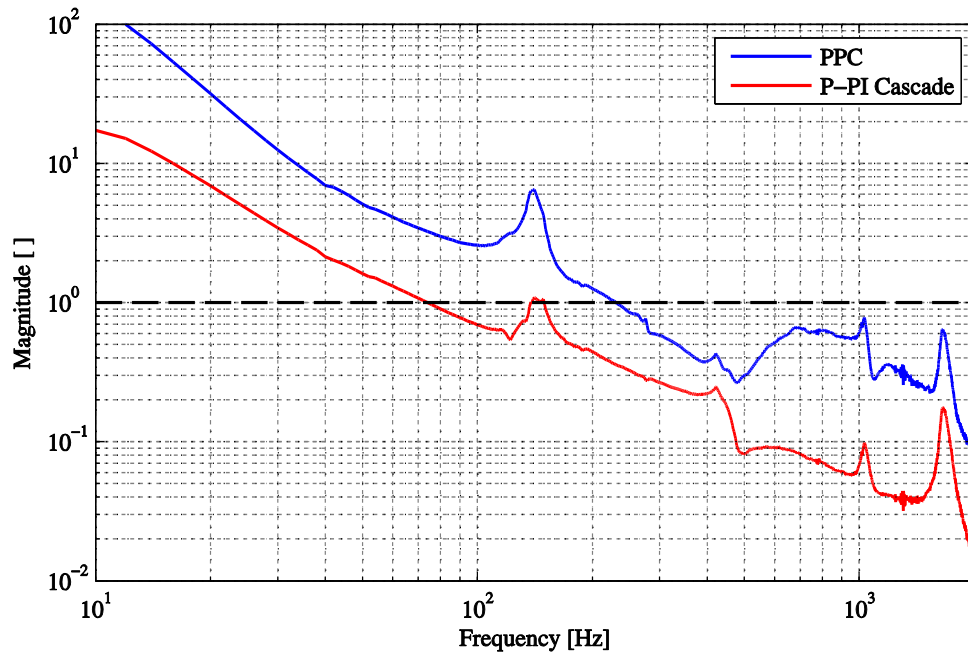


**Figure 4.20: Loop transfer function magnitude for PPC+LS and P-PI schemes.**

This filter provides  $61.9^\circ$  phase lead around  $\omega_c$ . By examining the loop shape (Figure 4.21), its gain contribution around  $\omega_c$  was set to  $\sim 0.7$ , in order to obtain adequate stability margins. The lead filter dramatically improves the specifications and disturbance rejection achievable with PPC. Without it, PPC tuning could only be increased up to  $\beta=4$ ,  $\lambda=\omega=50$  Hz and  $\zeta=0.707$ , as previously reported in [3]. The magnitude plot of the disturbance FRF was presented earlier in Figure 2.8 to show this improvement in disturbance rejection. The magnitude of the most negative real part of the disturbance FRF is inversely proportional to the critical limiting depth of cut, above which, chatter vibration occurs [115]. As can be seen in Figure 4.22, among the cases presented, this index is largest for the P-PI controller and smallest for the controller designed in [3]. Although the PPC design in this thesis is not quite as good as the one in [3] in terms of stability against chatter, it is better compared to the industrial P-PI controller.

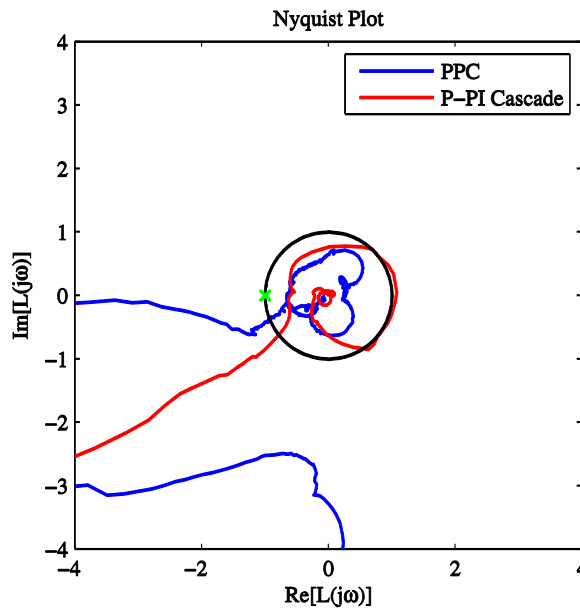


Figure 4.21: Nyquist diagrams for PPC + loop shaping and P-PI control.

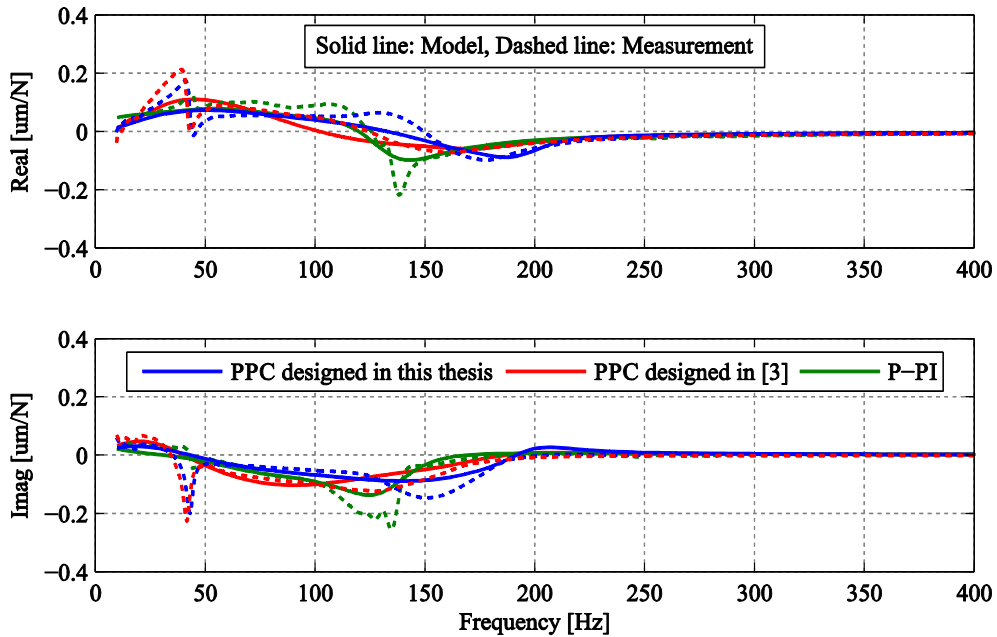


Figure 4.22: Real and imaginary plots of the load side disturbance response.

*Notch filters:* The challenge in damping a low frequency mode is ensuring that higher frequency modes are not excited in a way which can cause instability. On the setup, such modes originate mainly from rotational dynamics, which are little influenced by table position and can be suppressed

with a notch filter pack  $N(s)$ . The spikes in the input sensitivity function  $S(s)=1/(1+L(s))$  provide useful indicators of frequencies that require notching. In order not to induce too much phase loss at lower frequencies (and near the crossover), the notch effect has to be used sparingly. Hence,  $N(s)$  was designed as:

$$N(s) = \prod_{m=1}^4 \frac{s^2 + 2\zeta_m \omega_m s + \omega_m^2}{s^2 + 2\zeta_D \omega_m s + \omega_m^2} \quad (4.24)$$

Above,  $\omega_1=280$  Hz,  $\omega_2=420$  Hz,  $\omega_3=1080$  Hz,  $\omega_4=1750$  Hz,  $\zeta_1=0.40$ ,  $\zeta_2=0.15$ ,  $\zeta_3=0.03$ ,  $\zeta_4=0.10$ ,  $\zeta_D=0.707$ . In the case of PPC + LS, traces of the modes at 1080 Hz and 1750 Hz can still be seen in Figure 4.20 and Figure 4.21. However, since at these frequencies,  $L(j\omega)$  is distant from ‘-1’, these modes are not problematic. In fact, further attenuation of these modes would add phase delay at lower frequency, thus worsening stability margins.

Command generator: The reference trajectory represents the desired motion for  $x_2$ . The rotational position command has to be adjusted to account for the anticipated elastic deformation of the drive. Hence, a command generator is used in the form:

$$\mathbf{G}_r(s) = \begin{bmatrix} G_{r1} \\ G_{r2} \end{bmatrix}, \text{ where: } G_{r1} = \frac{m_2 s^2 + (b_2 + c)s + k}{cs + 1}, G_{r2} = 1 \quad (4.25)$$

$G_{r1}$  is obtained by considering the free body diagram for  $m_2$  in Figure 2.5b when no disturbance is active.

Model inverse and trajectory prefilter: To improve command following, an inverse of the drive model is used in feedforward. Also, a trajectory prefilter is employed to correct for distortions in the tracking transfer function ( $x_2/x_r$ ) caused by discretization and causal implementation of the controller terms:

$$G_f = 1 + K_{vel} G_{lpf} s + K_{acc} G_{lpf}^2 s^2 + K_{jerk} G_{lpf}^3 s^3 + K_{snap} G_{lpf}^4 s^4 \quad (4.26)$$

Above,  $G_{lpf}$  is a first order filter with 80 Hz cut-off frequency.  $K_{vel}$ ,  $K_{acc}$ ,  $K_{jerk}$ ,  $K_{snap}$  are tuned automatically from a single tracking experiment, so that correlations of the velocity, acceleration, jerk, and snap commands in the tracking error profile are minimized. The development of this prefilter was presented in [3].

To investigate the effect of mass and stiffness variations on the tracking performance of the proposed controller, a series of time-domain simulations were conducted in which the load side inertia ( $m_2$ ) and the stiffness coefficient ( $k$ ) were altered by a percentage of their nominal values. The results for this analysis are shown in Figure 4.23 for the P-PI and PPC controllers. It is clear from this figure that for certain data points (i.e. mass-stiffness pairs), the PPC controller outperforms the P-PI controller in terms of positional accuracy. An example of this situation occurs when  $m/m_{\text{norm}} = 3$ ,  $k/k_{\text{norm}} = 0.6$ . On the other hand, there are data points for which the P-PI controller shows a better performance. An example of this is when  $m/m_{\text{norm}} = 7$ ,  $k/k_{\text{norm}} = 1$ . Another conclusion from this figure is that the PPC controller maintains a good positional accuracy in the face of load-side mass increase of up to 200% even if there is a large variation in the stiffness.

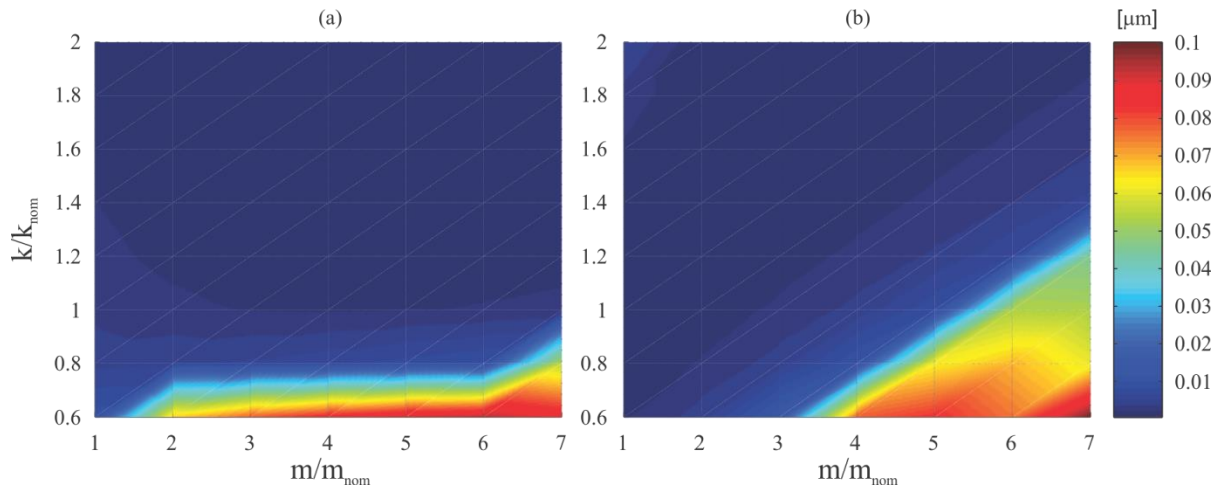


**Figure 4.23: Simulated tracking errors for: (a) P-PI cascade controller, and (b) PPC controller.**

#### 4.2.1 Experimental Results

The disturbance response optimized controller has been validated in machining and high speed tracking experiments. Cutting tests were performed by slotting Aluminum 6065 with a 1 inch diameter 2 flute helical end mill at a chip load of 0.254 mm/tooth. The spindle speed was varied in steps of 600, 1200, 1800, 2400, 3000, 3500 rpm, and the feed motion was provided by the ball screw drive. Experimental tracking errors, measured from the linear encoder, are shown in Figure 4.24.

For comparison, results for the P-PI controller are also presented. To ensure the repeatability of the results, each cut was performed three times. Considering Figure 4.24, PPC+LS provides much more uniform disturbance rejection as the frequency content of the cutting force varies. In addition,

disturbance rejection of PPC+LS is, in general, much better than that of P-PI cascade control, particularly around the resonance frequency of the drive. The observed trends are also consistent with the disturbance responses in Figure 4.19.

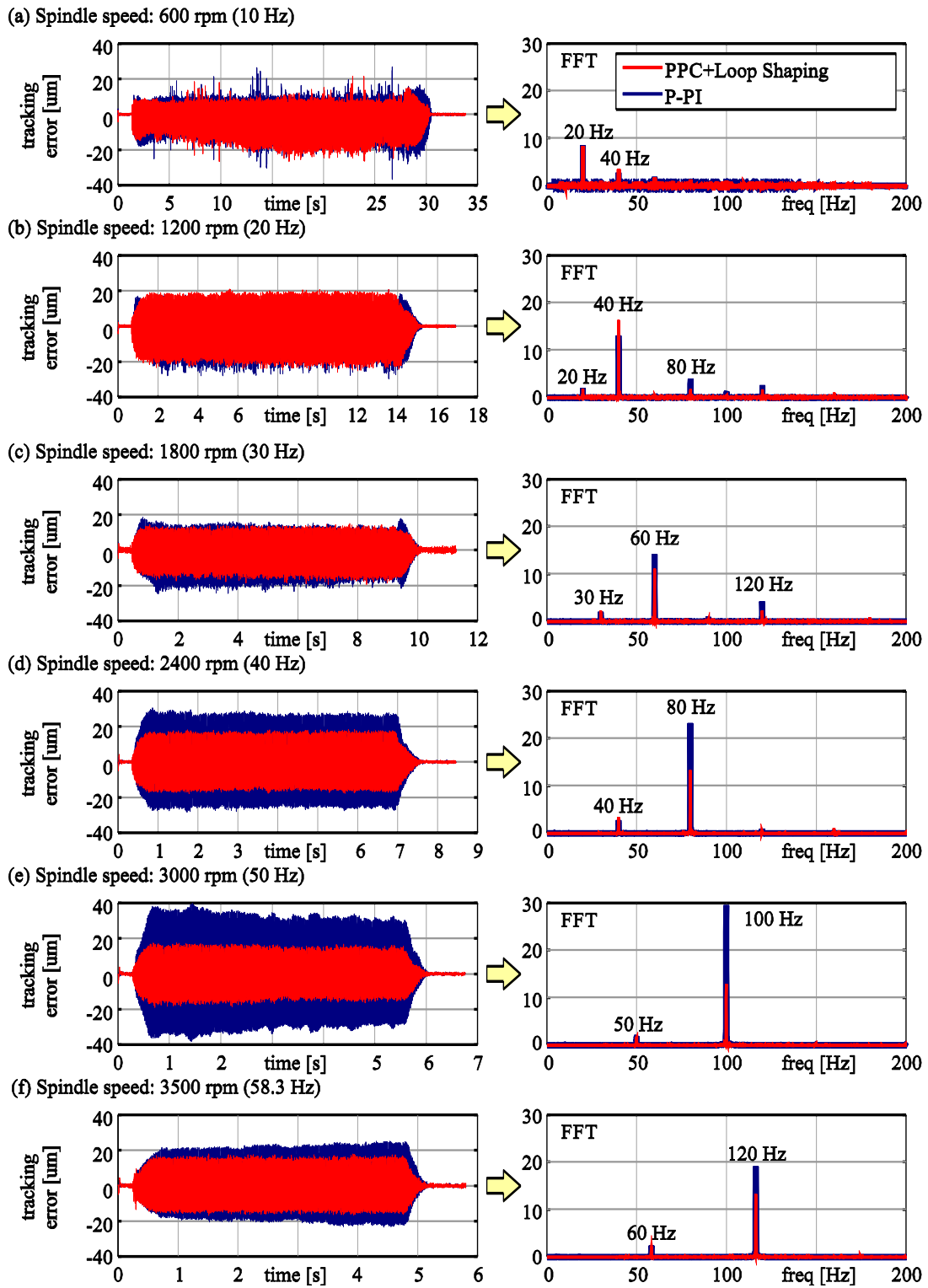
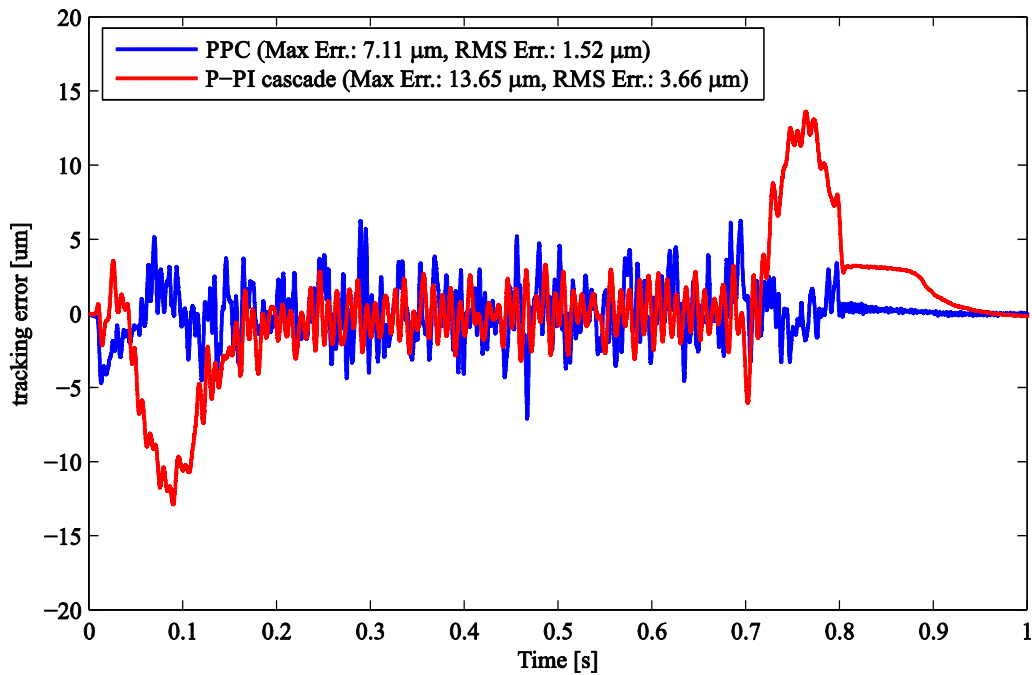


Figure 4.24: Table positioning errors during machining.

Maximum and RMS values of table positioning errors during machining are listed in Table 4.1.

**Table 4.1: Maximum and RMS values of table positioning errors during machining.**

Spindle Speed [RPM]	Error (RMS) [ $\mu\text{m}$ ]		Error (Max) [ $\mu\text{m}$ ]	
	P-PI	PPC + Loop Shaping	P-PI	PPC + Loop Shaping
3500	15.4	10.1	31.8	20.8
3000	18.6	8.5	37.6	17.1
2400	14.5	8.9	28.3	18.7
1800	9.6	7.6	23.8	18.6
1200	9.6	11.0	29.4	26.8
600	6.6	6.5	33.7	29.9



**Figure 4.25: High speed tracking (velocity: 0.5 m/s, acceleration: 8.2 m/s<sup>2</sup>, jerk: 200 m/s<sup>3</sup>).**

Considering Figure 4.25, the proposed PPC+LS design also provides superior tracking over P-PI cascade control. In implementing both controllers, neither friction nor lead error compensation was used. Since PPC+LS has higher loop gain, it also has a tendency to amplify the effect of lead errors

more. These errors, which can be considered as ‘output’ type disturbances [13], are typically smaller than the errors caused by cutting forces. However, depending on the application of a ball screw mechanism, a different compromise may need to be struck between sensitivity to cutting forces versus lead errors and sensor noise. Then, the design procedure outlined in this section can be applied accordingly.

### 4.3 Controller Design for Rigid Body Dynamics and Multiple Vibration Modes

In this section, an attempt is made to increase the bandwidth of the closed loop system by incorporating a higher order model in control law design. In order to do that, the rigid body plus multiple resonator model, identified in Section 3.4.2, is used to design a Kalman filter for estimating states of the system. Therefore, the state space representation is adopted in this section for controller design and analysis. The rigid body dynamics can be represented in state-space form as follows:

$$\bar{x} = \frac{1}{s(J_{est}s + B_{est})} u \rightarrow \begin{cases} \begin{bmatrix} \dot{\bar{z}} \\ \ddot{\bar{z}} \end{bmatrix} = \underbrace{\begin{bmatrix} 0 & 1 \\ 0 & -\frac{B_{est}}{J_{est}} \end{bmatrix}}_{A_r} \begin{bmatrix} \bar{z} \\ \dot{\bar{z}} \end{bmatrix} + \underbrace{\begin{bmatrix} 0 \\ 1 \end{bmatrix}}_{B_r} [u] \\ \bar{x} = \underbrace{\begin{bmatrix} 1 & 0 \\ \frac{1}{J_{est}} & 0 \end{bmatrix}}_{C_r} \begin{bmatrix} \bar{z} \\ \dot{\bar{z}} \end{bmatrix} + \underbrace{\begin{bmatrix} 0 \\ 1 \end{bmatrix}}_{D_r} [u] \end{cases} \quad (4.27)$$

To find a state-space representation for the vibratory dynamics, we recall from Section 3.4.2 that the contribution of the  $k^{\text{th}}$  mode to the response at the motor side is:

$$x_{1k} = \frac{\left( \frac{\alpha_{1k}}{\omega_{nk}^2} s + \frac{\beta_{1k}}{\omega_{nk}^2} \right) \omega_{nk}^2}{s^2 + 2\zeta_k \omega_{nk} s + \omega_{nk}^2} u \quad (4.28)$$

Similarly, the  $k^{\text{th}}$  mode contributes to the response at the load sides as:

$$x_{2k} = \frac{\left( \frac{\alpha_{2k}}{\omega_{nk}^2} s + \frac{\beta_{2k}}{\omega_{nk}^2} \right) \omega_{nk}^2}{s^2 + 2\zeta_k \omega_{nk} s + \omega_{nk}^2} u \quad (4.29)$$

State space realizations for transfer functions in Equations (4.28) and (4.29) are presented below:

$$\begin{aligned}
\begin{bmatrix} \dot{z}_{mk} \\ \ddot{z}_{mk} \end{bmatrix} &= \begin{bmatrix} 0 & 1 \\ -\omega_{nk}^2 & -2\zeta_k \omega_{nk} \end{bmatrix} \begin{bmatrix} z_{mk} \\ \dot{z}_{mk} \end{bmatrix} + \begin{bmatrix} 0 \\ \omega_{nk}^2 \end{bmatrix} u \\
\begin{bmatrix} x_{1k} \\ x_{2k} \end{bmatrix} &= \underbrace{\begin{bmatrix} \beta_{1k} & \alpha_{1k} \\ \omega_{nk}^2 & \omega_{nk}^2 \end{bmatrix}}_{C_{1mk}} \begin{bmatrix} z_{mk} \\ \dot{z}_{mk} \end{bmatrix} + \underbrace{\begin{bmatrix} 0 \\ \omega_{nk}^2 \end{bmatrix}}_{D_{1mk}} u \rightarrow x_{1k} = C_{1mk} z_{mk} + D_{1mk} u \\
\begin{bmatrix} x_{2k} \end{bmatrix} &= \underbrace{\begin{bmatrix} \beta_{2k} & \alpha_{2k} \\ \omega_{nk}^2 & \omega_{nk}^2 \end{bmatrix}}_{C_{2mk}} \begin{bmatrix} z_{mk} \\ \dot{z}_{mk} \end{bmatrix} + \underbrace{\begin{bmatrix} 0 \\ \omega_{nk}^2 \end{bmatrix}}_{D_{2mk}} u \rightarrow x_{2k} = C_{2mk} z_{mk} + D_{2mk} u
\end{aligned} \tag{4.30}$$

Therefore, if the loop delay is ignored for now, the state space model for the feed drive can be put together as follows:

$$\begin{aligned}
\begin{bmatrix} \dot{z}_r \\ \dot{z}_{m1} \\ \vdots \\ \dot{z}_{mn} \end{bmatrix} &= \underbrace{\begin{bmatrix} A_r & & 0 \\ & A_{m1} & \\ & & \ddots \\ 0 & & & A_{mn} \end{bmatrix}}_{A_z} \begin{bmatrix} z_r \\ z_{m1} \\ \vdots \\ z_{mn} \end{bmatrix} + \underbrace{\begin{bmatrix} B_r \\ B_{m1} \\ \vdots \\ B_{mn} \end{bmatrix}}_{B_z} u \\
\begin{bmatrix} x_1 \\ x_2 \end{bmatrix} &= \underbrace{\begin{bmatrix} C_r & C_{1m1} & \dots & C_{1mn} \\ C_r & C_{2m1} & \dots & C_{2mn} \end{bmatrix}}_{C_z} \begin{bmatrix} z_r \\ z_{m1} \\ \vdots \\ z_{mn} \end{bmatrix} + \underbrace{\begin{bmatrix} 0 \\ 0 \end{bmatrix}}_{D_z} u
\end{aligned} \tag{4.31}$$

However, as mentioned in Section 4.2, the phase plots of the measured FRFs indicate a time delay of 0.333 ms in the plant. To account for this delay in the plant model, a second order Pade approximation is used to represent a pure delay:

$$e^{-t_d s} \approx \frac{1 - \frac{t_d}{2} s + \frac{t_d^2}{12} s^2}{1 + \frac{t_d}{2} s + \frac{t_d^2}{12} s^2} \tag{4.32}$$

Equation (4.32) can be cast into state space form as follows:

$$\begin{aligned}
\dot{z}_d &= A_d z_d + B_d u \\
u_d &= C_d z_d + D_d u
\end{aligned} \tag{4.33}$$

Above,  $z_d$  is the vector of states representing the delay dynamics,  $u$  is the actual input, and  $u_d$  is the delayed input. In order to consider the loop delay,  $u$  in Equation (4.31) needs to be replaced with  $u_d$ . Therefore, the state transition equation including the effect of loop delay takes the following form:

$$\dot{z} = A_z z + B_z u_d = A_z z + B_z (C_d z_d + D_d u) \quad (4.34)$$

Consequently, if the state vector  $z$  is augmented with the delay state vector  $z_d$ , the plant state space model including the effect of loop delay can be written as follows:

$$\begin{aligned} \begin{bmatrix} \dot{z} \\ \dot{z}_d \end{bmatrix} &= \begin{bmatrix} A_z & B_z C_d \\ 0 & A_d \end{bmatrix} \begin{bmatrix} z \\ z_d \end{bmatrix} + \begin{bmatrix} B_z D_d \\ B_d \end{bmatrix} [u] \\ &\quad \underbrace{\hspace{10em}}_{A_{z2}} \quad \underbrace{\hspace{10em}}_{z_2} \quad \underbrace{\hspace{10em}}_{B_{z2}} \\ [y] &= \begin{bmatrix} C_z & 0 \end{bmatrix} \begin{bmatrix} z \\ z_d \end{bmatrix} + \begin{bmatrix} 0 \end{bmatrix} [u] \\ &\quad \underbrace{\hspace{10em}}_{C_{z2}} \quad \underbrace{\hspace{10em}}_{z_2} \quad \underbrace{\hspace{10em}}_{D_{z2}} \end{aligned} \quad (4.35)$$

Following the same approach as in Section 4.2, the integrated table position is also introduced as an additional state ( $x_{2i}(t) = \int_0^t x_2(\tau) d\tau$ ), to boost low frequency disturbance rejection on the load side by enforcing integral action. Considering that  $x_2 = C_{z2}(2,:) \cdot z_2 = \dot{x}_{2i}$ , in which,  $C_{z2}(:,2)$  denotes the second row in  $C_{z2}$ , the new state transition equation, including  $x_{2i}$ , can be written as follows:

$$\begin{bmatrix} \dot{z}_2 \\ \dot{x}_{2i} \end{bmatrix} = \begin{bmatrix} A_{z2} & 0 \\ C_{z2}(2,:) & 0 \end{bmatrix} \begin{bmatrix} z_2 \\ x_{2i} \end{bmatrix} + \begin{bmatrix} B_{z2} \\ 0 \end{bmatrix} [u] \quad (4.36)$$

$\underbrace{\hspace{10em}}_{A_{des}} \quad \underbrace{\hspace{10em}}_{z_3} \quad \underbrace{\hspace{10em}}_{B_{des}}$

$A_{des}$  and  $B_{des}$  in Equation (4.36) are inputs to the pole placement algorithm. The output is the state gain vector:  $K$ . The pole placement algorithm is employed to shift the real component of the oscillatory closed loop poles of the system further to the left of the s-plane by amounts determined by the designer. The poles related to rigid body motion are also placed as far left as possible:

$$\left. \begin{aligned} p_1 &= -\lambda \\ p_{2,3} &= -\zeta\omega \pm \omega\sqrt{\zeta^2 - 1} \end{aligned} \right\} \text{where: } \begin{aligned} \lambda &= 80 \text{ Hz} \\ \omega &= 80 \text{ Hz}, \zeta = 0.707 \end{aligned} \quad (4.37)$$

The delay related poles, approximated from Pade formula (Equation (4.32)), are kept unchanged. The pole shift factors are tuned concurrently with the Kalman filter. For Kalman filter design, the state space model in Equation (4.35) is augmented with an integrated white noise disturbance model:

$$\begin{aligned} \begin{bmatrix} \dot{z}_2 \\ \dot{d} \end{bmatrix} &= \begin{bmatrix} A_{z2} & B_{z2} \\ 0 & 0 \end{bmatrix} \begin{bmatrix} z_2 \\ d \end{bmatrix} + \begin{bmatrix} B_{z2} \\ 0 \end{bmatrix} [u] + \begin{bmatrix} 0 \\ 1 \end{bmatrix} [w] \\ [y] &= [C_{z2} \quad 0] \begin{bmatrix} z_2 \\ d \end{bmatrix} + [0][u] + [0][w] + [v] \end{aligned} \quad (4.38)$$

Above,  $w$  is a white process noise with variance  $R_w$ , and  $v$  is a white measurement noise with variance  $R_v$ . In practice,  $R_w$  acts as a tuning parameter which determines the bandwidth of the Kalman filter. The higher the value of  $R_w$ , the faster the state estimates track the actual states. On the down side, however, the sensitivity of the Kalman filter to measurement noise increases with an increase in  $R_w$ . The Kalman filter can be represented by a transfer matrix relating the input vector to the vector of state estimates:

$$[z_2] = [K_{est}] \begin{bmatrix} u \\ x_1 \\ x_2 \end{bmatrix} \quad (4.39)$$

The overall control scheme including the Multi-Mode Pole Placement Controller (MMPPC) and the Kalman filter is shown in Figure 4.26. Considering Figure 4.26, the loop transfer function can then be derived as follows:

$$L(s) = C_{1 \times 2}(s).G_{2 \times 1}(s) = K_1(s).G_1(s) + K_2(s).G_2(s) \quad (4.40)$$

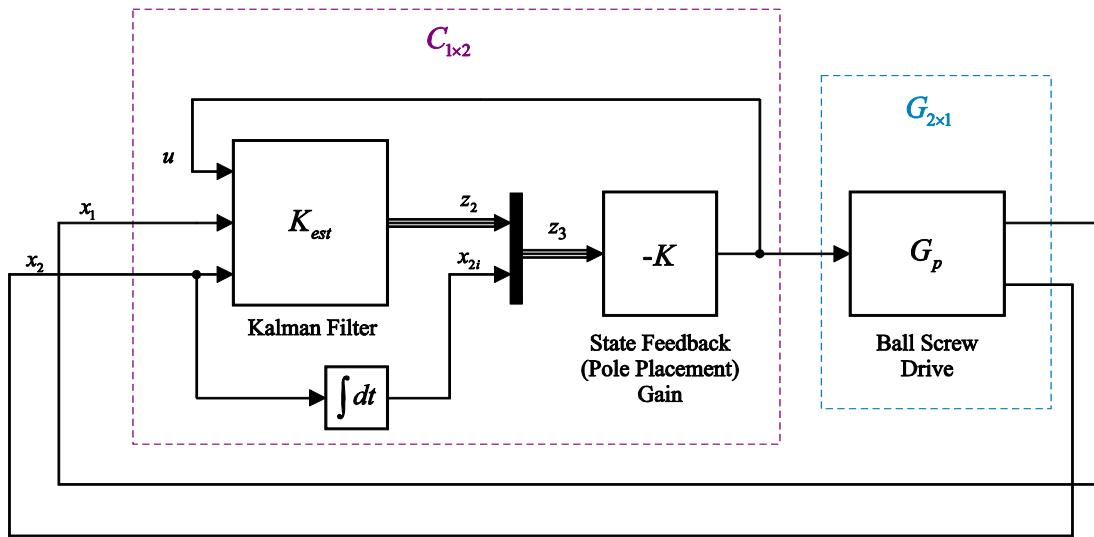


**Figure 4.26: Multi-mode Pole Placement Controller (PPC) with a Kalman filter observer.**  
 (Subsystems that are used in derivation of the loop transfer function are indicated by dashed lines.)

$C_{1 \times 2}$  was obtained by applying adequate interconnections between the Kalman filter and the MMPPC. This was done using existing interconnection definitions in Matlab:

$$C_{1 \times 2} = \text{feedback}(-K * [K_{est} ; [0 ; 0 ; \underbrace{\text{ss}(\text{tf}([Ts \ 0], [1 \ -1], Ts))}_{\text{Integrator}}]], \quad 1, \text{feedback gain}, 1, 1, +1)$$

This control design was tested in simulations for different combinations of pole shifting factors and Kalman filter tuning parameter ( $R_w$ ). Figure 4.27 shows the simulated position response of the load side to a step disturbance on the motor side for different pole shifting factors when the Kalman filter tuning parameter is  $R_w = 1 \times 10^6 \text{ V}^2$ .

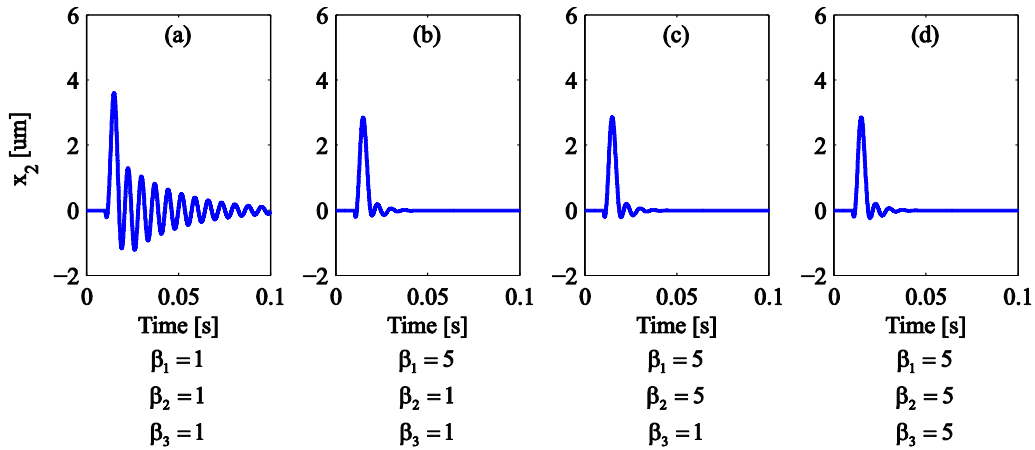


**Figure 4.27: Simulated position response of the load side to a step disturbance on the motor side for  $R_w = 1e6$  and different choices of pole shifting factors.**

It appears from the results in Figure 4.27 that the idea of active vibration damping has been realized successfully with this control scheme. This observation is reaffirmed by inspection of the simulated time responses of certain states in Figure 4.28. In this figure,  $q_1$ ,  $q_2$  and  $q_3$  represent the response of each resonator in the modal coordinates. It is clear from this figure that increasing the pole shifting factor has increased the decay rate of oscillations in the corresponding states of the system.

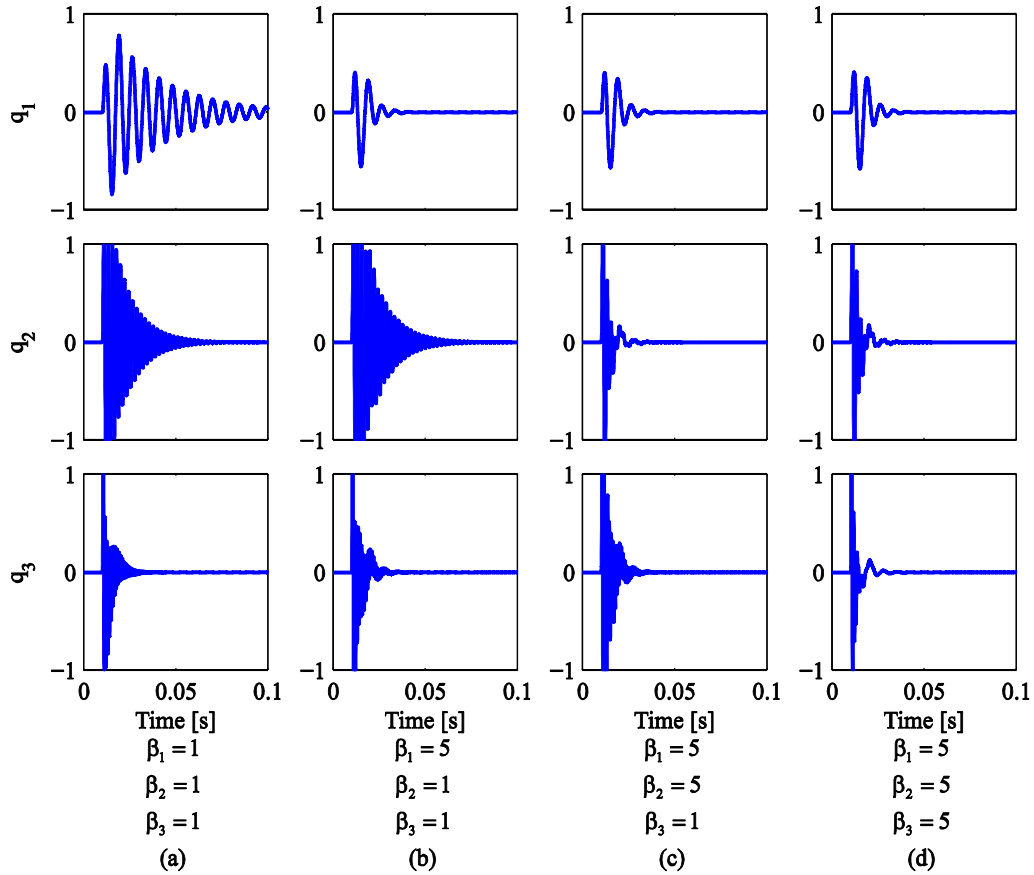


**Figure 4.28: Simulated time response of plant oscillatory states to a step disturbance on the motor side for  $R_w = 1e6$  and different choices of pole shifting factors.**

Although, the simulation results look promising, the Nyquist stability analysis, conducted using modeled and measured drive response FRFs, shown in Figure 4.30, predicts that this controller destabilizes the actual plant. The mismatch between the measured and modeled data in Nyquist plot is the result of mismatch between the measured and modeled position response of the table to the motor torque, as shown in Figure 3.32, amplified by  $K_2(s)$  in Equation (4.40). The singular value analysis of  $K_2(s)$  as shown in indicates that the amplification factor that was discussed above is large at the frequency range that the discrepancy is significant ( $f > 400$  Hz).

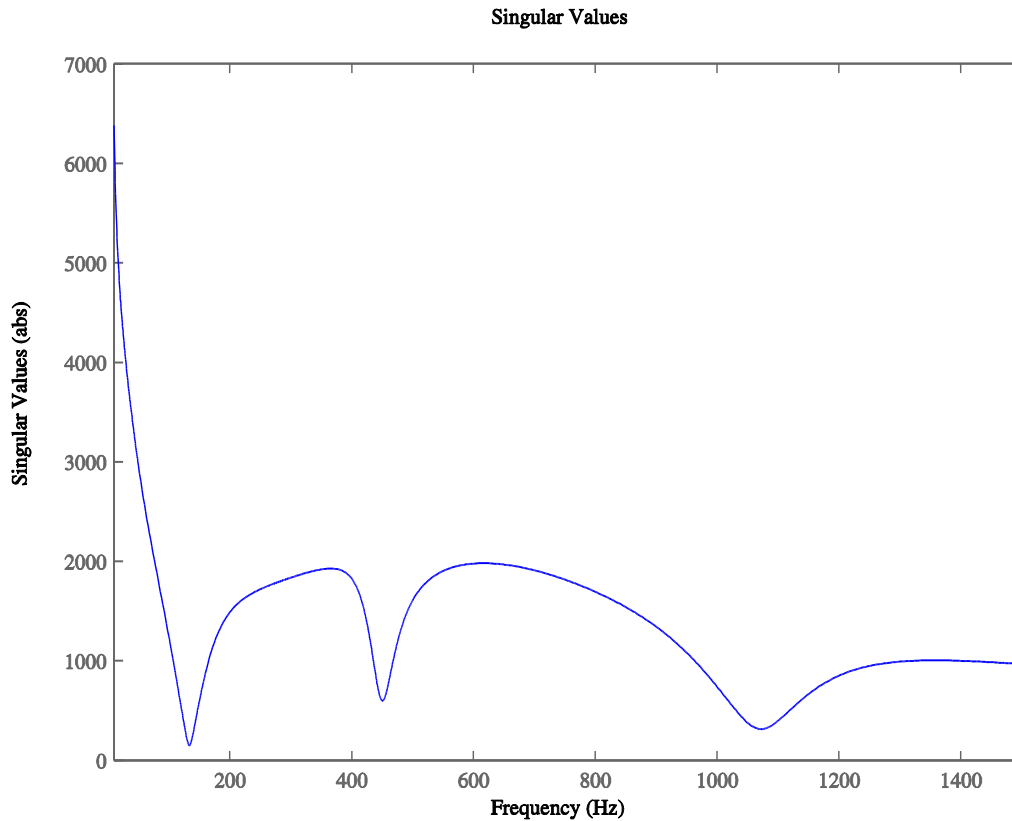


**Figure 4.29: Singular values of  $K_2(s)$  in Equation (4.40).**

The stability can be improved by detuning the Kalman filter through selecting a smaller value of  $R_w$ . For example, if  $R_w = 2 \times 10^3 \text{ V}^2$  is selected, the Nyquist plot in Figure 4.31 indicates that the control loop should be stable with about 10 degrees of phase margin. However,  $PM = 10^\circ$  is too low for industrial safety standards. Decreasing  $R_w$  also aggravates the ability of the Kalman filter to track the actual estates. This fact is reflected in the simulated results shown in Figure 4.32 and Figure 4.33. It can be seen that although the pole shifting factors are kept the same as before, this controller cannot adequately damp out the high frequency modes.

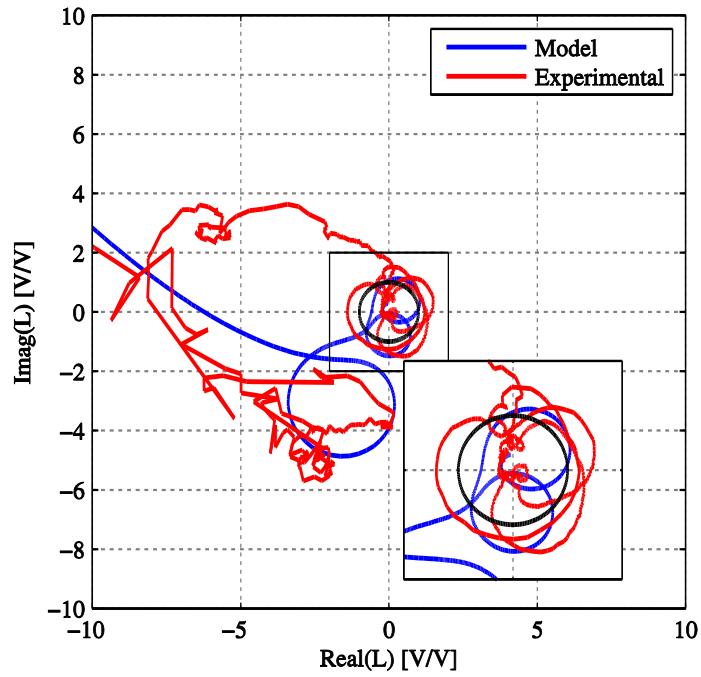


Figure 4.30: Nyquist plot for MMPPC ( $\beta_1=\beta_2=\beta_3=5$ ) with a Kalman filter observer ( $R_w = 1e6$ ).

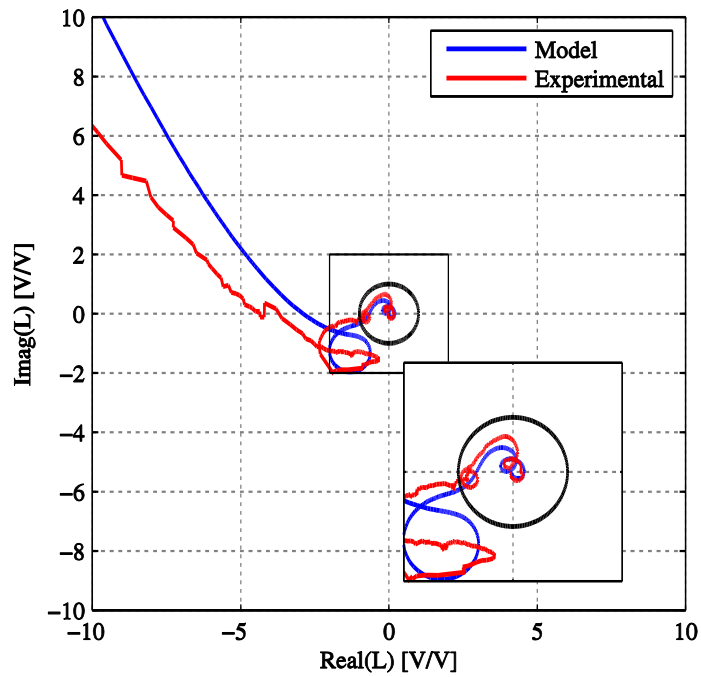


Figure 4.31: Nyquist plot for MMPPC ( $\beta_1=\beta_2=\beta_3=5$ ) with a Kalman filter observer ( $R_w = 2e3$ ).

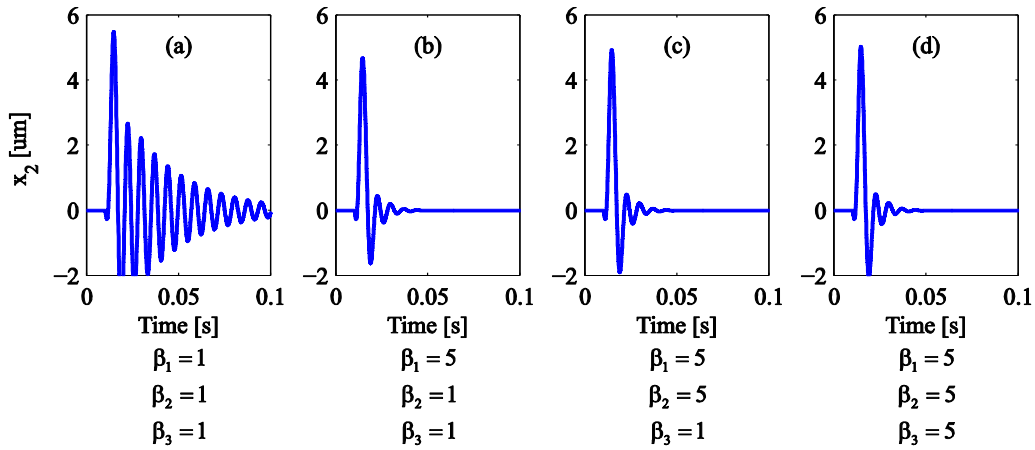


Figure 4.32: Simulated position response of the load side to a step disturbance on the motor side for  $R_w = 2e3$  and different choices of pole shifting factors.

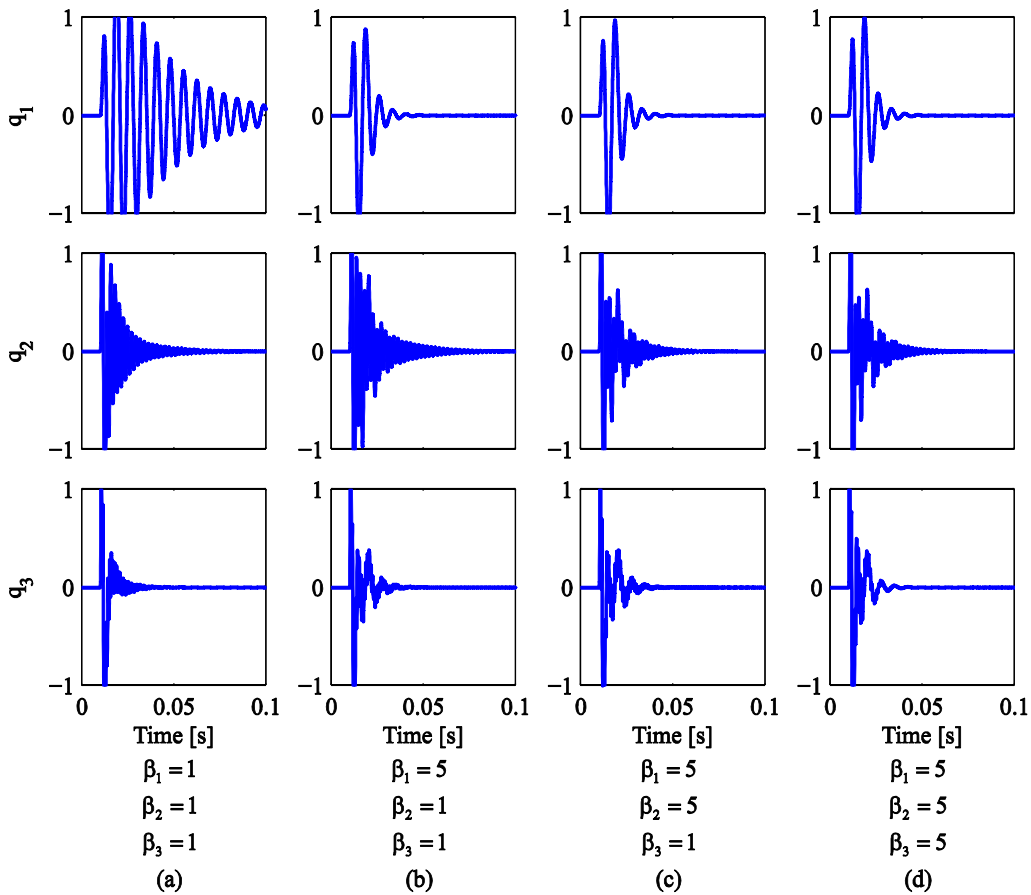
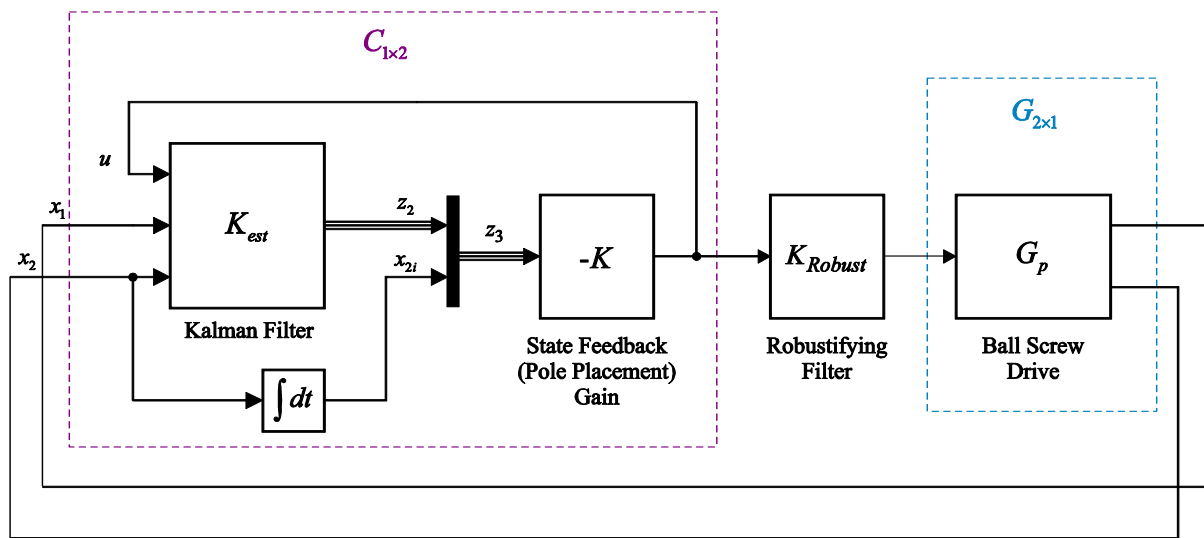
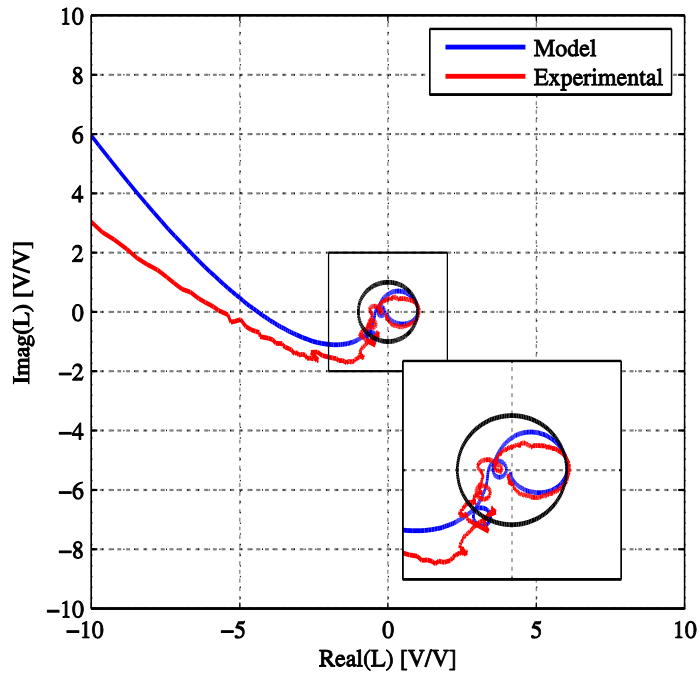


Figure 4.33: Simulated time response of plant oscillatory states to a step disturbance on the motor side for  $R_w = 2e3$  and different choices of pole shifting factors.

In another attempt, to ensure robust stability, the Glover–McFarlane  $H_\infty$  loop shaping procedure [4] was employed to design a robustifying filter for the original loop transfer function (i.e.  $L(s)$  in Equation (4.40) is treated as the shaped plant). As shown in Figure 4.34, the robustifying filter is placed right before the plant input. This filter allows increasing the pole shifting factors while maintaining adequate stability margins. For instance, if  $\beta = 5$  is selected again for all oscillatory poles, the value of phase margin, computed using the measured drive FRF, become 38 degrees as shown in Figure 4.35.



**Figure 4.34: Multi-mode Pole Placement Controller (PPC) with Glover–McFarlane robustification.**



**Figure 4.35: Nyquist diagrams for MM PPC+Kalman filter ( $R_w = 2e3$ ) with Glover–McFarlane robustification.**

To demonstrate the effect of pole shifting factors on the time response of plant outputs and states in this case, again a step disturbance was applied to the motor side in simulation and the changes in system’s outputs and states were recorded. The results are shown in Figure 4.36 and Figure 4.37. Here, the shifting factors are selected to supposedly enhance the vibration decay rate of each resonator by 5 times. However, the simulation results indicate that this is not what happens in reality. This can be explained by observing where the closed loop poles migrate after applying the robustifying filter (Figure 4.38). It is evident that the robustifying filter moves the oscillatory poles, whose locations were set during the pole placement step, back close towards the imaginary axis. This in effect nullifies much of the improvements resulting from the pole placement approach.

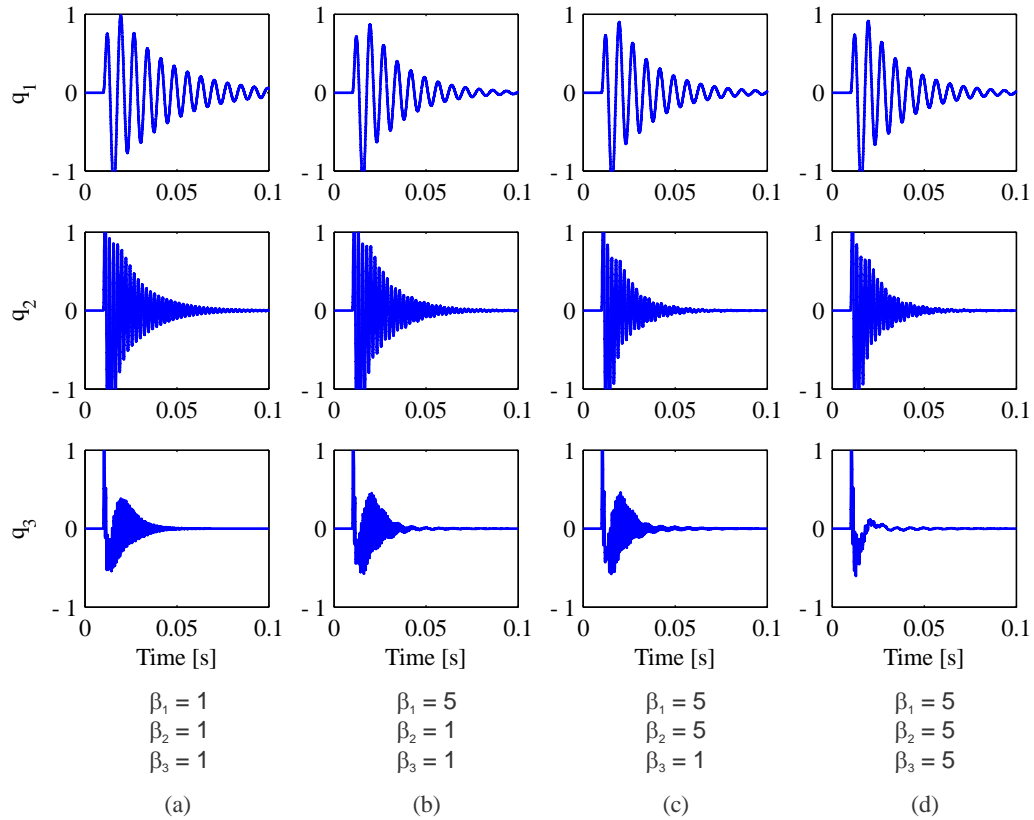


**Figure 4.36: Simulated time response of system states to a step disturbance on the motor side for different choices of shifting factors in a robustified MMPPC+Kalman filter ( $R_w = 2e3$ ).**

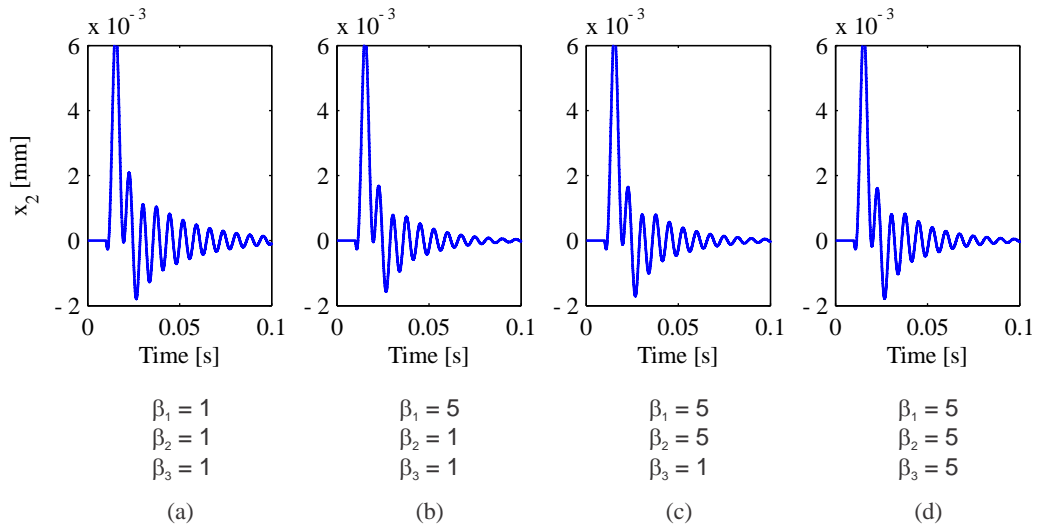


**Figure 4.37: Simulated position response of the load side to a step disturbance on the motor side for different choices of shifting factors in a robustified MMPPC+Kalman filter ( $R_w = 2e3$ ).**

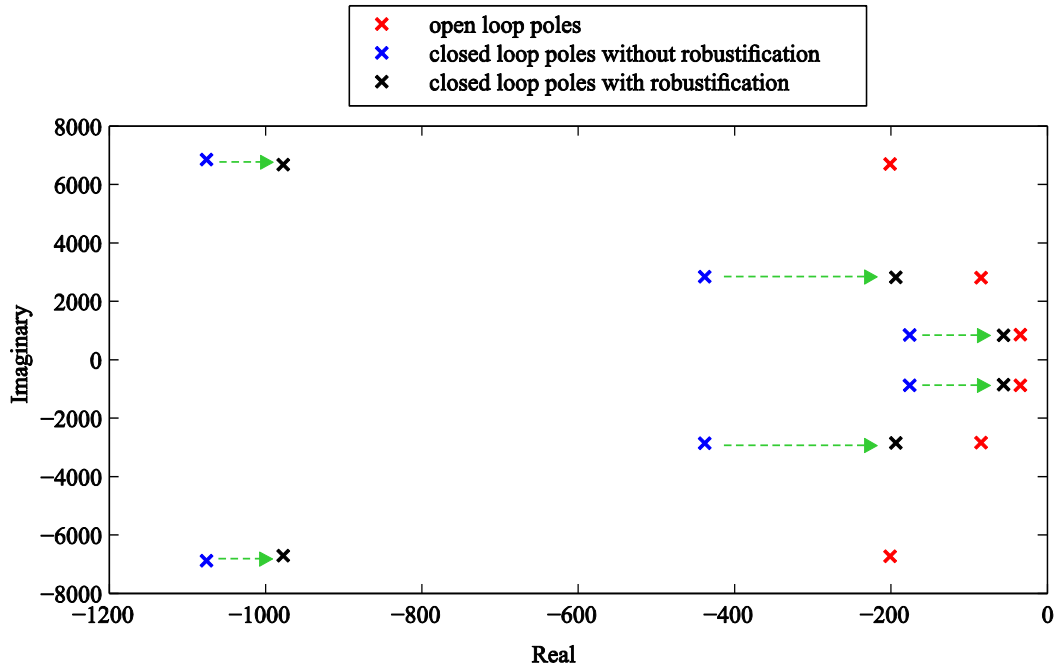


**Figure 4.38: Oscillatory pole map of the plant and the closed loop system.**

Furthermore, as far as the disturbance rejection is concerned, the designed Multi-Mode Pole Placement Controller (MMPPC) is predicted to exhibit inferior performance compared to the industrial P-PI cascade controller as shown in Figure 4.39. For example, Figure 4.39 indicates that the closed-loop dynamic stiffness at 10 Hz is almost 9 times higher for the P-PI controller compared to the MMPPC. It should be noted that the FRFs shown in this figure are not measured directly through impact hammer testing of the table under closed loop control, because, unlike the case of COM, P-PI and MC-PPC + LS, it was not possible to get the experimental implementation of this controller to work successfully. Rather, the frequency response data calculated from the sensitivity transfer matrix were combined according to Equation (4.18) with the experimentally measured open loop disturbance FRFs of the plant to generate the FRFs shown in Figure 4.39.

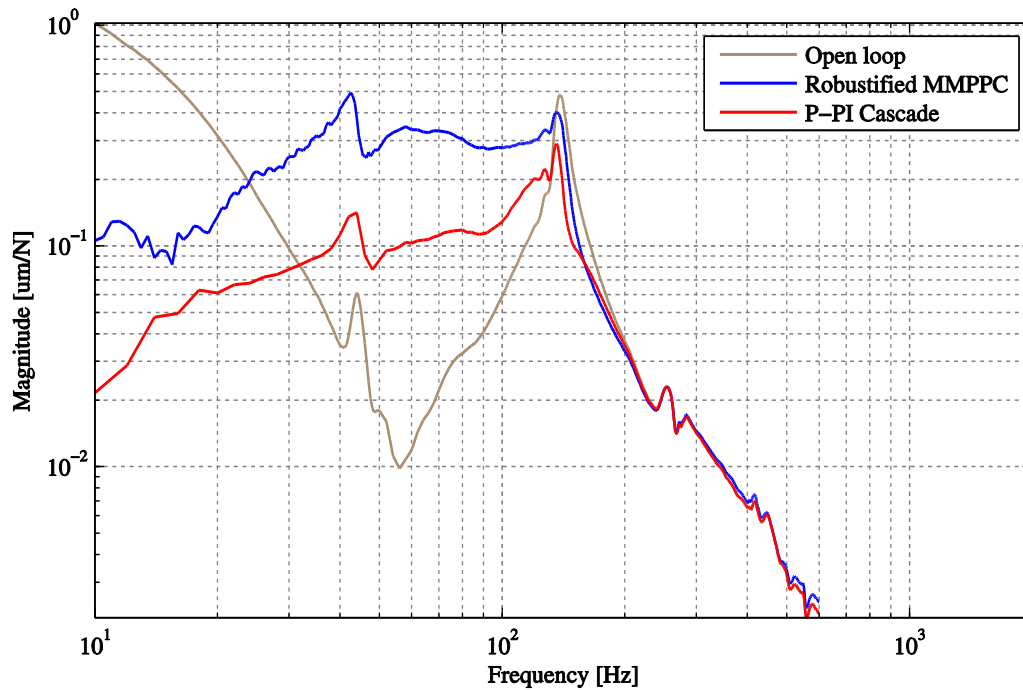


Figure 4.39: Load side disturbance response for open- and closed-loop cases.

#### 4.4 Conclusions

In this chapter, three methods for designing vibration damping feed drive controllers were explored. The first method worked based on decoupling the rigid body dynamics from the vibratory dynamics and applying active damping to suppress the first mode of vibration. This controller was shown to exhibit superior performance compared to the industrial mainstream P-PI controller in certain circumstances. However, in tuning a compromise needed to be made between high frequency vibration damping, and low frequency disturbance rejection.

In the second approach a lead filter was designed to compensate for the effect of phase lag due to current loop dynamics. Loop shaping and pole placement techniques were used concurrently for directly optimizing the cutting force disturbance response of the electro-mechanical system. The guidelines for tuning of this controller were shown to be straightforward and intuitive. The new control law displayed superior rejection of cutting force disturbances compared to the established P-PI cascade architecture. The tracking performance was also very good. This control law is one of the main contributions in this thesis.

In a third approach, a higher order model capable of capturing three modes of vibration was used in the controller design. A Kalman filter was also used to estimate the state feedback, which was used in pole placement control. A robustifying filter needed to be added to improve stability margins. However, unfortunately, this filter nullified the effect of active damping to a great extent, and as result, the disturbance rejection of the controller turned out to be unsatisfactory.

Hence, the single mode controller is adequately sufficient in a large class of ball screw drives for capturing and damping out the main dynamics. Incremental performance improvement towards damping out higher order modes is difficult and significant robustness challenges need to be overcome.

## Chapter 5

### Rejection of Harmonic Disturbances in Ball Screw Drives

In rotating machinery, vibrations are often induced by periodic disturbances. The detrimental effect of these disturbances may be amplified by the control loop for certain ranges of frequency. When the frequency of disturbance is known, the remedy is to increase the loop gain at the disturbance frequency, without significantly altering the loop shape elsewhere. As pointed out in Chapter 2, this can be accomplished by using techniques such as Repetitive Control (RC) or Adaptive Feedforward Cancellation (AFC).

In this Chapter, the AFC method has been adopted for designing appropriate compensators to deal with periodic disturbances in ball-screw feed drives. When a ball-screw feed drive is used in a milling machine, the periodic forces from the cutting process are the dominant source of disturbance. In addition, certain periodic disturbances originate from the position-dependent errors that repeat with each turn of the screw shaft. The former type of disturbances is time periodic, whereas the latter is displacement periodic. According to Fourier expansion theorem, each periodic signal can be treated as a superposition of several pure harmonic signals. Therefore, from here on, the disturbances are assumed to be harmonic.

In Section 5.1 of this chapter, the origins of the periodic disturbances in ball screw drives are discussed in further detail. Section 5.2 provides a general overview of the AFC algorithm, and argues its equivalence to a Linear Time Invariant (LTI) filter when the target frequency is constant. In Section 5.3, selection and update of AFC parameters for milling, and high speed tracking applications are discussed based on the stability analysis of the closed loop control system. Then, the experimental results from implementation of the AFC in these particular applications are presented and analyzed. Finally, the conclusions are presented in Section 5.4.

#### 5.1 Periodic Disturbances in Ball Screw Driven Machines

Understanding the origins of a disturbance and developing appropriate models are helpful for simulation and design of control systems. For example, when ball screw drives are used in milling machines, disturbances are mainly due to the periodic cutting forces. These forces are exerted on the load side, and excite the mechanical structure of the feed drive at the cutter rotation frequency, and its multiples. Another source of disturbance is friction. Following the method detailed in [12], the

maximum frictional torque in our setup was measured to be 0.75 N.m. Considering the gear ratio of the ball screw ( $h_p= 0.02$  m), this is equivalent to 236 N of table load. However, since the commanded velocity in typical milling operations varies smoothly, the friction acts as a low-frequency disturbance, and therefore, can be effectively counteracted by the integral action of the main controller.

A numerical method for simulation of milling forces when the cutting tool is a helical end-mill has been presented in [115]. This model has been validated extensively in machining literature. Using this method, cutting forces were simulated for slot milling of aluminum 6061 with a 2-flute, and 4-flute helical end-mills respectively. The axial depth of cut in both cases was selected to be 1 mm. Spindle speed of 3000 rpm, and feedrate of 1524 mm/min were considered. The simulated forces are presented in Figure 5.1 and Figure 5.2. In this simulation, cutter run-out is not taken into consideration. Therefore, the fundamental frequency corresponds to the tooth-passing frequency, whereas in reality, due to cutter run-out, the cutter rotation speed dictates the fundamental frequency.

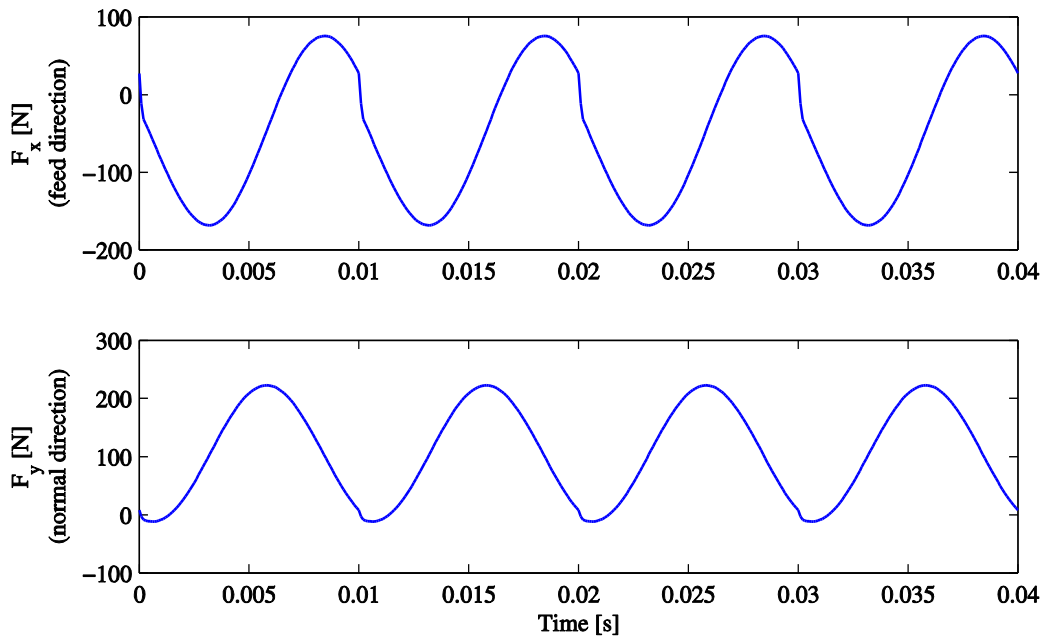


**Figure 5.1: Simulated forces for machining aluminum 6061 with a 2-flute cutter at 3000 rpm spindle speed and 1524 mm/min feed.**

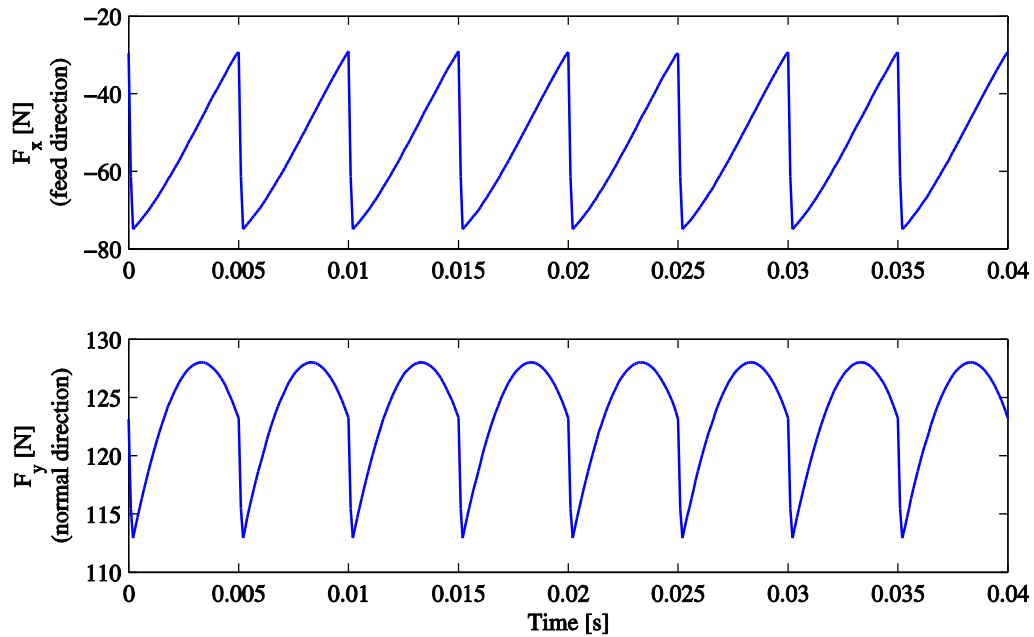


**Figure 5.2: Simulated forces for machining aluminum 6061 with a 4-flute cutter at 3000 rpm spindle speed and 1524 mm/min feed.**

When the ball screw feed drive is used for high speed positioning, another source of disturbance gains importance. This has to do mainly with repetitive lead errors along the screw shaft, and the encoder runout. To characterize the lead errors, the table was commanded to move 340 mm, from one end of its stroke to the other, and then back to its initial position, at a constant speed of 10 mm/s (Figure 5.3). Because the pitch of the ball screw in the test-bed setup is 20 mm, the table speed of 10 mm/s corresponds to 0.5 Hz rotation frequency of the screw shaft. This slow speed was chosen to minimize the duration of acceleration and deceleration periods, and thereby diminish the effect of inertial forces on axial deformation of the screw shaft.

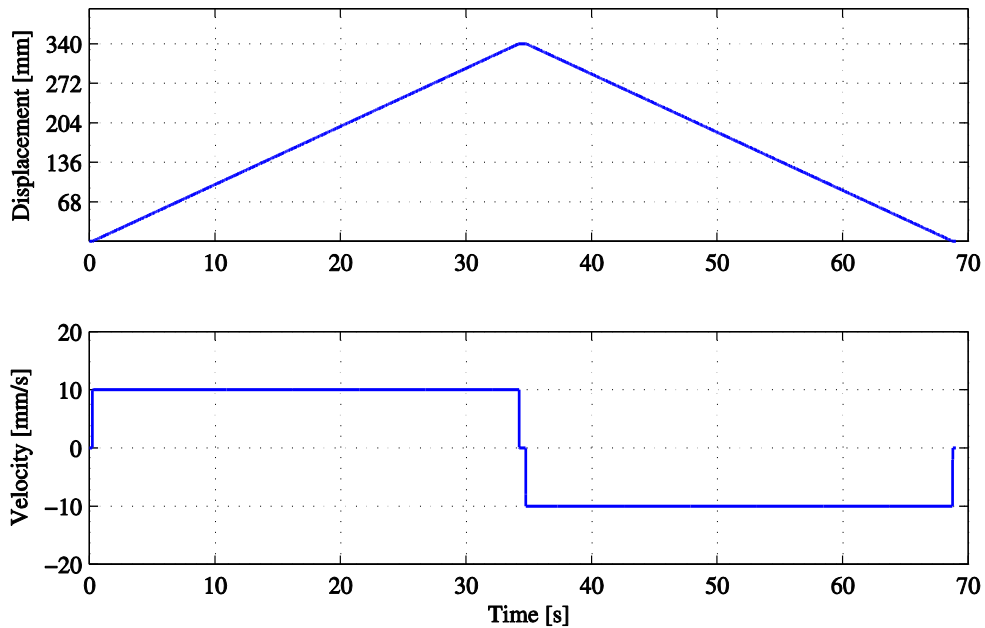


**Figure 5.3: Commanded motion profile in lead error measurement experiment.**

During the table motion, the difference between the readings of linear and rotary encoders was recorded. The data collected are presented, side by side, with their Fast Fourier Transform (FFT) in Figure 5.4, for five runs of the test. In the FFT plots, two types of peaks are recognizable: a repetitive peak at 0.5 Hz, which shows up consistently in all the measurements, and non-repetitive random peaks which change their location from measurement to measurement. The repetitive peak is attributed to the harmonic lead errors, while the non-repetitive peaks are possibly the result of wear in the recirculating balls. The harmonic lead error profile can be obtained by multiplying the FFT data by a rectangular window encompassing the lead error frequency (band-pass filtering), and then, reconstructing the signal in the time domain using the inverse FFT. Figure 5.5 shows the average of the signals obtained this way, which is plotted against the table displacement. It is clear from this figure that the lead errors impose a periodic disturbance to the system. The frequency of this disturbance is proportional to the table speed, and as a result, when the table is in high speed motion, classical controllers turn out to be inadequate in cancelling out its effect.

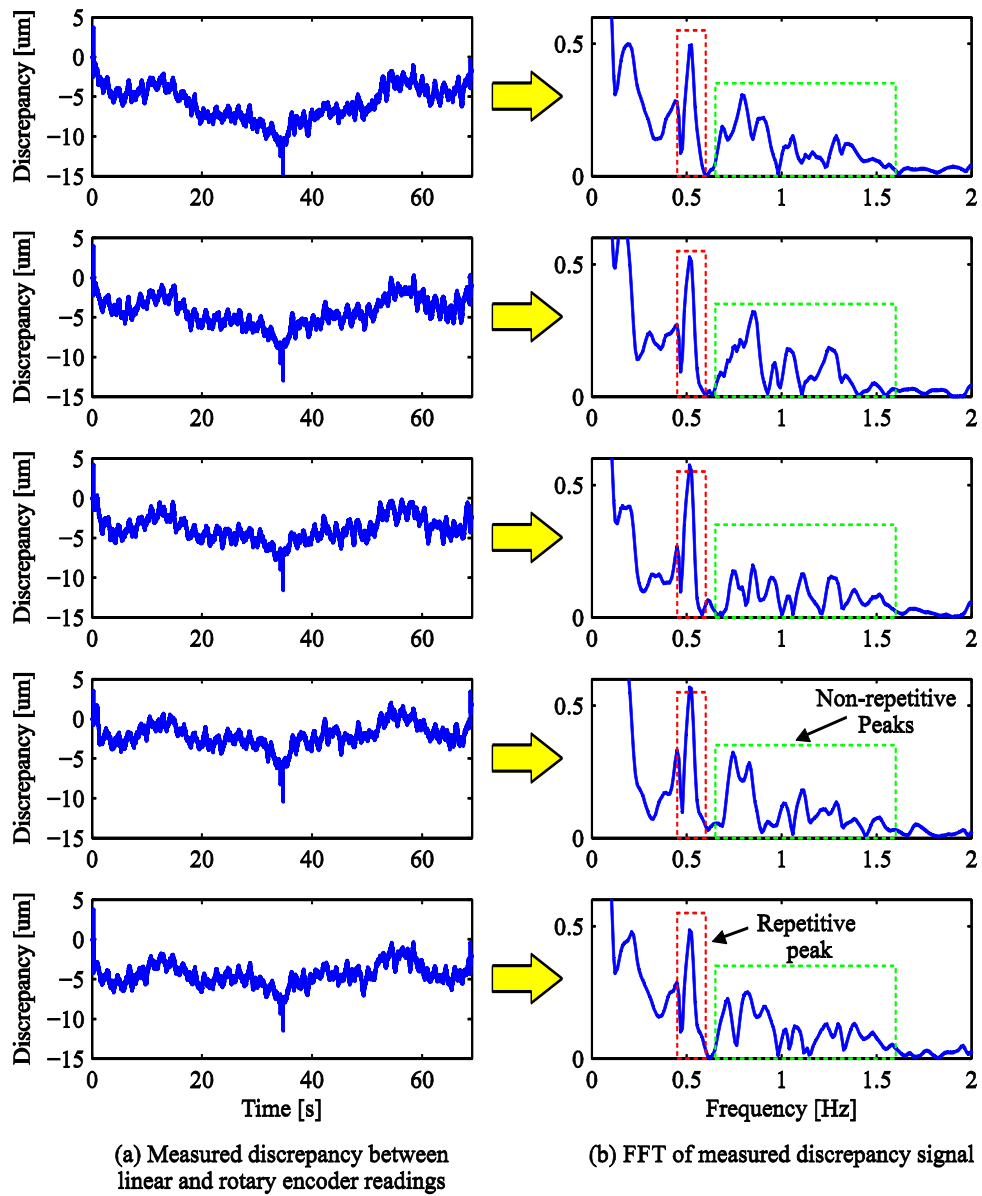


Figure 5.4: Five runs of discrepancy measurement between readings of linear and rotary encoders for feedrate of 10 mm/s.

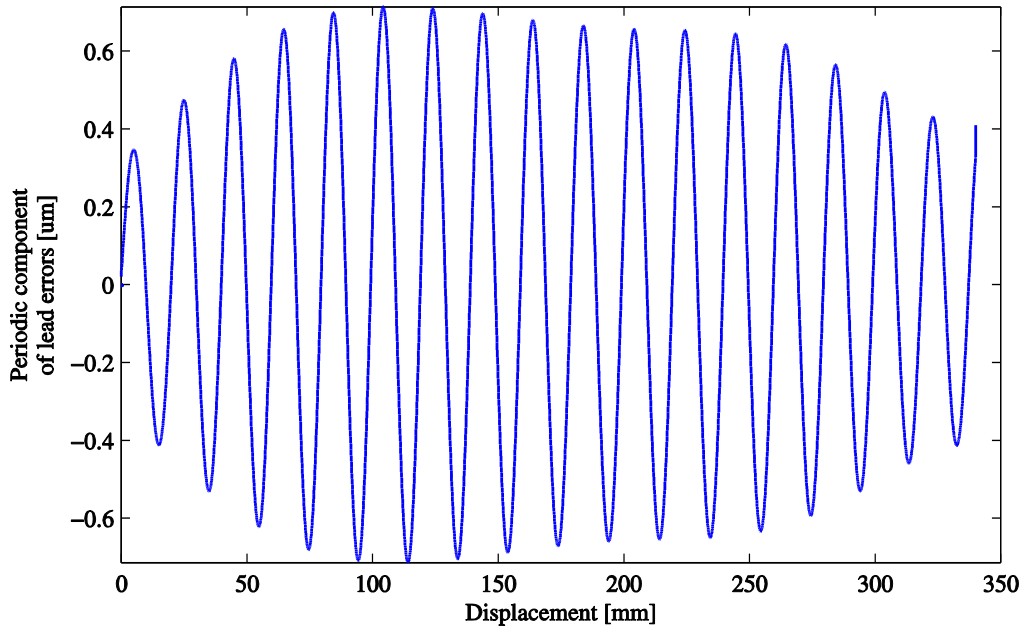


Figure 5.5: Periodic profile of lead errors along the screw shaft.

## 5.2 Structure and Frequency Response of AFC Resonators

In contrast to classic closed-loop control schemes, the correction signal in AFC is not generated as part of the regular servo feedback control. Instead, an external block is used to adaptively estimate the magnitude and phase of the “equivalent” disturbance causing the harmonic error, and inject an appropriate cancellation signal into the control loop to cancel its effect out. This external block is referred to, in this thesis, as the AFC resonator. The internal structure of an AFC resonator is presented in Figure 5.6.

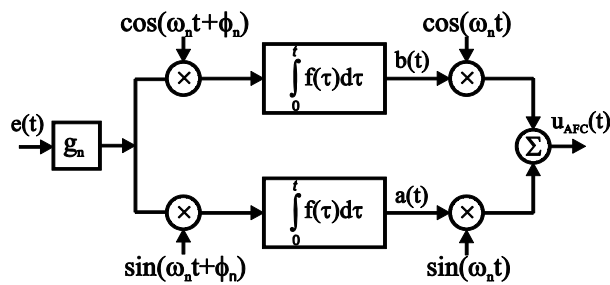


Figure 5.6: Structure of the AFC compensator [93].

The AFC resonator takes as the input a tracking error signal  $e(t)$ , and amplifies it by a gain  $g_n$ , and then de-modulates it by harmonic signals generated at the assumed disturbance frequency  $\omega_n$  with a

phase shift of  $\phi_n$ . A parameter adaptation law is applied to calculate the harmonic participation gains ( $a(t)$  and  $b(t)$  in Figure 5.6), and from them, the equivalent cancellation signal is calculated:

$$u_{\text{AFC}}(t) = a(t) \cdot \sin(\omega_n t) + b(t) \cdot \cos(\omega_n t) \quad (5.1)$$

It can be verified from Figure 5.6 that the inputs to the integrators are:

$$\begin{aligned} \dot{a}(t) &= g_n e(t) \cdot \sin(\omega_n t + \phi_n) \\ \dot{b}(t) &= g_n e(t) \cdot \cos(\omega_n t + \phi_n) \end{aligned} \quad (5.2)$$

Therefore:

$$\begin{aligned} a(t) &= \int_0^t g_n e(\tau) \cdot \sin(\omega_n \tau + \phi_n) d\tau \\ b(t) &= \int_0^t g_n e(\tau) \cdot \cos(\omega_n \tau + \phi_n) d\tau \end{aligned} \quad (5.3)$$

Substituting Equation (5.3) into Equation (5.1):

$$u_{\text{AFC}}(t) = \sin(\omega_n t) \int_0^t g_n e(\tau) \cdot \sin(\omega_n \tau + \phi_n) d\tau + \cos(\omega_n t) \int_0^t g_n e(\tau) \cdot \cos(\omega_n \tau + \phi_n) d\tau \quad (5.4)$$

Since  $\tau$  is the variable of integration, the sine and cosine terms can be taken inside the integrals:

$$u_{\text{AFC}}(t) = \int_0^t g_n e(\tau) [\sin(\omega_n t) \sin(\omega_n \tau + \phi_n) + \cos(\omega_n t) \cos(\omega_n \tau + \phi_n)] d\tau \quad (5.5)$$

Using the trigonometric identity for the difference of two angles simplifies the above equation to:

$$u_{\text{AFC}}(t) = \int_0^t g_n e(\tau) \cos(\omega_n [t - \tau] - \phi_n) d\tau \quad (5.6)$$

Equation (5.6) indicates a convolution of two signals:

$$\begin{aligned} u_{\text{AFC}}(t) &= e(t) \otimes g_n \cos(\omega_n t - \phi_n) \\ &= e(t) \otimes g_n [\cos(\omega_n t) \cos(\phi_n) + \sin(\omega_n t) \sin(\phi_n)] \end{aligned} \quad (5.7)$$

Equation (5.7) can now be converted into the s-domain using the convolution theorem of the Laplace transform:

$$U_{\text{AFC}}(s) = E(s)g_n \frac{s \cos \phi_n + \omega_n \sin \phi_n}{s^2 + \omega_n^2}$$

$$\therefore C_{\text{AFC}}(s) = \frac{U_{\text{AFC}}(s)}{E(s)} = g_n \frac{s \cos \phi_n + \omega_n \sin \phi_n}{s^2 + \omega_n^2} \quad (5.8)$$

The derivation presented above, which is taken from [93], clearly shows that the AFC scheme is equivalent to a Linear-Time Invariant (LTI) filter, when the disturbance frequency is assumed constant. This equivalent linear model is used in this chapter for stability analysis and gain tuning as proposed by Byl et al. in [93]. The frequency response of an AFC resonator can be calculated for different values of  $\phi_n$  (the phase advance parameter) using Equation (5.8) as shown in Figure 5.7.

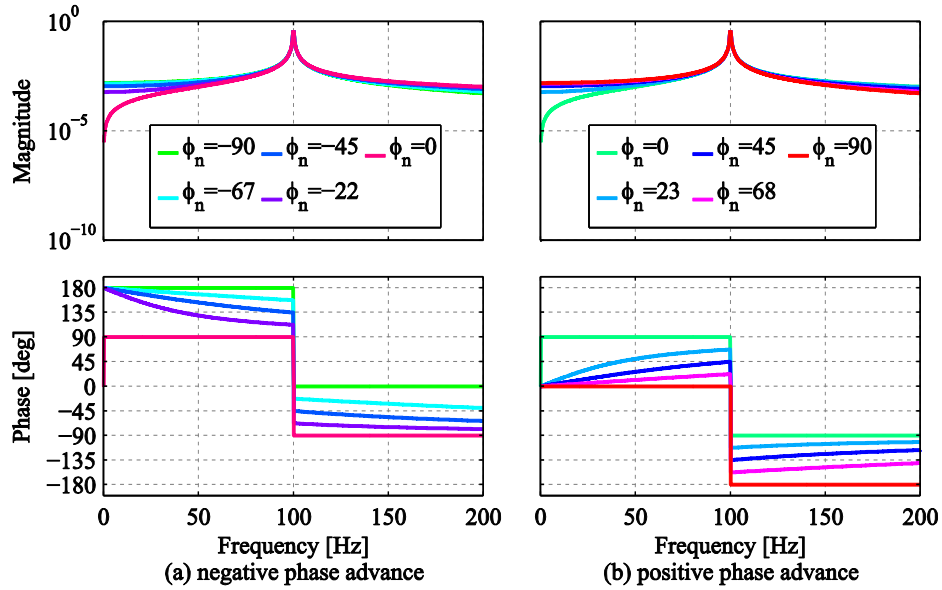


**Figure 5.7: FRF of an AFC resonator with a pair of complex conjugate poles at 100 Hz for different values of the phase advance parameter.**

It is noticeable from Figure 5.7 that a rapid 180 degree phase change occurs around the AFC resonance frequency due to the absence of a damping factor in the denominator. Another important observation is that the change in phase is centered around  $-\phi_n$ . This observation gives a hint about how to select the phase advance parameter. If it is assumed that the AFC resonator ( $C_{\text{AFC}}(s)$ ) is to be used in series with a general plant ( $G_p(s)$ ), as shown in Figure 5.8, the loop transfer function becomes:

$$L(s) = C_{AFC}(s)G_p(s) \quad (5.9)$$

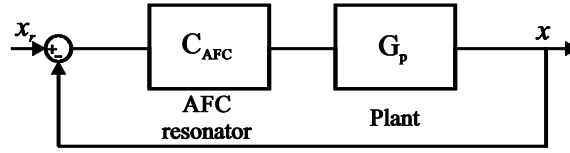


**Figure 5.8: Closed control loop including the AFC resonator and a plant.**

Now, assuming that the phase of the plant at  $\omega_n$  (resonance frequency of the AFC) is  $\phi_p$ , if  $\phi_n$  (the phase advance parameter) is set equal to  $\phi_p$ , then the phase of the AFC resonator at  $\omega_n$  is  $-\phi_p$ , and therefore, the phase of the loop transfer function at this frequency lies at zero:

$$\begin{aligned} \angle L(s) \Big|_{s=j\omega_n} &= \angle C_{AFC}(s)G_p(s) \Big|_{s=j\omega_n} \\ &= \angle C_{AFC}(s) \Big|_{s=j\omega_n} + \angle G_p(s) \Big|_{s=j\omega_n} = -\phi_p + \phi_p = 0 \end{aligned} \quad (5.10)$$

With this selection of  $\phi_n$ , the phase of the loop transfer function (Equation (5.9)) jumps from  $+90$  to  $-90$  degrees around the resonance frequency (Figure 5.9a). This reflects in the Nyquist plot, as a straight line parallel to the imaginary axis, which in effect establishes a phase margin close to  $90$  degrees (Figure 5.9b).

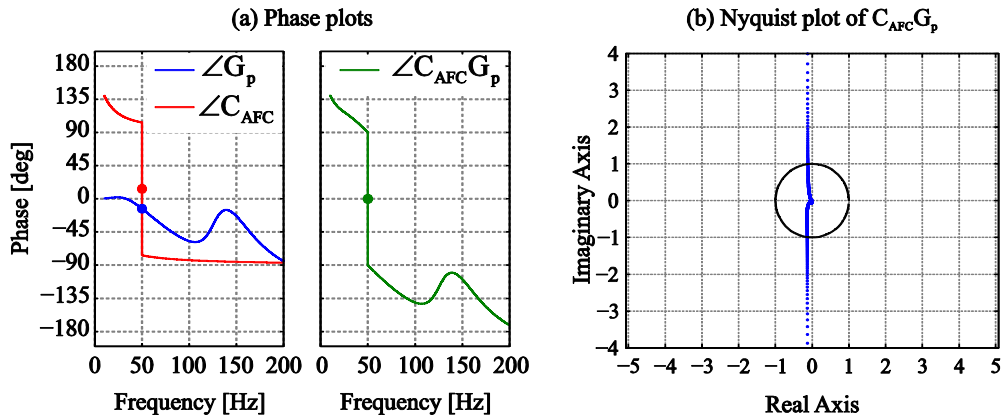


**Figure 5.9: The effect of the proposed phase advance parameter on the Nyquist plot.**

If the error signal is composed of harmonics of different frequencies, first, for each target frequency an AFC resonator is designed. Then, they are all stacked together in parallel to generate the corrective signal (Figure 5.10). These resonators together are referred to as the AFC compensator.

The integration of the AFC compensator into the control system of a ball screw drive is discussed in the next section.

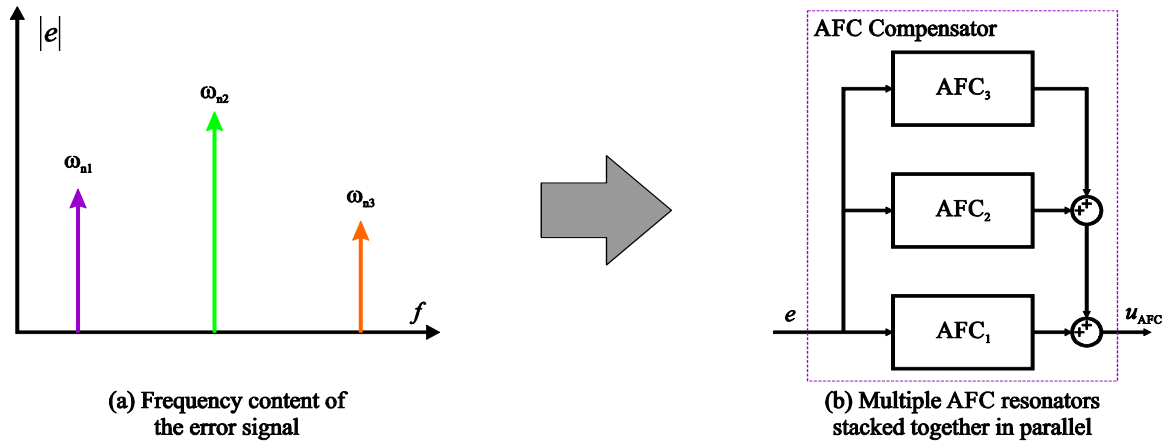


Figure 5.10: AFC for compensation of multiple harmonics.

### 5.3 Position Control of Ball screw Drives Using AFC Compensators

As mentioned earlier in Section 2.3.2, there are different configurations for integrating the AFC compensator into a closed-loop control system. In this thesis, the serial configuration, as shown in Figure 5.11, is adopted for this purpose. However, the design methods detailed in this section are also applicable to the parallel configuration, as reported in [17]. The in-depth study of pros and cons of each configuration is kept outside the scope of this thesis, and can be considered a topic for future research.

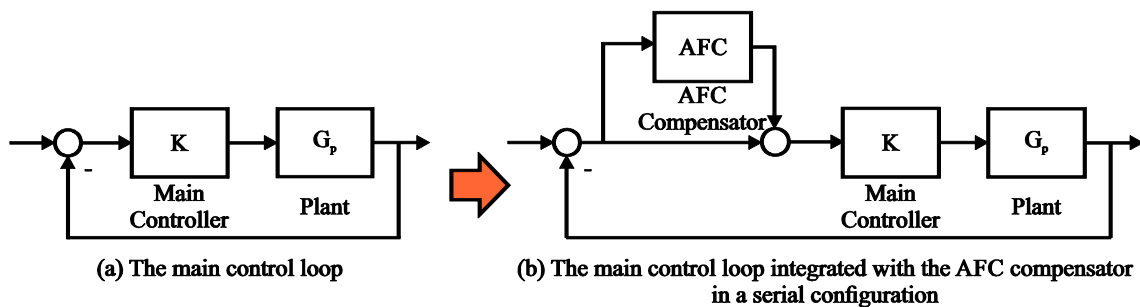


Figure 5.11: Serial integration of the AFC compensator into the control system.

#### 5.3.1 Tuning of Adaptation Gains and Stability Analysis

Stability analysis of the linear systems involving the AFC compensators is facilitated by considering the equivalent LTI representation of the AFC in the analysis. Within this framework, large phase and

gain margins are reliable indicators of robust stability. Thus, the AFC adaptation gains are selected to ensure adequate phase and gain margins. A simple rule for selection of the phase advance parameter of an AFC resonator was explained in Section 5.2. In order for that rule to be applicable, the AFC compensator should be in series with a general plant in a control loop. Hence, the block diagram shown in Figure 5.11b is rearranged in such a way that it consists of two nested loops: an inner loop that contains all the blocks except for the AFC compensator, and an outer loop as shown in Figure 5.12a. Further simplification turns this block diagram into the one shown in Figure 5.12b. Now, the AFC compensator is in series with a new plant in the control loop. Therefore, in order to ensure adequate phase margin, the phase advance parameter of each AFC resonator can be set as follows:

$$\phi_n = \angle \frac{K(s)G_p(s)}{1+K(s)G_p(s)} \Big|_{s=j\omega_n} \quad (5.11)$$

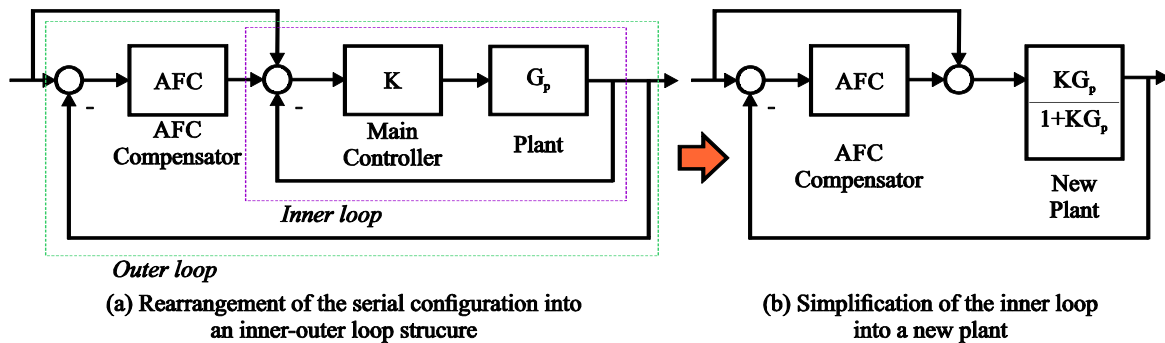


**Figure 5.12: An alternative perspective on the control loop topology.**

The gain of each AFC resonator ( $g_n$  in block diagram of Figure 5.6) is then tuned by trial and error until acceptable gain margins are achieved. These gain margins are computed from the loop transfer function corresponding to the serial configuration shown in Figure 5.11b:

$$L(s)=[1+AFC(s)].K(s).G_p(s) \quad (5.12)$$

Following this approach, an AFC compensator including three resonators was designed to boost the disturbance rejection performance of a Pole Placement Controller (PPC), introduced in [3], at frequencies of 50 Hz, 100 Hz and 200 Hz. The tuned AFC resonator gains corresponding to each of these frequencies are listed in Table 5.1.

**Table 5.1: Tuned AFC resonator gains.**

Resonator number	Resonator frequency [Hz]	Resonator gain []
1	50	20
2	100	40
3	200	80

The effect of enabling each of these resonators inside the AFC compensator can be seen in the bode diagram of the loop transfer function in the form of a resonance peak at the frequency of that resonator. For example, if only the first resonator is enabled, the Bode and Nyquist diagrams of the loop transfer function turns out to be as shown in Figure 5.13 and Figure 5.14. When the second and third resonators are enabled, the corresponding peaks appear in the frequency response of  $L(s)$ , as shown in Figure 5.15 and Figure 5.17. The related Nyquist plots are shown in Figure 5.16 and Figure 5.18.

In order to clearly see the effect of AFC resonators on the frequency response of the loop transfer function, the bode plot has to be created with a high frequency resolution. Although experimental measurement of the frequency response of the ball screw drive at very small frequency steps is possible, it is tedious and time-consuming. Therefore, in this analysis, the identified two mass model of the drive (Section 3.4.1) combined the with loop delay dynamics is used instead to calculate the loop transfer function according to Equation (5.12). This is not problematic in terms of stability analysis, because, on one hand, the effects of AFC resonators away from the frequency that they target is negligible, and on the other hand there is a good agreement in terms of frequency response between the identified two-mass model of the plant and the actual plant up to frequency of 250 Hz, which is higher than the frequency of the third AFC resonator (200 Hz).

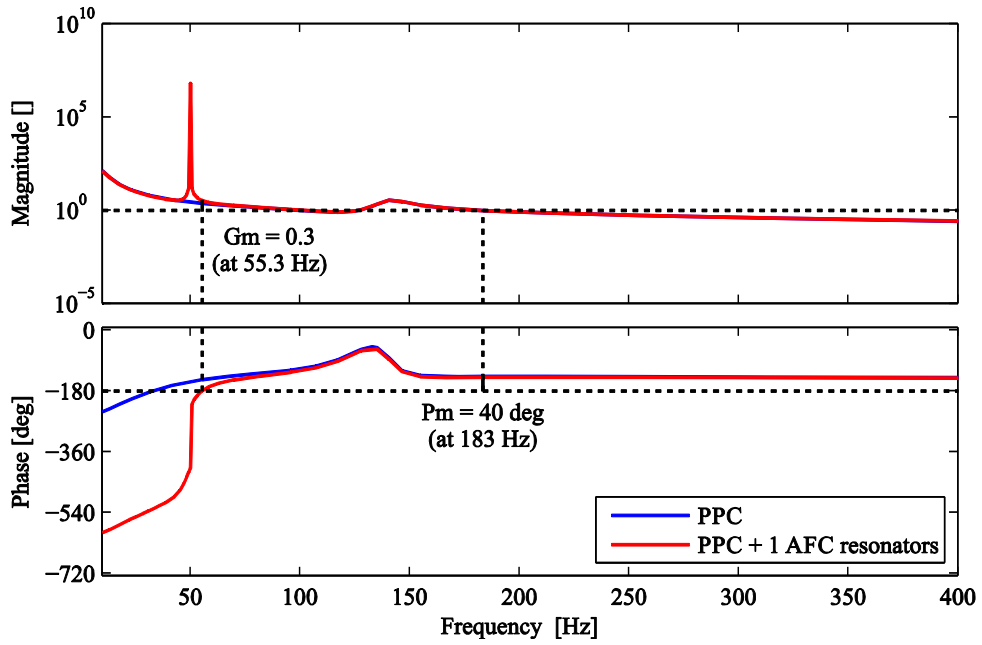


Figure 5.13: Bode plot of the loop transfer function when only one AFC resonator is implemented.

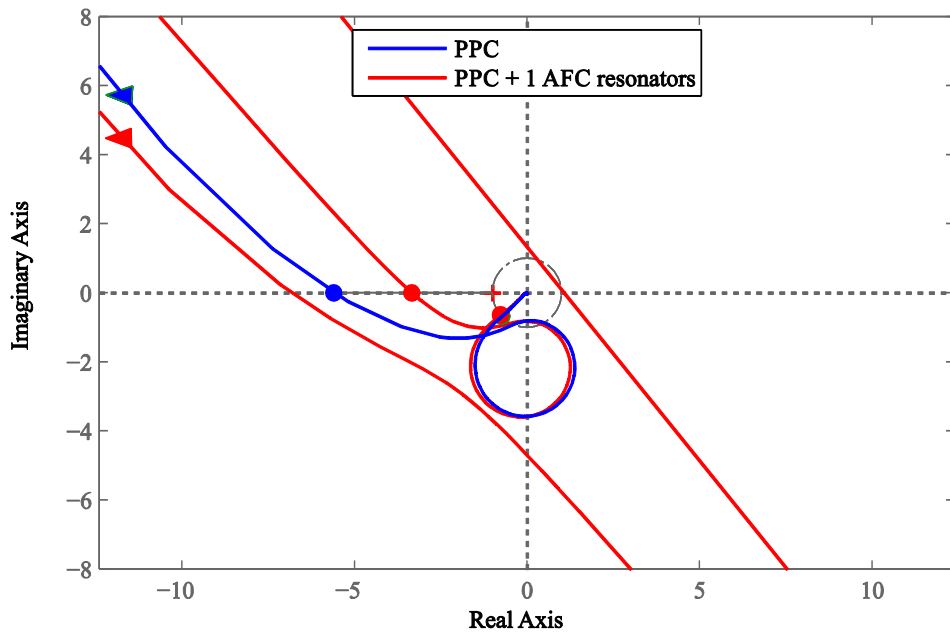


Figure 5.14: Nyquist plot of the loop transfer function when only one AFC resonator is implemented.

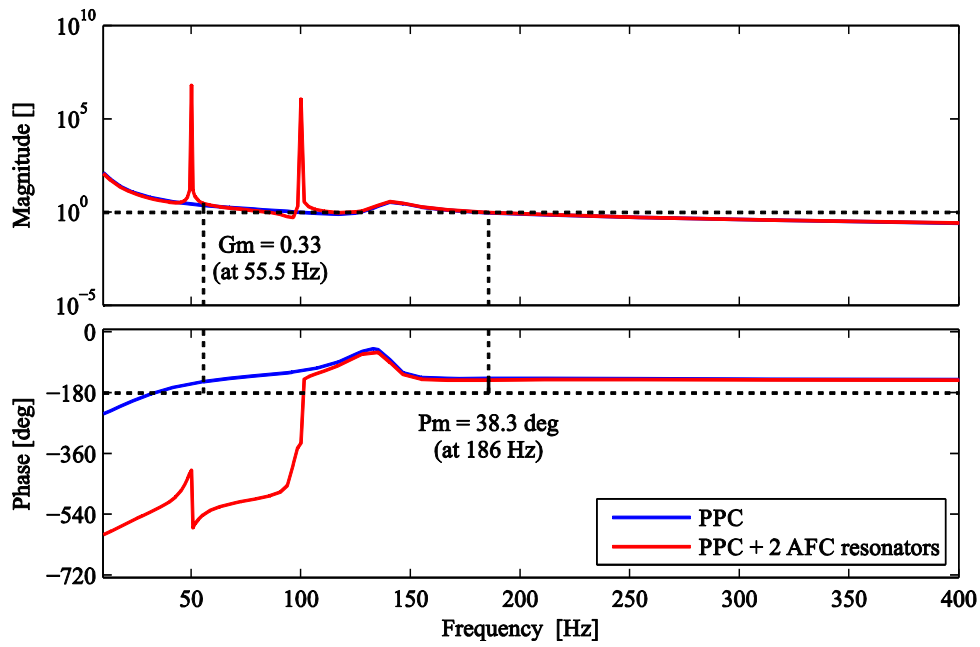


Figure 5.15: Bode plot of the loop transfer function with two AFC resonators.

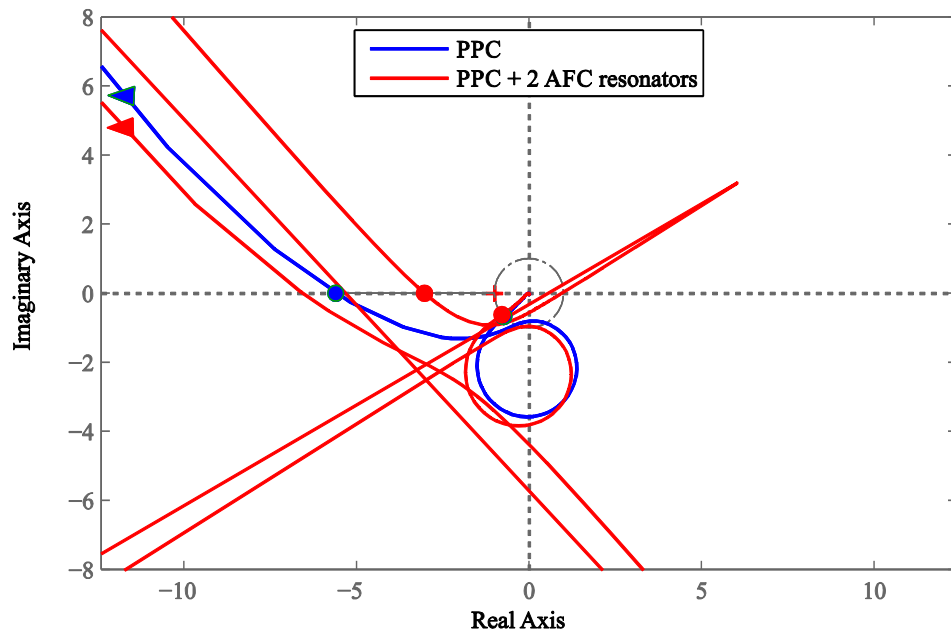


Figure 5.16: Nyquist plot of the loop transfer function with two AFC resonators.

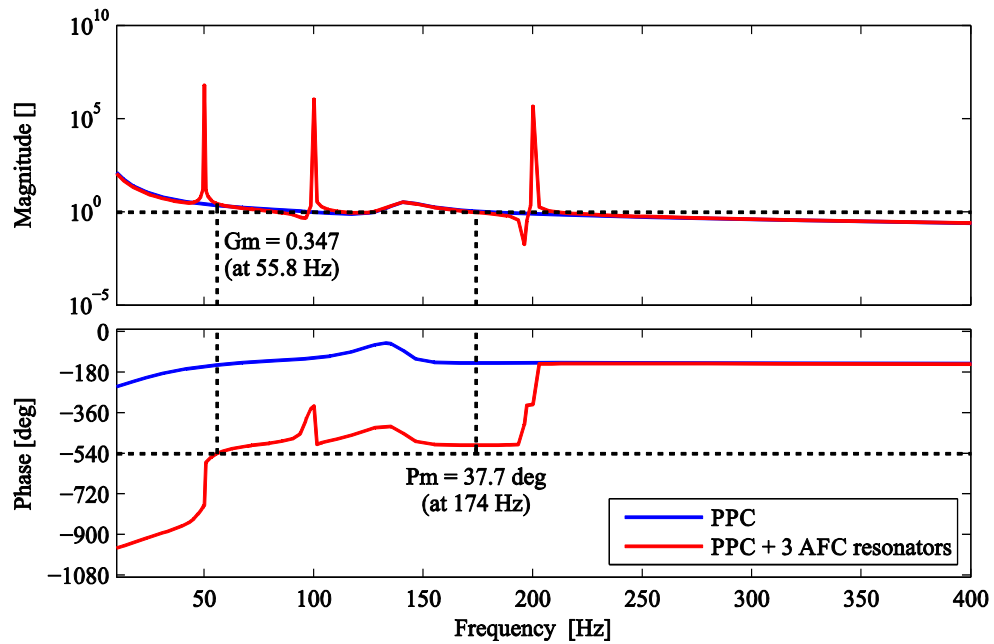


Figure 5.17: Bode plot of the loop transfer function with three AFC resonators.

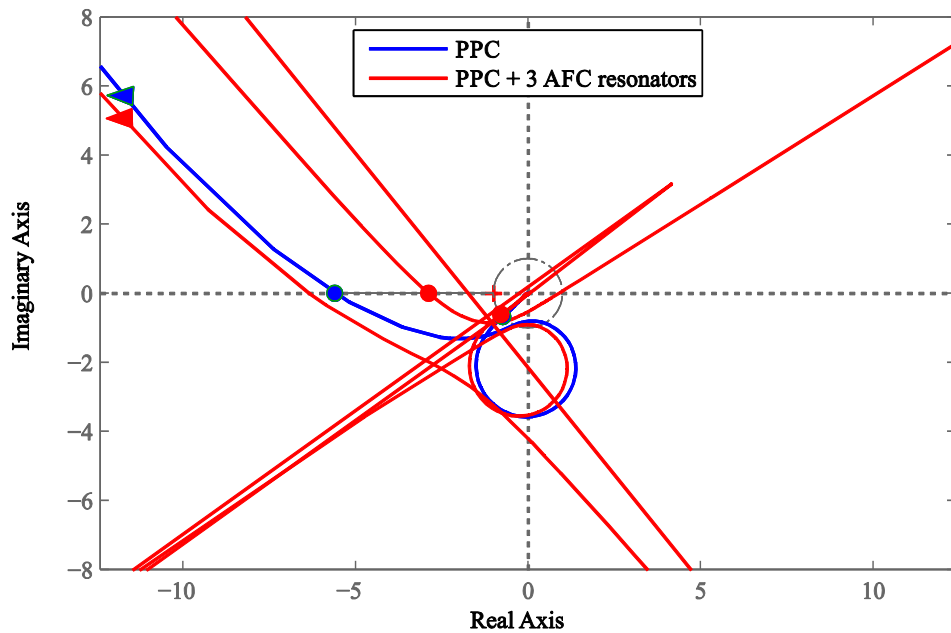
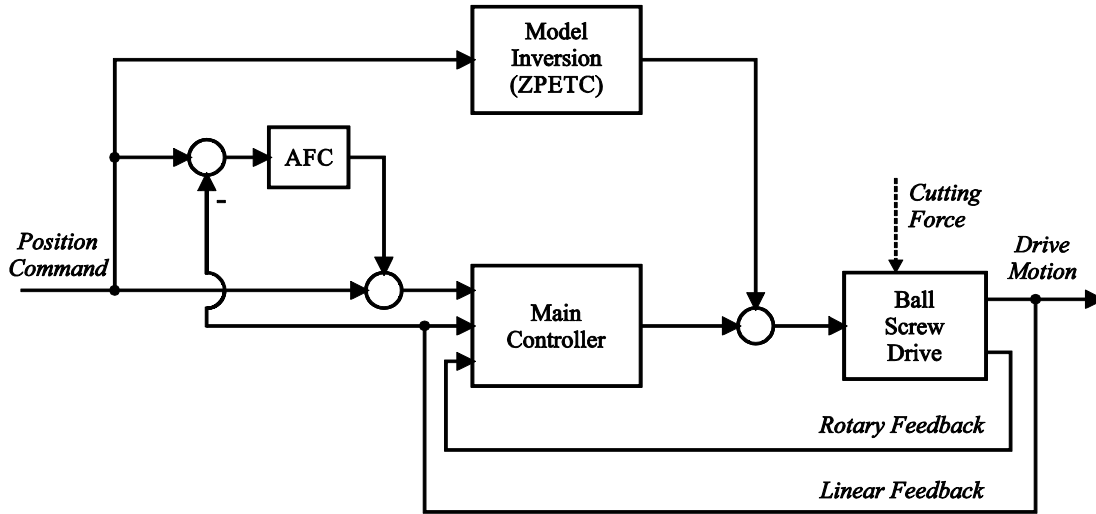


Figure 5.18: Nyquist plot of the loop transfer function with three AFC resonators.

### 5.3.2 Using AFC in Milling Experiments

The AFC design was utilized with several different main servo controllers to further attenuate the tracking errors that are caused by the periodic forces during milling. Figure 5.19 shows the overall

scheme of the control system, in which, a serial configuration of the AFC is implemented. To minimize the tracking errors due to high-order polynomial reference commands during acceleration and deceleration periods, a model inversion is implemented in feedforward. Since the discretized version of the plant model is non-minimum phase, only an approximate inversion is possible. The inversion technique that is used in this control scheme is the Zero Phase Error Tracking Controller (ZPETC) [52].



**Figure 5.19: Overall scheme of the AFC integrated control system for machining.**

The milling experiments were conducted with 2-flute and 4-flute end-mills at different spindle speeds and feed rates. In the first round of experiments, an AFC controller with the gains shown in Table 5.1 was used along with a PPC controller [3] to maintain positioning accuracy during slot milling of aluminum 6061 with a 4-flute cutter at spindle speed of 3000 rpm, feedrate of 10 mm/s, and axial depth of cut of 0.5 mm. Using FFT analysis, the dominant frequency components of the tracking error were determined to occur at the spindle speed (50 Hz run-out frequency), its second harmonic (100 Hz), and at the tooth-passing frequency (200 Hz). Consequently, the AFC resonators were designed to target these frequencies. The blue signal in Figure 5.20 represents the tracking error when only the main PPC controller is used (i.e. the AFC compensator is disabled). On the other hand, the red and green signals represent the tracking error when this experiment is repeated with AFC resonators enabled. It is clear from the red signal that enabling the AFC resonators that target the harmonic components at 50 Hz and 100 Hz reduces the tracking error significantly. Moreover, the green signal shows that additional improvement in tracking accuracy is achievable by enabling the

200 Hz AFC resonator as well. This observation is consistent with the maximum and RMS error values reported in Table 5.2.

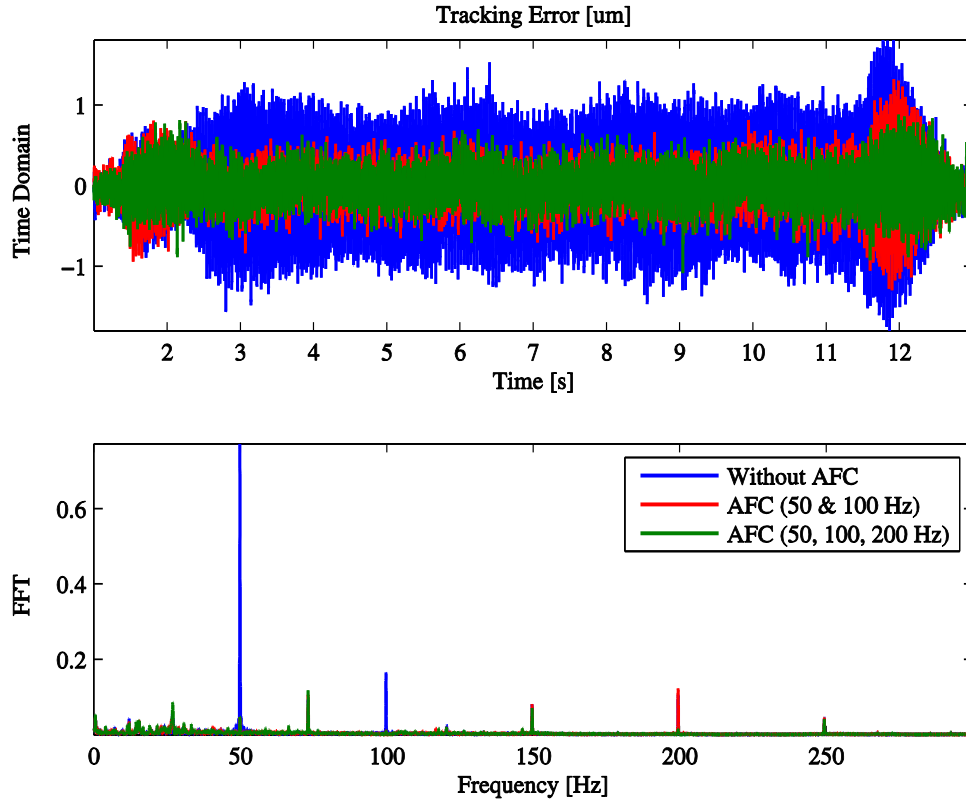


**Figure 5.20: Improvement in tracking accuracy when AFC resonators are enabled at target frequencies.**

**Table 5.2: Maximum and RMS value of the tracking errors for the results presented in Figure 5.20.**

	Without AFC	AFC (50, 100, 200 Hz)
Max Error [ $\mu\text{m}$ ]	1.8	1.08
RMS Error [ $\mu\text{m}$ ]	0.57	0.21

In another set of experiments, the AFC compensator was used along with the PPC controller designed in Chapter 4 of this thesis. This time, a 2-flute cutter was used for machining aluminum 6061. To try out different target frequencies with AFC, three different spindle speeds were

commanded, and the feedrates were chosen accordingly, to keep the chip load constant at 0.254 mm/tooth in all cases. The axial depth of cut was also set to 1 mm. Table 5.3 summarizes the cutting parameters used in this experiment, as well as, the target frequencies and gain parameters of the AFC resonators. At each spindle speed, the AFC compensator is configured to target two frequencies: the first frequency is the run-out frequency, and the second one is the tooth-passing frequency. The tracking errors resulted from these experiments are shown in Figure 5.21. The maximum and RMS error values are summarized in Table 5.4.

**Table 5.3: Cutting and AFC compensator parameters.**

Spindle Speed [rpm]	Feedrate [mm/s]	Runout Freq. [Hz]	Tooth-pass. Freq. [Hz]	AFC Resonator #1 Gain []	AFC Resonator #2 Gain []
3000	25.40	50.00	100.00	50	50
2000	16.93	33.33	66.66	50	50
1000	8.47	16.67	33.33	50	50

**Table 5.4: Maximum and RMS value of the tracking errors for the results presented in Figure 5.21.**

Spindle Speed [RPM]	Without AFC			With AFC		
	1000	2000	3000	1000	2000	3000
Max Error [ $\mu\text{m}$ ]	30.6	24.6	22.4	18.0	10.1	13.6
RMS Error [ $\mu\text{m}$ ]	12.9	13.5	10.9	3.5	1.9	3.5

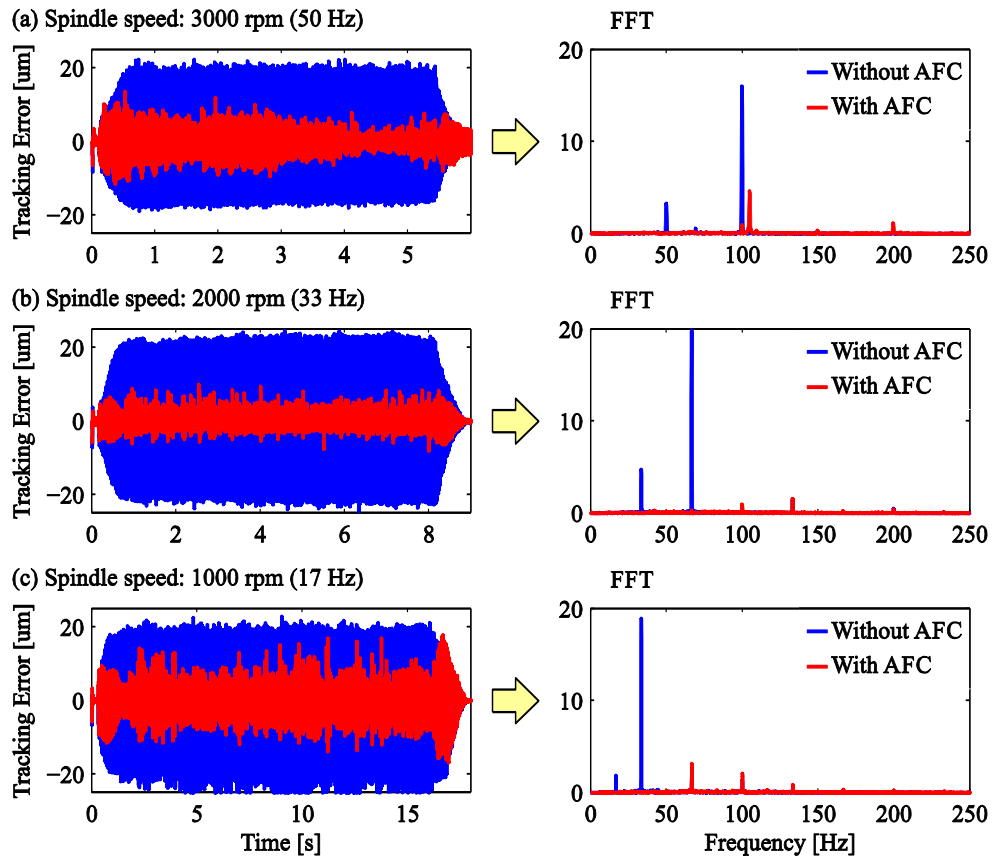


**Figure 5.21: AFC improves table positioning accuracy during machining when the PPC is the main controller.**

For comparison purposes, this particular AFC compensator was also integrated with the P-PI controller that was discussed before in Chapter 4. This P-PI+AFC control scheme was again used to perform the same slot cutting experiment, as in the PPC+AFC case. The results are shown in Figure 5.22. The maximum and RMS error values are summarized in Table 5.5.

**Table 5.5: Maximum and RMS value of the tracking errors for the results presented in Figure 5.22.**

	Without AFC			With AFC		
	1000	2000	3000	1000	2000	3000
Spindle Speed [RPM]	1000	2000	3000	1000	2000	3000
Max Error [ $\mu\text{m}$ ]	29.3	23.0	36.2	24.2	9.3	130.1
RMS Error [ $\mu\text{m}$ ]	7.3	11.8	17.9	3.9	2.2	58.5

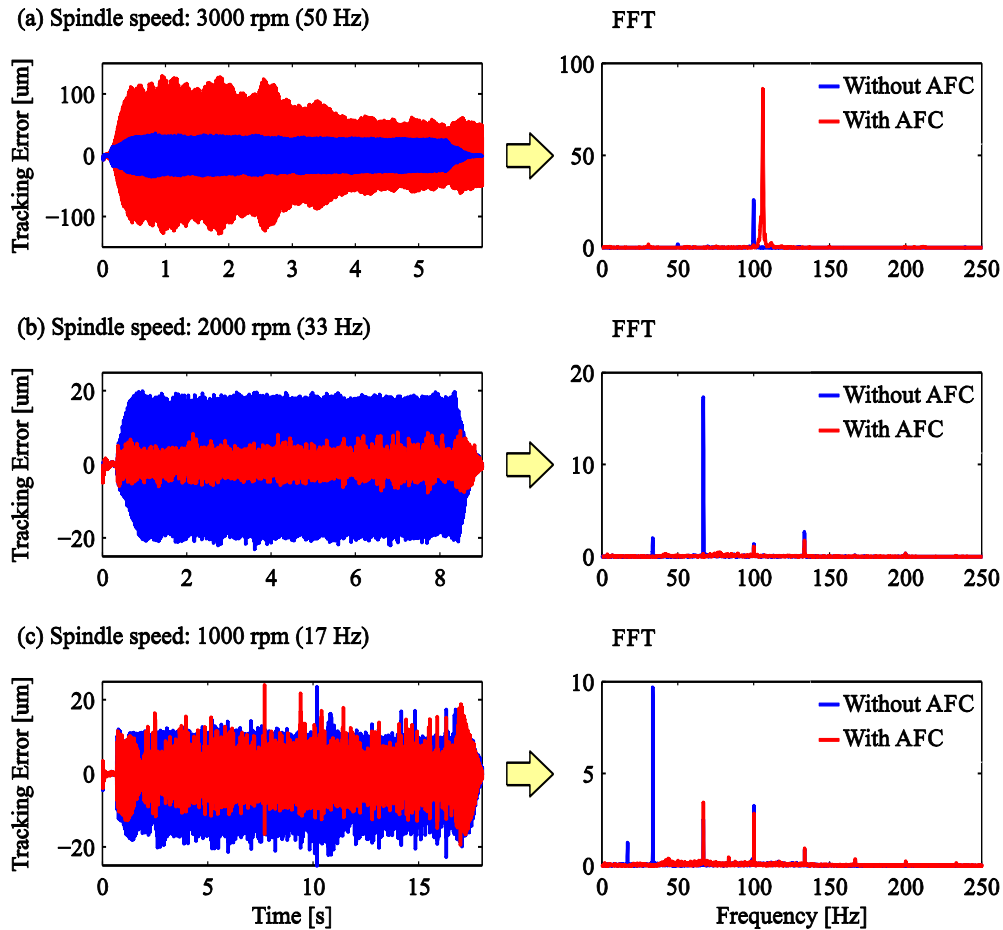


**Figure 5.22: The effect of AFC on table positioning accuracy during machining when the P-PI is the main controller.**

It is noticeable from Figure 5.22 that although enabling the AFC mitigates the tracking errors at spindle speeds of 1000 rpm and 2000 rpm, it has an opposite effect when the spindle speed is at 3000 rpm. This unexpected observation can be explained by comparing the magnitude of sensitivity functions between the P-PI+AFC and PPC+AFC control schemes (Figure 5.23). It should be reminded that the transfer function of each AFC resonator varies depending on its target frequency, which itself is a function of spindle speed. This fact makes the control loop sensitivity a function of the spindle speed.

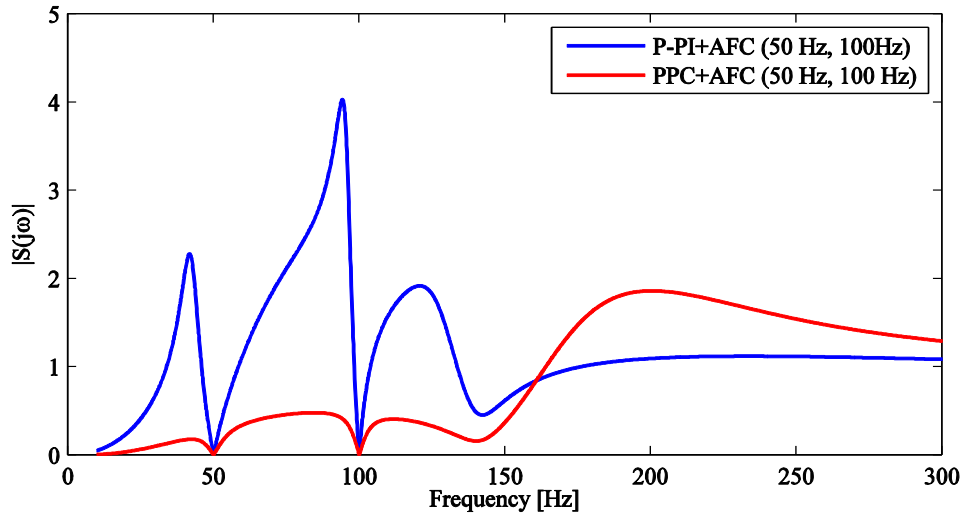


**Figure 5.23: Sensitivity magnitude for P-PI+AFC versus PPC+AFC at target AFC frequencies of 50 Hz and 100 Hz.**

Figure 5.23 clearly shows that compared to the PPC+AFC controller, the P-PI+AFC controller has a much larger sensitivity in the vicinity of the AFC target frequencies (50 Hz, 100 Hz). This makes the P-PI+AFC more susceptible to variations in the nominal spindle speed. Therefore, when the AFC compensator, targeting frequencies of 50 Hz and 100 Hz, is enabled along with the main P-PI controller, it makes the tracking errors worse. It was tried to alleviate this problem by de-tuning the AFC gains. However, even with small AFC gains, no improvement in tracking accuracy was observed compared to the results obtained by using the P-PI alone.

### 5.3.3 Harmonic Disturbance Rejection for Ball Screw Lead, Mechanism, and Encoder Misalignment Errors

The AFC technique can also be used for rejection of position-dependent harmonic disturbances. However, in this case, to maintain stability the phase advance parameter needs to be updated continually in the real time to accommodate the change in the frequency of the disturbance, which is proportional to the rotational velocity. To avoid adding more feedback loops that can cause stability problems, the reference velocity, instead of the actual velocity, has been used here to generate a real-time trajectory for the phase advance parameter. At each sample time, the disturbance frequency is calculated from the reference velocity first, and then, it is set as the target frequency of the AFC resonator, and the phase advance parameter is updated according to Equation (5.11).

Position dependent periodic disturbances become problematic in terms of their effect on tracking accuracy mainly when the ball screw drive is commanded to move at a high speed. Otherwise, they act as low frequency disturbances, which are adequately compensated by the main controller. Longer periods of acceleration and deceleration are expected to emerge when a high-speed motion is commanded. Since the ZPETC does not provide a perfect inversion, during the acceleration and deceleration periods, cubic acceleration reference commands result in tracking errors that are typically of the same order of magnitude as the errors caused by the periodic disturbances. If these errors are not removed from the input to the AFC compensator, the AFC may end up causing more harm than good in terms of the overall tracking accuracy. To avoid this situation, two approaches are utilized in this thesis:

In the first approach, a predictor block that predicts the tracking error was implemented as part of the overall control scheme. Inside this block, the entire closed loop system, including a digital model of the plant, is simulated in real-time. The predicted tracking error signal generated by this block is then removed from the input to the AFC compensator as shown in Figure 5.24.

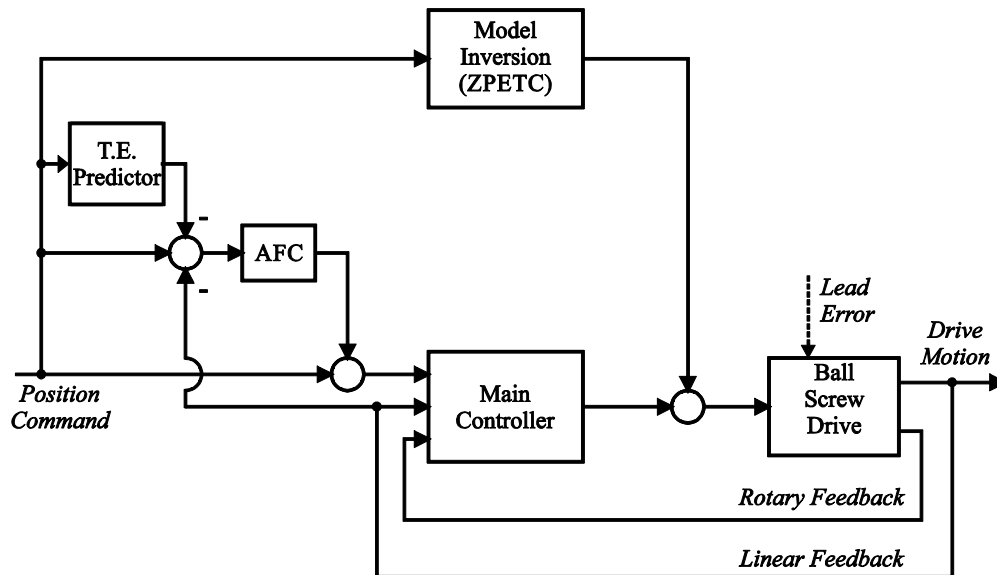


**Figure 5.24: Overall scheme of the control system including the AFC and a tracking error predictor for high speed tracking.**

In the second approach, discussed earlier in Section 4.2, a pre-filter was designed for estimating the tracking error as a linear combination of the first three derivatives of the reference trajectory. The predicted tracking error signal is then added to the original reference trajectory in a feedforward

manner as illustrated in Figure 5.25. This technique was observed to reduce the tracking errors, caused by imperfect inversion, by an order of magnitude. As a result, the actual tracking error signal turned out to be mainly dominated by the traces of the position-dependent periodic disturbances. This tracking error signal could be directly fed into the AFC compensator.

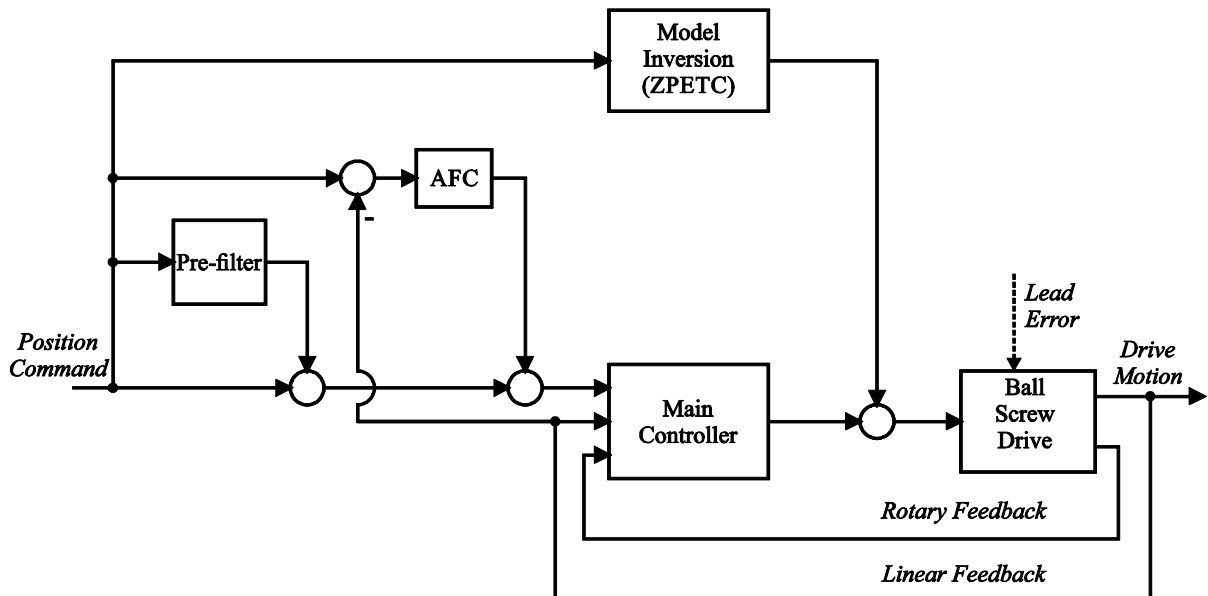


**Figure 5.25: Overall scheme of the control system including the AFC and a pre-filter for high speed tracking.**

### 5.3.4 Experimental Results

In order to mitigate the tracking errors due to position dependent periodic disturbances, the AFC compensator was integrated with a Pole Placement Controller (PPC) [3], first, according to the scheme shown in Figure 5.24. In the tracking experiments conducted with the AFC, only one harmonic component, with a spatial frequency of once per screw shaft revolution, was targeted by the AFC compensator. The reference trajectory for this experiment is shown in Figure 5.26. Since the maximum reference velocity is 1000 mm/s, and the ball screw has a pitch of 20 mm, the disturbance frequency corresponding to the rotational velocity at maximum table speed is 50 Hz. Figure 5.27a shows that the tracking errors are reduced considerably after enabling the AFC. Analysis of the data collected from this experiment also shows that the Root Mean Square (RMS) error has reduced from 2.40  $\mu\text{m}$  to 1.78  $\mu\text{m}$ . This reduction in error is easily detectable in the FFT plot for the tracking error

(Figure 5.27b). From this plot, it can be seen that the peak at 50 Hz has been quenched significantly, due to the AFC action.

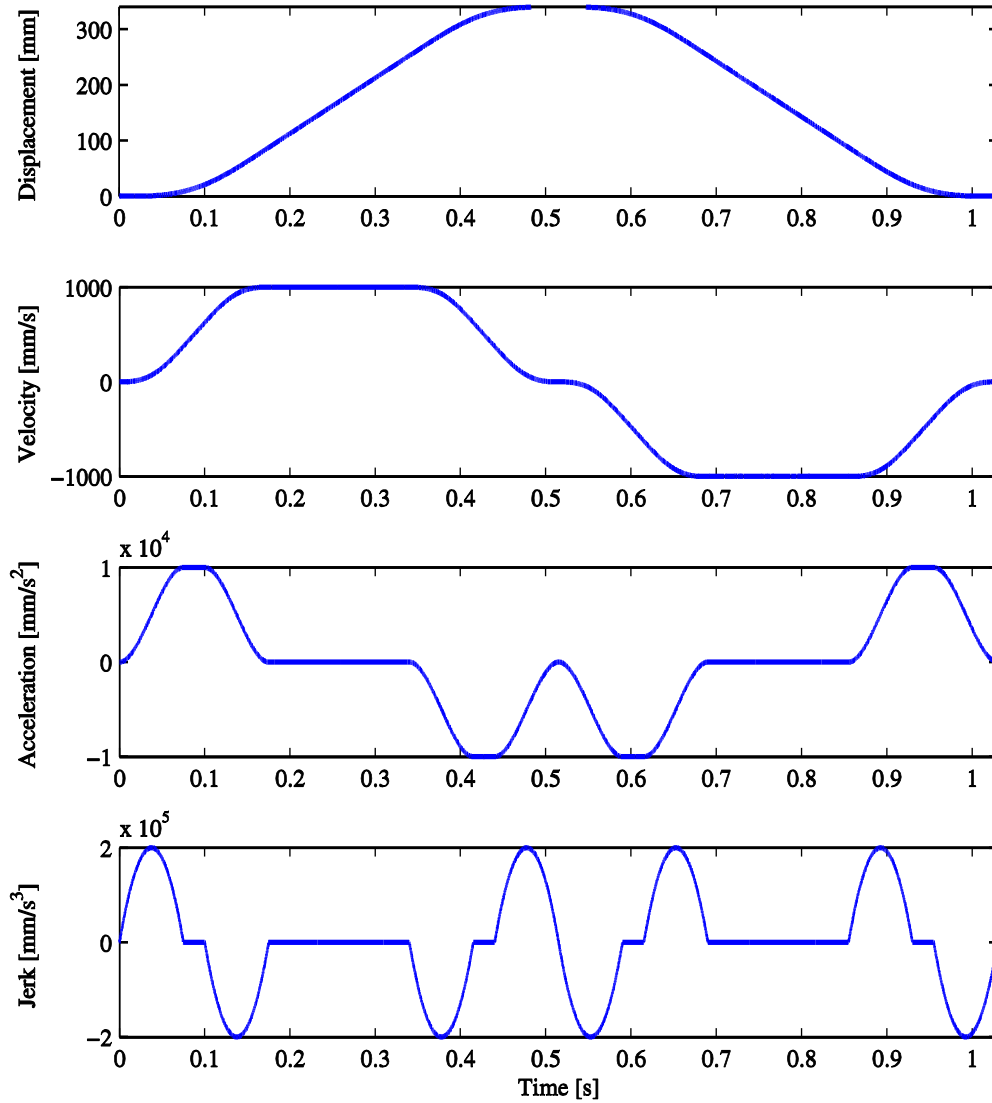


**Figure 5.26: Reference trajectory (displacement: 0.34 m, velocity: 1 m/s, acceleration: 10 m/s<sup>2</sup>, jerk: 200 m/s<sup>3</sup>).**

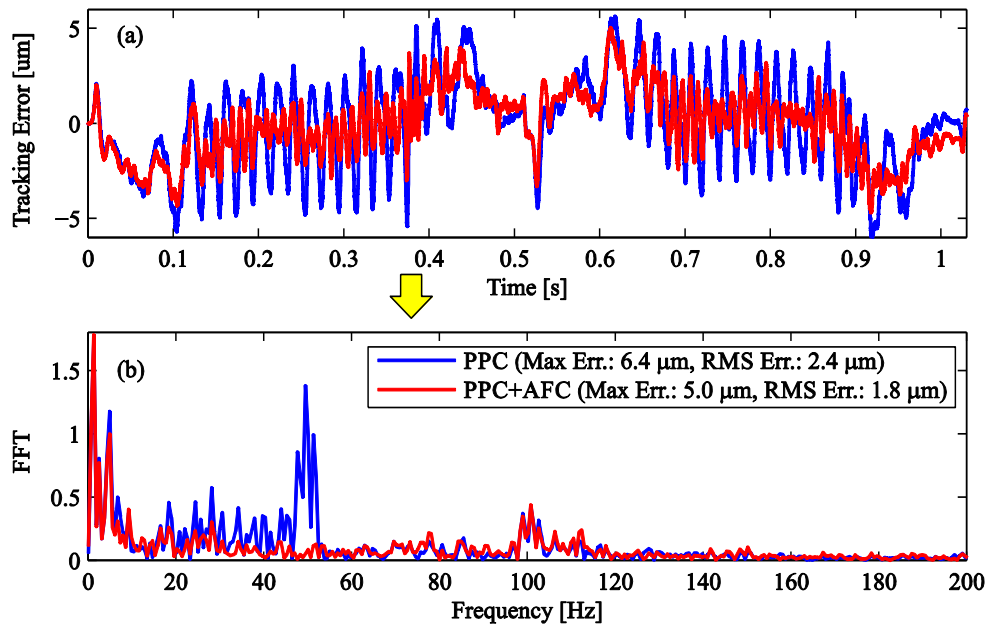


**Figure 5.27: Tracking errors with PPC+T.E. Predictor before and after enabling the AFC.**

Another tracking experiment was conducted to evaluate the use of the AFC according to the control scheme presented in Figure 5.25. For this experiment, the main controller, the reference trajectory, and the AFC settings were kept the same as before. However, instead of using a tracking error predictor to remove low frequency content from the input to the AFC, a pre-filter was used to manipulate the reference trajectory, and thereby push down the low frequency content of the actual tracking error. In order to verify the reliability of the AFC method in the face of changes in the lead error profile of the ball screw, two trials of this experiment were conducted: one when the ball screw was brand new, and the other, two years later, when the ball screw groove and recirculating balls were to some extent worn out. Figure 5.28 compares the results of these two trials. It is apparent from this figure that when the ball screw is new, the lead errors contribute more significantly to the tracking errors. Nevertheless, in both cases, the AFC has successfully suppressed the harmonic component of the tracking error related to the lead errors. In the first trial, which was conducted when the ball screw was brand new, the use of AFC reduced the RMS error from  $2.4\ \mu\text{m}$  to  $1.78\ \mu\text{m}$ . In the second trial, conducted two years later, the RMS error was reduced from  $1.01\ \mu\text{m}$  to  $0.86\ \mu\text{m}$  as shown in Table 5.6. To get a better sense of the change in the lead error profile of the ball screw over the two-year period, the discrepancy between the readings of the linear and rotary encoders in each tracking trial is compared in Figure 5.29. As can be seen, the local peak-to-valley values, which are

indicators of the lead error amplitudes, were roughly two times larger when the ball screw was brand new.

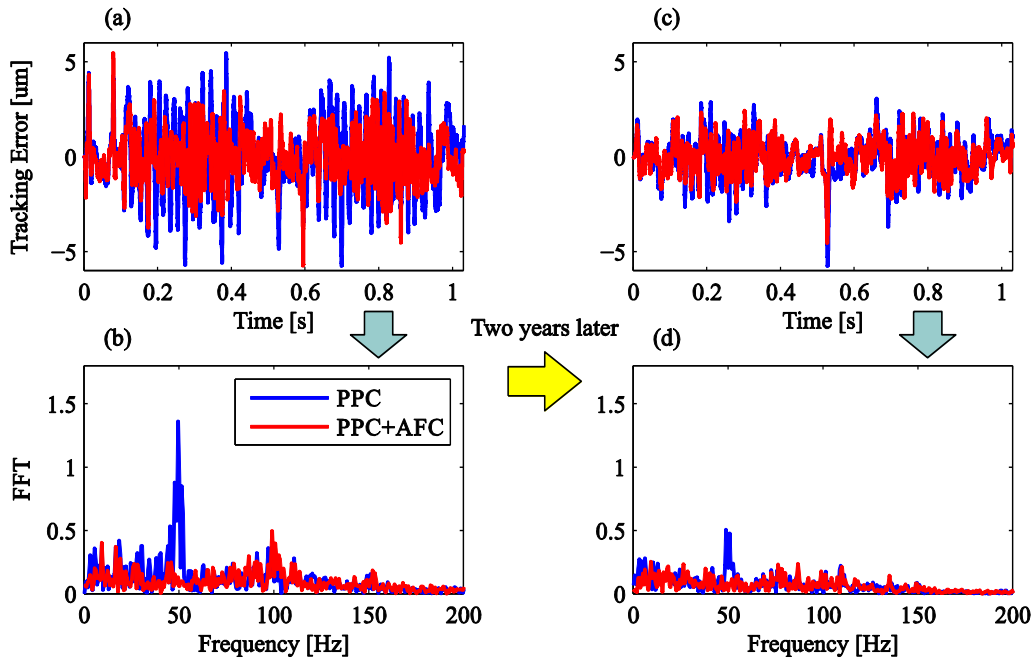
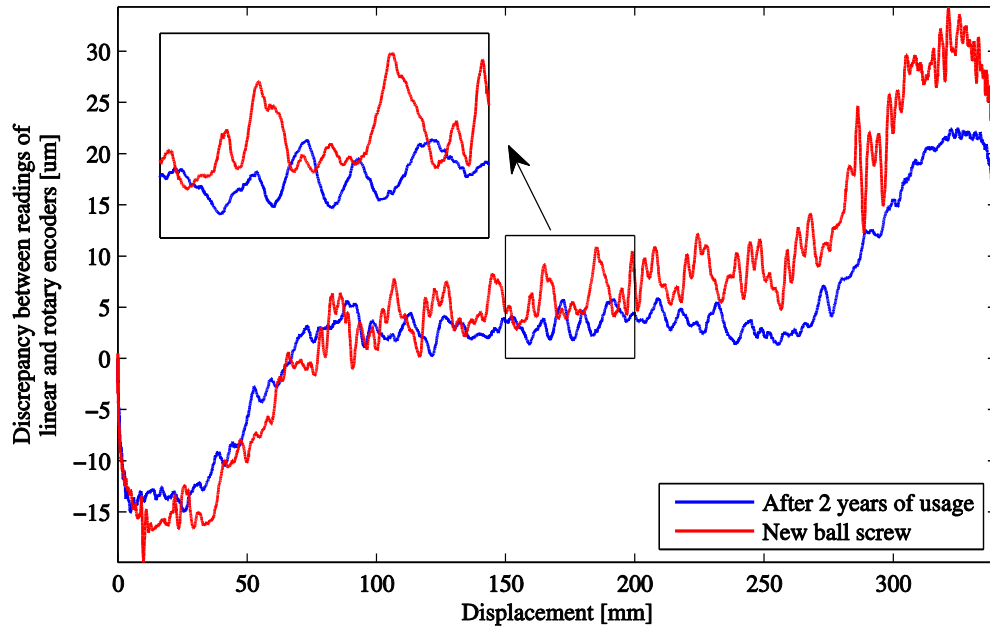


Figure 5.28: Tracking errors with PPC+Pre-filter before and after enabling the AFC.

Table 5.6: Maximum and RMS value of the tracking errors for the results presented in Figure 5.28.

	Brand new ball screw		After two years of usage	
	Without AFC	With AFC	Without AFC	With AFC
Max Error [ $\mu\text{m}$ ]	6.4	5.1	5.8	4.5
RMS Error [ $\mu\text{m}$ ]	2.4	1.8	1.01	0.86



**Figure 5.29: Change in lead error profile of the ball screw over a two-year period.**

The fact that the AFC can reject the harmonic disturbances regardless of the exact profile of the lead errors distinguishes this method from the model-based feedforward alternatives, such as the one proposed in [13], that require the re-calibration of the lead error model from time to time in order to be effective.

## 5.4 Conclusions

In this chapter, common causes of periodic disturbances in ball screw feed drives were identified. It was discussed that these disturbances are either time periodic, as in the case of milling forces, or space periodic, as in the case of lead errors. For both of these scenarios, the design and implementation of AFC compensators were demonstrated, and it was shown that this method works effectively in suppressing target harmonics both in milling applications, as well as, in high-speed positioning applications.

## Chapter 6

### Conclusions & Future Work

In this thesis, an attempt has been made to accurately model electrical and mechanical subsystems of ball screw drives, and develop new control methods for high performance command following and disturbance rejection for this type of feed drives. A Finite Element (FE) code has been developed to solve for natural frequencies and mode shapes of a custom-made ball screw drive. The FE predictions have been verified against experimentally measured Frequency Response Functions (FRFs). The FE code has been used also for investigating the effect of moving table on the modal characteristics of the plant.

The idea of using the Center of Mass (COM) location feedback in controller design has been explored in detail, and a novel control strategy has been proposed that combines the COM control with active vibration damping, and direct integral position control of the load side. The tuning procedure for this control scheme has been explained, and the results of metal cutting and high speed tracking experiments have been demonstrated that confirm the effectiveness of the method in reducing positioning errors. In another design, the effect of system delays has been accounted for by using a lead filter that compensates the phase loss around the crossover frequency. It has been shown that recovering the phase facilitates the design of a more aggressive state feedback control law with the pole placement technique. In order to design the lead filter, manual optimization has been used to minimize the magnitude of the load side disturbance response across the frequency range of interest. This new design is one of the main contributions in this thesis, and the improvements that it offers in comparison with the mainstream industrial P-PI cascade control have been demonstrated in metal cutting and high-speed tracking experiments. Multi-mode vibration suppression has also been investigated in another pole placement design. A Kalman filter has been designed to estimate the required states. This control concept has been verified in simulations. However, due to the plant/model mismatch and the stability problems caused by that, the attempts to implement this control law experimentally did not succeed. Even if it could have been implemented this control law was verified to have poor disturbance rejection.

Finally, an Adaptive Feedforward Cancellation (AFC) scheme has been integrated with a main controller to reject harmonic disturbances of known frequency. The successful implementation of this method for attenuating the effects of periodic milling forces on table positioning errors was

demonstrated. In addition, the AFC has also been successfully employed to reduce the effect of lead errors on the positioning accuracy during high speed movements. To the best knowledge of the author, the application of AFC for improving the positioning accuracy of ball screw drives is studied in this thesis for the first time. The results obtained from metal cutting and high speed tracking tests have shown that a significant improvement in the tracking accuracy is achievable with the AFC method.

## **6.1 Future Research Directions**

The control methods developed in this thesis was proven effective in damping out the first mode of vibration. This mode was also accurately predicted by the finite element method. However, high frequency modes could not be predicted with the same level of accuracy. The attempts for targeting these modes for active damping were also, so far unsuccessful. Considering that the bandwidth of the current regulation loop is around 400 Hz, the reliability of the measured frequency response data at higher frequencies is under question. To minimize the nonlinear effects that dominate the dynamic response at higher frequencies, it is recommended to upgrade the motor servo driver. The new servo driver should provide at least a bandwidth of 5000 Hz. If the linearity of the system at high frequency range is improved, the system can be modeled and identified with much greater accuracy. This, in turn, helps successful implementation of control methods that target multi-mode vibration suppression.

Regarding harmonic cancellation, one important improvement that can be made is considering the effect of actuator saturation in the control design. Since the position response of the table rolls off quickly beyond the frequency of resonance, the perfect compensation of high frequency disturbances may demand control signals that exceed the saturation limits of the actuator. In this situation, the AFC generates large signals that can destabilize the control system. However, if the effect of saturation is accounted for, the partial compensation of the harmonic disturbances should be made possible by the AFC without violating the saturation limits.

As mentioned in Chapter 2, there are different configurations for integration of the AFC with a main controller. The pros and cons of each configuration should be studied in more detail, especially if they are going to be used with some sort of anti-windup strategy for preventing actuator saturation.

## Bibliography

- [1] Okwudire, C. E., and Altintas, Y., 2009, "Hybrid Modeling of Ball Screw Drives with Coupled Axial, Torsional, and Lateral Dynamics," *ASME Journal of Mechanical Design*, **131**(7), pp. 071002-1-071002-9.
- [2] Ellis, G., and Lorenz, R. D., 2000, "Resonant Load Control Methods for Industrial Servo Drives," *Conference Record of the 2000 IEEE Industry Applications Conference*, Rome, Italy, **3**, pp.1438-1445.
- [3] Gordon, D. J., and Erkorkmaz, K., 2013, "Accurate Control of Ball Screw Drives using Pole-Placement Vibration Damping and a Novel Trajectory Prefilter," *Precision Engineering*, **37**(2), pp. 308-322.
- [4] McFarlane, D., and Glover, K., 1992, "A Loop-Shaping Design Procedure using  $H_{\infty}$  Synthesis," *IEEE Transactions on Automatic Control*, **37**(6), pp. 759-769.
- [5] Kelling, L. U. C., 1955, "Numerical Control of Machine Tools," *IRE Transactions on Industrial Electronics*, **2**(1), pp. 3-8.
- [6] Kroll, L., Blau, P., Wabner, M., 2011, "Lightweight Components for Energy-Efficient Machine Tools," *CIRP Journal of Manufacturing Science and Technology*, **4**(2), pp. 148-160.
- [7] Luttrell, D., and Dow, T., 1987, "Development of a High Speed System to Control Dynamic Behaviour of Mechanical Structures," *Precision Engineering*, **9**(4), pp. 191-200.
- [8] Pritschow, G., 1998, "A Comparison of Linear and Conventional Electromechanical Drives," *CIRP Annals-Manufacturing Technology*, **47**(2), pp. 541-548.
- [9] Lopez de Lacalle, N.L., and Lamikiz, A., 2009, *Machine Tools for High Performance Machining*, Springer, London, UK.
- [10] Crowder, R., 2006, *Electric Drives and Electromechanical Systems: Applications and Control*, Elsevier, Amsterdam, The Netherlands.
- [11] Varanasi, K. K., and Nayfeh, S. A., 2004, "The Dynamics of Lead-Screw Drives: Low-Order Modeling and Experiments," *ASME Journal of Dynamic Systems, Measurement, and Control*, **126**(2), pp. 388-396.
- [12] Erkorkmaz, K., and Altintas, Y., 2001, "High Speed CNC System Design. Part II: Modeling and Identification of Feed Drives," *International Journal of Machine Tools and Manufacture*, **41**(10), pp. 1487-1509.
- [13] Kamalzadeh, A., and Erkorkmaz, K., 2007, "Compensation of Axial Vibrations in Ball Screw Drives," *CIRP Annals-Manufacturing Technology*, **56**(1), pp. 373-378.

- [14] Sato, K., and Maeda, G. J., 2009, "A Practical Control Method for Precision Motion: Improvement of NCTF Control Method for Continuous Motion Control," *Precision Engineering*, **33**(2), pp. 175-186.
- [15] Hakoda, F., Sone, Y., Yamauchi, A., 2009, "Sliding Mode Control with Frequency-Shaped Hyperplane for a Ball Screw Driving Stage," *Journal of System Design and Dynamics*, **3**(1), pp. 25-36.
- [16] Sakata, K., Fujimoto, H., and Saiki, K., 2008, "Positioning of Large-Scale High-Precision Stage with Vibration Suppression PTC," *Proceedings of 17th IFAC World Congress*, Seoul, Korea, pp.3124-3129.
- [17] Hosseinkhani, Y., and Erkorkmaz, K., 2012, "High Frequency Harmonic Cancellation in Ball-Screw Drives," *Procedia CIRP*, **1**(1), pp. 615-620.
- [18] Frey, S., Dadalau, A., and Verl, A., 2012, "Expedient Modeling of Ball Screw Feed Drives," *Production Engineering*, **6**(2), pp. 205-211.
- [19] Holroyd, G., 2007, "The Modelling and Correction of Ball-Screw Geometric, Thermal and Load Errors on CNC Machine Tools," Ph.D. thesis, University of Huddersfield.
- [20] Okwudire, C., 2009, "Modeling and Control of High Speed Machine Tool Feed Drives," Ph.D. thesis, University of British Columbia.
- [21] Gordon, D. J., and Erkorkmaz, K., 2012, "Precision Control of a T-Type Gantry using Sensor/Actuator Averaging and Active Vibration Damping," *Precision Engineering*, **36**(2), pp. 299-314.
- [22] Ewins, D.J., 1984, *Modal Testing : Theory and Practice*, Research Studies Press, Letchworth, UK.
- [23] Campomanes, M.L., 1998, "Dynamics of Milling Flexible Structures," M.Sc. thesis, University of British Columbia.
- [24] Richardson, M. H., and Formenti, D. L., 1982, "Parameter Estimation from Frequency Response Measurements using Rational Fraction Polynomials," *Proceedings of the 1st International Modal Analysis Conference*, Orlando, FL, USA, **1**, pp.167-186.
- [25] Halevi, Y., 2005, "Control of Flexible Structures Governed by the Wave Equation using Infinite Dimensional Transfer Functions," *Journal of Dynamic Systems, Measurement and Control, Transactions of the ASME*, **127**(4), pp. 579-588.
- [26] Meirovitch, L., 1980, *Computational Methods in Structural Dynamics*, Sijthoff & Noordhoff, The Netherlands.

- [27] Cook, R.D., Malkus, D.S., Plesha, M.E., 2002, *Concepts and Applications of Finite Element Analysis*, Wiley, New York, NY, USA.
- [28] Van Brussel, H., Sas, P., Nemeth, I., 2001, "Towards a Mechatronic Compiler," *IEEE/ASME Transactions on Mechatronics*, **6**(1), pp. 90-105.
- [29] Okwudire, C., 2005, "Finite Element Modeling of Ballscrew Feed Drive Systems for Control Purposes," M.Sc. thesis, University of British Columbia.
- [30] Smith, D.A., 1999, "Wide Bandwidth Control of High-Speed Milling Machine Feed Drives," Ph.D. thesis, University of Florida.
- [31] Kamalzadeh, A., 2008, "Precision Control of High Speed Ball Screw Drives," Ph.D. thesis, University of Waterloo.
- [32] Zaeh, M. F., and Oertli, T., 2004, "Finite Element Formulation of Pre-Stressed Ball Screw Drives," *Proceedings of the 7th Biennial Conference on Engineering Systems Design and Analysis*, Manchester, UK, **3**, pp.289-296.
- [33] Dadalau, A., Mottahedi, M., Groh, K., 2010, "Parametric Modeling of Ball Screw Spindles," *Production Engineering*, **4**(6), pp. 625-631.
- [34] Tomizuka, M., 1996, "Robust Digital Motion Controllers for Mechanical Systems," *Robotics and Autonomous Systems*, **19**(2), pp. 143-149.
- [35] Armstrong-Hélouvry, B., Dupont, P., and De Wit, C. C., 1994, "A Survey of Models, Analysis Tools and Compensation Methods for the Control of Machines with Friction," *Automatica*, **30**(7), pp. 1083-1138.
- [36] Dahl, P.R., 1968, "A solid friction model," The Aerospace Corporation, TOR-158(3107-18), El Segundo, CA.
- [37] De Wit, C. C., Olsson, H., Astrom, K. J., 1995, "A New Model for Control of Systems with Friction," *IEEE Transactions on Automatic Control*, **40**(3), pp. 419-425.
- [38] Dupont, P., Hayward, V., Armstrong, B., 2002, "Single State Elastoplastic Friction Models," *IEEE Transactions on Automatic Control*, **47**(5), pp. 787-792.
- [39] Swevers, J., Al-Bender, F., Ganseman, C. G., 2000, "An Integrated Friction Model Structure with Improved Presliding Behavior for Accurate Friction Compensation," *IEEE Transactions on Automatic Control*, **45**(4), pp. 675-686.
- [40] Al-Bender, F., Lampaert, V., and Swevers, J., 2005, "The Generalized Maxwell-Slip Model: A Novel Model for Friction Simulation and Compensation," *Automatic Control, IEEE Transactions On*, **50**; **50**(11), pp. 1883-1887.

- [41] Jamaludin, Z., 2008, "Disturbance Compensation for Machine Tools with Linear Motor Drives," Ph.D. thesis, Katholieke Universiteit Leuven.
- [42] Mekid, S., 2004, "A Non-Linear Model for Pre-Rolling Friction Force in Precision Positioning," Proceedings of the Institution of Mechanical Engineers, Part J: Journal of Engineering Tribology, **218**(4), pp. 305-312.
- [43] Ro, P. I., and Hubbel, P. I., 1992, "Nonlinear Micro-Dynamic Behavior of a Ball-Screw Driven Precision Slide System," Precision Engineering, **14**(4), pp. 229-236.
- [44] Cuttino, J. F., Dow, T. A., and Knight, B. F., 1997, "Analytical and Experimental Identification of Nonlinearities in a Single-Nut, Preloaded Ball Screw," Journal of Mechanical Design, **119**(1), pp. 15-19.
- [45] Otsuka, J., and Masuda, T., 1998, "The Influence of Nonlinear Spring Behavior of Rolling Elements on Ultraprecision Positioning Control Systems," Nanotechnology, **9**(2), pp. 85-92.
- [46] Marinescu, I.D., Hitchiner, M., Uhlmann, E., 2006, *Handbook of Machining with Grinding Wheels*, CRC Press, New York, NY, USA.
- [47] Kurfess, T.R., 2004, *Robotics and Automation Handbook*, CRC Press, Boca Raton, FL, USA.
- [48] Donmez, M. A., Blomquist, D. S., Hocken, R. J., 1986, "A General Methodology for Machine Tool Accuracy Enhancement by Error Compensation," Precision Engineering, **8**(4), pp. 187-196.
- [49] Portman, V. T., and Rubenchik, Y. L., 2003, "Uncertainty Assessment of the Geometric Accuracy of the 2D Machined Profile," Measurement Science Review, **3**(3), pp. 83-86.
- [50] Pritschow, G., 1996, "On the Influence of the Velocity Gain Factor on the Path Deviation," CIRP Annals-Manufacturing Technology, **45**(1), pp. 367-371.
- [51] Åström, K. J., Hagander, P., and Sternby, J., 1984, "Zeros of Sampled Systems," Automatica, **20**(1), pp. 31-38.
- [52] Tomizuka, M., 1987, "Zero Phase Error Tracking Algorithm for Digital Control." Journal of Dynamic Systems, Measurement, and Control, **109**(1), pp. 65-68.
- [53] Fujimoto, H., Hori, Y., and Kawamura, A., 2001, "Perfect Tracking Control Based on Multirate Feedforward Control with Generalized Sampling Periods," IEEE Transactions on Industrial Electronics, **48**(3), pp. 636-644.
- [54] Pritschow, G., and Philipp, W., 1992, "Research on the Efficiency of Feedforward Controllers in Direct Drives," CIRP Annals-Manufacturing Technology, **41**(1), pp. 411-415.
- [55] Chan, D., 2010, "Development of an Inkjet Printing System on a Flatbed Router," M.Sc. thesis, University of Waterloo.

- [56] Franklin, G.F., Powell, J.D., and Emami-Naeini, A., 2009, *Feedback Control of Dynamic Systems*, Pearson Prentice Hall, Upper Saddle River, NJ, USA.
- [57] Lorenz, R. D., Lipo, T. A., and Novotny, D. W., 1994, "Motion Control with Induction Motors," *Proceedings of the IEEE*, **82**(8), pp. 1215-1240.
- [58] Toochinda, V., Hollott, C. V., and Chait, Y., 2002, "Disturbance Attenuation in a SITO Feedback Control System," *Proceedings of the American Control Conference*, Anchorage, Alaska, USA, pp.481-486.
- [59] Ellis, G.H., 2004, *Control System Design Guide: A Practical Guide*, Elsevier Academic Press, Boston, MA, USA.
- [60] Ferretti, G., Lucchini, F., Magnani, G., 2005, "A Mechatronic Approach to the Control of Machine Tools," *Proceedings of the 16th IFAC World Congress*, Czech Republic, **16**, pp.1247-1247.
- [61] Chen, Y., and Tlustý, J., 1995, "Effect of Low-Friction Guideways and Lead-Screw Flexibility on Dynamics of High-Speed Machines," *CIRP Annals-Manufacturing Technology*, **44**(1), pp. 353-356.
- [62] Schmidt, P. B., and Lorenz, R. D., 1992, "Design Principles and Implementation of Acceleration Feedback to Improve Performance of DC Drives," *IEEE Transactions on Industry Applications*, **28**(3), pp. 594-599.
- [63] Erkorkmaz, K., and Kamalzadeh, A., 2006, "High Bandwidth Control of Ball Screw Drives," *CIRP Annals - Manufacturing Technology*, **55**(1), pp. 393-398.
- [64] Aström, K., and Wittenmark, B., 1997, *Computer-Controlled Systems : Theory and Design*, Prentice Hall, Upper Saddle River, NJ, USA.
- [65] Franklin, G.F., Workman, M.L., and Powell, D., 1998, *Digital Control of Dynamic Systems*, Addison-Wesley Longman, Menlo Park, CA, USA.
- [66] Kautsky, J., Nichols, N. K., and Van Dooren, P., 1985, "Robust Pole Assignment in Linear State Feedback," *International Journal of Control*, **41**(5), pp. 1129-1155.
- [67] Ogata, K., 2002, *Modern Control Engineering*, Prentice Hall, Upper Saddle River, NJ, USA.
- [68] Utkin, V., 1977, "Variable Structure Systems with Sliding Modes," *IEEE Transactions on Automatic Control*, **22**(2), pp. 212-222.
- [69] Slotine, J., and Weiping, L., 1988, "Adaptive Manipulator Control: A Case Study," *IEEE Transactions on Automatic Control*, **33**(11), pp. 995-1003.

- [70] Altintas, Y., Erkorkmaz, K., and Zhu, W. H., 2000, "Sliding Mode Controller Design for High Speed Feed Drives," *CIRP Annals - Manufacturing Technology*, **49**(1), pp. 265-270.
- [71] Won, M., and Hedrick, J., 2001, "Disturbance Adaptive Discrete-Time Sliding Control with Application to Engine Speed Control." *Journal of Dynamic Systems, Measurement, and Control*, **123**(1), pp. 1-9.
- [72] Okwudire, C., and Altintas, Y., 2009, "Minimum Tracking Error Control of Flexible Ball Screw Drives using a Discrete-Time Sliding Mode Controller," *Journal of Dynamic Systems, Measurement, and Control*, **131**(5), pp. 051006-1-051006-12.
- [73] Itoh, K., Iwasaki, M., and Matsui, N., 2004, "Robust Fast and Precise Positioning of Ball Screw-Driven Table System on Machine Stand," *Proceedings of the 8th IEEE International Workshop on Advanced Motion Control*, Kawasaki, Japan, **1**, pp.511-515.
- [74] Symens, W., Van Brussel, H., and Swevers, J., 2004, "Gain-Scheduling Control of Machine Tools with Varying Structural Flexibility," *CIRP Annals - Manufacturing Technology*, **53**(1), pp. 321-324.
- [75] Sepasi, D., Nagamune, R., and Sassani, F., 2012, "Tracking Control of Flexible Ball Screw Drives with Runout Effect and Mass Variation," *IEEE Transactions on Industrial Electronics*, **59**(2), pp. 1248-1256.
- [76] Ludwick, S. J., Chargin, D. A., Calzaretta, J. A., 1999, "Design of a Rotary Fast Tool Servo for Ophthalmic Lens Fabrication," *Precision Engineering*, **23**(4), pp. 253-259.
- [77] Crudele, M., and Kurfess, T. R., 2003, "Implementation of a Fast Tool Servo with Repetitive Control for Diamond Turning," *Mechatronics*, **13**(3), pp. 243-257.
- [78] Chew, K., and Tomizuka, M., 1990, "Digital Control of Repetitive Errors in Disk Drive Systems," *Control Systems Magazine, IEEE*, **10**(1), pp. 16-20.
- [79] Onuki, Y., and Ishioka, H., 2001, "Compensation for Repeatable Tracking Errors in Hard Drives using Discrete-Time Repetitive Controllers," *IEEE/ASME Transactions on Mechatronics*, **6**(2), pp. 132-136.
- [80] Cosner, C., Anwar, G., and Tomizuka, M., 1990, "Plug in Repetitive Control for Industrial Robotic Manipulators," *Robotics and Automation, 1990. Proceedings., 1990 IEEE International Conference On*, pp.1970-1975.
- [81] Francis, B. A., and Wonham, W. M., 1976, "The Internal Model Principle of Control Theory," *Automatica*, **12**(5), pp. 457-465.
- [82] Hara, S., Yamamoto, Y., Omata, T., 1988, "Repetitive Control System: A New Type Servo System for Periodic Exogenous Signals," *IEEE Transactions on Automatic Control*, **33**(7), pp. 659-668.

- [83] Weiss, G., 1997, "Repetitive Control Systems: Old and New Ideas," *in: Systems and Control in the 21st Century*, Springer, Boston, MA, USA, pp. 389-404.
- [84] Liu, J. J., and Yang, Y. P., 2004, "Frequency Adaptive Control Technique for Rejecting Periodic Runout," *Control Engineering Practice*, **12**(1), pp. 31-40.
- [85] Yamaguchi, T., Hirata, M., and Pang, C.K., 2012, *High Speed Precision Motion Control*, CRC Press, Boca Raton, FL, USA.
- [86] Hwang, J., and Chung, E. S., 2003, "In-Process Cutter Runout Compensation using Repetitive Learning Control," *International Journal of Precision Engineering and Manufacturing*, **4**(4), pp. 13-18.
- [87] Ludwick, S. J., and Profeta, J. A., 2010, "A User's Guide to Repetitive Control Systems and the Internal Model Principle," *Proceedings of ASPE Spring Topical Meeting - Control of Precision Systems*, Cambridge, MA, USA, .
- [88] Kempf, C., Messner, W., Tomizuka, M., 1993, "Comparison of Four Discrete-Time Repetitive Control Algorithms," *IEEE Control Systems*, **13**(6), pp. 48-54.
- [89] Messner, W., and Bodson, M., 1995, "Design of Adaptive Feedforward Algorithms using Internal Model Equivalence," *International Journal of Adaptive Control and Signal Processing*, **9**(2), pp. 199-212.
- [90] Chen, Q., 2009, "Design and Control of a Fast Long Range Actuator for Single Point Diamond Turning," Ph.D. thesis, North Carolina State University.
- [91] Bodson, M., Sacks, A., and Khosla, P., 1994, "Harmonic Generation in Adaptive Feedforward Cancellation Schemes," *IEEE Transactions on Automatic Control*, **39**(9), pp. 1939-1944.
- [92] Ludwick, S.J., 1999, "A Rotary Fast Tool Servo for Diamond Turning of Asymmetric Optics," Ph.D. thesis, Massachusetts Institute of Technology.
- [93] Byl, M. F., Ludwick, S. J., and Trumper, D. L., 2005, "A Loop Shaping Perspective for Tuning Controllers with Adaptive Feedforward Cancellation," *Precision Engineering*, **29**(1), pp. 27-40.
- [94] Guo, X., and Bodson, M., 2010, "Equivalence between Adaptive Feedforward Cancellation and Disturbance Rejection using the Internal Model Principle," *International Journal of Adaptive Control and Signal Processing*, **24**(3), pp. 211-218.
- [95] Hosseinkhani, Y., and Erkorkmaz, K., 2011, "Harmonic Disturbance Rejection in Tracking Control of Ball Screw Drives," *Proceedings of the 26th ASPE Annual Meeting*, Denver, Colorado, USA, **52**, pp.137-140.

- [96] Blaschke, F., 1971, "A New Method for the Structural Decoupling of AC Induction Machines," *Proceedings of the 2nd Symposium on Multivariable technical Control Systems (IFAC)*, Dusseldorf, Germany, **1**, pp.1-15.
- [97] Takahashi, I., and Ohmori, Y., 1989, "High-Performance Direct Torque Control of an Induction Motor," *IEEE Transactions on Industry Applications*, **25**(2), pp. 257-264.
- [98] Jahns, T. M., Kliman, G. B., and Neumann, T. W., 1986, "Interior Permanent-Magnet Synchronous Motors for Adjustable-Speed Drives," *IEEE Transactions on Industry Applications*, **IA-22**(4), pp. 738-747.
- [99] Morimoto, S., Takeda, Y., and Hirasu, T., 1990, "Current Phase Control Methods for Permanent Magnet Synchronous Motors," *IEEE Transactions on Power Electronics*, **5**(2), pp. 133-139.
- [100] Rashid, M.H., 2001, *Power Electronics Handbook*, Academic Press, San Diego, CA, USA.
- [101] Lattarulo, F., 2011, *Electromagnetic Compatibility in Power Systems*, Elsevier Science, San Diego, CA, USA.
- [102] Wishart, M., Diana, G., and Harley, R., 1990, "Controller Design for Applying Field-Oriented Control to the Permanent Magnet Synchronous Machine," *Electric Power Systems Research*, **19**(3), pp. 219-227.
- [103] Buso, S., and Mattavelli, P., 2006, *Digital Control in Power Electronics*, Morgan & Claypool Publishers, San Rafael, CA, USA.
- [104] Mihailovic, Z., 1998, "Modeling and Control Design of Vsi-Fed Pmsm Drive Systems with Active Load," M.Sc. Thesis, Virginia Polytechnic Institute and State University.
- [105] d'Azzo, J.J., and Houpis, C.D., 1988, *Linear Control System Analysis and Design: Conventional and Modern*, McGraw-Hill Higher Education, New York, NY, USA.
- [106] Przemieniecki, J.S., 1985, *Theory of Matrix Structural Analysis*, Dover, New York.
- [107] Friswell, M.I., and Mottershead, J.E., 1995, *Finite Element Model Updating in Structural Dynamics*, Kluwer Academic Publishers, Dordrecht, The Netherlands.
- [108] NSK Ltd., 2003, *Precision Machine Components*, NSK Catalog No. E3161, Chap. B.
- [109] TB Wood's Inc., 2007, *Flexible Couplings Catalog*, Section F5, from: <http://www.altraliterature.com/pdfs/P-1690-TBW.pdf>.
- [110] Altintas, Y., Verl, A., Brecher, C., 2011, "Machine Tool Feed Drives," *CIRP Annals-Manufacturing Technology*, **60**(2), pp. 779-796.

- [111] Altintas, Y., and Khoshdarregi, M., 2012, "Contour Error Control of CNC Machine Tools with Vibration Avoidance," *CIRP Annals-Manufacturing Technology*, **61**(1), pp. 335-338.
- [112] Weng, M., Lu, X., and Trumper, D. L., 2002, "Vibration Control of Flexible Beams using Sensor Averaging and Actuator Averaging Methods," *IEEE Transactions on Control Systems Technology*, **10**(4), pp. 568-577.
- [113] Meriam, J., and Kraige, L., 1987, *Engineering Mechanics: Dynamics*, John Willy & Sons Inc, New York, NY, USA.
- [114] Gawronski, W., 1998, *Dynamics and Control of Structures: A Modal Approach*, Springer, Berlin, Germany.
- [115] Altintas, Y., 2012, *Manufacturing Automation: Metal Cutting Mechanics, Machine Tool Vibrations, and CNC Design*, Cambridge university press, New York, NY, USA.
- [116] Rivin, E.I., 1999, *Stiffness and Damping in Mechanical Design*, Marcel Dekker, Inc., New York, NY.

## Appendix A

### Finite Element Modeling of Ball Screw-Driven Feed Drives

This appendix explains the details of the finite element formulations used in this thesis. The equations presented in Section A.3 are derived by Okwudire in [1].

#### A.1 Proposed Finite Element Scheme for the Test Setup

Figure A.1 shows the proposed scheme for the finite element modeling of the test setup. The motor shaft can be modeled either as a rigid or flexible part. Because the stiffness of the motor shaft is usually much higher than the stiffness of the other components, it has been treated as a rigid part in this work. A lumped-mass two-node element is used for modeling the mechanical coupling. The stiffness of this element depends on the stiffness of the coupling itself, and the stiffness of the fasteners connecting the coupling hubs to the motor shaft on one side, and to the screw shaft on the other side. The effects of the bearings are taken into account by applying appropriate boundary conditions, or by directly incorporating their stiffness properties into the model (when such information is available). Beam elements are used to discretize the screw shaft. Here, the Timoshenko beam formulation is selected for this purpose, because it provides more accurate results compared to the Euler-Bernoulli formulation when it comes to dynamic analysis. The nut-table assembly is modeled altogether as a rigid part.

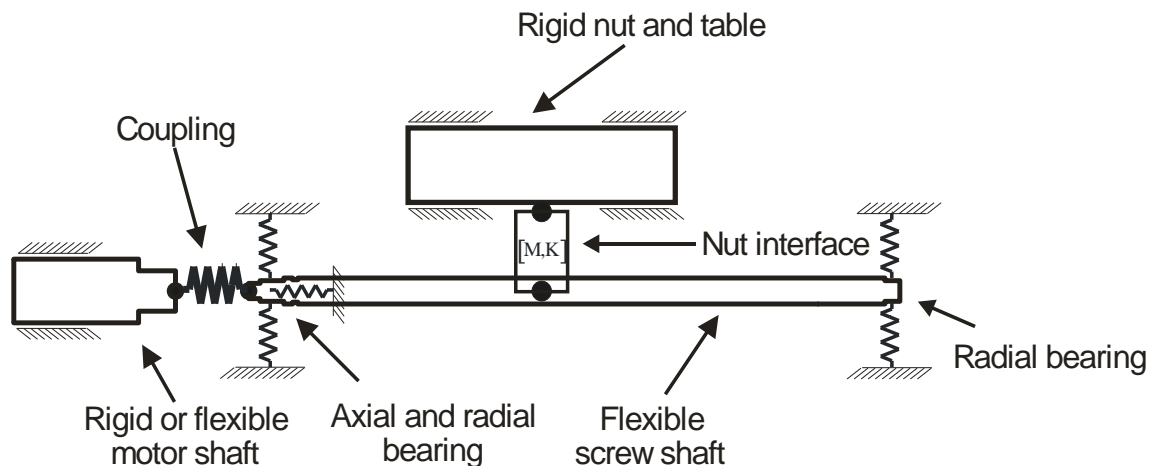


**Figure A.1: Proposed FE modeling scheme for ball screw-driven feed drives.**

## A.2 Finite Element Modeling of the Screw Shaft

Despite the three-dimensional geometry of the helical thread, the screw shaft can be modeled as a beam-type structure. However, the equivalent diameters must be implemented when formulating the stiffness and mass matrices of the elements. To find out the equivalent diameters for mass matrix calculations, a CAD model of the threaded portion of the screw shaft needs to be constructed. The equivalent diameter for calculating the second moment of inertia in the mass matrix formulations is obtained from the following equation:

$$(d_{eq})_r = \sqrt[4]{\frac{32J}{\rho\pi L}} \quad (\text{A.1})$$

Above,  $\rho = 7850 \text{ Kg/m}^3$  is the material density for steel,  $L$  is the length of the threaded portion, and  $J$  is the polar second moment of inertia calculated by the CAD geometric modeler.

The equivalent diameter for calculating the linear inertia terms in mass matrix calculation is obtained from the following equation:

$$(d_{eq})_l = \sqrt{\frac{4V}{\pi L}} \quad (\text{A.2})$$

Above,  $V$  is the volume calculated by the CAD geometric modeler. The values obtained in Equations (A.1) and (A.2) are also applicable for calculating the area, and the second moment of area of the cross section in stiffness matrix calculations. In our setup, the length of the threaded portion of the screw shaft is 1010 mm. The volume of this portion is calculated by the CAD program as  $V = 303,688 \text{ mm}^3$  and its polar second moment of inertia is also calculated as  $J = 115.1202 \times 10^{-6} \text{ Kg.m}^2$ . Therefore, the following values are obtained for equivalent diameters of the threaded portion of the screw shaft:

$$(d_{eq})_r = 19.61 \text{ mm}, (d_{eq})_l = 19.57 \text{ mm} \quad (\text{A.3})$$

As can be seen, for this particular ball screw, these values are close to each other. However, in short-lead ball screws, with large-diameter balls, this may not be the case.

### A.2.1 Three-Dimensional Modeling

Three-dimensional Euler-Bernoulli and Timoshenko beam formulations are well known and widely used in engineering applications. Although the Euler-Bernoulli beam model leads to reasonable results when the cross-sectional dimensions of the beam are small compared to its length, for dynamic





### A.3 Modeling of the Ball screw-Nut Interface

To increase the stiffness and positioning accuracy of precision ball screws, preloading is usually applied. There are different methods for imposing preload on the ball screw-nut interface. In our setup, preload comes from the compression of the oversized balls in the helical grooves of the screw-nut interface. This type of compression results in four points of contact between the balls and the surrounding grooves. By neglecting the effect of friction, it can be assumed that the force transmission in each ball occurs only along the two contact normals. Here, separate names are given to each of these two force-transmission configurations: referring to Figure A.3 , one configuration is called the “L-configuration”, because in that case, the elastic force passes through the lower contact point between the ball and the screw, whereas the other one, in which the upper contact point is involved, is called the “U-configuration”. The motive behind this separation is to formulate the stiffness contribution corresponding to each configuration individually. The principle of superposition is then implemented to add up the effect of each configuration, and find out the total stiffness.

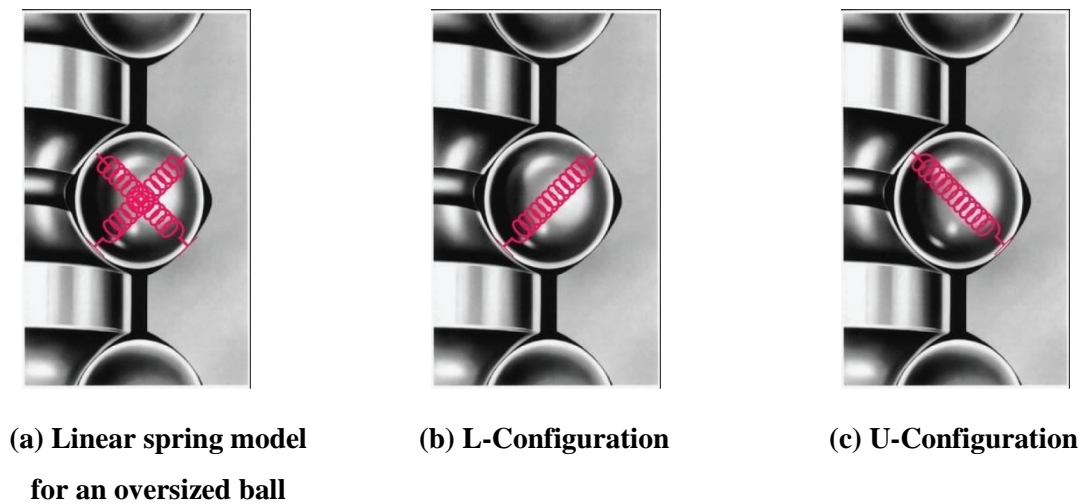


**Figure A.3: Linear spring model for an oversized ball (a) and its decomposition into “L” (lower) and “U” (upper) configurations (b and c).**

As mentioned in Chapter 3, the method used in this thesis for calculating the stiffness matrix of the ball screw-nut interface is based on the work published by Okwudire and Altintas [1], which is currently the most comprehensive model in the literature. This method starts out with considering the stiffness properties of a single ball in the normal contact direction. After a series of successive geometric transformations, the stiffness of each load carrying ball is transformed into a global

coordinate system. To lump all the stiffness values together, the relative motion of each load carrying ball with respect to the global coordinate system is taken into account.

### A.3.1 Introduction of the Intermediate Coordinate Systems

As shown in Figure A.4a, when a ball rolls over the groove surface, its center moves along a helical curve. We call this curve the “Constructive Helix”. Corresponding to each position of the ball, Coordinate System 1 (CS1) is defined such that its origin coincides with the ball center, and its x-axis is tangent to the constructive helix at the ball center. The z-axis of the CS1 is defined in the direction of the contact normal. Both contact normal vectors in the L and U configurations lie in a plane which is normal to the constructive helix, and passes through the ball center. We call this plane the “Normal Plane”. The y-axis of the CS1 also lies in the normal plane, and its direction can be determined using the right hand rule. Figure A.4b shows a section view of the screw shaft with a contacting ball. Here, the normal plane has been used to define the section view.

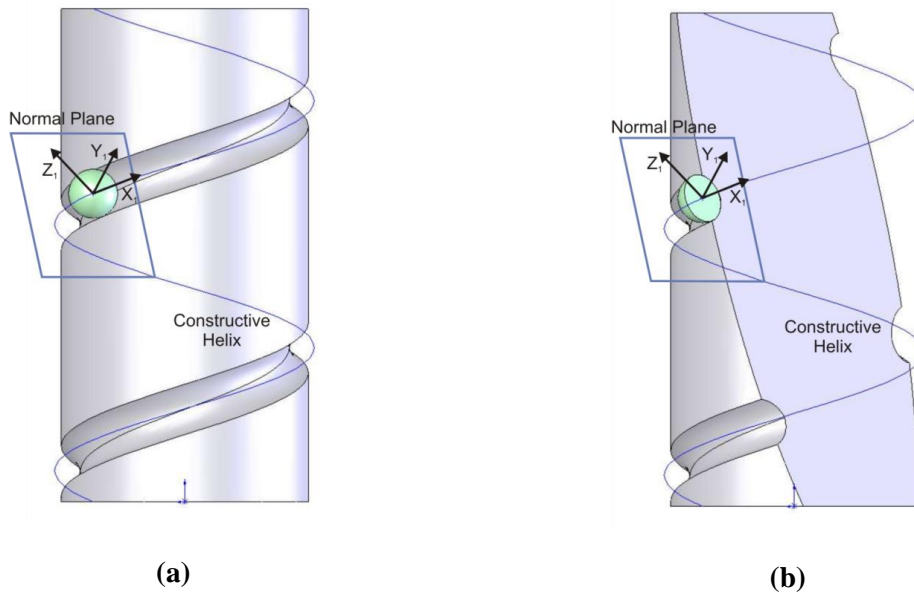


**Figure A.4: CS1 definition shown for L-Configuration in (a) full view and (b) section view.**

A closer view of this section is demonstrated in Figure A.5. When ball screws are designed based on oversized-ball type of preloading, a Gothic-arch profile is chosen for the cross sectional profile of the helical groove [116]. This profile can be identified easily in the figure. The Coordinate System 2 (CS2) has the same origin and x-axis as CS1. Therefore, its y and z axes also lie in the same normal plane. However, the y-axis of CS2 is aligned with the axis of symmetry of the Gothic arc. Fig. 34

shows that the CS2 coincides with the CS1 after a rotation  $\beta$  (in L-configuration) or  $-\beta$  (in U-configuration) around its x-axis. Angle  $\beta$  is called the “contact angle”.

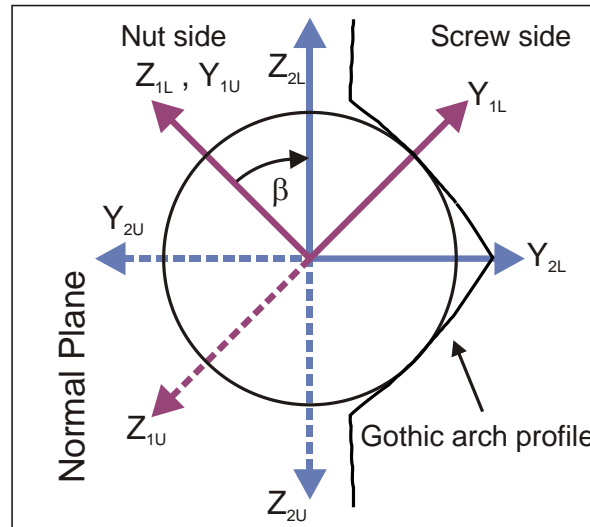


**Figure A.5: CS1 and CS2 definitions in L and U configurations.**

The origin of the Coordinate System 3 (CS3) is also located at the center of the contacting ball. However, its axes are defined based on the cylindrical geometry of the screw shaft, such that its Z-axis is parallel to the main axis of the cylinder, its X-axis is in the circumferential direction, and its Y-axis is defined correspondingly in the radial direction. Figure A.6 shows that the CS3 coincides with CS2, after a rotation  $-\alpha$  (in L-configuration) or  $\alpha$  (in U-configuration) around its y-axis. Angle  $\alpha$  is the “lead angle” of the screw shaft.

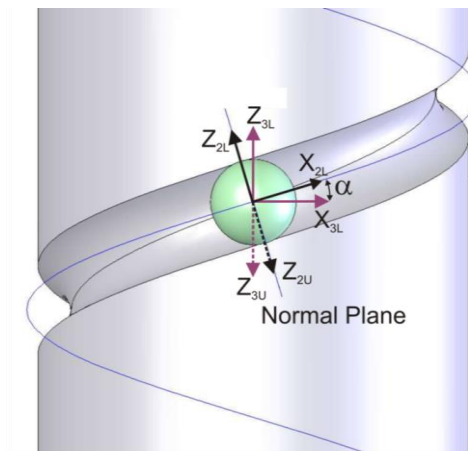


**Figure A.6: The definition of the CS3.**

All the coordinate systems defined so far are dependent on the local position of the contacting ball with respect to the screw shaft. In order to formulate the stiffness matrix of the ball screw-nut interface, a global coordinate system is also needed. This coordinate system is called CS5 (Figure A.7). The origin of CS5 is located on the main axis of the screw shaft, with which its z-axis is collinear. Its x and y axes are defined such that the portion of the constructive helix passing through the balls can be described in CS5 by the following equation:

$$\mathbf{r} = \begin{bmatrix} R \sin \phi \\ -R \cos \phi \\ r_g \phi \end{bmatrix}, \quad \begin{matrix} -\phi_{Boundary} \leq \phi \leq \phi_{Boundary} \\ r_g = \frac{l}{2\pi} \end{matrix} \quad (\text{A.6})$$

Above,  $R$  is the pitch circle radius of the balls,  $l$  is the ball screw lead, and  $\phi$  is the azimuth angle which simultaneously defines the axial and circumferential position of the ball center with respect to the screw shaft. The angle  $\phi_{Boundary}$  specifies the position in which the balls enter the nut's return-tube or exit from it.

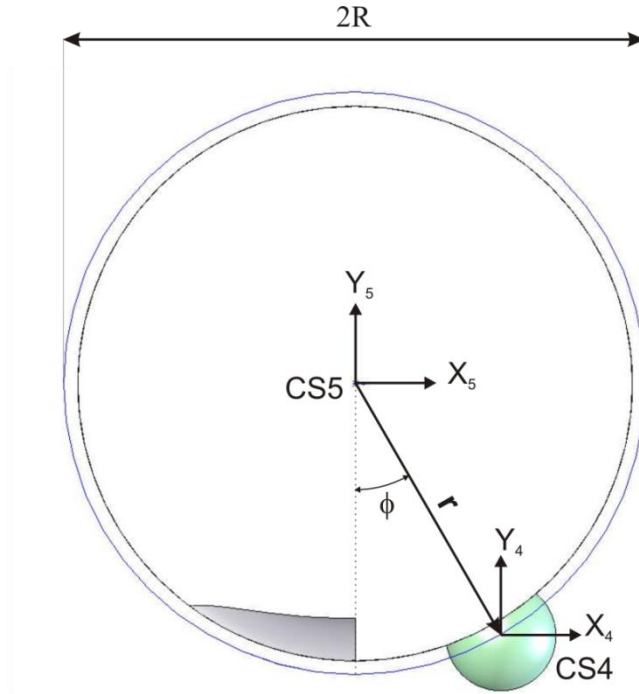


**Figure A.7: Definition of CS5 and CS4.**

The axes of Coordinate System 4 (CS4) are parallel to their corresponding axes in the CS5. However, the origin of the CS4 is located at the center of the ball. Corresponding to each coordinate

system defined so far, two parallel extra coordinate systems can be considered: the origin of one is located at the ball-screw shaft contact point, whereas the origin of the other is at the nut-ball contact point. Subscripts “BS” and “N” are used here to refer to these extra coordinate systems. For example, CS1, CS1<sub>N</sub>, and CS1<sub>BS</sub> are shown in Figure A.8. CS5<sub>N</sub> and CS5<sub>BS</sub> are defined to be coincident with the origin of CS5. However, they are attached to the nut, and to the screw shaft, respectively.

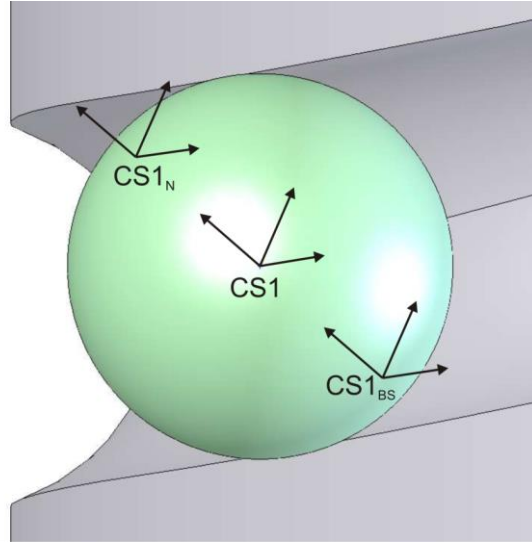


**Figure A.8: Definition of CS1<sub>N</sub> and CS1<sub>BS</sub> with respect to CS1.**

The intermediate coordinate systems defined in this section are used for transforming the unidirectional stiffness properties of each ball to the global coordinate system (CS5). The details of these transformations are elaborated in the next section.

### **A.3.2 Derivation of the Stiffness Matrix for the Ball screw-Nut Interface**

As mentioned earlier, each load-carrying ball is modeled as a 2-node linear spring. The locations of the nodes are at the contact points in two opposite sides of the ball. The displacements in the z-direction of the CS1<sub>N</sub> and CS1<sub>BS</sub> can be used as the minimum set of generalized coordinates, required for fully defining the stiffness properties of this element. Using this set of coordinates ( $\mathbf{q}_1$ ), the stiffness matrix of this element can be written as follows:

$$([\mathbf{K}]_{ball})_1 = \begin{bmatrix} k_{ball} & -k_{ball} \\ -k_{ball} & k_{ball} \end{bmatrix}, \mathbf{q}_1 = \begin{bmatrix} (z)_{CS1_{BS}} \\ (z)_{CS1_N} \end{bmatrix} \quad (\text{A.7})$$

Above and hereafter, the subscripts refer to the coordinate system in which the equations hold. In order to define a single stiffness matrix for the whole ball screw-nut interface, utilization of the following coordinates is desired:

$$\mathbf{q}_5 = \begin{bmatrix} (x)_{CS5_{BS}} \\ (y)_{CS5_{BS}} \\ (z)_{CS5_{BS}} \\ (\theta_x)_{CS5_{BS}} \\ (\theta_y)_{CS5_{BS}} \\ (\theta_z)_{CS5_{BS}} \\ (x)_{CS5_N} \\ (y)_{CS5_N} \\ (z)_{CS5_N} \\ (\theta_x)_{CS5_N} \\ (\theta_y)_{CS5_N} \\ (\theta_z)_{CS5_N} \end{bmatrix} = \begin{bmatrix} (\mathbf{u})_{CS5_{BS}} \\ (\boldsymbol{\theta})_{CS5_{BS}} \\ (\mathbf{u})_{CS5_N} \\ (\boldsymbol{\theta})_{CS5_N} \end{bmatrix} \quad (\text{A.8})$$

If the transformation matrix which converts  $\mathbf{q}_5$  to  $\mathbf{q}_1$  is denoted by  $T_{1-5}$ , then the contribution of the ball stiffness into the stiffness matrix of the interface can be obtained as:

$$([\mathbf{K}_{ball}]_5) = T_{1-5}^T \times ([\mathbf{K}_{ball}]_1) \times T_{1-5} \quad (\text{A.9})$$

Each ball contributes to the stiffness of the interface in both the L and U configurations. Therefore, it is necessary to find out the transformations applicable for each configuration. These transformations are denoted by  $T_{1-5}^L$  and  $T_{1-5}^U$  respectively, and the corresponding stiffness contributions are represented by:  $([\mathbf{K}_{ball}]_5)^L$  and  $([\mathbf{K}_{ball}]_5)^U$ .

$T_{1-5}$  can be decomposed into a series of body-fixed successive transformations:

$$\begin{aligned} T_{1-5}^L &= T_{1-2}^L \times T_{2-3}^L \times T_{3-4}^L \times T_{4-5}^L \\ T_{1-5}^U &= T_{1-2}^U \times T_{2-3}^U \times T_{3-4}^U \times T_{4-5}^U \end{aligned} \quad (\text{A.10})$$

Some of these transformations can be formulated in terms of standard rotation matrices. As a reminder, the standard rotation matrices are given in Equation (A.11).

$$\begin{aligned}
Rot_x(\theta) &= \begin{bmatrix} 1 & 0 & 0 \\ 0 & \cos\theta & -\sin\theta \\ 0 & \sin\theta & \cos\theta \end{bmatrix}, Rot_y(\theta) = \begin{bmatrix} \cos\theta & 0 & \sin\theta \\ 0 & 1 & 0 \\ -\sin\theta & 0 & \cos\theta \end{bmatrix}, \\
Rot_z(\theta) &= \begin{bmatrix} \cos\theta & -\sin\theta & 0 \\ \sin\theta & \cos\theta & 0 \\ 0 & 0 & 1 \end{bmatrix}
\end{aligned} \tag{A.11}$$

The derivations of the first three intermediate transformations ( $T_{1-2}, T_{2-3}, T_{3-4}$ ) are summarized below:

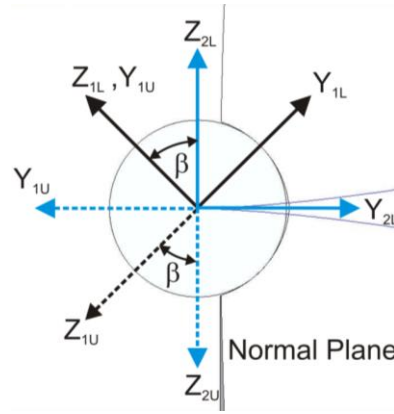


**Figure A.9: Definition of CS2 with respect to CS1.**

Based on the geometry in Figure A.9, the transformation between CS1 and CS2 can be written as follows:

$$\begin{aligned}
\mathbf{q}_1 &= \begin{bmatrix} 0 \\ 0 \\ (z)_{CS1_{BS}} \\ 0 \\ 0 \\ (z)_{CS1_N} \end{bmatrix}, \mathbf{q}_2 = \begin{bmatrix} (x)_{CS2_{BS}} \\ (y)_{CS2_{BS}} \\ (z)_{CS2_{BS}} \\ (x)_{CS2_N} \\ (y)_{CS2_N} \\ (z)_{CS2_N} \end{bmatrix}, \mathbf{q}_1 = T_{1-2}^{L/U} \mathbf{q}_2 \\
T_{1-2}^L &= \begin{bmatrix} Rot_{X_1}(-\beta) & 0 \\ 0 & Rot_{X_1}(-\beta) \end{bmatrix}_{6 \times 6} \\
T_{1-2}^U &= \begin{bmatrix} Rot_{X_1}(\beta) & 0 \\ 0 & Rot_{X_1}(\beta) \end{bmatrix}_{6 \times 6}
\end{aligned} \tag{A.12}$$

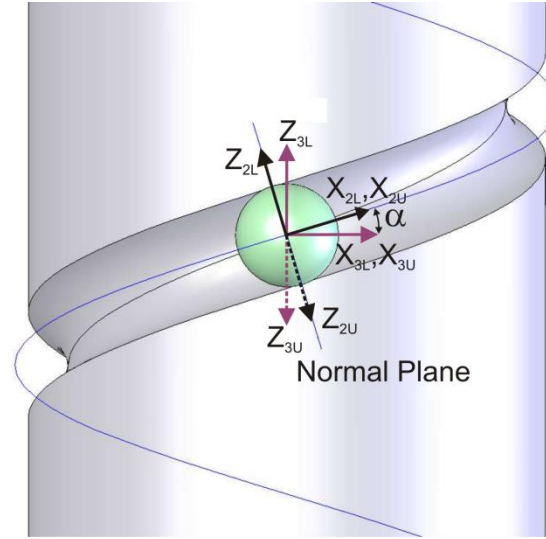


**Figure A.10: Position of CS2 with respect to CS3.**

The transformation between CS2 and CS3 is presented in Equation (A.13) based on the geometry in Figure A.10:

$$\mathbf{q}_2 = \begin{bmatrix} (x)_{CS2_{BS}} \\ (y)_{CS2_{BS}} \\ (z)_{CS2_{BS}} \\ (x)_{CS2_N} \\ (y)_{CS2_N} \\ (z)_{CS2_N} \end{bmatrix}, \mathbf{q}_3 = \begin{bmatrix} (x)_{CS3_{BS}} \\ (y)_{CS3_{BS}} \\ (z)_{CS3_{BS}} \\ (x)_{CS3_N} \\ (y)_{CS3_N} \\ (z)_{CS3_N} \end{bmatrix}, \mathbf{q}_2 = T_{2-3}^{L/U} \mathbf{q}_3 \tag{A.13}$$

$$T_{2-3}^L = \begin{bmatrix} Rot_{Y_{2L}}(\alpha) & 0 \\ 0 & Rot_{Y_{2L}}(\alpha) \end{bmatrix}_{6 \times 6}$$

$$T_{2-3}^U = \begin{bmatrix} Rot_{Y_{2U}}(-\alpha) & 0 \\ 0 & Rot_{Y_{2U}}(-\alpha) \end{bmatrix}_{6 \times 6}$$

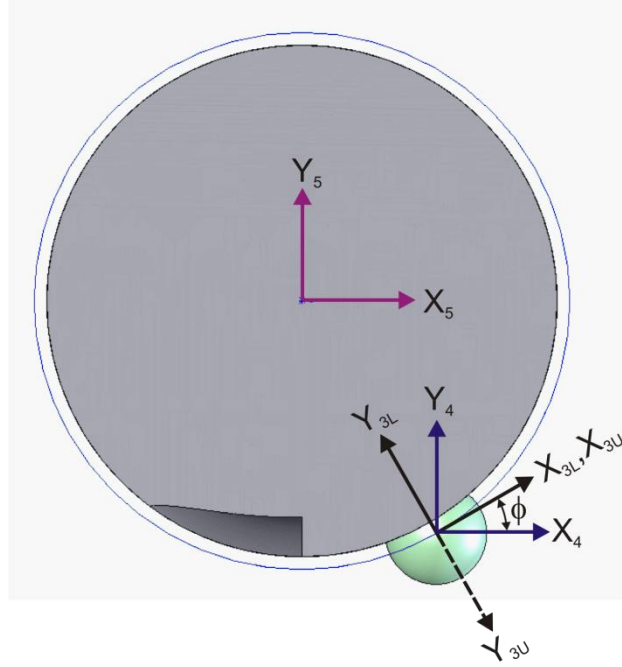


**Figure A.11: Position of CS3 with respect to CS4.**

Considering Figure A.11, the relation between CS3 and CS4 can be established as follows:

$$\mathbf{q}_3 = \begin{bmatrix} (x)_{CS3_{BS}} \\ (y)_{CS3_{BS}} \\ (z)_{CS3_{BS}} \\ (x)_{CS3_N} \\ (y)_{CS3_N} \\ (z)_{CS3_N} \end{bmatrix}, \mathbf{q}_4 = \begin{bmatrix} (x)_{CS4_{BS}} \\ (y)_{CS4_{BS}} \\ (z)_{CS4_{BS}} \\ (x)_{CS4_N} \\ (y)_{CS4_N} \\ (z)_{CS4_N} \end{bmatrix}, \mathbf{q}_3 = T_{3-4}^{L/U} \mathbf{q}_4 \tag{A.14}$$

$$T_{3-4}^L = \begin{bmatrix} Rot_{Z_{3L}}(-\phi) & 0 \\ 0 & Rot_{Z_{3L}}(-\phi) \end{bmatrix}_{6 \times 6}$$

$$T_{3-4}^U = \begin{bmatrix} 1 & 0 & 0 \\ 0 & -1 & 0 \\ 0 & 0 & -1 \end{bmatrix} \times \begin{bmatrix} Rot_{Z_{3L}}(-\phi) & 0 \\ 0 & Rot_{Z_{3L}}(-\phi) \end{bmatrix}_{6 \times 6}$$

While the transformations derived so far have been merely based on the geometric considerations, the rigid-body kinematics equations need to be employed for derivation of the last transformation ( $T_{4-5}$ ).

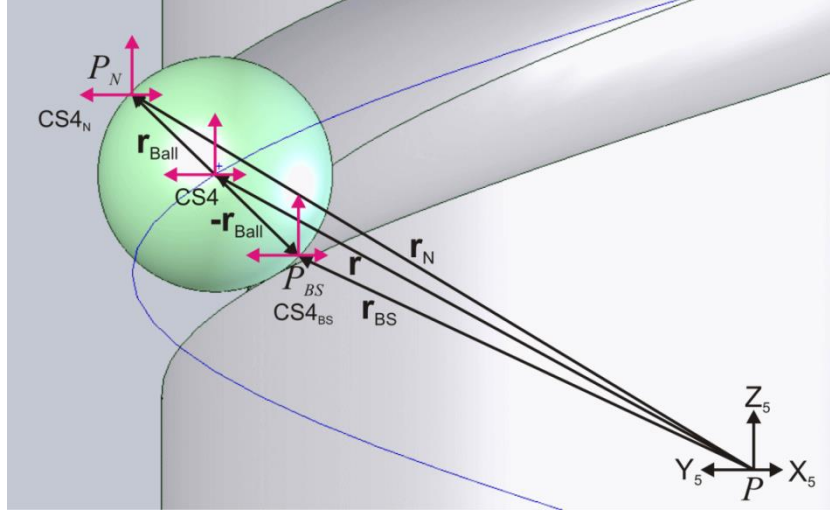


**Figure A.12: Position of CS4 with respect to CS5.**

If  $P$  is the origin of the CS5, and  $P_{BS}, P_N$  are the origins of the CS4<sub>BS</sub>, and CS4<sub>N</sub> respectively (Figure A.12), then the following kinematic relationship holds between the velocities of these points:

$$\begin{aligned} \mathbf{V}_{P_{BS}} &= \mathbf{V}_P + \boldsymbol{\omega}_{BS} \times \mathbf{r}_{BS} \text{ or } \left( \frac{d\mathbf{r}}{dt} \right)_{P_{BS}} = \left( \frac{d\mathbf{r}}{dt} \right)_P + \left( \frac{d\boldsymbol{\psi}}{dt} \right)_{BS} \times \mathbf{r}_{BS} \\ \mathbf{V}_{P_N} &= \mathbf{V}_P + \boldsymbol{\omega}_N \times \mathbf{r}_N \text{ or } \left( \frac{d\mathbf{r}}{dt} \right)_{P_N} = \left( \frac{d\mathbf{r}}{dt} \right)_P + \left( \frac{d\boldsymbol{\psi}}{dt} \right)_N \times \mathbf{r}_N \end{aligned} \quad (\text{A.15})$$

Above,  $\mathbf{r}$  is the linear position of the point and  $\boldsymbol{\psi}$  is the angular position of the rigid body, both expressed in CS5. The above equations can be integrated over an infinitesimal period of time (which also implies infinitesimal angular displacements). If  $d\mathbf{r}$  is replaced by  $\mathbf{u}$  and  $d\boldsymbol{\psi}$  is replaced by  $\boldsymbol{\theta}$ , the integrated form of Equation (A.15) can be written as:

$$\begin{aligned} (\mathbf{u})_{P_{BS}} &= (\mathbf{u})_P - \mathbf{r}_{BS} \times (\boldsymbol{\theta})_{BS} \\ (\mathbf{u})_{P_N} &= (\mathbf{u})_P - \mathbf{r}_N \times (\boldsymbol{\theta})_N \end{aligned} \quad (\text{A.16})$$

Considering Figure A.12,  $\mathbf{r}_{BS}$  and  $\mathbf{r}_N$  can be expressed in terms of  $\mathbf{r}$  and  $\mathbf{r}_{Ball}$  for both L and U configurations as:

$$\begin{aligned}\mathbf{r}_{BS}^{L/U} &= (\mathbf{r})_{CS5} - (\mathbf{r}_{Ball})_{CS4}^{L/U} \\ \mathbf{r}_N^{L/U} &= (\mathbf{r})_{CS5} + (\mathbf{r}_{Ball})_{CS4}^{L/U}\end{aligned}\tag{A.17}$$

Vector  $\mathbf{r}$  is already known in CS5 (Equation (A.6)). To convert  $\mathbf{r}_{Ball}$  from CS1 to CS4, the following equations are used:

L-Configuration:

$$(\mathbf{r}_{Ball})_{CS4}^L = [T_{1-2}^L \times T_{2-3}^L \times T_{3-4}^L]^{-1} (\mathbf{r}_{Ball})_{CS1}^L$$

U-Configuration:

$$(\mathbf{r}_{Ball})_{CS4}^U = [T_{1-2}^U \times T_{2-3}^U \times T_{3-4}^U]^{-1} (\mathbf{r}_{Ball})_{CS1}^U\tag{A.18}$$

$$(\mathbf{r}_{Ball})_{CS1}^{L/U} = \begin{bmatrix} 0 \\ 0 \\ R_{Ball} \end{bmatrix}$$

Knowing  $\mathbf{r}_{BS}$  and  $\mathbf{r}_N$  in CS5, Equation (A.16) can be rewritten in matrix form to give  $T_{4-5}$ :

$$\mathbf{q}_4 = \begin{bmatrix} (\mathbf{u})_{P_{BS}} \\ (\mathbf{u})_{P_N} \end{bmatrix}, \mathbf{q}_5 = \begin{bmatrix} (\mathbf{u})_{CS5_{BS}} \\ (\boldsymbol{\theta})_{CS5_{BS}} \\ (\mathbf{u})_{CS5_N} \\ (\boldsymbol{\theta})_{CS5_N} \end{bmatrix}, \mathbf{q}_4 = T_{4-5}^{L/U} \mathbf{q}_5\tag{A.19}$$

$$T_{4-5}^L = \begin{bmatrix} I_{3 \times 3} & -S(\mathbf{r}_{BS}^L) & 0_{3 \times 3} & 0_{3 \times 3} \\ 0_{3 \times 3} & 0_{3 \times 3} & I_{3 \times 3} & -S(\mathbf{r}_N^L) \end{bmatrix}_{6 \times 12},$$

$$T_{4-5}^U = \begin{bmatrix} I_{3 \times 3} & -S(\mathbf{r}_{BS}^U) & 0_{3 \times 3} & 0_{3 \times 3} \\ 0_{3 \times 3} & 0_{3 \times 3} & I_{3 \times 3} & -S(\mathbf{r}_N^U) \end{bmatrix}_{6 \times 12}$$

Above, operator S is the matrix equivalent of the vector cross product:

$$\mathbf{r} = \begin{bmatrix} r_x \\ r_y \\ r_z \end{bmatrix}, S(\mathbf{r}) = \begin{bmatrix} 0 & -r_z & r_y \\ r_z & 0 & -r_x \\ -r_y & r_x & 0 \end{bmatrix}\tag{A.20}$$

After deriving all intermediate transformations, Equations (A.9) and (A.10) are used to calculate the stiffness contribution of a single ball located at the azimuth angle  $\phi$ . To calculate the average

stiffness contribution of a load-carrying ball to the interface stiffness, Equation (A.9) should be integrated over  $-\phi_{Boundary} \leq \phi \leq \phi_{Boundary}$  and divided by  $2\phi_{Boundary}$  :

$$\mathbf{K}_{ball}^{av} = \frac{\int_{-\phi_{Boundary}}^{\phi_{Boundary}} \left( [\mathbf{K}_{ball}]_5^L + [\mathbf{K}_{ball}]_5^U \right) d\phi}{2\phi_{Boundary}} \quad (\text{A.21})$$

Finally, the stiffness matrix of the ball screw-nut interface can be obtained by multiplying the average ball stiffness with the number of load-carrying balls ( $N$ ):

$$\mathbf{K}_{interface} = N \times \mathbf{K}_{ball}^{av} \quad (\text{A.22})$$

This is a symmetric matrix which can be partitioned into four 6 by 6 sub-matrices, each of which representing the stiffness properties of a single node:

$$\mathbf{K}_{interface} = \begin{bmatrix} \mathbf{k}_{node} & -\mathbf{k}_{node} \\ -\mathbf{k}_{node} & \mathbf{k}_{node} \end{bmatrix}_{12 \times 12} \quad (\text{A.23})$$

Following the method presented in this section, the general form of  $\mathbf{k}_{node}$  is obtained as follows:

$$\mathbf{k}_{node} = \begin{bmatrix} k_{xx} & 0 & k_{xz} & k_{x\theta_x} & 0 & k_{x\theta_z} \\ 0 & k_{yy} & 0 & 0 & k_{y\theta_y} & 0 \\ k_{zx} & 0 & k_{zz} & k_{z\theta_x} & 0 & k_{z\theta_z} \\ k_{\theta_x x} & 0 & k_{\theta_x z} & k_{\theta_x \theta_x} & 0 & k_{\theta_x \theta_z} \\ 0 & k_{\theta_y y} & 0 & 0 & k_{\theta_y \theta_y} & 0 \\ k_{\theta_z x} & 0 & k_{\theta_z z} & k_{\theta_z \theta_x} & 0 & k_{\theta_z \theta_z} \end{bmatrix} \quad (\text{A.24})$$

### A.3.3 The Mass Matrix for the Ball screw-Nut Interface

In developing the nut interface element, the nut and the table are modeled altogether as a rigid part. Therefore, the linear and rotary inertia of the table has been lumped into the inertia properties of the second node of the interface element:

$$[\mathbf{M}]_{\text{interface}} = \begin{bmatrix} 0 & 0 & 0 & 0 & 0 & 0 & 0 & 0 & 0 & 0 & 0 & 0 \\ 0 & 0 & 0 & 0 & 0 & 0 & 0 & 0 & 0 & 0 & 0 & 0 \\ 0 & 0 & 0 & 0 & 0 & 0 & 0 & 0 & 0 & 0 & 0 & 0 \\ 0 & 0 & 0 & 0 & 0 & 0 & 0 & 0 & 0 & 0 & 0 & 0 \\ 0 & 0 & 0 & 0 & 0 & 0 & 0 & 0 & 0 & 0 & 0 & 0 \\ 0 & 0 & 0 & 0 & 0 & 0 & 0 & 0 & 0 & 0 & 0 & 0 \\ 0 & 0 & 0 & 0 & 0 & 0 & m & 0 & 0 & 0 & 0 & 0 \\ 0 & 0 & 0 & 0 & 0 & 0 & 0 & m & 0 & 0 & 0 & 0 \\ 0 & 0 & 0 & 0 & 0 & 0 & 0 & 0 & m & 0 & 0 & 0 \\ 0 & 0 & 0 & 0 & 0 & 0 & 0 & 0 & 0 & I_{xx} & I_{xy} & I_{xz} \\ 0 & 0 & 0 & 0 & 0 & 0 & 0 & 0 & 0 & I_{yx} & I_{yy} & I_{yz} \\ 0 & 0 & 0 & 0 & 0 & 0 & 0 & 0 & 0 & I_{zx} & I_{zy} & I_{zz} \end{bmatrix} = \begin{bmatrix} \mathbf{M}_{\text{node1}} & 0 \\ 0 & \mathbf{M}_{\text{node2}} \end{bmatrix}_{12 \times 12} \quad (\text{A.25})$$